Workshop II

Evolution of Galaxies

Chairmen:

Dr. Bohdan Hnatyk (IAPMM NASU, Ukraine)
Prof. Igor Karachentsev (SAO RAS, Russia)
Dr. Claus Leitherer (STScI, USA)
Dr. Sergiy Silich (MAO NASU, Ukraine)

STAR FORMATION AND METAL PRODUCTION IN THE EARLY UNIVERSE

C. Leitherer

Space Telescope Science Institute
3700 San Martin Drive, Baltimore, MD 21218, USA
e-mail: leitherer@stsci.edu

Recent advances in our understanding of star formation and the associated production of heavy elements at high redshift are reviewed. First, the host galaxies of star-formation regions at 2 – 4 redshift are characterized, and a comparison with their local counterparts is made. Then I will summarize the properties of the stellar content in these objects. A major theme is the interaction and feedback between star formation and the dynamical state of the interstellar medium of the host galaxy. Star formation enriches the interstellar medium with chemically processed material and may be able to drive the galaxy ISM into the intergalactic medium via powerful superwinds. The chemical composition of star-forming galaxies at high redshift is compared to abundances derived for damped Lyman-α absorbers and the Lyman-α forest. A consistent scenario for the metal production can be derived if the heavy elements produced in star-forming galaxies leave their formation sites and are effectively dispersed in the universe by a yet to be determined mechanism.

THE GALAXY POPULATION AT HIGH REDSHIFT

One of the most notable recent breakthroughs in observational cosmology was the direct verification of star formation in galaxies at an epoch when the universe was young. This progress was made possible largely due to our better understanding of the restframe ultraviolet (UV) light emitted by star forming galaxies in the local and distant universe.

The Hubble Deep Fields North and South are among the most influential astronomical images ever taken (Ferguson, Dickinson, & Williams, 2000). The images for the two Hubble Deep Fields (HDFs) were obtained in four passbands and cover the wavelength range 2500 to 9000 Å. They are suitable for performing a deep optical census of the universe at the highest angular resolution. At low redshift, $z < 1$, the comoving volume sampled in the HDF field of view is rather small, and only about 20 $L^\star$ galaxies are expected for a local galaxy luminosity function. The HDF exposures are deep enough to detect essentially all $L^\star$ galaxies with redshift up to $z = 3$. In this case meaningful statistics can be done: the HDF comoving volume $\times$ the luminosity function predicts about 500 $L^\star$ galaxies, all of which can be detected even allowing for some light loss due to dust absorption.

The morphologies of the galaxies seen in the HDFs resemble those of local peculiar late-type spiral and irregular galaxies with approximately $L^\star$ luminosities. There are very few, if any, ellipticals and spirals with bulges and disks at $z > 2$. Since these types are abundant ($z < 1$) their formation must have occurred at redshifts between 1 and 2. We note that the Hubble sequence was created at $1 < z < 2$.

Combination of the optical HDFs with HST NICMOS Deep Fields at 1.1 μm and 1.6 μm allows an evaluation of the importance of morphological K-corrections. Ferguson *et al.* (2000) compared galaxies viewed at optical and near-infrared (IR) wavelengths in the HDFs. Despite some differences, the overall morphologies in the optical and near-IR are remarkably similar. This suggests that K-corrections are insignificant and that dust does not have a major effect on the galaxy morphologies (Dickinson, 2000). The possibility exists that some galaxies are obscured from view *both* in the optical and near-infrared due to large amounts of dust. The galaxies detected by SCUBA in the sub-mm region may fall into this category (Hughes *et al.*, 1998). However, it is unlikely that this population *dominates* the star formation and metal production at $z \approx 3$ (Ferguson, 1999). If the SCUBA galaxies are at $z \approx 3$ (which is subject to debate), it is a distinct population and not the red tail of the HDF galaxies with a large dust obscuration.

The dust attenuation in those galaxies, which are actually detected, can be estimated from their spectral energy distribution and a comparison with model spectra. Generally, the observed colors suggest star-forming galaxies with ages of order 10^8 yr and reddening $0.1 < E(B - V) < 0.4$ if the starburst attenuation law of Calzetti, Kinney, & Storchi-Bergmann (1994) is adopted. The corresponding attenuation of the V flux is about a factor of 5 to 10. Taking into account the reddening corrections, the luminosities are approximately $L^\star$-like, consistent with viral-mass estimates from emission lines in the infrared.

Invited paper.

In summary, the galaxy population at redshift around 3 has morphologies similar to those of luminous late-type/irregular galaxies. The galaxies are actively forming stars, and they show signs of dust obscuration with optical attenuation factors between 5 and 10.

STAR FORMATION IN THE LOCAL AND DISTANT UNIVERSE

Galaxy morphologies and colors allow an overall estimate of the stellar content of galaxies at high redshift. Spectroscopy of representative examples provides more quantitative insight. Steidel and collaborators identified bona fide star-forming galaxies suitable for spectroscopy by pre-selecting them from their strong Lyman breaks. The restframe UV spectra of these galaxies turn out to be quite similar to those of local star-forming galaxies (Steidel *et al.*, 1996). This supports the view that the properties of the late-type/irregular galaxies seen in the HDF are similar to those of UV-selected star-forming galaxies in the local universe. Therefore, we can apply locally calibrated techniques to derive the rates of star formation and metal production at high redshift.

Before discussing the properties of a high redshift star-forming galaxy in detail, I will review some key results found for the local galaxy population — assuming an extrapolation to high redshift is justified, for the reasons given before. A particularly well-studied local example is the interacting (merging?) NGC 1741 system. Conti, Leitherer, & Vacca (1996) proposed this galaxy as a template to be used for comparison with distant star-forming galaxies. NGC 1741 is at a distance of 50 Mpc, its luminosity is close to $L^\star$, and the metallicity is $\frac{1}{4}$ $Z_\odot$. The star formation is concentrated in a ~500 pc large region where the star-formation *intensity* is almost 3 orders of magnitude higher than in our Galaxy. The hot, massive stars with masses above 10 $M_\odot$ are currently forming at rate producing an ionizing photon output 100 times that of the 30 Doradus region. Yet, the stellar mass function in the NGC 1741 starburst and in 30 Doradus are very similar: both follow the classical Salpeter power law (Johnson *et al.*, 1999). In the optical, the morphology of NGC 1741 shows a disturbed disk composed of intermediate-age stars, with the starburst region offset at the periphery. When observed in the UV at 2200 Å, the starburst completely dominates, and an irregular morphology is suggested. Hibbard & Vacca (1997) simulated the appearance of NGC 1741 and similar objects when projected at high redshift; NGC 1741 would look very similar to the irregular, clumpy $L^\star$ galaxies observed in the HDFs.

Moving back to the high-redshift universe, the MS 1512-cB58 galaxy has become the Rosetta Stone for spectroscopic studies. This object was originally discovered in the CNOC cluster redshift survey by Yee *et al.* (1996) and subsequently found to be a lensed star-forming galaxy (Seitz *et al.*, 1998) at a redshift of $z = 2.7$. Its star-formation history and general properties were explored by Ellingson *et al.* (1996), de Mello *et al.* (2000), Pettini *et al.* (2000), and Teplitz *et al.* (2000). The star-formation intensity in MS 1512-cB58 is a few $M_\odot$ yr^{-1} kpc^{-2}, almost identical to the value derived for NGC 1741. In MS 1512-cB58, however, the star formation is likely to extend all over the disk, leading to a total rate of $\sim 10^2$ $M_\odot$ yr^{-1}. This is close to the maximum rate possible, when the total gas mass is converted into stars on a dynamical timescale.

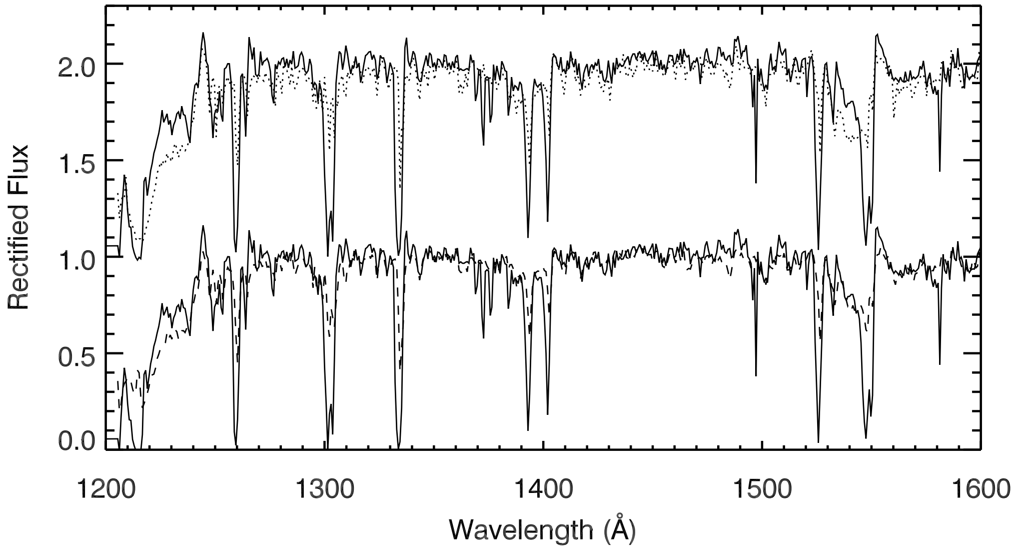

Figure 1: Comparison between the observed spectrum of MS 1512-cB58 (solid lines) and two synthetic models at $Z = \frac{1}{4}$ $Z_\odot$ (lower; dashed) and $Z = Z_\odot$ (upper; dotted). The models have continuous star formation, age 100 Myr, and Salpeter IMF between 1 and 100 $M_\odot$. Adopted from Leitherer *et al.* (2000)

Apart from the spatial extent of the star formation, the stellar population in MS 1512-cB58 seems to be quite similar to that of NGC 1741 and other local starburst galaxies. In Figure 1 a comparison is shown between a restframe UV spectrum of MS 1512-cB58 (Pettini *et al.*, 2000) and synthetic models with a standard stellar initial mass function, which fits local starburst galaxies (Leitherer *et al.*, 2000). The agreement between the observations and the modeled low-Z (lower) spectrum is excellent. The stellar-wind features N V λ1240, Si IV λ1400, and C IV λ1550 are reproduced quite well, except for the narrow interstellar contributions. The mismatch of the interstellar components is expected since the interstellar lines in MS 1512-cB58 are broadened by macroturbulence and blending of multiple components due the energy input from stellar winds and supernovae in starbursts. Generally, the interstellar medium (ISM) in starburst galaxies is more turbulent than in, *e.g.*, the Milky Way and the Magellanic Clouds so that even saturated lines are stronger in starbursts (Heckman & Leitherer, 1997). The comparison in Fig. 1 indicates that the overall spectral fit at $\frac{1}{4}$ $Z_\odot$ is much improved over that with solar composition. Therefore, the conclusion is that MS 1512-cB58, which is observed at a redshift corresponding to an age of the universe of about 2 Gyr, has an LMC/SMC-like chemical composition.

The chemical composition of MS 1512-cB58 and high-redshift galaxies in general is difficult to determine. Due to their redshift, a traditional emission-line analysis is not feasible since some of the key diagnostic lines, like [O III] λ4363, are inaccessible from the ground and/or are simply too faint to be observed. Nevertheless, Teplitz *et al.* (2000) were able to estimate an oxygen abundance $\frac{1}{3}$ $Z_\odot$ from near-IR spectroscopy, using the approximate R_{23} method (*e.g.*, Kobulnicky, Kennicutt, & Pizagno, 1999). Pettini *et al.* (2000) analyzed weak interstellar absorption lines of Si II, S II, and Ni II to infer an abundance of about $\frac{1}{4}$ $Z_\odot$. Each of these analyses may be quite uncertain, but taken together, they give firm evidence for a relatively high metallicity in MS 1512-cB58.

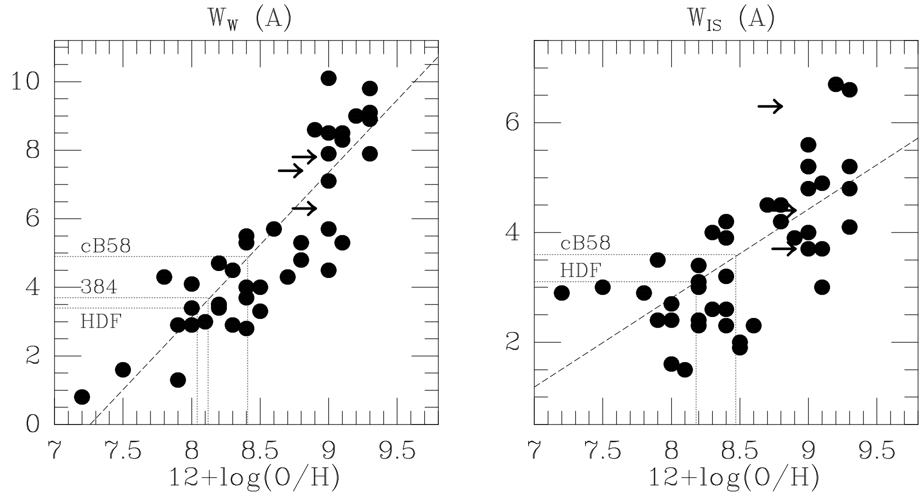

Figure 2: Correlation of the mean stellar-wind (left) and interstellar (right) line equivalent widths with metallicity. Full circles: measurements for the local galaxy sample; arrows: upper limits; dashed line: least squares fit to the data points; dotted lines: observed equivalent widths of MS 1512-cB58, the 384 object, and the HDF sample and corresponding metallicities. Adopted from Leitherer (1999)

MS 1512-cB58 fits rather well the general correlation between the equivalent widths of the UV interstellar (like Si II or C II) and stellar-wind (like Si IV or C IV) lines and metallicity discussed by Leitherer (1999). MS 1512-cB58 is added to this relation in Figure 2. The metallicities of MS 1512-cB58 and other high-z galaxies are in the range $8.0 < 12 + \log(O/H) < 8.9$, with average values close to those of the LMC and SMC. This range is in reasonable agreement with other estimates.

FEEDBACK BETWEEN STAR FORMATION AND THE INTERSTELLAR MEDIUM

Close inspection of Figure 1 shows that the interstellar lines, such as Si II λ1526, are not only broadened due to the dynamics and structure of the ISM, but also blueshifted with respect to the model fiducials. Pettini *et al.* (2000) measure velocity offsets of 200 km s^{-1}. Since the interstellar lines are almost black in their cores, indicating large covering factors, we are witnessing a large-scale outflow of the galactic ISM. Together with the column density of (mildly saturated) interstellar lines, an outflow rate of order 10^2 $M_\odot$ yr^{-1} is found. This rate is surprisingly similar to the derived star-formation rate.

I will return back to the nearby universe in order to compare MS 1512-cB58 with a local paradigm. He 2-10, a blue compact dwarf galaxy, has been the subject of numerous investigations since Allen, Wright, & Goss (1976) first found signatures of Wolf-Rayet stars in its optical spectrum. At a distance of 9 Mpc, He 2-10 is relatively nearby, and has an optical diameter of about 2.8 kpc (Johnson *et al.*, 2000). An HST GHRS spectrum of this galaxy is shown in Figure 3. In this figure the observed spectrum of He 2-10 is compared to a model spectrum for a starburst age of 4 Myr. Apparently, all *stellar* photospheric and wind lines are reproduced extremely well by the model. Compare, for instance, the blue wings of the Si IV λ1400 and C IV λ1550 wind lines, the standard indicators for massive stars. On the other hand, the deep, narrow interstellar absorptions are much broader and more blueshifted in the observations than in the model. The lines are purely interstellar ones arising in the interstellar medium in and around the starburst. The sharp interstellar lines seen in the model spectra can be used to measure the outflow velocity in He 2-10, suggesting a bulk motion of at least $\sim$360 km s^{-1}. The energy sources are almost certainly winds and supernovae. They are capable of initiating large-scale outflows of interstellar gas via so-called galactic superwinds (Chevalier & Clegg, 1985). Johnson *et al.* (2000) estimate that the mass-loss rate of the interstellar medium is quite similar to the star-formation rate in He 2-10. Taken at face value, this suggests that the available gas reservoir will not only be depleted by the star-formation process but, more importantly, by the removal of interstellar material. Starbursts may determine their own fate by prodigious release of their kinetic energy into the interstellar medium.

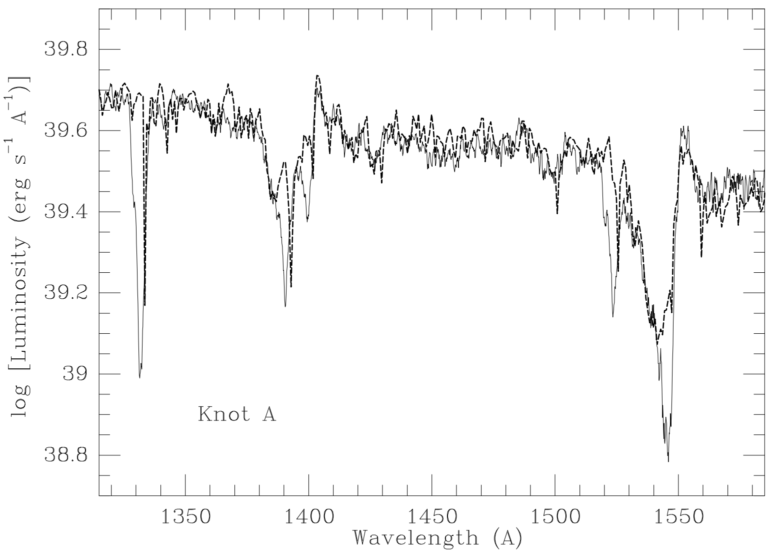

Figure 3: HST GHRS spectrum of He 2-10. The dashed spectrum is a model fit to the *broad* stellar lines. The *narrow* interstellar lines are offset by $\sim$400 km s^{-1}. From Johnson *et al.* (2000)

The dynamical state of the ISM in He 2-10 (and in other local starburst galaxies – see González Delgado *et al.*, 1998) is remarkably similar to that in MS 1512-cB58. This suggests that regions of active star formation generally affect the dynamics of the galactic ISM via non-thermal energy input and remove the interstellar gas locally, possibly initiating global outflows. An important observational consequence is that the line widths of interstellar lines are more sensitive to the stirring by stellar winds and supernova explosions than to the bulk motion of the gas in the gravitational potential of the galaxy. Therefore, these lines are not suitable to estimate the virialized mass (Heckman & Leitherer, 1997).

GALACTIC SUPERWINDS

The combined effect of stellar winds and supernovae overpressurizes the surrounding gas, producing a hot ($10^7 - 10^8$ K), expanding ($\sim 10^2$ km s^{-1}) cavity in the ISM. As discussed in Leitherer *et al.* (1999), the relative importance of stellar winds and supernovae is a function of the age and metallicity of the starburst. For typical starburst parameters, the rate of supply of mechanical energy is of order 1% of the bolometric luminosity of the starburst and typically 10 to 30% of the Lyman continuum luminosity. Some fraction of this mechanical energy may be radiated away by dense shock-heated material inside the starburst. However, observations of superwinds imply that a significant fraction is available to drive the outflow and that radiation losses are not important enough to stall the flow. The hot wind-blown bubble keeps expanding, thereby driving the ambient cold interstellar material from the star-formation site. This outflowing cold material is seen in the blueshifted narrow absorption lines in Figures 1 and 3. Typical sizes of starburst regions are tens to hundreds of parsecs. The regions are often (but not always) in the centers of the host galaxies. If there is a preferred axis, such as in a disk galaxy, the bubble will preferentially expand along the maximum pressure gradient, which is the minor axis of the galaxy. After a few scale heights (~kpc) the Rayleigh-Taylor instabilities set in, the bubble wall leaks, and the hot interior material can escape into the galactic halo. The dynamical evolution of such galactic superwinds was discussed, *e.g.*, by Tomisaka & Bregman (1993) and Suchkov *et al.* (1994, 1996).

Galactic superwinds are able to transport a dust and chemically enriched material from the star-formation sites into the galactic halo. The ultimate fate of the superwind depends on the starburst geometry (Tenorio-Tagle *et al.*, 1999), the mass of the galaxy (Ferrara & Tolstoy, 2000), and on the properties of the halo (Ferrara, Pettini, & Shchekinov, 2000). The material may fall back onto the galaxy disk or become unbound, with the second alternative being more likely in less massive galaxies.

After a characteristic time the outflow will reach pressure equilibrium with the ambient intergalactic medium (IGM) at some distance R_e from the galaxy. Hydrodynamic models by Ferrara *et al.* (2000) predict $R_e \approx 50$ kpc. This is small in comparison with the separation of objects with mass $\sim 10^{10}$ $M_\odot$ formed in the early universe according to Cold Dark Matter models, which is of order 1 Mpc. Therefore, in the absence of an additional dispersal process, the metals transported out of the galaxies by superwinds essentially stay close to their birthplace from a cosmological point of view. It is not unreasonable to assume that additional dispersal mechanisms exist. Large-scale diffusion processes in the IGM, peculiar motions of galaxies, and galaxy-galaxy mergers and interactions all tend to disperse the ejected metals into larger volumes. An alternative scenario was proposed by Gnedin (1998). Protogalaxies can merge at large velocity in a head-on collision. Stars and dark matter experience significantly different forces than the gas. As a result, the two components have different spatial distributions, and the gas, which has already been enriched in metals by the first generations of stars, escapes into the IGM. Currently both models are considered viable mechanisms for the dispersal of metals in the early universe.

Whatever dispersal mechanism operates, an approximate picture for the star formation, metal production, and pollution of the IGM at high redshift is beginning to emerge:

- Late-type/irregular galaxies with peculiar morphologies at redshift around 3 are forming stars at high rates, but otherwise have properties similar to those in the local universe.
- Stellar winds and supernova explosions are an efficient mechanism to transport heavy elements from the galaxy centers to the halos, and possibly into the IGM.
- Depending on the existence of a dispersal mechanism (or if protogalaxy mergers are important), the metals are distributed over large volumes and pollute the IGM early in the evolution of the universe.

METAL ABUNDANCES AT HIGH REDSHIFT

Observational constraints on the chemical composition of galaxies at high redshift are still rather scarce. This is in contrasts with the state of knowledge of the heavy-element abundances in the IGM. The situation is summarized in Figure 4. In addition to the previously discussed Lyman-break galaxies, as the star-forming galaxies at high redshift are referred to, the figure contains damped Lyman-α (DLA) systems and the Lyman-α forest.

DLA systems are thought to be the cross sections of the outer regions and halos of (proto)-galaxies seen along the sightlines of quasars. DLA systems may trace the halos of star-forming galaxies but such galaxies are unlikely to account for the majority of the systems. One argument against DLA systems being halos of galaxies with active star formation is the redshift dependence of the zinc abundance (an element with negligible depletion and ionization corrections) in DLAs (Pettini, 2000). No redshift evolution of the column density weighted metallicity is found. This is contrary to the expectation from chemical models of galaxies, whose metallicity should steadily rise to $\sim Z_\odot$ at $z = 0$ (Pei & Fall, 1995). Most likely, DLA systems arise from a diverse population of galaxies, and various selection effects are conspiring, such as selective dust obscuration of the more metal-rich and more actively star-forming galaxies. Therefore, it is difficult to relate the metal production in star-forming galaxies at high z to the metallicities in DLA systems.

The Lyman-α forest is predicted by cold dark matter models to result from structure formation in the presence of an ionizing background (Weinberg, Katz, & Hernquist, 1998). The Lyman-α forest had long been thought to be truly primordial but recent Keck spectroscopy revealed a weak but significant C IV λ1550 absorption in almost all sight lines with H I columns above 10^{15} cm^{-2} (Cowie *et al.*, 1995). The corresponding carbon abundances are strongly dependent on the ionization correction but are thought to be about $\frac{1}{30}$ $Z_\odot$. It is worth highlighting that already at a redshift of 3 the IGM has a carbon abundance, which is higher than that of very metal-poor stars in the halo of our Galaxy (Wheeler, Sneden, & Truran, 1989).

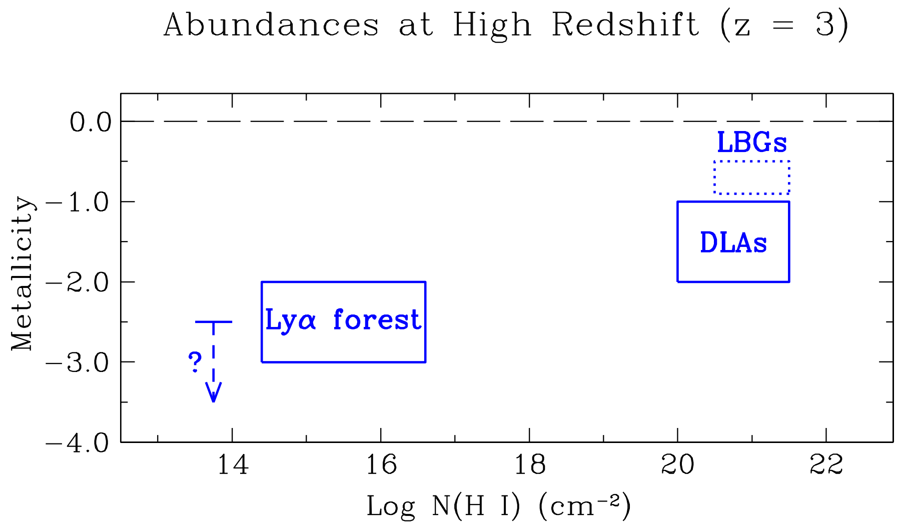

Figure 4: Summary of our current knowledge of abundances at high redshift. Plotted are metallicity (relative to solar) *vs.* H I column density. The approximate location of Lyman-break galaxies, damped Lyman-α systems, and the Lyman-α forest is indicated by boxes. Adopted from Pettini (2000)

The high metal abundance in the IGM clearly requires the enrichment early in the evolution of the universe. The metals could have been produced by a first generation of the Population III stars, which are capable to account for the amount of metals, and at the same time could have provided copious ionizing photons, as metal and photon production are closely correlated. Alternatively, star-forming galaxies with redshift at and above 3 could be the production sites of the metals seen in the universe. Even at a redshift of $\sim$3, the average chemical composition of Lyman-break galaxies is of about $\frac{1}{4}$ $Z_\odot$. It is likely that the metals are removed from the star-formation sites by galactic superwinds. If they can be effectively dispersed and mixed outside the galaxies, the metals seen in the Lyman-α forest may have their origin in galaxies similar to, *e.g.*, MS 1512-cB58.

EPILOGUE: THE FIRST GENERATION OF STARS?

A previously unexpected discovery is the relatively high metal abundance of star-forming galaxies at $z \approx 3$. Already at that redshift and a correspondingly young age of the universe of about 2 Gyr, the multiple stellar generations must have been at work to built up the metal content.

Where is the first generation of stars? Dickinson *et al.* (2000) discovered an extremely red object in the HDF North whose spectral energy distribution is consistent with a star-forming galaxy with its Lyman break in the J band. If this interpretation turns out to be true, the object could be a young galaxy at $z > 10$ forming its first stellar generation. Spectroscopic verification of this hypothesis will be a challenge for the more distant future.

Acknowledgements. I wish to thank the LOC in Kyiv for the excellent organization of this meeting and for their kind hospitality. I am grateful to Max Pettini for providing Figure 4. This work was supported by HST grant GO-07437.01-96A from the Space Telescope Science Institute, which is operated by the Association of Universities for Research in Astronomy, Inc., under NASA contract NAS5-26555.

REFERENCES

[1] *Allen D. A., Wright A. E., Goss W. M.* // Mon. Notic. Roy. Astron. Soc.–1976.–**177**.–P. 91.

[2] *Calzetti D., Kinney A. L., Storchi-Bergmann T.* // Astrophys. J.–1994.–**429**.–P. 582.

[3] *Chevalier R. A., Clegg A. W.* // Nature.–1985.–**317**.–P. 44.

[4] *Conti P. S., Leitherer C., Vacca W. D.* // Astrophys. J. Lett.–1996.–**461**.–P. L87.

[5] *Cowie L. L., Songaila A., Kim T.-S., Hu E.* // Astron. J.–1995.–**109**.–P. 1522.

[6] *de Mello D. F., Leitherer C., Heckman T. M.* // Astrophys. J.–2000.–**530**.–P. 251.

[7] *Dickinson M.* // Building Galaxies: From the Primordial Universe to the Present / Eds F. Hammer, T. X. Thuan, V. Cayatte, *et al.*–Singapore: World Scientific, 2000.–P. 253.

[8] *Dickinson M., Hanley C., Elston R., et al.*// Astrophys. J.–2000.–**531**.–P. 624.

[9] *Ellingson E., Yee H. K. C., Bechtold J., Elston R.* // Astrophys. J.–1996.–**466**.–P. L71.

[10] *Ferguson H. C.* // Photometric Redshifts and the Detection of High Redshift Galaxies / Eds R. Weymann, L. Storrie-Lombardi, M. Sawicki, R. Brunner.–San Francisco: ASP, 1999.–P. 51.

[11] *Ferguson H. C., Dickinson M., Williams R. E.* // Annu. Rev. Astron. and Astrophys.–2000.–**38**.–in press.

[12] *Ferrara A., Pettini M., Shchenikov Y.* // Mon. Notic. Roy. Astron. Soc.–2000.–in press.

[13] *Ferrara A., Tolstoy E.* // Mon. Notic. Roy. Astron. Soc.–2000.–**313**.–P. 291.

[14] *Gnedin N. Y.* // Mon. Notic. Roy. Astron. Soc.–1998.–**298**.–P. 44.

[15] *González Delgado R. M., Leitherer C., et al.* // Astrophys. J.–1998.–**495**.–P. 698.

[16] *Heckman T. M., Leitherer C.* // Astron. J.–1997.–**114**.–P. 69.

[17] *Hibbard J. E., Vacca W. D.* // Astron. J.–1997.–**114**.–P. 1741.

[18] *Hughes D. H., Serjeant S., Dunlop J., et al.* // Nature.–1998.–**394**.–P. 241.

[19] *Johnson K. E., Leitherer C., Vacca W. D., Conti P. S.* // Astron. J.–2000.–**120**.–P. 1273.

[20] *Johnson K. E., Vacca W. D., Leitherer C., et al.* // Astron. J.–1999.–**117**.–P. 1708.

[21] *Kobulnicky H. A., Kennicutt R. C., Pizagno J. L.* // Astrophys. J.–1999.–**514**.–P. 544.

[22] *Leitherer C.* // Chemical Evolution from Zero to High Redshift / Eds J. Walsh, M. Rosa.–Berlin: Springer, 1999.–P. 204.

[23] *Leitherer C., Leão J. R., Heckman T. M., et al.* // Astrophys. J.–2000.–submitted.

[24] *Leitherer C., Schaerer D., Goldader J. D., et al.* // Astrophys. J. Suppl. Ser.–1999.–**123**.–P. 3.

[25] *Pei Y. C., Fall S. M.* // Astrophys. J.–1995.–**454**.–P. 69.

[26] *Pettini M.* // Building Galaxies: From the Primordial Universe to the Present / Eds F. Hammer, T. X. Thuan, V. Cayatte, *et al.*–Singapore: World Scientific, 2000.–P. 297.

[27] *Pettini M., Steidel C. C., Adelberger K. L., et al.* // Astrophys. J.–2000.–**528**.–P. 96.

[28] *Seitz S., Saglia R. P., Bender R., et al.* // Mon. Notic. Roy. Astron. Soc.–1998.–**298**.–P. 945.

[29] *Steidel C. C., Giavalisco M., Pettini M., et al.* // Astrophys. J. Lett.–1996.–**462**.–P. L17.

[30] *Suchkov A. A., Balsara D. S., Heckman T. M., Leitherer C.* // Astrophys. J.–1994.–**430**.–P. 511.

[31] *Suchkov A. A., Berman V. G., Heckman T. M., Balsara D. S.* // Astrophys. J.–1996.–**463**.–P. 528.

[32] *Tenorio-Tagle G., Silich S. A., Kunth D., et al.* // Mon. Notic. Roy. Astron. Soc.–1999.–**309**.–P. 332.

[33] *Teplitz H. I., McLean I. S., Becklin E. E., et al.* // Astrophys. J. Lett.–2000.–**533**.–P. L65.

[34] *Tomisaka K., Bregman J. N.* // Publs Astron. Soc. Jap.–1993.–**45**.–P. 513.

[35] *Weinberg D. H., Katz N., Hernquist L.* // Origins / Eds C. E. Woodward, J. M. Shull, H. A. Thronson Jr.–San Francisco: ASP, 1998.–P. 21.

[36] *Wheeler J. C., Sneden C., Truran Jr. J. W.* // Annu. Rev. Astron. and Astrophys.–1989.–**27**.–P. 279.

[37] *Yee H. K. C., Ellingson E., Bechtold J., et al.* // Astron. J.–1996.–**111**.–P. 1783.

INTERSTELLAR MOLECULES IN STAR FORMING REGIONS

H. R. Dickel[1,2,3]

[1] *ASTRON (Netherlands Foundation for Research in Astronomy)*
P.O. Box 2, 7990AA Dwingeloo, Netherlands

[2] *Astronomical Institute, 'Anton Pannekoek'*
University of Amsterdam, Kruislaan 403, 1098SJ
Amsterdam, The Netherlands

[3] *Astronomy Department, University of Illinois at Urbana-Champaign*
1002 West Green Street, Urbana IL 61801, USA
e-mail: `lanie@astro.uiuc.edu`

We discuss some of the characteristics of interstellar molecules and their radiation, concentrating on the rotational transitions of molecules in the gas phase. An up-to-date (November 2000) list of interstellar, circumstellar and cometary molecules is presented.
The Berkeley-Illinois-Maryland-Association array of radio telescopes is described and some of the recent BIMA observations of molecular emission from selected star-forming regions is presented. These include evidence for collapse in W 49 A north, complex molecules coming off of grain surfaces in Sgr B2 north, images tracing the molecular emission in the energetic DR 21 bipolar outflow, and large velocity gradients in the CO emission associated with the neutral columns of the Eagle Nebula.

INTRODUCTION

Only a few molecules were known to exist in interstellar space when OH, the first interstellar molecule to be discovered by radio techniques, was observed in 1963 [22]. By the year 2000, over 120 molecules have been discovered with the most complex, $HC_{11}N$, having 13 atoms [2]. The molecules are found in clouds of cold gas and dust which are distributed throughout the Milky Way Galaxy. These clouds are huge; they can have masses up to a million times the mass of the Sun and diameters of 300 light years. Molecular clouds fragment into small clumps which collapse to form stars. The more massive stars ionize their surroundings and begin to disrupt the remaining molecular clouds. Because molecular clouds are opaque to "visible" light, infrared and radio telescopes are required to study the dramatic activity within them.

CHARACTERISTICS OF INTERSTELLAR MOLECULES AND THEIR RADIATION

Radiation from molecules arises from 3 main types of transitions: between electronic states, vibrational states, and rotational states. Electronic transitions require considerable energy (kinetic temperatures, T_K, in the thousands of K) to excite the levels and the emission occurs in the optical part of the spectrum. Vibrational transitions require less energy ($T_K \sim 300-1000$K) and the emission occurs in the infrared and far infrared. The simplest transitions which require the least energy ($T_K \sim$3K to 300K) are the rotational transitions which occur in the radio at cm, mm and submm wavelengths. Details of the microwave spectroscopy of molecular radiation are given by Townes and Schawlow [21].

In a typical molecular cloud with 10^9 hydrogen molecules per cubic meter there are approximately 10,000 CO molecules. For other molecular species such as CS, HCN, H_2CO, there is about 1 molecule each. Molecules are comprised of simple atoms in more or less their cosmic abundance, H, C, O, N, Si, S [9, 11]. The time between collisions is from hours to several hundreds years. Therefore, in the gas phase, only two body, not three body reactions occur. Simple molecules (other than H_2) can form in the gas phase whereas H_2 and more complex molecules are presumed to form through chemical reactions on the surfaces of interstellar grains.

The first 4 molecules detected by radio telescopes were found at cm wavelengths – OH [22], NH_3 [4], H_2CO [19], H_2O [5]. Once the 36′ radio telescope of the National Radio Astronomy Observatory became operational at 3 mm, many more molecules were discovered and the number has grown to over 120 molecules. Table 1 shows the list of interstellar, circumstellar, and cometary molecules as of November 2000 [16]. Compared to terrestrial laboratories, conditions in interstellar space are essentially a vacuum near absolute zero K.

Because the mean free path for a molecule in a molecular cloud can be as small as the diameter of the earth or as large as the solar system, there are few interactions. Therefore, it is not unusual to find free radicals –

Table 1: A list of the 126 reported gas-phase interstellar, circumstellar and cometary molecules. This list was compiled by L. E. Snyder, November 2000

2	AlF	AlCl	C_2	CH	CH^+	CN
	CN^+	CO	CO^+	CP	CS	CSi
	H_2	HCl	HF	KCl	LiH	N_2^+
	NH	NO	NS	NaCl	OH	OH^+
	PN	S_2	SH	SO	SO^+	SiN
	SiO	SiS				
3	C_3	C_2H	C_2O	C_2S	CH_2	CO_2
	HCN	HCO	HCO^+	HCS^+	H_3^+	HOC^+
	H_2O	H_2S	HNC	HNO	MgCN	MgNC
	NH_2	N_2H^+	N_2O	NaCN	OCS	SO_2
	c-SiC_2					
4	c-C_3H	l-C_3H	C_3N	C_3O	C_3S	C_2H_2
	CH_3	HCCN	$HCNH^+$	HNCO	HNCS	$HOCO^+$
	H_2CO	H_2CN	H_2CS	H_3O^+	NH_3	SiC_3
5	C_5	C_4H	C_4Si	l-C_3H_2	c-C_3H_2	CH_2CN
	CH_4	HC_3N	HC_2NC	HCOOH	H_2CHN	H_2COH^+
	H_2C_2O	H_2NCN	HNC_3	SiH_4		
6	C_5H	C_2H_4	CH_3CN	CH_3NC	CH_3OH	CH_3SH
	HC_4H	HC_3NH^+	HC_3HO	$HCONH_2$	l-H_2C_4	C_5N
7	C_6H	CH_2CHCN	CH_3C_2H	HC_5N	$HCOCH_5$	NH_2CH_3
	c-C_2H_4O					
8	CH_2OHCHO	CH_3COOH	CH_3C_3N	$HCOOCH_3$	C_7H	HC_6H
	H_2C_6					
9	CH_3C_4H	CH_3CH_2CN	$(CH_3)_2O$	CH_3CH_2OH	HC_7N	C_8H
10	$(CH_3)_2CO$					
11	HC_9N					
13	$HC_{11}N$					

OH [22], molecular ions – HCO^+ [3], and long chains – $HC_{11}N$ [2] in molecular clouds. The pace of discovery has not slowed, the latest detection being the first sugar – glycolaldehyde [10].

RADIO TELESCOPES – THE BIMA ARRAY

Many of early discoveries were made with NRAO 36′ (11-m) telescope at a wavelength 3 mm. The early maps had a resolution of about 1 arcmin. During the 1980s, larger radio telescopes and mm-wave arrays were constructed. For example, the **B**erkeley-**I**llinois-**M**aryland-**A**ssociation (BIMA) array shown in Fig. 1 is a 10 antenna aperture synthesis telescope which operates at wavelengths of 3 mm and 1 mm [24]. The BIMA telescopes are 6.1 m in diameter yielding a FWHP beam of 100″ at 115 GHz (~3 mm). The antennas may be located at various stations along an approximately T-shaped track to obtain angular resolutions between about $0\farcs4$ and 14″ at 100 GHz. Nine of the 10 antennas have both 3 mm (70–116 GHz) and 1 mm (210–270 GHz) SiS receivers. The tenth (of older design) has a 3 mm Schottky diode receiver.

The interferometer is insensitive to the very largest scale features. However, there are several advantages of interferometers over single dishes for detecting and imaging molecular line emission. One can image at high resolution over a large field of view, separate out different velocity structures which would overlap at lower resolution, and can locate the source of the emission within the field of view.

Figure 1: The 10-element BIMA mm-wave array in Northern California

RECENT INVESTIGATIONS OF STAR-FORMING REGIONS WITH THE BIMA ARRAY

W 49 A north – inverse P-Cygni profiles and collapse?

Welch *et al.* [23] imaged W 49 A north in the J=1−0 transition of HCO^+ with the **B**erkeley-**I**llinois-**M**aryland-**A**ssociation (BIMA) array at a resolution of ~7″ and found an inverse P Cygni-like profile toward H II region **G** which they interpreted as being due to collapse of the overall molecular envelope onto the inner ring of ultracompact H II regions of which **G** is the most prominent one. Dickel & Auer [6] modeled the radiative transfer for such a global inside-out collapse and found that such a collapse model could satisfactorily reproduce observations of both the J=1−0 and the J=3−2 transitions of HCO^+ toward the dominant H II region. More recently, Dickel *et al.* [7] observed the J=2−1 transition of CS towards W49 A north and found the same inverse P-Cygni profile. Fig. 2 shows the effect of degrading the resolution and how important high resolution is for detecting the absorption and hence an inverse P-Cygni profile.

Sgr B2 north – Site for Complex Molecules

One of the best sites to search for new molecules is the Galactic Center region Sgr B2. Many of the complex molecules recently discovered in Sgr B2 with the BIMA array, such as ethyl cyanide, acetic acid, and possibly glycine are confined to Sgr B2 north where stars have only begun to form [17, 13, 18]. Complex molecules are thought to form on grain surfaces and are released into the gas phase once a star forms and heats the surroundings [20]. There is a window of opportunity to find complex molecules in the gas phase which is after star-formation

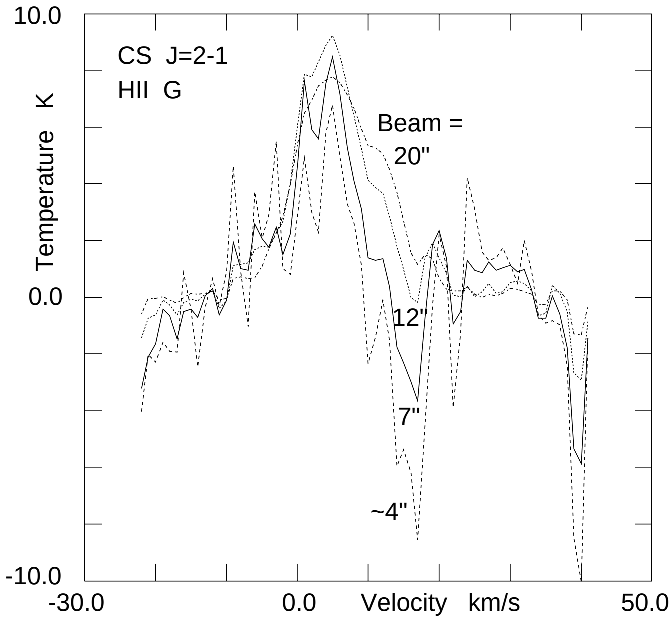

Figure 2: Effects of different resolutions on the observed inverse P-Cygni CS profile towards H II region G of W 49 A north

activity has released them from the grain surfaces but before they break apart and/or interact with other molecules.

DR 21 – Energetic Bipolar Outflows

A common phase of stellar evolution is the formation of large, bipolar outflows of molecular gas near young stellar objects [1]. One of the most massive and energetic outflows ($M > 3000\ M_\odot$, $E > 2\times10^{48}$ ergs) is found in the DR 21 star-forming region and has been imaged in HCO^+ with the BIMA array [8]. H I absorption against the continuum emission from the central H II regions shows an accelerating jet of H I gas originating between two of the exciting stars and extending out to the eastern HCO^+ lobe [15].

Eagle Nebula (M 16) – Disruption of Molecular Clouds

The Eagle Nebula (M 16) has been made famous by the beautiful images from the Hubble Space Telescope. Much of the material has been photoionized by nearby O stars. Columns of remaining dense neutral gas or "elephant trunks" are seen projected against the ionized gas. Around 70 "evaporating gaseous globules" (EGGS), small versions of the elephant trunks, have been uncovered as the columns are eroded away. Pound [14] imaged the Eagle Nebula in CO with the BIMA array. The CO emission is confined to the neutral columns where velocity gradients reach up to 20 km s^{-1} and point directly back to the O stars. These observations reveal the active destruction of a molecular cloud by the intense activity of nearby O stars.

Acknowledgements. I acknowledge partial support from the Laboratory of Astronomical Imaging which is operated with funds provided by the Berkeley-Illinois-Maryland-Association; such research is partially supported by the National Science Foundation through grant 96–13999 to the University of Illlinois. I wish to thank the Civil Research Development Foundation for travel funds to attend the "Astronomy in Ukraine 2000 and beyond" conference.

REFERENCES

[1] *Bally J., Lada C.* The high-velocity molecular flows near young stellar objects // Astrophys. J.–1983.–**265**, N 2.–P. 824–847.

[2] *Bell M., Feldman P., Travers M., et al.* Detection of $HC_{11}N$ in the cold dust cloud TMC-1 // Astrophys. J. Lett.–1997.–**483**, N 1.–P. L61–L64.

[3] *Buhl D., Snyder L.* Unidentified Interstellar Microwave Line // Nature.–1970.–**228**, N 5268.–P. 267–269.

[4] *Cheung A., Rank D., Townes C., et al.* NH_3 Molecules in the Interstellar Medium by their Microwave Emission // Phys. Rev. Lett.–1968.–**21**, N 25.–P. 1701–1705.

[5] *Cheung R. D., Townes C., Thornton D., Welch W.* Detection of Water in Interstellar Regions by it Microwave Radiation // Nature.–1969.–**221**, N 5181.–P. 626–628.

[6] *Dickel H., Auer L.* Modeling Radiative Transfer in Molecular Clouds I. HCO^+ in the Star-Forming Region W 49 A North // Astrophys. J.–1994.–**437**, N 1.–P. 222–238.

[7] *Dickel H., Williams J., Upham D., et al.* Measurements of the J=2−1 Lines of CS and $C^{18}O$ toward the Star−forming Region W49A North // Astrophys. J. Suppl. Ser.–1999.–**125**, N 2.–P. 413–426.

[8] *Garden R. P., Carlstrom J. E.* High-velocity HCO^+ emission associated with the DR 21 molecular outflow // Astrophys. J.–1992.–**392**, N 2.–P. 602–615.

[9] *Goldsmith F.* Molecular Clouds: An Overview // Interstellar Processes / Eds Hollenbach and Thronson.–Astrophys. and Space Sci. Lib.–1987.–**134**,–P. 51–70.

[10] *Hollis J., Lovas F., Jewell P.* Interstellar Glycolaldehyde: The First Sugar // Astrophys. J.–2000.-**-540**, N 2.–P. L107-L110.

[11] *Irvine W., Goldsmith P., Hjalmarson A.* Chemical Abundances in Molecular Clouds // Interstellar Processes / Eds Hollenbach and Thronson.–Astrophys. and Space Sci. Lib.–1987.–**134**.–P. 561–609.

[12] *Lovas F., Snyder L.* Table of Interstellar Molecules / Ed. Lide.–CRC Handbook of Chemistry and Physics.–2001.–**81**.–in press.

[13] *Mehringer D.. Snyder L., Miao Y., Lovas F.* Detection and Confirmation of Interstellar Acetic Acid // Astrophys. J.–1997.–**480**, N 1.–P. L71–L74.

[14] *Pound M.* Molecular Gas in the Eagle Nebula // Astrophys. J.–1998.–**493**, N 2.–P. L113–L116.

[15] *Roberts D. A., Dickel H. R., Goss W. M.* High Resolution HI Zeeman Absorption Observations of DR21 // Astrophys. J.–1997.–**476**, N 1.–P. 209–220.

[16] *Snyder L.* List of reported gas-phase interstellar, circumstellar, and cometary molecules // Priv. Communic.–2000.

[17] *Snyder L.* Detection of large interstellar molecules with radio interferometers // Instruments, Methods, and Missions for the Investigation of Extraterrestrial Microorganisms / Ed. Hoover.–Proc. SPIE.–1997.–**3111**.–P. 296–304.

[18] *Snyder L.* The Search for Interstellar Glycine // Planetary and Interstellar Processes Relevant to the Origins of Life / Ed. Whittet.–Kluwer Acad. Publ., 1997.–P. 115.

[19] *Snyder L., Buhl D., Zuckerman B., Palmer P.* Microwave detection of interstellar formaldehyde // Phys. Rev. Lett.–1969.–**22**, N 13.–P. 679–681.

[20] *Tielens A., Allamandola L.* Composition, Structure and Chemistry of Interstellar Dust // Interstellar Processes / Eds Hollenbach and Thronson.–Astrophys. and Space Sci. Lib.–1987.–**134**.–P. 397–469.

[21] *Townes C., Schawlow A.* Microwave Spectroscopy.–Dover Publ. NY, 1975.

[22] *Weinreb S., Barrett A., Meeks M., Henry J.* Radio observations of OH in the interstellar medium // Nature.–1963.–**200**, N 4909.–P. 829–831.

[23] *Welch W., Dreher J., Jackson J., et al.* Star formation in W49A - Gravitational collapse of the molecular cloud core toward a ring of massive stars // Science.–1987.–**238**, N 4833.–P. 1550–1555.

[24] *Wright M. C. H., Lugten J., Urry L., et al.* The Berkeley-Illinois-Maryland-Association Millimeter Array // Publs Astron. Soc. Pacif.–1996.–**108**.–P. 93–103.

STARBURST BLOWN SUPERBUBBLES: GAS METALICITY AND X–RAY EMISSION

S. Silich[1,2] and G. Tenorio-Tagle[2]

[1] *Main Astronomical Observatory, NAS of Ukraine*
27 Akademika Zabolotnoho, 03680 Kyiv, Ukraine
e-mail: silich@mao.kiev.ua; silich@inaoep.mx

[2] *Instituto Nacional de Astrofisica Optica y Electronica, AP 51, 72000 Puebla, Mexico*
e-mail: gtt@inaoep.mx

The X-ray emission from star forming regions in different types of galaxies is discussed. Special attention is paid to cases with an obvious discrepancy between model predictions and observed X-ray luminosities. A new solution of this problem, based on time dependent calculations of the X-ray emitting gas metalicity, is here given. Our results show that supernovae metal ejection leads to a high overabundance of the hot bubble interior, that allows for up to an order of magnitude higher X-ray luminosities compared with standard predictions.

INTRODUCTION

Interstellar bubbles, holes, and expanding shells are common astrophysical phenomenon. They are observed around Wolf-Rayed (WR) and O stars, luminous blue variables, and planetary nebulae. On the larger scale, bubbles are produced by the collective action of stellar winds and supernova explosions within OB associations. This coherent massive stars activity reaches an extreme limit in the giant star-forming regions of young starburst galaxies, with thousands and billions of stars concentrated within local (several hundred parsecs) central regions.

These objects can be observed in a variety of energy bands from radio to visible, but the most direct probe for the bubble basic properties is provided by their X-ray emission. Indeed, while the optical lines arise in the dense partly ionized shell segments, which occupy only a small volume, the X-ray emission comes from the hot bubble interior, which contains all starburst (SB) produced energy, mass and metals, and fills most of the SB disturbed volume. X-ray observations, therefore, provide many straightforward restrictions on the star forming region parameters and highly constrain the possible theoretical scenarios.

Here we briefly review most recent X-ray observational results related to multisupernovae activity in different types of the galaxies. We stress the existing discrepancies between the model standard predictions and observed X-ray luminosities. We then propose a new approach to reconcile the observations with the model predictions, and demonstrate that the standard X-ray bubble model may underestimate the X-ray luminosity by almost an order of magnitude.

THE STANDARD BUBBLE MODEL

The observed shells can be tentatively classified into three distinct categories. The smallest ones (type S) are produced by a wind or explosion of a single individual star. Large bubbles (type L) result from the correlated action of a few to several tens of star members of a typical OB-association, and huge ones (type H) result from violent, space correlated star forming activity in SB galaxies.

The general understanding of the observed properties of bubbles is based on the standard bubble model (see Figure 1), which consists of four zones: a) freely expanding wind; b) hot shocked wind; c) dense shell; and d) external ISM [20]. For a moderate energy deposition, the shell cools during the early evolution, and the X-ray emission comes mainly from the hot shocked wind contaminated with interstellar gas evaporated from the cold outer shell as well as from small interstellar clouds disrupted by hydrodynamic instabilities and thermal evaporation.

The X-ray emissivity in the ROSAT 0.1–2.4 KeV energy band is little dependent on temperature within the wide energy range $\sim 10^6 - 10^8$K, and as a first approximation it may be taken to be constant

$$\Lambda_x \approx 3\,\xi \times 10^{-23}\,\mathrm{erg\ s^{-1}}, \tag{1}$$

where ξ is the gas metalicity. This fact has been used by Chu & Mac Low [3], who proposed a rather simple

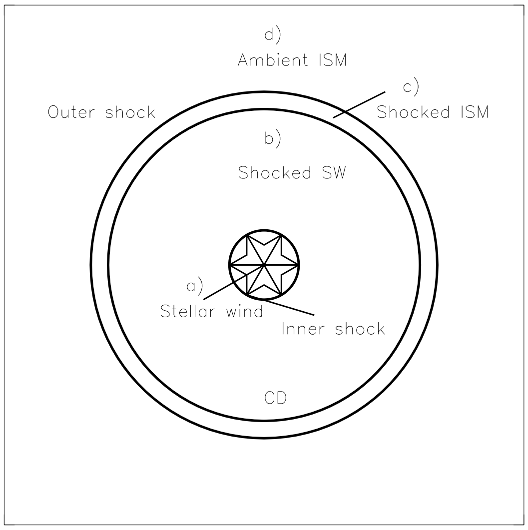

Figure 1: The structure of interstellar bubbles

analytical model for a spherical bubble evolving in a constant density medium. They found (using Weaver *et al.* [20] density and temperature profiles) that the X-ray luminosity of the shocked wind region can be expressed as:

$$L_x = 10^{36} \xi I(\tau) L_{38}^{33/35} n_{ISM}^{17/35} t_7^{19/35} \, \mathrm{erg\,s^{-1}}, \tag{2}$$

where L_{38} is the wind mechanical luminosity in 10^{38} erg s^{-1} units, and t_7 is the elapsed time in 10^7 yr units, n_{ISM} is the ambient gas number density, and ξ is the ISM gas metalicity in Solar units. $I(\tau)$ is a dimensionless integral

$$I(\tau) = \frac{125}{33} - 5\tau^{1/2} + \frac{5}{3}\tau^3 - \frac{5}{11}\tau^{11/2}, \tag{3}$$

where τ is the ratio of the X-ray cutoff temperature ($T_{cut} \sim 10^5$K) to the bubble central temperature.

Note that in this model most of the soft X-ray radiation comes from the rather thin outer bubble layers. For mass loading bubbles this leads to a more picked in time X-ray luminosity, but does not change the maximum value significantly (particularly if one assumes that the additional mass from the cloud destruction process is homogeneously distributed throughout the bubble volume [14]).

LMC BUBBLES AND THE X–RAY DISCREPANCY

Due to its proximity and almost face-on position the Large Magellanic Cloud (LMC) provides an excellent possibility to study individual massive star clusters and their connection to the surrounding medium. The photometric, spectral, X-ray and neutral hydrogen observations constrain the main input model parameters that one needs to compare the model predictions with the observed values.

Chu & Mac Low [3] have examined the *Einstein Observatory* catalog for 75 LMC OB associations and revealed diffuse X-ray emission around 15 of them. The regions with X-ray excess correlate well with the H_α emission, and can be associated to hot L-type bubbles. The bubble X-ray luminosities range from $7{\times}10^{34}$ to $7{\times}10^{36}$ erg s^{-1}. The comparison of the observed values with the model predictions revealed an intriguing result: **most of the X-ray bright bubbles have an X-ray luminosity more than an order of magnitude larger than the expected value**.

This study was later confirmed with ROSAT data, and several X-ray dim bubbles (DEM 31, DEM 105, DEM 106, and DEM 137) have also been analysed. However, in these cases the calculated X-ray emission is comparable with the ROSAT observational limit, and deeper exposure, or more sensitive observations are needed to determine their real X-ray luminosities. In fact the only confirmed exception to date in the LMC is H II complex N11 [6].

Note that X-ray bright and X-ray dim objects also demonstrate different hydrodynamical properties. The X-ray luminous bubbles show an obvious "growth rate discrepancy", *i.e.*, their expansion velocities are found to exceed the model predicted value for a given bubble radius [8].

X–RAY BUBBLES IN NEARBY STAR–FORMING GALAXIES

Large neutral hydrogen cavities and expanding shells have been found in many (if not in all) of the nearby galaxies with a moderate star formation activity (see for review [2]). These cavities are believed to have been blown in the ISM by strong stellar winds and subsequent correlated supernova explosions within massive OB associations containing of few to several hundreds of stars with $M \geq 8\,M_\odot$. Within the framework of the general theory these cavities are expected to by filled with hot, supernovae heated gas, and have to be traced as patches of the powerful diffuse X-ray emission. Several attempts recently have been undertaken to confirm this theoretical predictions by direct X-ray observations. However, the observational evidence still remains very scarce.

Walter *et al.* [19] provided a multiwavelength study of a giant neutral hydrogen shell in the north-east quadrant of the nearby dwarf galaxy IC 2574, which is a member of the M81 cluster of galaxies. This shell with 1000×500 pc size and $\sim$25 km s^{-1} expansion velocity was observed with ROSAT PSPC camera. The observations recovered a diffuse X-ray emission with a luminosity $L_x \approx 1.6\times10^{38}$ erg s^{-1} in the 0.1–2.4 KeV energy band. As it was estimated in [19] this luminosity is also about an order of magnitude higher than that predicted by the model [3].

The opposite problem is also well represented by another member of the M81 group. The dwarf irregular galaxy HoII has been well studied in the 21 cm wavelength band by Puche *et al.* [12] and exhibits a violent ISM, which contains a total of 51 neutral hydrogen holes of different sizes and expansion velocities. This galaxy is one of the most luminous dwarf irregulars. However, Zezas *et al.* [21] have demonstrated that the X-ray emission comes only from a single point source embedded into a large H II region. The high X-ray luminosity ($L_x \approx 3\times10^{40}$ erg s^{-1}) and the short (days) and long (years) time variability favor a compact supernova remnant or a massive X-ray binary origin of this emission. The mass of the accreting object, however, was estimated to be $\sim$ 200 $M_\odot$, well in excess of the mass limit for a stellar black hole candidate. However, the most unexpected result in the framework of our consideration is the lack of diffuse X-ray emission from the numerous HI hole population. To add to the confusion Rhode *et al.* [13] have proclaimed that at least in several of the Holmberg II holes the observed stellar cluster brightness is strongly inconsistent with that predicted by the coherent supernovae model value.

X–RAY EMISSION FROM STARBURST GALAXIES

Coherent stellar winds and supernovae explosions gain their peak activity in starburst galaxies, where the present rate of star formation may be supported only for a small fraction of the Hubble time and is concentrated in a small fraction of the space volume. Usually young stars are concentrated in luminous H_α knots as in VII Zw403 galaxy. The energy output rate in the starburst region exceeds that of the rest of the galaxy $L_{SB} \gg L_{gal}$. The common believe is that in many cases this activity leads to a powerful gas outflow from the SB region, which sometimes is even able to remove an essential fraction of the ISM and supernovae produced metals off a galaxy [5]. However, this conclusion is still a matter of comprehensive analysis and debates. Recent numerical studies [15, 4] have shown that in the presence of the dark matter and extended gaseous halos the ISM ejection efficiency is much below than what it was expected by previous studies.

Now, let us make a quick survey of nearby X-ray emitting galaxies with violent star forming activity.

NGC 5253 is one of the nearest (4.1 Mpc) and the youngest up to date known starburst. WR stars identified in two of the five central massive star clusters constrain the age to 3–5 Myr only. An extended soft X-ray emission with $L_x \approx 6.5\times10^{38}$ erg s^{-1} from the central part of the galaxy has been revealed by Martin & Kennicutt [7]. They also found that the simple superbubble model underpredicts the NGC 5253 X-ray luminosity by a factor of 16. Strickland & Stevens [17], however, revealed instead of a single huge bubble a system of at least five sources of X-ray emission connected with the young massive star clusters. The X-ray luminosities of the individual components range between $(2\text{–}7)\times10^{37}$ erg s^{-1}, which is in a better agreement with the model predictions.

VII Zw403 is the nearest blue compact dwarf (BCD) galaxy. This is an isolated system with a total mass $2\times10^8\,M_\odot$, a neutral hydrogen mass of $7\times10^7\,M_\odot$, and a low interstellar gas metalicity $Z = 0.06\,Z_\odot$, also considered as a member of the M81 group. Recent HST observations, however, moved it 1.5 kpc farther away, to a 4.5 Mpc distance. Papaderos *et al.* [9] revealed an extended round kpc-scale region of the diffuse X-ray emission with the total X-ray luminosity $L_x \approx 2.3\times10^{38}$ erg s^{-1}. Our estimations show the same, as in LMC, IC 2574 and NGC 5253, a more than an order of magnitude difference between the observed X-ray luminosity and the standard model prediction.

NGC 1569. The ASCA 0.5–6 KeV broad-band observations showed an extended X-ray emission. The total X-ray luminosity was estimated to be $L_x \approx 3.1\times10^{38}$ erg s^{-1} and may be best fitted with two spectral components. The soft component is best described by a hot plasma model with temperature T=(0.6–0.8) KeV that provides around 60% of the total X-ray emission. It is clearly extended and associated with the system of H_α filaments.

About 40% of this emission comes from the unresolved central region, whereas the rest comes from the extended diffuse component.

NGC 253 is one of the three nearest galaxies with prominent superwind features. It presents an extended X-ray region 9 kpc along the galaxy minor axis, and also shows a large number of X-ray point sources both in the mid-plane of the galaxy and its vicinity. The ASCA [11] and BeppoSAX [10] observations revealed soft (0.5–2.0) KeV and hard (2.0–10.0) KeV emission with luminosities $L_x \approx 7.7\times10^{39}$ erg s^{-1} and $L_x \approx 1.6\times10^{40}$ erg s^{-1}, respectively. These observations allowed to estimate the hot inner bubble gas metalicity. The absolute abundances were best estimated to be $Z_{Fe} = 0.25\,Z_\odot$ for iron, and $Z_\alpha=1.7\,Z_\odot$ for α-elements, however, still remain highly model-dependent. The relative abundances are more definite and confirm an obvious overabundance of the α-elements.

METALICITY OF SUPERBUBBLES

Careful analysis of the X-ray data has led thus to the conclusion that in many cases the observed X-ray luminosities are in clear disagreement with the standard model predictions. Here we relax the standard model assumption which associates the inner bubble metalicity with those of the surrounding ISM. This assumption is being recognized as an idealization due to the contact discontinuity that inhibits mixing of SN ejected metals with the surrounding ISM [18]. The total amount of gas ejected by supernovae (SNe) includes an important fraction of newly synthesized metals and these are well mixed with the thermalized ejected matter and the gas that evaporates from the cold radiative shell segments. Consequently, **the metals ejected by sequential SNe are to be found in the hot bubble interior, causing drastic changes to its metalicity. The later is important because the main contribution to the soft X-ray band comes from the emission lines of oxygen and others α-elements**.

Our initial model includes: a Salpeter initial mass function for a star cluster mass distribution and reasonable approximations for massive stars, main sequence life times, and oxygen yields.

The galaxy model incorporates stars, a dark matter component and a low abundance ($Z = 0.1\,Z_\odot$) ISM, which allows for two isothermal components. One is related to a central dense molecular disk with a mass of 5×10^7 M$_\odot$ and the second represents the low density, extended neutral halo. In all cases the total mass of the host galaxy amounts to be $10^{10}\,M_\odot$, while the gas mass amounts to only $10^9\,M_\odot$. To follow the bubble evolution we used our 3D numerical code, based on the thin layer approximation [1, 15].

THE RESULTS OF THE CALCULATIONS

The calculations [16] follow the bubble time evolution and the change in metalicity of the hot bubble interior due to the SB ejected metals, mixing with the shell evaporated matter. Figure 2 shows the evolution of the metalicity of the superbubble interior as a function of time. It reaches $Z_O \sim 2\,Z_\odot$ after 6 Myr of evolution that is 20 times of the assumed ISM metalicity ($Z_{ISM} = 0.1\,Z_\odot$), falling below solar metalicity just after 10 Myr to slowly approach $0.1\,Z_\odot$ at the end of the calculation. This consequently leads to an enhance X-ray luminosity.

Figure 3 shows the time evolution of L_X for a bubble blown by $10^6\,M_\odot$ starburst. The dotted line represents the standard model with a fixed gas metalicity $Z = 0.1\,Z_\odot$. It reaches first rather a high value of about 10^{39} erg s^{-1}. During this stage, however, the main contribution to a total X-ray emission comes from the adiabatic shell rather than from the hot bubble interior. The shell contribution to the total X-ray emission is most important immediately after blow-out of the remnant from the central gas component into the extended halo of the host galaxy, when the shock reaches speeds of several hundreds of km s^{-1} that lead to the high post-shock temperature of $T \sim 1.4\times10^7\, v_{shock}^2$. The shell contribution becomes rapidly less important as the shock slows down and the shell cools below the X-ray cut-off temperature ($\sim 5\times10^5$) and condenses into a narrow and dense outer boundary of the superbubble. Later on, the main contribution to the bubble X-ray emission comes from the hot bubble interior, marking a dramatic difference between the standard model (dotted line) and of calculations with a time dependent gas metalicity (solid line). The X-ray luminosity reaches approximately an order of magnitude larger values after 10Myrs of evolution caused mainly by an enhanced inner gas metalicity. In this case the luminosity of the superbubble interior is found to remain within the range of $10^{38} - 5\times10^{39}$ erg s^{-1} throughout the evolution.

CONCLUSION

The calculations presented here show large differences in the hot interior gas metalicity with respect to the outer ISM value. The effect of new metals injected into the superbubble interior is most noticeable during the first 10 Myr. If oxygen is used as a tracer, the hot gas abundance reaches values well above solar immediately after the start of the SN phase. It reaches the maximum value after 3 to 5 Myr from the beginning of SN explosions. Later, mixing with the evaporated mass slowly reduces the impact of SNe metal ejection.

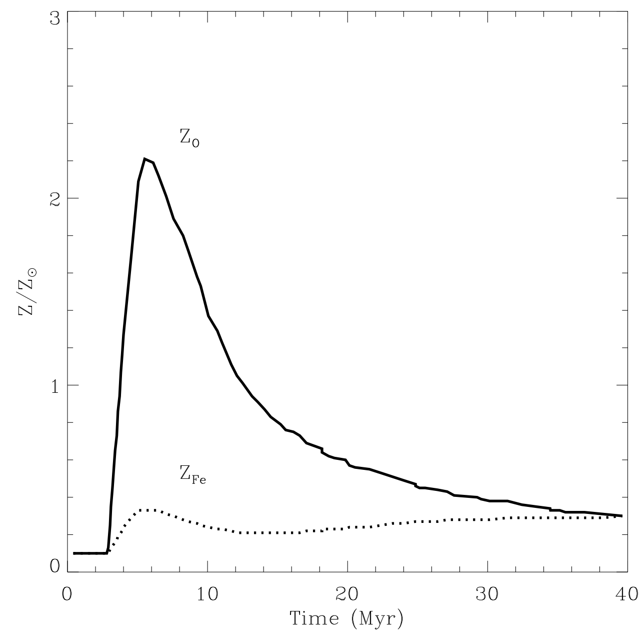

Figure 2: The hot bubble interior oxygen metalicity as function of time

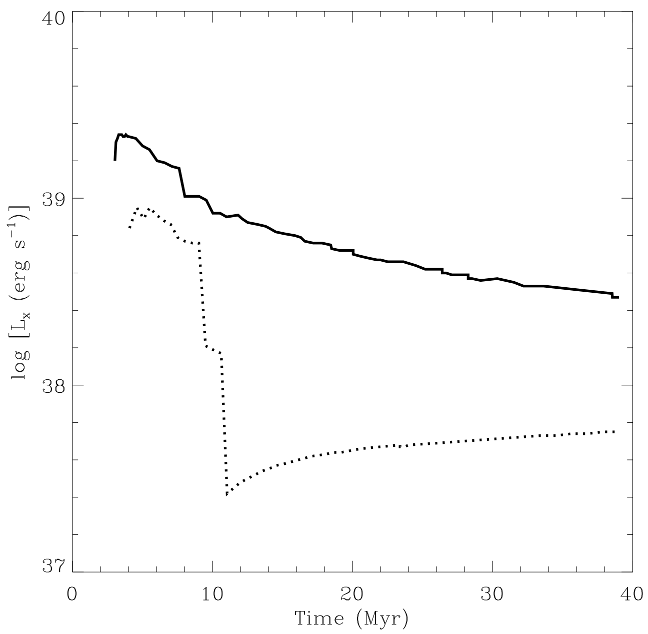

Figure 3: The calculated bubble X-ray luminosity (solid line) as it is compared with the standard bubble model (dashed line)

The most important conclusion is that the enhanced metalicity of superbubble interiors can strongly influence their X-ray luminosity, bringing theory and observations into a better agreement.

Acknowledgments. The authors acknowledge support from IoA Cambridge, where all calculations have been performed. They also highly appreciate fruitful discussions with their collaborators Elena and Roberto Terlevich and Hagai Netzer.

REFERENCES

[1] *Bisnovatyi-Kogan G., Silich S.* Shock-wave propagation in the nonuniform interstellar medium // Rev. Mod. Phys.–1995.–**67**.–P. 661–712.

[2] *Brinks E.* The cool phase of the Interstellar Medium: Atomic gas // The interstellar Medium in Galaxies / Eds H. A. Thronson and J. M. Shull.–Netherlands: Kluwer Acad. Publ., 1990.–P. 39–65.

[3] *Chu Y.-H., Mac Low M.-M.* X-rays from Superbubbles in the Large Magellanic Cloud // Astrophys. J.–1990.–**365**.–P. 510–521.

[4] *D'Ercole A., Brighenti F.* Galactic Winds and Circulation of the ISM in Dwarf Galaxies // Mon. Notic. Roy. Astron. Soc.–1999.–**309**.–P. 941–954.

[5] *De Young D., Heckman T.* The effect of central starbursts on the interstellar medium of dwarf galaxies // Astrophys. J.–1994.–**431**.–P. 598–603.

[6] *Mac Low M.-M., Chang T. H., Chu Y.-H., et al.* X-rays from Superbubbles in the Large Magellanic Cloud V. The H II Complex N11 // Astrophys. J.–1998.–**493**.–P. 260–273.

[7] *Martin C. L., Kennicutt Jr.* Soft X-ray emission from NGC 5253 and the ionized interstellar medium // Astrophys. J.–1995.–**447**.–P. 171–183.

[8] *Oey M. S.* The dynamics of Superbubbles in the Large Magellanic Cloud // Astrophys. J.–1996.–**467**.–P. 666–675.

[9] *Papaderos P., Fricke K. J., Thuan T. X., Loose H.-H.* Hot gas outflow in the blue compact dwarf galaxy VII Zw 403 // Astrophys. J.–1994.–**291**.–P. L13–l16.

[10] *Persic M., Mariani S., Cappi M., et al.* BeppoSAX detection of the Fe K line in the nearby starburst galaxy NGC 253 // Astron. and Astrophys.–1998.–**339**.–P. L33–L36.

[11] *Ptak A., Serlemitsos P., Yaqoob T., Mushotzky R.* The complex X-ray spectra of M82 and NGC 253 // Astron. J.–1997.–**113**.–P. 128–134.

[12] *Puche D., Westpfahl D., Brinks E., Roy J.-R.* // Astron. J.–1992.–**103**.–P. 1841–1858.

[13] *Rhod K. L., Salzer J. J., Westpfahl D. J., Radice L. A.* A test of the standard hypothesis for the origion of the HI holes in Holmberg II // Astron. J.–1999.–**118**.–P. 323–336.

[14] *Silich S., Franco J., Palous J., Tenorio-Tagle G.* Three-dimensional calculations of the evolution of Superbubbles in a cloudy medium // Astrophys. J.–1996.–**468**.–P. 722–738.

[15] *Silich S., Tenorio-Tagle G.* On the fate of processed matter in dwarf galaxies // Mon. Notic. Roy. Astron. Soc.–1998.–**299**.–P. 249–266.

[16] *Silich S., Tenorio-Tagle G., Terlevich R., et al.* Evolution of the X-ray luminosity and metallicity of starburst blown superbubbles // Mon. Notic. Roy. Astron. Soc.–2001.–**324**.–P. 191.

[17] *Strickland D. K., Stevens I. R.* Multiple superbubbles in the starburst nucleus of NGC 5253? Implications for mass loss from dwarf galaxies // Mon. Notic. Roy. Astron. Soc.–1999.–**306**.–P. 43–63.

[18] *Tenorio-Tagle G.* Interstellar Matter Hydrodynamics and the Dispersal and Mixing of Heavy Elements // Astron. J.–1996.–**111**.–P. 1641–1650.

[19] *Walter F, Kerp J., Duric N., et al.* X-ray emission from an expanding supergiant shell in IC 2574 // Astrophys. J. Lett.–1998.–**502**.–P. L143–L147.

[20] *Weaver R., McCray R., Castor J., et al.* // Astrophys. J.–1977.–**218**.–P. 377.

[21] *Zezas A. L., Georgantopoulos I., Ward M. J.* ROSAT observations of the dwarf starforming galaxy Holmberg II (UGC 4305) // Mon. Notic. Roy. Astron. Soc.–1999.–**308**.–P. 302–308.

DYNAMICAL SPH + N–BODY CODE FOR CHEMO–PHOTOMETRIC EVOLUTION OF DISK GALAXIES

P. Berczik

Main Astronomical Observatory, NAS of Ukraine
27 Akademika Zabolotnoho, 03680 Kyiv, Ukraine
e-mail: berczik@mao.kiev.ua

The chemical and photometric evolution of star forming disk galaxies is investigated. Numerical simulations of the complex gasdynamical flows are based on our own coding of the Chemo – Dynamical Smoothed Particle Hydrodynamical (CD – SPH) approach, which incorporates the effects of star formation. As a first application, the model is used to describe the chemical and photometric evolution of a disk galaxy like the Milky Way.

INTRODUCTION

Galaxy formation is a highly complex subject requiring many different approaches of investigation. Recent advances in computer technology and numerical methods have allowed detailed modeling of baryonic matter dynamics in a universe dominated by collisionless dark matter and, therefore, the detailed gravitational and hydrodynamical description of galaxy formation and evolution. The most sophisticated models include radiative processes, star formation and supernova feedback, *e.g.*, [8, 13, 6].

The results of numerical simulations are fundamentally affected by the star formation algorithm incorporated into modeling techniques. Yet star formation and related processes are still not well understood on either small or large spatial scales. Therefore, the star formation algorithm by which gas is converted into stars can only be based on simple theoretical assumptions or on empirical observations of nearby galaxies.

Among the numerous methods developed for modeling complex three dimensional hydrodynamical phenomena, Smoothed Particle Hydrodynamics (SPH) is one of the most popular [10]. Its Lagrangian nature allows easy combination with fast N–body algorithms, making possible the simultaneous description of complex gas-stellar dynamical systems [6]. As an example of such a combination, an TREE – SPH code [7, 11] was successfully applied to the detailed modeling of disk galaxy mergers [9] and of galaxy formation and evolution [8]. A second good example is an GRAPE – SPH code [13, 14] which was successfully used to model the evolution of disk galaxy structure and kinematics.

MODEL

The hydrodynamical simulations are based on our own coding of the Chemo – Dynamical Smoothed Particle Hydrodynamics (CD – SPH) approach, including feedback through star formation (SF). The dynamics of the "star" component is treated in the frame of a standard N–body approach. Thus, the galaxy consists of "gas" and "star" particles. For a detailed description of the CD – SPH code (the star formation algorithm, the SNII, SNIa and PN production, the chemical enrichment and the initial conditions) the reader is referred to [1, 2]. Here we briefly describe the basic features of our algorithm.

We modify the standard SPH SF algorithm [8, 13, 14], taking into account the presence of chaotic motion in the gaseous environment and the time lag between the initial development of suitable conditions for SF, and SF itself.

Inside a "gas" particle, the SF can start if the absolute value of the "gas" particle gravitational energy exceeds the sum of its thermal energy and energy of chaotic motions:

$$\mid E_i^{gr} \mid > E_i^{th} + E_i^{ch}. \tag{1}$$

The chosen "gas" particle produces stars only if the above condition holds over the time interval exceeding its free-fall time:

$$t_{ff} = \sqrt{\frac{3 \cdot \pi}{32 \cdot G \cdot \rho}}. \tag{2}$$

We also check that the "gas" particles remain cool, *i.e.,* $t_{cool} < t_{ff}$. We rewrite these conditions following [11]:

$$\rho_i > \rho_{crit}. \tag{3}$$

We set the value of $\rho_{crit} = 0.03$ cm^{-3}.

When the collapsing particle i is defined, we create the new "star" particle with mass m^{star} and update the "gas" particle m_i using these simple equations:

$$\begin{cases} m^{star} = \epsilon \cdot m_i, \\ \\ m_i = (1 - \epsilon) \cdot m_i. \end{cases} \tag{4}$$

In the Galaxy, on the scale of giant molecular clouds, the typical values for SF efficiency are in the range $\epsilon \approx 0.01 \div 0.4$ [4, 16].

We did not fix this value but rather also derived ϵ from the "energetics" condition:

$$\epsilon = 1 - \frac{E_i^{th} + E_i^{ch}}{\mid E_i^{gr} \mid}. \tag{5}$$

At the moment of birth, the positions and velocities of new "star" particles are set equal to those of parent "gas" particles. Thereafter these "star" particles interact with other "gas" and "star" or "dark matter" particles only by gravity.

For the thermal budget of the ISM, SNIIs play the main role. Following to [8, 6], we assume that the energy from the explosion is converted totally to thermal energy. The total energy released by SNII explosions (10^{44} J per SNII) within "star" particles is calculated at each time step and distributed uniformly between the surrounding "gas" particles [12].

In our SF scheme, every new "star" particle represents a separate, gravitationally bound, star formation macro region (like a globular clusters). The "star" particle has its own time of birth t_{begSF} which is set equal to the moment the particle is formed. After the formation, these particles return the chemically enriched gas into surrounding "gas" particles due to SNII, SNIa and PN events.

We concentrate our treatment only on the production of ^{16}O and ^{56}Fe, yet attempt to describe the full galactic time evolution of these elements, from the beginning up to present time (*i.e.,* $t_{evol} \approx 15.0$ Gyr).

In our calculations and as a first approximation, it is assumed that the model galaxy halo contains the CDMH component with Plummer – type density profiles [5]:

$$\rho_{halo}(r) = \frac{M_{halo}}{\frac{4}{3}\pi b_{halo}^3} \cdot \frac{b_{halo}^5}{(r^2 + b_{halo}^2)^{\frac{5}{2}}}. \tag{6}$$

Therefore, for the external force acting on the "gas" and "star" particles we can write:

$$-\nabla_i \Phi_i^{ext} = -G \cdot \frac{M_{halo}}{(\mathbf{r}_i^2 + b_{halo}^2)^{\frac{3}{2}}} \cdot \mathbf{r}_i. \tag{7}$$

The code also includes the photometric evolution of each "star" particle, based on the idea of the Single Stellar Population (SSP) [3, 15].

At each time – step, absolute magnitudes: M_U, M_B, M_V, M_R, M_I, M_K, M_M and M_{bol} are defined separately for each "star" particle. The SSP integrated colours (UBVRIKM) are taken from [15]. The spectro – photometric evolution of the overall ensemble of "star" particles forms the Spectral Energy Distribution (SED) of the galaxy.

We do not model the energy distribution in spectral lines nor the scattered light by dust. However, according to [15] our approximation is reasonable, especially in the UBV spectral brand.

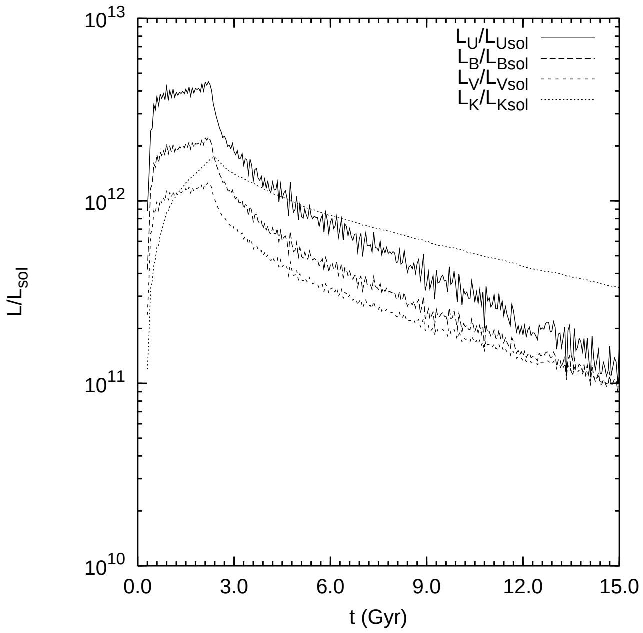

Figure 1: Luminosity evolution of the model

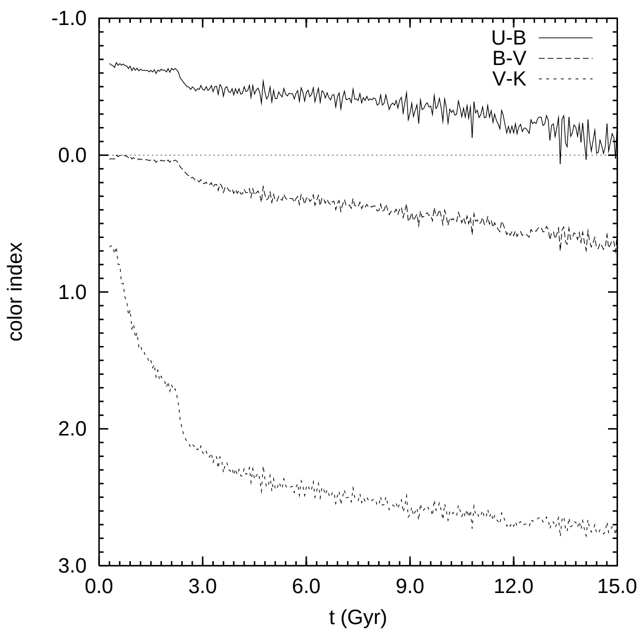

Figure 3: Color index evolution of the model

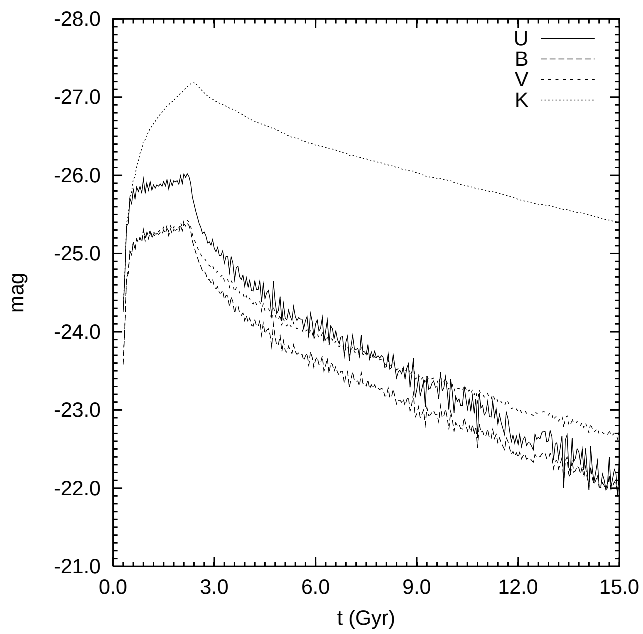

Figure 2: Photometric evolution of the model

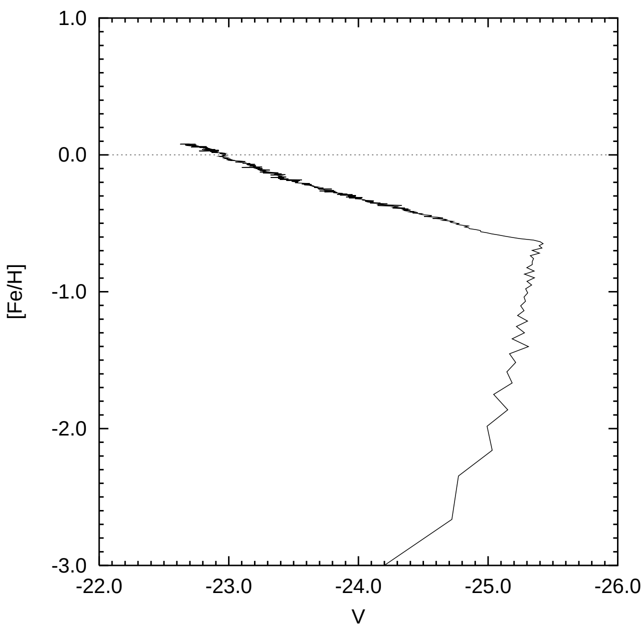

Figure 4: Evolution of model in the [Fe/H] *vs.* V plane

RESULTS

The model presented describes well the time evolution of the basic chemical and photometric parameters of a disk galaxy similar to the Milky Way. The metallicity, luminosity and colors obtained are typical of such disk galaxies.

- Figure 1. Luminosity evolution of the model galaxy.
- Figure 2. Photometric evolution of the model galaxy.
- Figure 3. Color index evolution of the model galaxy.
- Figure 4. Evolution of the model galaxy in the [Fe/H] *vs.* V plane.

This simple model provides a reasonable, self–consistent picture of the processes of galaxy formation and star formation in the galaxy. The dynamical, chemical and photometric evolution of the modeled disk-like galaxy is coincident with observations for our own Galaxy. The results of our modeling give a good base for a wide use of the proposed SF and chemical enrichment algorithm in other SPH simulations.

Acknowledgements. The work was supported by the German Science Foundation (DFG) under grants N. 436 UKR 18/2/99, 436 UKR 17/11/99 and partially supported by NATO grant NIG 974675. Special thanks for hospitality to the Astronomisches Rechen-Institute (ARI), Heidelberg, where part of this work has been done.

REFERENCES

[1] *Berczik P., Kravchuk S. G.* 3D modelling of forming galaxies // Astrophys. and Space Sci.–1996.–**245**.–P. 27–42.

[2] *Berczik P.* Chemo-dynamical smoothed particle hydrodynamic code for evolution of star forming disk galaxies // Astron. and Astrophys.–1999.–**348**.–P. 371–380.

[3] *Bressan A., Chiosi C., Fagotto F.* Spectrophotometric evolution of elliptical galaxies. I. Ultraviolet excess and color-magnitude-redshift relations // Astrophys. J.–1994.–**94**.–P. 63–115.

[4] *Duerr R., Imhoff C. L., Lada C. J.* Star formation in the λ Orionis region. I. The distribution of young objects // Astrophys. J.–1982.–**261**.–P. 135–150.

[5] *Douphole B., Colin J.* Globular clusters as a new constraint for the potential of our Galaxy // Astron. and Astrophys.–1995.–**300**.–P. 117–125.

[6] *Friedli D., Benz W.* Secular evolution of isolated barred galaxies. II. Coupling between stars and interstellar medium via star formation // Astron. and Astrophys.–1995.–**301**.–P. 649–665.

[7] *Hernquist L., Katz N.* TREESPH: A unification of SPH with the hierarchical TREE method // Astrophys. J. Suppl. Ser.–1989.–**70**.–P. 419–446.

[8] *Katz N.* Dissipational galaxy formation. II. Effects of star formation // Astrophys. J.–1992.–**391**.–P. 502–517.

[9] *Mihos J. C., Hernquist L.* Gasdynamics and starbursts in major mergers // Astrophys. J.–1996.–**464**.–P. 641–663.

[10] *Monaghan J. J.* Smoothed Particle Hydrodynamics // Annu. Rev. Astron. and Astrophys.–1992.–**30**.–P. 543–574.

[11] *Navarro J. F., White S. D. M.* Simulations of dissipative galaxy formation in hierarchically clustering universes – I. Tests of the code // Mon. Notic. Roy. Astron. Soc.–1993.–**265**.–P. 271–300.

[12] *Raiteri C. M., Villata M., Navarro J. F.* Simulations of Galactic chemical evolution. I. O and Fe abundances in a simple collapse model // Astron. and Astrophys.–1996.–**315**.–P. 105–115.

[13] *Steinmetz M., Muller E.* The formation of disk galaxies in a cosmological context: populations, metallicities and metallicity gradients // Astron. and Astrophys.–1994.–**281**.–P. L97–L100.

[14] *Steinmetz M., Muller E.* The formation of disk galaxies in a cosmological context: structure and kinematics // Mon. Notic. Roy. Astron. Soc.–1995.–**276**.–P. 549–562.

[15] *Tantalo R., Chiosi C., Bressan A., Fagotto F.* Spectro-photometric evolution of elliptical galaxies. II. Models with infall // Astron. and Astrophys.–1996.–**311**.–P. 361–383.

[16] *Wilking B. A., Lada C. J.* The discovery of new embedded sources in the centrally condensed core of the Rho Ophiuchi dark cloud: The formation of a bound cluster? // Astrophys. J.–1983.–**274**.–P. 698–716.

WOLF–RAYET GALAXIES AND MASSIVE STELLAR POPULATION

N. G. Guseva

Main Astronomical Observatory, NAS of Ukraine
27 Akademika Zabolotnoho, 03680 Kyiv, Ukraine
e-mail: guseva@mao.kiev.ua

On the basis of up-to-date models we analyze the results of investigation of the large sample a newly discovered WR galaxies (∼40 galaxies) obtained with various big telescopes. There are 10 galaxies in this sample with heavy element abundances less 1/10 $Z_\odot$ [4] and some galaxies are with abundances more than solar [13]. The statistics of massive stellar population including WR population has been analysed. The metallicity effects on the determination of $N(\mathrm{WR})/N(\mathrm{O+WR})$ and $N(\mathrm{WC})/N(\mathrm{WN})$ ratio, constraints on the initial mass function, the age and duration of star formation bursts as well as the origin of He II λ 468.6 nm emission line in WR galaxies are discussed.

INTRODUCTION

Wolf-Rayet galaxies show broad stellar emission lines in the integrated spectra of the whole galaxy or its part produced by all Wolf-Rayet stars in unresolved stellar clusters. This definition of Wolf-Rayet galaxy distinguishes a distant Wolf-Rayet galaxies from nearby galaxies, where Wolf-Rayet stars can be studied individually. The Wolf-Rayet galaxies are undergoing star formation now or very recently. Therefore, most massive O stars evolve to the Wolf-Rayet stage. The age of Wolf-Rayet stars is a few million years. Hence, the existence of Wolf-Rayet stars in these galaxies means very young age of star-forming regions.

Different parameters of WR populations in WR galaxies are very strongly dependent on the metallicity. However, the observational data and models are well studied only for the regions with metallicity close to solar one. We increase the range of metallicity and study the properties of Wolf-Rayet galaxies with both extremely small and extremely large metallicities.

From the observations of Wolf-Rayet galaxies and up-to-date models we derived the number of Wolf-Rayet stars, the number of all massive stars, the number of different subtypes of Wolf-Rayet stars (nitrogen and carbon sequences), and obtained the constraints on the parameters of IMF (slope and upper limit), the age and duration of the burst of star formation.

WOLF–RAYET GALAXIES

In 1999 Schaerer, Contini and Pindao [12] presented a new catalog of 139 Wolf-Rayet galaxies compiled from all literature data, including 39 Wolf-Rayet galaxies which are taken from original catalog of Guseva, Izotov and Thuan [4]. The majority galaxies in this catalog are newly discovered Wolf-Rayet galaxies. All spectra in [4] were obtained with high signal-to-noise ratio at the Kitt Peak National Observatory 4-m and 2.1-m telescopes and were performed in the same way, therefore, we detect Wolf-Rayet features not only in the blue bump, but also in the rarely observed so-called red bump. The spectrum of I Zw 18 was obtained with the Multiple Mirror Telescope [6]. The spectrum of SBS 0335-052 was obtained with W. M. Keck telescope [5]. The examples of two Wolf-Rayet galaxies SBS 1130+495 (Mrk 178) and SBS 1036-069 (Mrk 1259) with oxygen abundance $12+\log(\mathrm{O/H})=7.82$ and 8.95 ($Z=1/12\,Z_\odot$ and $Z\sim Z_\odot$, respectively) are shown in Fig. 1.

In 1991 Smith [15] showed that the WR features are observed only in galaxies with oxygen abundances $12+\log(\mathrm{O/H})$ more than 7.9 (solar oxygen abundance $12+\log(\mathrm{O/H})=8.90$ [3]). The decrease of the blue bump luminosity with decreasing metallicity is expected from massive stellar evolution models of Maeder [9], Meynet [10], Schaerer and Vacca [14]. These models predict Wolf-Rayet features at low metallicities which are below the detectability limit.

The earlier observations of Wolf-Rayet galaxies had in fact no galaxies with abundance less 7.9. In this connection the discovery of the WR features in the most metal-deficient galaxies I Zw 18 (metallicity is $1/50\,Z_\odot$) in 1997 independently by Izotov *et al.* [6] and by Legrand *et al.* [8] was especially surprising. Wolf-Rayet features in the spectrum of second most metal-deficient galaxy SBS 0335-052 (metallicity is $1/40\,Z_\odot$) have been also revealed [5] (Fig. 2).

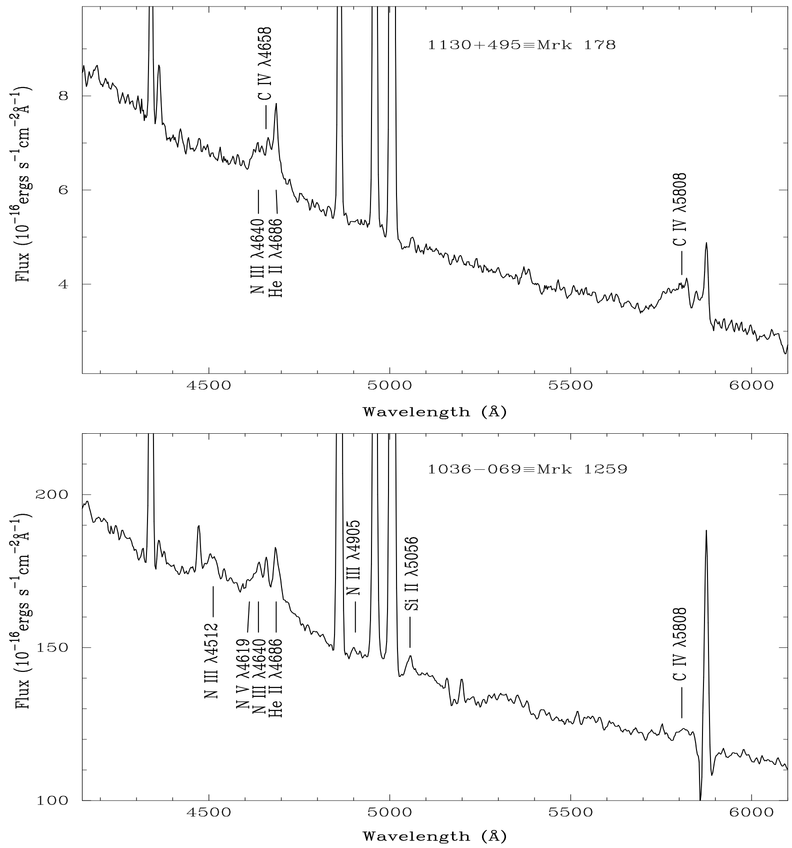

Figure 1: The 4-m and 2.1-m Kitt Peak telescopes spectra of the galaxies Mrk 178 and Mrk 1259 with Wolf-Rayet features in the blue and red bumps [4]

The data of new sample of WR galaxies [4] confirm the dependences of blue bump luminosity and number ratio of WR stars to all massive stars on oxygen abundance. The luminosity of blue bump and the fraction of Wolf-Rayet stars relative to other massive stars increases with increasing metallicity in agreement with predictions of evolutionary synthesis models [9, 10].

The dependence of the WC-to-WN star number ratio on oxygen abundance for the low-metallicity WR galaxies can be quite well explained in terms of the bursting nature of the star formation. The dependence of the N(WR)/N(O+WR) ratio and the equivalent widths of the blue and red bumps as a function of the age of an instantaneous burst is a strong function of the heavy element mass fraction Z and has a good general agreement with the theoretical predictions of evolutionary synthesis models by [14] with Salpeter slope of initial mass function and upper mass limit 120 $M_\odot$. However, the agreement is not so good for the most metal-deficient galaxies. It is likely that the disagreement comes from the different properties of Wolf-Rayet stars at low metallicities as compared to those in our Galaxy and Local Group galaxies. We suspect that the luminosity of single WCE star in the blue and red bumps at low metallicity are $\sim$ 2–4 times larger than those adopted in models. Note that observational data for single Wolf-Rayet stars are not available at such low metallicities.

The observations of Wolf-Rayet galaxies with highly super solar metallicities (2–4 times larger than solar) are well reproduced by models with $Z = Z_\odot$, Salpeter slope of initial mass function and upper mass limit 120 $M_\odot$, assuming extended burst of star formation with duration 4–10 Myr seen at ages of 7–15 Myr as indicated by EW(H_β) [13]. This naturally explains both the observed Wolf-Rayet populations and the presence of red supergiants (indicated by TiO bands) simultaneously in the same spectra of Wolf-Rayet galaxies. A very good fit between observations and models is obtained to the overall spectral energy distribution. This requires, however, less extinction for the stellar continuum than for the gas. For the metal-rich WR galaxies we put a lower limit on the value of upper limit of initial mass function M_{up} from the intensities of the WR lines. Our data compatible with a large upper mass cut-off $M_{up} \leq 30\ M_\odot$ for a Salpeter slope. We also find similar values $M_{up} \sim 30$–$50\ M_\odot$ from comparison of H_β equivalent widths in metal-rich H II regions with models [13].

So far the origin of strong nebular He II λ4686 emission line is not yet understood and this problem is often discussed. Its intensity is several orders of magnitude larger than theoretical values predicted by models of

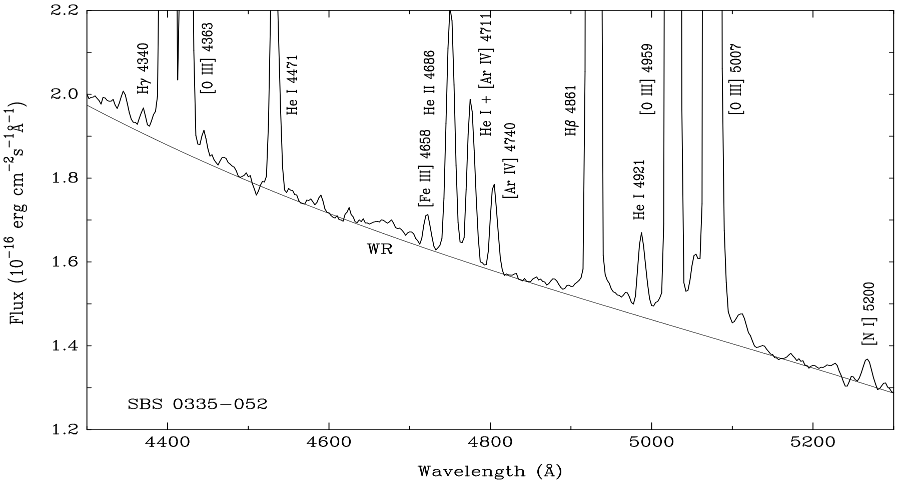

Figure 2: The 10-m W. M. Keck telescope spectrum of the second most metal deficient blue compact galaxy SBS 0335-052. The broad Wolf-Rayet feature is marked

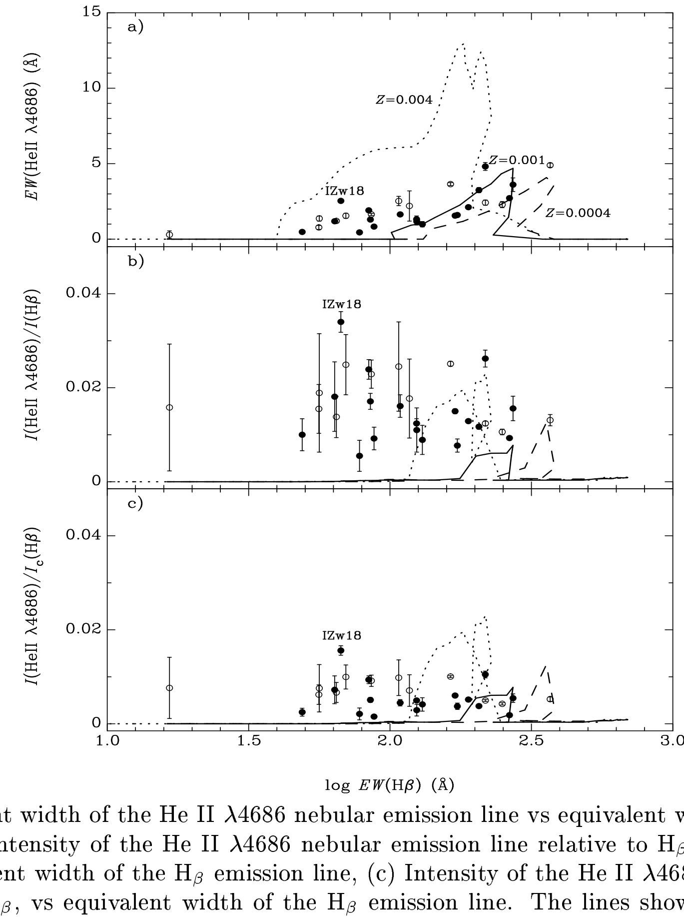

Figure 3: (a) Equivalent width of the He II λ4686 nebular emission line vs equivalent width of the H_β emission line for the data from [4]; (b) Intensity of the He II λ4686 nebular emission line relative to H_β, the latter not being corrected for aperture, vs equivalent width of the H_β emission line, (c) Intensity of the He II λ4686 nebular emission line relative to aperture-corrected H_β, vs equivalent width of the H_β emission line. The lines show the theoretical predictions for the heavy element mass fractions Z = 0.004 (dotted), 0.001 (solid) and 0.0004 (dashed), respectively [14]. H II regions with detected and non-detected WR features shown by filled and open circles, respectively

photoionized H II regions of Stasińska [16]. It was suggested by Bergeron [1] that the He II emission in dwarf emission-line galaxies could arise in the atmospheres of Of stars. Garnett *et al.* [2] examined several possible excitation mechanisms, concluding that the radiation field associated with star-forming regions can be harder than previously thought and suggested that radiative shocks in star-forming regions can produce relatively strong He II emission under certain conditions. Schaerer [11] predicted a strong nebular He II emission due to a significant fraction of WC stars for the WR galaxies with heavy element mass fraction $Z_\odot/5 \leq \mathrm{Z} \leq Z_\odot$ in the early Wolf-Rayet phases of the burst.

We gathered a sample of 30 galaxies with nebular He II emission line from our total sample of BCGs [4, 7]. Fig. 3 displays the dependence of the equivalent width and intensity of the nebular He II λ4686 emission line as a function of the H_β equivalent width. Theoretical predictions are also shown for stellar populations with Z = 0.0004, 0.001, 0.004 by dashed, solid and dotted lines, respectively [14]. Taking into account the model assumptions and observational uncertainties we find a satisfactory general agreement between models and our observations. The points representing galaxies with detected (filled circles) and non-detected Wolf-Rayet features (open circles) are mixed in this Figure. This implies that WR stars are probably not the sole origin of He II λ4686 emission in star-forming regions. Other mechanisms such as for example radiative shocks need to account for He II λ4686 nebular emission.

The high quality observational data of WR galaxies are important for the testing of stellar evolution models for most massive stars. We found a good general agreement between our observational data obtained with various big telescopes (with high signal-to-noise ratio) [4, 13] and predictions of present-day evolutionary synthesis models [14].

Acknowledgements. Author acknowledges the financial support of the INTAS grants 96–0500 and 97–0033.

REFERENCES

[1] *Bergeron J.* Characteristics of the blue stars in the dwarf galaxies I Zw 18 and II Zw 40 // Astrophys. J.–1977.–**211**, N 1.–P. 62–67.

[2] *Garnett D. R., Kennicutt R. C. J., Chu Y.-H., Skillman E. D.* He II emission in extragalactic H II regions // Astrophys. J.–1991.–**373**, N 2.–P. 458–464.

[3] *Grevesse N., Noels A.* Standard abundances // Cosmic abundances: ASP Conf. Ser. / Eds S. S. Holt, G. Sonneborn.–1996.–**99**–P. 117–126.

[4] *Guseva N. G., Izotov Y. I., Thuan T. X.* A spectroscopic study of a large sample of Wolf-Rayet galaxies // Astrophys. J.–2000.–**531**, N 2.–P. 776–803.

[5] *Izotov Y. I., Chaffee F. H., Foltz C. B., et al.* Helium abundance in the most metal-deficient blue compact galaxies: I Zw 18 and SBS 0335-052 // Astrophys. J.–1999.–**527**, N 2.–P. 757–777.

[6] *Izotov Y. I., Foltz C. B., Green R. F., et al.* I Zw 18: a new Wolf-Rayet galaxy // Astrophys. J.–1997.–**487**, N 2.–P. L37–L40.

[7] *Izotov Y. I., Thuan T. X.* Heavy-element abundances in blue compact galaxies. // Astrophys. J.–1999.–**511**, N 2.–P. 639–659.

[8] *Legrand F., Kunth D., Roy J.-R., et al.* Detection of Wolf-Rayet stars in the metal-poor starburst galaxy IZw18 // Astron. and Astrophys.–1997.–**326**, N 1.–P. L17–L20.

[9] *Maeder A.* The relative numbers of Wolf-Rayet stars in galaxies with active star formation: the metallicity effect // Astron. and Astrophys.–1991.–**242**, N 1.–P. 93–111.

[10] *Meynet G.* Wolf-Rayet population syntheses for starburst galaxies // Astron. and Astrophys.–1995.–**298**, N 3.–P. 767–783.

[11] *Schaerer D.* About the initial mass function and He II emission in young starbursts // Astrophys. J.–1996.–**467**, N 1.–P. L17–L20.

[12] *Schaerer D., Contini T., Pindao M.* New catalogue of Wolf-Rayet galaxies and high-excitation extra-galactic H II regions // Astron. and Astrophys. Suppl. Ser.–1999.–**136**, N 1.–P. 35–52.

[13] *Schaerer D., Guseva N. G., Izotov Y. I., Thuan T. X.* Massive star populations and IMF in metal-rich starbursts // Astron. and Astrophys.–2000.–**362**, N 1.–P. 53–68.

[14] *Schaerer D., Vacca W. D.* New models for Wolf-Rayet and O star populations in young starbursts // Astrophys. J.–1998.–**497**, N 2.–P. 618–644.

[15] *Smith L. F.* Wolf-Rayet populations in dwarf galaxies // Wolf-Rayet stars and interrelations with other massive stars in galaxies: IAU Symp., 1991 / Eds K. A. Van der Hucht, B. Hidayat.–1991.–P.601–612.

[16] *Stasińska G.* A grid of a model H II regions for extragalactic studies // Astron. and Astrophys. Suppl. Ser.–1990.–**83**, N 3.–P. 501–538.

STAR FORMATION RATE IN MARKARIAN GALAXIES

I. Yu. Izotova, S. L. Parnovsky

Astronomical Observatory, Taras Shevchenko National University
3 Observatorna St., 04053 Kyiv-53, Ukraine
e-mail: izotova@aoku.freenet.kiev.ua, par@aoku.freenet.kiev.ua

Study of current star formation rates in Markarian galaxies has been carried out. The tight correlation between the galaxy luminosity in the far infrared range and radio one (radiocontinuum at $\lambda = 21$ cm) has been revealed. The current star formation rates (averaged over the past 2×10^6 yr) have been derived both from the luminosity in the far infrared range ($SFR_{\rm FIR}$) and from the luminosity in the radio range ($SFR_{\rm 21cm}$). The Salpeter shape of the initial mass function (IMF) and a low-mass cut-off of 0.1 $M_\odot$ in IMF has been assumed for the $SFR_{\rm FIR}$ calculation. We derived the $SFR_{\rm 21cm}$ assuming that a radio free-free emission at $\lambda = 21$ cm is caused by the thermal gas ionized by massive stars radiation. The $SFR_{\rm 21cm}$ is about 3.3 and 5.0 times larger than $SFR_{\rm FIR}$ for starburst and Seyfert galaxies, respectively. $SFR_{\rm FIR}$ and $SFR_{\rm 21cm}$ can be considered as a lower and an upper limits, respectively of the genuine galaxy current star formation rate.

Star formation is one of the most fundamental processes in galaxies. Understanding of nature of this phenomenon is believed to contribute substantially to our insight into the subject of galaxies evolution. Star forming processes in galaxies are characterized by two parameters: an initial mass function (IMF) and a star formation rate (SFR). In the present paper we use the Salpeter IMF with a slope coefficient $\alpha = 2.35$. The low-mass cut-off of 0.1 $M_\odot$ in IMF and Hubble constant $H_0 = 75$ km s^{-1} Mpc^{-1} are taken as well. There are several methods to derive the star formation rate. Two most popular methods are based on the galaxy luminosities in the H$_\alpha$ line and in the far infrared range [4, 2]. We use data from the First Byurakan Survey (FBS) and new NRAO VLA Sky Survey (NVSS) in the radiocontinuum at $\lambda = 21$ cm [1] to derive $SFR_{\rm FIR}$ following the technique described in [4], and $SFR_{\rm 21cm}$ in accordance with [3]. In Fig. 1a and 1b we show the radio-continuum luminosities $L_{\rm 21cm}$ *vs.* the far infrared luminosities $L_{\rm FIR}$ for subsamples of starburst and Seyfert galaxies, respectively. The tight correlation implies that emission in these wavelengths originates in star forming regions.

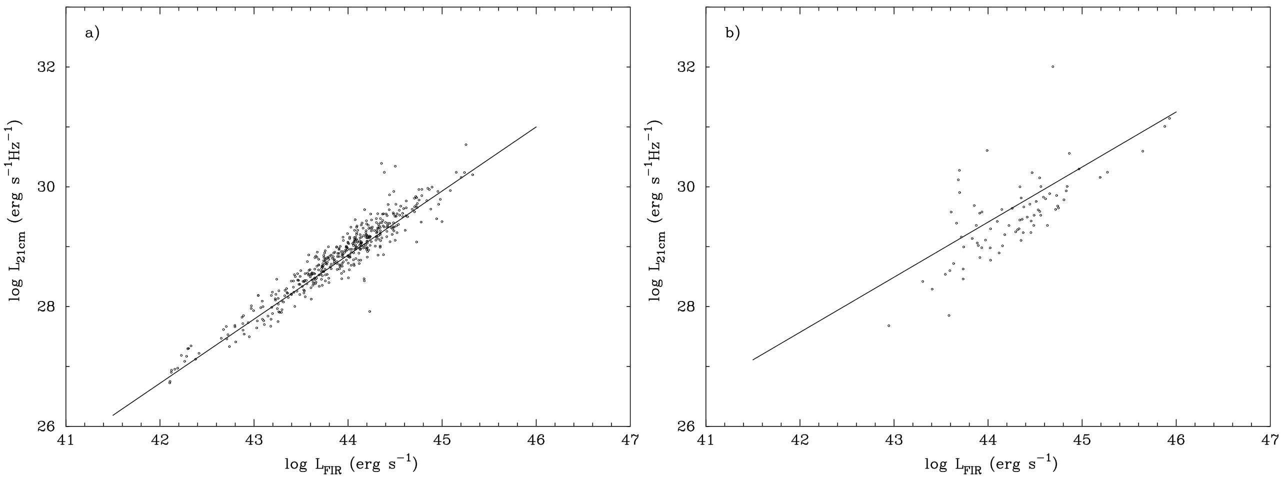

Figure 1: **a).** log $L_{\rm 21cm}$ *vs.* $L_{\rm FIR}$ for starburst galaxies. **b).** log $L_{\rm 21cm}$ *vs.* $L_{\rm FIR}$ for Seyfert galaxies

In Fig. 2a and 2b we show the differential distribution of ratios $SFR_{\rm 21cm}/SFR_{\rm FIR}$ for two subsamples. The tail in the distribution for Seyfert galaxies substantially affects the average values, hence the median value is more appropriate characteristic of the SFR ratios than an average. One can see from Table 1 that $SFR_{\rm 21cm}$ is about 3.3 and 5.0 times as large as $SFR_{\rm FIR}$ for starburst and Seyfert galaxies, respectively. The differences

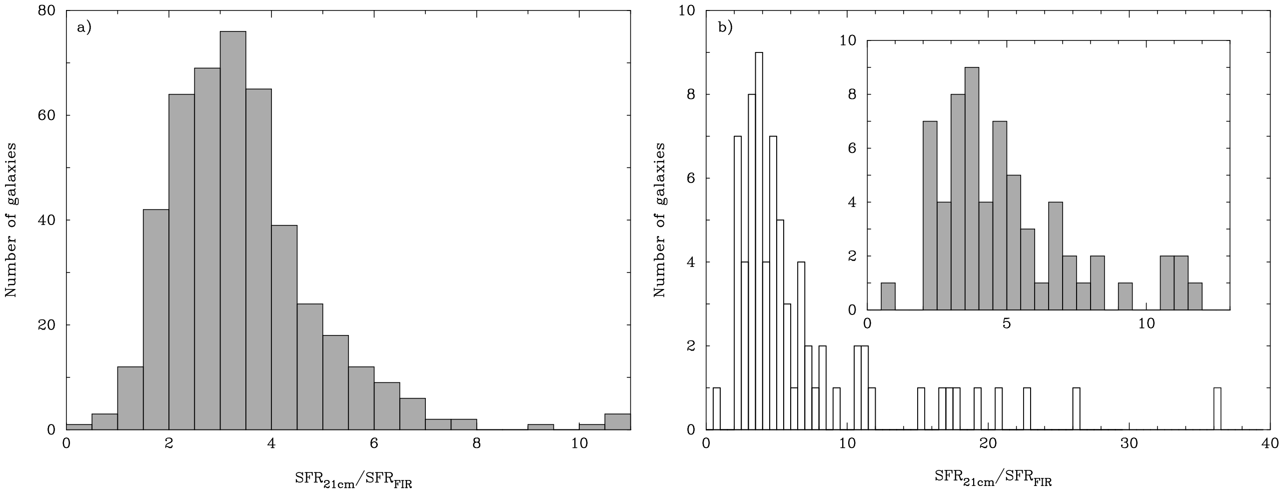

Figure 2: **a).** Distribution of ratios $SFR_{21\mathrm{cm}}/SFR_{\mathrm{FIR}}$ for starburst galaxies. **b).** Distribution of ratios $SFR_{21\mathrm{cm}}/SFR_{\mathrm{FIR}}$ for Seyfert galaxies. Part of the distribution for ratios $SFR_{21\mathrm{cm}}/SFR_{\mathrm{FIR}} < 12$ is shown separately

between median ratios could be caused by contribution of nonthermal radiation from Seyfert active nuclei. For the total sample of Markarian galaxies the ratio $SFR_{21\mathrm{cm}}/SFR_{\mathrm{FIR}}$ is about 3.4. The reasons of difference between SFR_{FIR} and $SFR_{21\mathrm{cm}}$ for blue compact dwarf galaxies, discussed in [3], could be valid for Markarian galaxies as well. SFR_{FIR} and $SFR_{21\mathrm{cm}}$ can be suggested as a lower and an upper limits respectively of the genuine galaxy current star formation rate.

Table 1: Some characteristics of starburst and Seyfert galaxies from FBS

	Starburst galaxies		Seyfert galaxies		Total sample	
	median	N	median	N	median	N
SFR_{FIR} ($M_{\odot}\mathrm{yr}^{-1}$)	16.1	442	34.8	77	16.3	519
$SFR_{21\mathrm{cm}}$ ($M_{\odot}\mathrm{yr}^{-1}$)	48.7	435	210.3	76	53.4	511
$SFR_{21\mathrm{cm}}/SFR_{\mathrm{FIR}}$	3.3	449	5.0	78	3.4	527

REFERENCES

[1] *Condon J. J., Cotton W. D., Greisen E. W., et al.* The NRAO VLA sky survey // Astron. J.–1998.–**115**, N 5.–P. 1693–1716.

[2] *Hunter D. A., Galagher J. S.* Stellar populations and star formation in irregular galaxies // Publs Astron. Soc. Pacif.–1986.–**98**, N 1.–P. 5–28.

[3] *Izotova I. Yu., Izotov Yu. I.* Star formation rate in blue compact galaxies from the Second Byurakan survey // Kinematics and Physics of Celestial Bodies.–1999.–**15**, N 3.–P. 195–205.

[4] *Thronson H. A., Telesco C. M.* Star formation in active dwarf galaxies // Astrophys. J.–1986.–**311**, N 1.–P. 98–112.

A NEW LOOK AT INHOMOGENEOUS CHEMICAL EVOLUTION

M. S. Oey

Space Telescope Science Institute
3700 San Martin Drive, Baltimore, MD, 21218, USA
e-mail: oey@stsci.edu

I present a simple, one-zone, analytic model for inhomogeneous chemical evolution, in the limit of no mixing. This model incorporates an ISM filling factor Q of newly-enriched gas, and Q is as important as the number of generations of star formation. This model can match the metallicity distributions of long-lived stars in the Galactic halo without invoking gas infall or pre-enrichment, and offers an alternative to the Simple, closed-box Model for interpreting the metallicities. The G-dwarf Problem for the Galactic disk also slightly improves.

INTRODUCTION

The study of galactic chemical evolution has developed such that we now have complex, chemodynamical codes (*e.g.*, Hensler & Burkert, 1990; Bradamante *et al.*, 1998; Berczik, 1999) to model observations of abundance patterns. They include a large number of free parameters, including inflow, outflow, radial flow, pre-enrichment, stellar initial mass function, variable star formation rate, *etc.* These codes are designed to address signatures of chemical evolution such as the time-integrated metallicity distributions of low-mass stars; element ratios; and age-metallicity relations. However, the *instantaneous* metallicity distribution function (MDF) at any given time, is a major diagnostic of chemical evolution that has yet to be fully exploited.

Most models consider only homogeneous evolution of a fully mixed system. Yet, Tinsley (1975) demonstrated that inhomogeneous evolution can have significant consequences for *all* of the resulting chemical signatures. In addition, Edmunds (1975) remarked that the dispersion in the MDF should decrease with time, as the individual enrichment units become a progressively smaller fraction of the mean metallicity level. This underappreciated point is relevant to the evolution of age-metallicity relations, but is rarely discussed. Edmunds showed that the most simplistic inhomogeneous evolution of overlapping supernova remnants, with no mixing, yields a present-day ISM that is orders of magnitude *more* homogeneous than what is presently observed. This issue has likewise received only occasional attention (*e.g.*, Roy & Kunth, 1995).

I, therefore, examine here the simplest consequences of purely inhomogeneous evolution, and compare the results to analogous analytic models, and observations. The standard approach for existing inhomogeneous chemical evolution models (*e.g.*, Malinie *et al.*, 1993; Pilyugin, 1993; Searle, 1977) is to adopt a given metallicity or age dispersion among an ensemble of regions that independently evolve according to the homogeneous Simple, closed-box Model (*e.g.*, Pagel & Patchett, 1975; Schmidt, 1963). Instead, the model summarized here from Oey (2000) predicts the form itself of the instantaneous MDF and its evolution.

INHOMOGENEOUS CHEMICAL EVOLUTION FROM FIRST PRINCIPLES

The basis is simple: random overlapping regions of contamination drive the chemical evolution, including the instantaneous MDF. There is no mixing at any time between the individual contaminating regions. We consider n generations of these individual star forming regions, *and each generation occupies a filling factor* Q in the ISM. This implies that the final, instantaneous MDF after n generations is,

$$N_{\rm ins}(z) = \sum_{j=1}^{n} P_j \; N_j(z), \tag{1}$$

where P_j is the probability of occurrence for j overlapping objects, and $N_j(z)$ is the MDF for regions having j overlapping objects. For the situation described, P_j is given simply by the binomial distribution in parameters Q and n:

$$P_j = \binom{n}{j} \; Q^j \; (1-Q)^{n-j}, \quad 1 \leq j \leq n. \tag{2}$$

The component distributions $N_j(z)$ approach normal distributions for large j, according to the Central Limit Theorem, provided that the metallicity distribution of parent enrichment events $f(z)$ remains constant. However, for small j, $N_j(z)$ depends on j and the form of $f(z)$. Oey (2000) argued that $f(z)$ should be a decreasing power-law:

$$f(z)\ dz \propto z^{-2}\ dz, \quad z_{\rm min} < z < z_{\rm max}. \tag{3}$$

This is based on observations that the H II region luminosity function (H II LF) is a power-law, and the associated size distribution of superbubbles generated by the parent Type II SNe is also a power-law (Oey & Clarke, 1997, 1998). The exponent of –2 (equation 3) assumes uniform distribution of the metal production into the volume of the superbubbles, and depends on the parent slope of the H II LF. Likewise, $z_{\rm min}$ and $z_{\rm max}$ are determined by the maximum and minimum sizes of the superbubbles, along with the SN yield. One can then compute Monte Carlo models for the components $N_j(z)$, for small j, by drawing j times from equation 3 and combining these. Equation 1 then yields the instantaneous MDF, using either Monte Carlo (small n) or analytic (large n) methods.

Likewise, the total, time-integrated MDF can be computed over all generations by,

$$N_{\rm tot}(z) = \frac{1}{n} \sum_{k=1}^{n} D_{k-1}\ N_{{\rm fin},k}(z), \tag{4}$$

where D_k is the fraction of original gas remaining after k generations, and $N_{{\rm fin},k}(z)$ is $N_{\rm fin}(z)$ for each generation k. This may then be compared to observations of long-lived stellar populations.

COMPARISON TO THE GALACTIC DISK AND HALO

This model predicts that the evolutionary state of a system is described by the mean of the binomial distribution, nQ (Oey, 2000). This is an important contrast from most other models, which are driven only by n, the number of generations. Since n is associated with age, and Q with global star formation efficiency, the combined parameter nQ offers a simple way to understand various combinations of age and metallicity. For example, a given nQ having a relatively high value of Q can explain a system with simultaneously ancient, yet high-metallicity stars (*e.g.*, the Galactic bulge); while a relatively low value of Q can explain a system that is presently metal-poor, yet shows the presence of old stars (*e.g.*, I Zw 18).

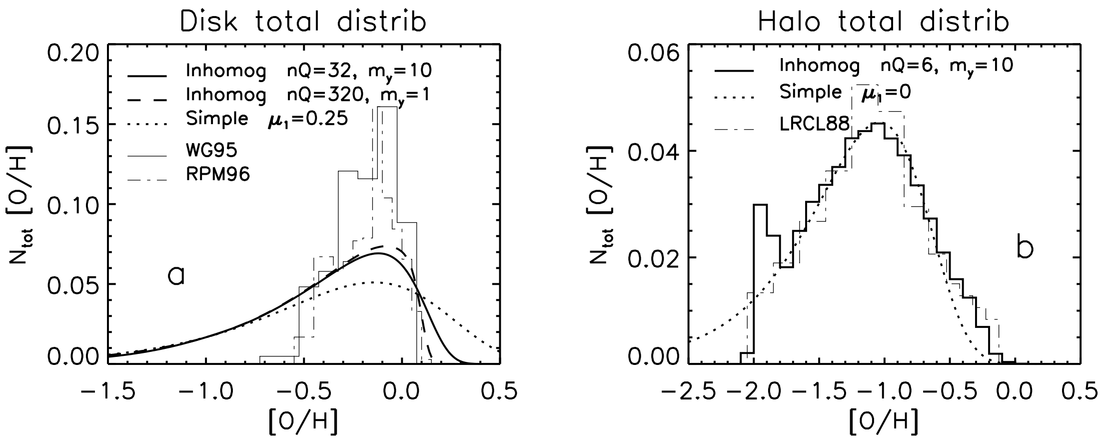

Figure 1: The empirical disk MDFs (a) from Wyse & Gilmore (1995) and Rocha-Pinto & Maciel (1996) is overplotted by an inhomogenous model with mean SN yield $m_y = 10\,{\rm M}_\odot$ (solid line); and a more evolved model having a yield of $1\,{\rm M}_\odot$ (dashed line). The dotted line shows the Simple Model for present-day solar metallicity. All disk models adopt $\mu_1 = 0.25$. The empirical halo MDF (b) from Laird *et al.* (1988) is overplotted by a Monte Carlo inhomogeneous model for $nQ = 6$ and $m_y = 10\,{\rm M}_\odot$ (solid line), and a Simple Model with present-day mean [O/H]$= -0.2$. Both halo models have $\mu_1 = 0$

Figure 1*a* shows the Galactic disk F/G-dwarf MDF in the solar neighborhood, as derived by Wyse & Gilmore (1995) and Rocha-Pinto and Maciel (1996). The dotted line shows the homogeneous Simple Model, where the consumption of gas to form stars leaves a present-day gas fraction $\mu_1 = 0.25$. The deviation of this model from the data clearly demonstrates the "G-dwarf Problem". The heavy, solid line shows the analytic, inhomogeneous model, for $nQ = 32$ and mean SN yield $m_y = 10\,\mathrm{M}_\odot$. The dashed line shows a model with a lower yield, $m_y = 1\,\mathrm{M}_\odot$, which is thereby 10 times more evolved for the given mean metallicity. Both these models also take $\mu_1 = 0.25$. The inhomogeneous models show a skewed distribution, and, although the G-dwarf Problem is still present, they are more similar to the data than the Simple Model. This has consequences for the form and rate of implied gas infall that is often used to explain the observed Galactic disk MDF. Malinie *et al.* (1993) emphasized the importance of also matching the high-metallicity tail of the MDF, and it is noteworthy that the inhomogeneous models are clearly better able to match the sharp drop-off in the data.

In fact, for this model, the high-metallicity tail of the MDFs can be an important probe of the parent $f(z)$ for each generation. Figure 1*b* shows the MDF for F/G-dwarfs in the Galactic halo from Laird *et al.* (1988; dot-dashed line). The Monte Carlo model for $nQ = 6$ is overplotted with the solid line. There is excellent agreement between the inhomogeneous model and the data. These halo data also agree with the Simple Model, shown by the dotted line, for $\mu_1 = 0$ and mean present-day metallicity [O/H] $= -0.2$. However, it is essential to note that *the shapes of the two models result from entirely different processes.* The high-metallicity turnover in the Simple Model results only from the consumption of gas into stars. In contrast, the high-metallicity tail of the inhomogeneous model represents the vestige of the $f(z)$ power-law; while the low-metallicity turnover results from the Central Limit Theorem, as the component distributions progress toward gaussians. (Note that in the limit of large nQ, the MDF will qualitatively have the form of the inhomogeneous models shown in Figure 1*a*.) Thus, the halo model (a) offers an alternative understanding/interpretation of the MDF *vs.* the Simple Model, and (b) reveals the importance of the high-metallicity tail in relatively unevolved systems, for probing the parent distribution $f(z)$.

Acknowledgements. I am grateful to Cathie Clarke, Mike Fall, and Rosie Wyse for discussions and suggestions.

REFERENCES

[1] *Berczik P.* // Astron. and Astrophys.–1999.–**348**.–P. 371.

[2] *Bradamante F., Matteucci F., D'Ercole A.* // Astron. and Astrophys.–1998.–**337**.–P. 338.

[3] *Edmunds M. G.* // Astrophys. and Space Sci.–1975.–**32**.–P. 483.

[4] *Hensler G., Burkert* // Astrophys. and Space Sci.–1990.–**170**.–P. 231.

[5] *Laird J. B., Rupen M. P., Carney B. W., Latham D.* // Astron. J.–1988.–**96**.–P. 1908.

[6] *Malinie G., Hartmann D. H., Clayton D. D., Mathews G. J.* // Astrophys. J.–1993.–**413**.–P. 633.

[7] *Oey M. S.* // Astrophys. J. Lett.–2000.–in press, astro-ph/0008302.

[8] *Oey M. S., Clarke C. J.* // Mon. Notic. Roy. Astron. Soc.–1997.–**289**.–P. 570.

[9] *Oey M. S., Clarke C. J.* // Astron. J.–1998.–**115**.–P. 1543.

[10] *Pagel B. E. J., Patchett B. E.* // Mon. Notic. Roy. Astron. Soc.–1975.–**279**.–P. 882.

[11] *Pilyugin L. S.* // Astron. and Astrophys.–1993.–**277**.–P. 42.

[12] *Rocha-Pinto H. J., Maciel W. J.* // Mon. Notic. Roy. Astron. Soc.–1996.–**279**.–P. 882.

[13] *Roy J.-R., Kunth D.* // Astron. and Astrophys.–1995.–**294**.–P. 432.

[14] *Schmidt M.* // Astrophys. J.–1963.–**137**.–P. 758.

[15] *Searle L.* // The Evolution of Galaxies and Stellar Populations / Eds B. M. Tinsley, R. B. Larson.–New Haven: Yale U. Obs., 1977.–P. 219.

[16] *Tinsley B. M.* // Astrophys. J.–1975.–**197**.–P. 159.

[17] *Wyse R. F. G., Gilmore G.* // Astron. J.–1995.–**110**.–P. 2771.

ON THE ROLE OF GALACTIC WINDS IN THE CHEMICAL EVOLUTION OF IRREGULAR GALAXIES

L. S. Pilyugin[1], F. Ferrini[2]

[1] *Main Astronomical Observatory, NAS of Ukraine*
27 Akademika Zabolotnoho, 03680 Kyiv, Ukraine
e-mail: pilyugin@mao.kiev.ua

[2] *Department of Physics, Section of Astronomy, University of Pisa, piazza Torricelli 2, 56100 Pisa, Italy*
(Present address: INTAS, 58 Avenue des Arts, 1000 Bruxelles, Belgium)
e-mail: ferrini@intas.be

The observed oxygen abundances in a number of irregular galaxies have been compared with predictions of the closed-box model for chemical and photometric evolution of galaxies, with the purpose of determination of the deficiency of oxygen abundance in irregular galaxies: this is an indicator of heavy elements loss via galactic winds. We have found that all the irregular galaxies considered have a significant oxygen abundance deficiency within their optical edges. The oxygen abundance deficiency within the optical edge of a galaxy cannot be explained by the mixing of interstellar medium with gas envelope observed outside the optical edge. This confirm the widely used hypothesis that the evolution of irregular galaxy is accompanied by the ejection of a significant part of heavy elements (gas) in the intergalactic medium.

It is widely accepted that irregular galaxies are open systems, and hence that galactic winds had to play a relevant role in their chemical evolution. Models for chemical evolution of irregular galaxies suggested that the galactic wind hypothesis allows to explain the observed chemical properties of these objects (see [6] and references therein). Outflows of ionized gas have been observed in a number of irregular galaxies [4]. However, the hydrodynamic simulations of irregular galaxies lead to conflicting conclusions [1, 10]. Skillman [11] has summarized the arguments for and against galactic wind dominated evolution of irregular galaxies and has concluded that either case, for and against galactic wind dominated evolution of irregular galaxies, is not very strong.

In our work [7], the concept of the oxygen abundance deficiency in galaxies has been introduced as a deficiency of the oxygen abundance observed in the galaxy in comparison to the oxygen abundance predicted by the closed-box model for the same gas mass fraction. Since the bulk of oxygen is produced by short-living massive stars the oxygen abundance in the closed-box system depends on the astration level and does not depend on the star formation history in the system, *i.e.*, there is one-to-one correspondence between oxygen abundance and astration level for a closed-box system. The variations of the value of oxygen abundance in the systems for a given value astration level (or gas mass fraction) can only be caused by the gas exchange between systems and their environments. The excess of oxygen abundance in comparison to the closed-box model of chemical evolution can be caused only by the inflow of over-enriched gas into the galaxy. Since such possibility seems to be unrealistic it can be adopted that the closed-box model gives the upper limit of oxygen abundance in the system with fixed value of gas mass fraction. The gas loss via galactic wind results in the oxygen abundance deficiency. The variations of the value of oxygen abundance deficiency from galaxy to galaxy can only be caused by the variations of efficiency of gas exchange between galaxies and their environments. In turn, the amount of oxygen abundance deficiency can be considered as indicative of the efficiency of mass exchange. The determination of oxygen abundance deficiency in irregular galaxies can clarify the role of galactic winds in the chemical evolution of irregular galaxies.

The variations in oxygen abundance from region to region in the best studied irregular galaxies are within observational errors [5], *i.e.*, radial oxygen abundance gradient is absent in irregular galaxies. Then, the chemical composition of irregular galaxy can be specified by a single parameter. Irregular galaxies can contain a large amount of dark matter [3] which do not take part directly to chemical evolution. The luminous mass rather than dynamical mass should be used in investigation of chemical properties of irregular galaxies. Mass of stars can be derived from the luminosity of the galaxy and stellar mass to light ratio [8].

The size of irregular galaxies in H I is larger than their optical size [9]. This raises the question – what diameter should be considered as defining the edge of irregular galaxies? This is not unrelevant: as it was indicated above the variations of oxygen abundance from region to region in the best studied irregular galaxies are within observational errors [5], a strong evidence that irregular galaxies are well mixed system within the optical diameter. If the zone of the mixing is not bounded by the optical edge but extends to H I edge then the matter outside the optical diameter can contain a significant part of the heavy elements produced by the stars and, therefore, can play an important role in the chemical evolution of the galaxy. Hunter & Gallagher [2] have found that the presence or absence of extended H I envelopes does not appear to be reflected in properties of the optical components of irregular galaxies. They concluded that only the gas within the optical edge plays an important role in the life of a galaxy. Then the optical radius R_{25} will be considered as the edge of irregular galaxies.

The mass of atomic hydrogen measured in the irregular galaxy is usually the total hydrogen mass. For a number of irregular galaxies there are measurements of radial distribution of surface mass density of atomic hydrogen that allows to determine the fraction of H I mass within the optical diameter R_{25}. The values of fraction of H I mass within optical diameter of a galaxy lie in a wide range (from 0.36 for GR 8 to 0.92 for NGC 55) for the considered galaxies. The derived values of oxygen abundance deficiency in irregular galaxies range from ~ 0.5 to ~ 0.9, *i.e.*, all the irregular galaxies show a significant value of oxygen abundance deficiency. For comparison the largest value of oxygen abundance deficiency among the spiral galaxies considered in [7] is equal to ~ 0.57 for the NGC 2403.

Can the oxygen abundance deficiency within optical edge of irregular galaxy be explained by the mixing of interstellar matter with gas outside the optical edge? To study this possibility, the values of oxygen abundance deficiency have been computed under the assumption that all the gas associated with a galaxy is well mixed. In the case when all the gas associated with a galaxy is taken into consideration significant values of oxygen abundance deficiency in irregular galaxies remain.

Thus, it has been found that all the irregular galaxies considered here have a significant oxygen abundance deficiency within their optical edges. The oxygen abundance deficiency within the optical edge of a galaxy cannot be explained by the mixing of interstellar medium with gas envelope observed outside the optical edge. This confirm the widely used hypothesis that the evolution of irregular galaxy is accompanied by the ejection of a significant part of heavy elements (gas) in the intergalactic medium.

The more detailed discussion can be found in [8].

Acknowledgements. This study was partly supported by the INTAS grant N 97–0033 and the NATO grant PST.CLG.976036.

REFERENCES

[1] *de Young D., Heckman T.* The effect of central starbursts on the interstellar medium of dwarf galaxies // Astrophys. J.–1994–**431**, N 2.–P. 598–603.

[2] *Hunter D. A., Gallagher J. S.* Irregular galaxies with extended H I emission // Astron. J.–1985.–**90**, N 9.–P. 1789–1795.

[3] *Kumai Y., Tosa M.* Metallicity and gas mass fraction in irregulars and blue compact galaxies: the effect of dark matter // Astron. and Astrophys.–1992.–**257**, N 2.–P. 511–514.

[4] *Marlowe A. T., Heckman T. M., Wyse R. F. G., Schommer R.* Observations of the impact of sturbursts on the interstellar medium in dwarf galaxies // Astrophys. J.–1995.–**438**, N 2–P. 563–589.

[5] *Pagel B. E. J., Edmunds M. G., Fosbury R. A. E., Webster B. L.* A survey of chemical compositions of H II regions in the Magellanic Clouds // Mon. Notic. Roy. Astron. Soc.–1978.–**184**, N 2.–P. 569–592.

[6] *Pilyugin L. S.* On the evolution of iron and oxygen abundances in the Large Magellanic Cloud // Astron. and Astrophys.–1996.–**310**, N 3.–P. 751–756.

[7] *Pilyugin L. S., Ferrini F.* On the oxygen abundance deficiency in spiral galaxies // Astron. and Astrophys.–1998.–**336**, N 1.–P. 103–115.

[8] *Pilyugin L. S., Ferrini F.* On the oxygen abundance deficiency in irregular galaxies // Astron. and Astrophys.–2000.–**354**, N 3.–P. 874–880.

[9] *Salpeter E. E., Hoffman G. L.* Correlation statistics of irregular and spiral galaxies mapped in H I // Astrophys. J.–1996.–**465**, N 2.–P. 595–607.

[10] *Silich S. A., Tenorio-Tagle G.* On the fate of processed matter in dwarf galaxies // Mon. Notic. Roy. Astron. Soc.–1998.–**299**, N 1.–P. 249–266.

[11] *Skillman E. D.* Evidence for and against galactoc wind dominated evolution of dwarf irregular galaxies // Rev. Mex. de Astronomia y Astrofisica Ser. de Conf.–1997.–**6**.–P. 36–42.

LOW–METALLICITY BLUE COMPACT DWARF GALAXIES DISCOVERED IN THE HAMBURG/SAO SPECTRAL SURVEY

N. G. Guseva[1], **F. H. Chaffee**[2], **Y. I. Izotov**[1], **A. Y. Kniazev**[3], **S. A. Pustilnik**[3], **A. V. Ugryumov**[3]

[1] *Main Astronomical Observatory, NAS of Ukraine*
27 Akademika Zabolotnoho, 03680 Kyiv, Ukraine
e-mail: guseva@mao.kiev.ua, izotov@mao.kiev.ua

[2] *W. M. Keck Telescope Observatory*
65-1120 Mamalahoa Hwy., Kamuela, HI 96743, Hawaii, USA
e-mail: fchaffee@keck.hawaii.edu

[3] *Special Astrophysical Observatory*
Nizhnij Arkhyz, Karachai-Circessia, 369167, Russia
e-mail: akn@sao.ru, sap@sao.ru, and@sao.ru

We present results of the spectrophotometric study of some of the most metal-deficient blue compact dwarf (BCD) galaxies discovered in the course of the Hamburg/SAO spectral survey. These findings might have important implications in the studies of the cosmological problems, origin of the elements and massive star evolution.

INTRODUCTION

The studies of various types of galaxies with strong current star formation (SF) are among the most popular in extragalactic astronomy. It is very important to deal with large enough and well selected samples of such objects, in particular, the studies of SF bursts in low-mass galaxies (H II–galaxies, or blue compact dwarf galaxies). There are two large BCD samples on the northern sky, each covering about 1000 sq. degrees. The first one is situated in the zone of the Second Byurakan Survey (SBS) (R. A. = 7^h40^m – 17^h20^m, Dec. = +49° – +61°). The second one is under completion and is situated in the region, which is a part of the zone of Case objective prism survey (R. A. = 8^h00^m – 16^h20^m, Dec. = +29° – +38°). The new Hamburg/SAO survey for emission-line galaxies (ELG) [9] is intended to cover the region in the gap between the regions of SBS and Case survey and to create a new BCD sample in that region.

More than 800 ELGs have been discovered in Hamburg/SAO survey. Several very metal-deficient blue compact dwarf galaxies with the heavy element mass fraction $Z \leq Z_\odot/20$ have been discovered. One of these BCDs, HS 0822+3542, was discovered by Pustilnik *et al.* [8]. Kniazev *et al.* [6] have shown that its oxygen abundance is less than 1/30 solar. Hence, HS 0822+3542 is the third most-metal deficient BCD known, after I Zw 18 and SBS 0335-052.

SPECTROSCOPIC AND PHOTOMETRIC DATA

The very blue colours of the disc $(B-V)_0 = 0.06 \pm 0.06$ mag and $(V-R)_0 = 0.26 \pm 0.09$ mag in HS 0822+3542 are reasonably consistent with the predictions for an instantaneous SF burst with a Salpeter IMF, a metallicity of 1/20 $Z_\odot$ and an age of ∼100 Myr [7]. If prolonged star formation is assumed, then the age of the oldest stellar population in the extended disc can be larger than that of the instantaneous burst. The observed colours can also be explained by continuous SF with a constant star formation rate from 500 Myr to 20 Myr ago. However, older stellar populations with an age of 10 Gyr are excluded. The derived age is somewhat lower for the outermost part of the of the disc with a bluer $(V-R)$ colour in comparison to its average value.

In Fig. 1 we show the 10-m W. M. Keck telescope spectrum of the brightest knot with active star formation and a very blue continuum. The continuum of the extended underlying galaxy is also blue. Very high signal-to-noise ratio spectrum (Fig. 1) has allowed us to discover the broad stellar emission feature which is attributed to the Wolf-Rayet stellar population. This stellar population is relatively common in BCDs (*e.g.*, [2]), however, very few most metal deficient BCDs are known to contain WR stars. Our finding makes HS 0822+3542 the fourth known BCD with heavy element abundances $\leq Z_\odot/20$ and WR population, after I Zw 18 [4, 7] SBS 0335–052 [3] and Tol 1214–277 [1]. We use the intensities of the emission lines to derive the abundances of the ionized species and the total abundances of O, N, Ne, S, Ar and He. We confirm the very low metallicity of HS 0822+3542

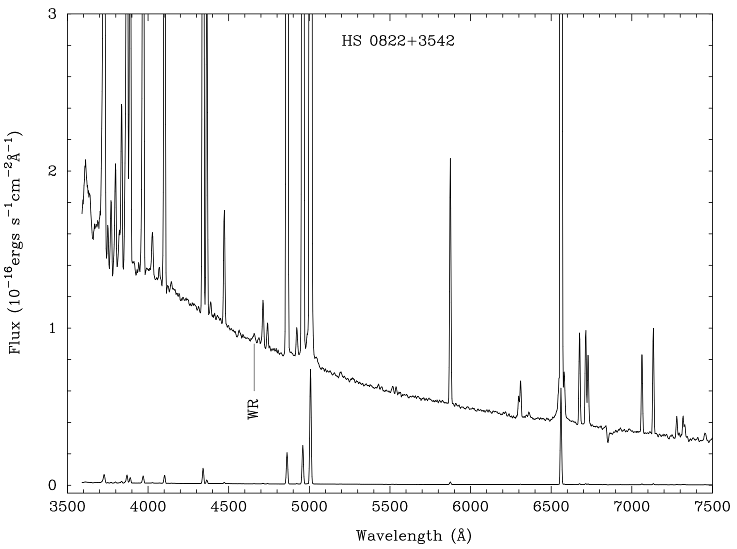

Figure 1: The 10-m W. M. Keck telescope spectrum of the brightest region in HS 0822+3542. The bottom spectrum is the spectrum divided by a factor of 100. The broad Wolf-Rayet feature is marked

derived by Kniazev *et al.* [6]. However, much better quality of the 10-m W. M. Keck telescope spectrum allows us to derive element abundances with much better precision. Our oxygen abundance in HS 0822+3542 is only $Z_{\odot}/30$, or slightly larger than the value $Z_{\odot}/35$ quoted by Kniazev *et al.* [6]. Other heavy element abundances relative to oxygen are in very good agreement with mean values for most metal deficient galaxies [5]. Very low metallicity of HS 0822+3542 makes it one of the best objects in the determination of the primordial helium abundance. Our derived value $Y = 0.244 \pm 0.005$ of the helium mass fraction in HS 0822+3542 is in excellent agreement with the Y determinations in other BCDs [3].

Acknowledgements. N. G. G., Y. I. I., A. Y. K., S. A. P. and A. V. U. acknowledge the financial support of the INTAS grants 96–0500 and 97–0033.

REFERENCES

[1] *Fricke K. J., Izotov Y. I., Guseva N. G., et al.* An imaging and spectroscopic study of the very metal-deficient blue compact dwarf galaxy Tol 1214-277 // Astron. J.–2001.–**121**, N 1.– P. 169–181.

[2] *Guseva N. G., Izotov Y. I., Thuan T. X.* A spectroscopic study of a large sample of Wolf-Rayet galaxies // Astrophys. J.–2000.–**531**, N 2.–P. 776–803.

[3] *Izotov Y. I., Chaffee F. H., Foltz C. B., et al.* Helium abundance in the most metal-deficient blue compact galaxies: I Zw 18 and SBS 0335-052 // Astrophys. J.–1999.–**527**, N 2.–P. 757–777.

[4] *Izotov Y. I., Foltz C. B., Green R. F., et al.* I Zw 18: a new Wolf-Rayet galaxy // Astrophys. J.–1997.–**487**, N 2.–P. L37–L40.

[5] *Izotov Y. I., Thuan T. X.* Heavy-element abundances in blue compact galaxies // Astrophys. J.–1999.–**511**, N 2.– P. 639–659.

[6] *Kniazev A. Y., Pustilnik S. A., Masegosa P., et al.* HS 0822+3542 – a new nearby extremely metal-poor galaxy // Astron. and Astrophys.–2000.–**357**, N 1.–P. 101–110.

[7] *Legrand F., Kunth D., Roy J.-R., et al.* Detection of Wolf-Rayet stars in the metal-poor starburst galaxy IZw18 // Astron. and Astrophys.–1997.–**326**, N 1.–P. L17–L20.

[8] *Pustilnik S. A., Engels D., Ugryumov A. V., et al.* The Hamburg/SAO survey for emission-line galaxies. II. The second list of 128 galaxies // Astron. and Astrophys. Suppl. Ser.–1999.–**137**, N 1.–P. 299–304.

[9] *Ugryumov A. V., Engels D., Lipovetsky V. A., et al.* The Hamburg/SAO survey for emission-line galaxies. I. A First list of 70 galaxies // Astron. and Astrophys. Suppl. Ser.–1999.–**135**, N 2.–P. 511-529.

ON THE ORIGIN OF THE L–Z RELATION FOR LATE–TYPE GALAXIES

L. S. Pilyugin[1], **F. Ferrini**[2]

[1] *Main Astronomical Observatory, NAS of Ukraine*
27 Akademika Zabolotnoho, 03680 Kyiv, Ukraine
e-mail: pilyugin@mao.kiev.ua

[2] *Department of Physics, Section of Astronomy, University of Pisa, piazza Torricelli 2, 56100 Pisa, Italy*
(Present address: INTAS, 58 Avenue des Arts, 1000 Bruxelles, Belgium e-mail: ferrini@intas.be)

We consider the roles of two widely invoked mechanisms for the metallicity-luminosity correlation among late-type galaxies: higher astration level and decreasing efficiency of heavy-element loss with increasing luminosity. We find that both mechanisms contribute about equally to the range in oxygen abundance between low ($\log L_B \sim 8$) and high ($\log L_B \sim 10.5$) luminosity galaxies. We also consider the transition from spirals to irregulars, finding that both the oxygen abundance deficiency (indicating the degree of mass exchange between a galaxy and its environment) and the gas fraction vary smoothly along the sequence. Thus, we find no "irregular versus spiral dichotomy".

On the origin of the L–Z relation. Twenty years ago Lequeux *et al.* [4] have revealed that the oxygen abundance correlates with total galaxy mass for irregular galaxies. Since the galaxy mass is a poorly known parameter, the luminosity – metallicity (L–Z) relation instead of the mass – metallicity relation is usually considered [11]. It has been found that the characteristic gas-phase abundances (the oxygen abundance at a predetermined galactocentric distance) and luminosities of spiral galaxies are also correlated [12, 13, 3], and this relationship maps almost directly on to the luminosity – metallicity relationship of irregular galaxies [13, 3].

It is widely suggested that the L–Z relation for irregular galaxies is caused by galactic winds of different efficiencies. In other words, the L–Z relation represents the ability of a given galaxy to keep the products of its own evolution rather than their ability to produce metals. On the other hand, it has been found that the astration level is higher in massive irregular galaxies than in dwarf ones [4]. The systematic increase of the astration level with luminosity can also play a role in the origin of the L–Z relationship.

In our works [8, 9] the values of gas mass fraction μ and oxygen abundance deficiency η (which is a good indicator of efficiency of mass exchange between a galaxy and its environments) have been derived for a number of spiral and irregular galaxies. Using these data, the roles of two mechanisms – astration level increasing with luminosity and efficiency of heavy elements loss decreasing – as causes of the L–Z correlation among later-type spiral and irregular galaxies will be examined, along with the transition from spirals to irregulars.

Our data shows that there is a correlation between the gas mass fraction μ and the galaxy's luminosity, $\mu \sim 0.8$ at $\log L_B = 7$ and $\mu \sim 0.2$ at $\log L_B = 10.5$. At the same time the oxygen abundance deficiency increases with decreasing luminosity over the large interval of luminosity. Then, one can expect that both mechanisms contribute to the effect. The available data allow to distinguish the contribution of the decrease of gas mass fraction with luminosity and the contribution of the decrease of galactic wind efficiency with luminosity to the difference in oxygen abundances of low- and high-luminosity galaxies.

We discuss first the contribution of the gas mass fraction. The relationship between it and galaxy luminosity can be approximated by the linear expression [10]. The oxygen abundance as a function of present-day gas fraction has been computed for closed-box model galaxies using the model of chemical and photometric evolution of galaxies [8]. Within the interval $\mu = 0.2$ to $\mu = 0.8$ the dependence can be well represented by the linear expression [10]. Then, it can be easy found that the variation in oxygen abundance caused by the increase of astration level with luminosity is given [10]

$$12 + \log O/H_{CB} = 6.55 + 0.24 \times \log L_B. \tag{1}$$

This relation can explain the difference in oxygen abundances between a galaxy of luminosity $\log L_B = 8$ and a galaxy of luminosity $\log L_B = 10.5$ around 0.6 dex, while the observed difference is around 1.2 dex. The increase in astration level causes about half of the effect, in agreement with the fact that elliptical galaxies have oxygen abundances exceeding those of comparably luminous dwarf irregulars [11], but not all of it. Thus, it can be concluded that both mechanisms contribute about equally to the range in oxygen abundance between low ($\log L_B \sim 8$) and high ($\log L_B \sim 10.5$) luminosity galaxies.

Irregulars versus spirals dichotomy. By tradition, the late-type galaxies are divided into two classes (irregulars and spirals), and these classes of galaxies are investigated individually. In particular, the existing models of chemical evolution of spiral galaxies are quite different from the ones applied to irregular galaxies. In order to reproduce the observational data (mainly for our Galaxy which is a giant spiral) various versions of the infall model, in which an infall of gas onto the disk takes place for a long time, have been suggested for spiral galaxies (see [2, 7] and references therein). The hypothesis of an infall of gas onto the disks of spiral galaxies is confirmed by the observational data. The Magellanic Stream is an excellent example of the present-day capture of the matter by our Galaxy from satellite galaxies. On the other hand, various versions of models in which an ejection of gas from the galaxy takes place, have been suggested for irregular galaxies (see [6] and references therein). The hypothesis of gas outflows from dwarf galaxies is also confirmed by observational data. Outflows of gas have been observed in a number of galaxies [5]. However, from Sc to Im the Hubble sequence is really a luminosity sequence [1]. The morphological properties of galaxies change in a gradual way along a sequence of decreasing luminosity (the bulge-to-disk ratio decreases along a sequence of decreasing luminosity in a gradual manner, and the bulge is lost in faint galaxies; the spiral structure gets more chaotic in fainter galaxies and is also lost) and do not show a sharp line of demarcation between irregulars and spirals (an "irregular versus spiral dichotomy").

The L_B versus μ diagram and the L_B versus η diagram provides a test of whether the properties of late-type galaxies change in a gradual way along a sequence of decreasing luminosity. Our data shows that there are no jump-like variations in astration level and oxygen abundance deficiency in going from spiral to irregular galaxies. Thus, the variations of astration level and oxygen abundance deficiency among late-type spiral and irregular galaxies provide additional evidence that the properties of late-type galaxies change in a gradual way along a sequence of decreasing luminosity.

The more detailed discussion can be found in [10].

Acknowledgements. This study was partly supported by the INTAS grant N 97–0033 and the NATO grant PST.CLG.976036.

REFERENCES

[1] *Binggeli B.* Dwarf galaxies: a morphological overview // Panchromatic view of galaxies – their evolutionary puzzle / Eds G. Hensler, Ch. Theis, J. Gallagher.–Editions Frontieres, 1994.–P. 173–191.

[2] *Ferrini F., Matteucci F., Pardi C., Penco U.* Evolution of spiral galaxies: Halo-disk connection for the evolution of the solar neighborhood // Astrophys. J.–1992.–**387**, N 1.–P. 138–151.

[3] *Garnett D. R., Shields G. A., Skillman E. D., et al.* Interstellar abundance gradients in NGC2403: comparison to M33 // Astrophys. J.–1997.–**489**, N 1.–P. 63–86.

[4] *Lequeux J., Peimbert M., Rayo J. F., et al.* Chemical composition and evolution of irregular and blue compact galaxies // Astron. and Astrophys.–1979.–**80**, N 1.–P. 155–166.

[5] *Marlowe A. T., Heckman T. M., Wyse R. F. G., Schommer R.* Observations of the impact of sturbursts on the interstellar medium in dwarf galaxies // Astrophys. J.–1995.–**438**, N 2.–P. 563–589.

[6] *Pilyugin L. S.* On the evolution of iron and oxygen abundances in the Large Magellanic Cloud // Astron. and Astrophys.–1996.–**310**, N 3.–P. 751–756.

[7] *Pilyugin L. S., Edmunds M. G.* Chemical evolution of the Milky Way Galaxy: On the infall model of galactic chemical evolution // Astron. and Astrophys.–1996.–**313**, N 3.–P. 783–791.

[8] *Pilyugin L. S., Ferrini F.* On the oxygen abundance deficiency in spiral galaxies // Astron. and Astrophys.–1998.–**336**, N 1.–P. 103–115.

[9] *Pilyugin L. S., Ferrini F.* On the oxygen abundance deficiency in irregular galaxies // Astron. and Astrophys.–2000.–**354**, N 3.–P. 874–880.

[10] *Pilyugin L. S., Ferrini F.* On the origin of the luminosity- metallicity relation for late-type galaxies: spirals to irregulars transition // Astron. and Astrophys.–2000.–**358**, N 1.–P. 72–76.

[11] *Richer M. G., McCall M. L.* Oxygen abundances in diffuse ellipticals and the metallicity-luminosity relations for dwarf galaxies// Astrophys. J.–1995.–**445**, N 2.–P. 642–659.

[12] *Vila-Costas M. B., Edmunds M. G.* The relation between abundance gradients and the physical properties of spiral galaxies // Mon. Notic. Roy. Astron. Soc.–1992.–**259**, N 1.–P. 121–145.

[13] *Zaritsky D., Kennicutt R. C., Huchra J. P.* HII regions and the abundance properties of spiral galaxies // Astrophys. J.–1994.–**420**, N 1.–P. 87–109.

ACTIVE GALACTIC NUCLEI: RESULTS AT THE CRIMEAN OBSERVATORY

Yu. S. Efimov, N. I. Merkulova, Yu. I. Neshpor, I. I. Pronik, V. I. Pronik, S. G. Sergeev, N. M. Shakhovskoy, A. A. Stepanian

Crimean Astrophysical Observatory, Ministry of Ukraine for Education and Science
Naukove, 98409 Crimea, Ukraine
e-mail: vpronik@crao.crimea.ua

Active Galactic Nuclei (AGNs) are studied at the Crimean Observatory in the spectral range from radio to gamma rays.
The research of AGNs in radio includes the observations of milliarcsecond structure of compact radio sources, extensive monitoring of them and survey of the northern sky at 3.5 cm.
Results obtained in optics concern: continuum variability to reveal the nature of AGNs central sources; connection between the flux variability of broad emission lines and continuum; the nature of the broad line region, its dimension and structure. Optical results are based on data of long time-scale spectral monitoring of AGNs and permit to investigate the evolution of the broad emission line profiles and other spectral characteristics. Data on $UBVRI$ flux variability of the nuclei of Seyfert galaxies obtained through 7 years permit to suspect that different sources caused variability occurred on intranight and extranight time scales.
Photopolarimetric observations of dozen of BL Lac type objects, which have been carried out since the 70s, have revealed the large variations of the polarization degree up to 40% and the position angle of polarization in long (months) and short (days) time scales. These variations confirm the shock wave model of blazar's jets and indicate the long-lived spiral structure of the magnetic field in the inner part of jet. The short-terms variations of the brightness and polarization parameters can be explained by the irregular structure of flux of relativistic electrons penetrating along the jet.
Differences in stellar content of circumnucleus of AGNs and normal galaxies and flux variability of several AGNs were obtained using 1600–3500 Å spectral observations with the scanning spectrometer of Space Station "Astron".
The observations of very high energy gamma radiation from AGNs were carried out at the Crimean Astrophysical Observatory with the aid of ground-based detector. The gamma-ray flux was detected from blazars Mkn 501 in observations in 1997–98 and 3C 66A in observations 1996–1997. The observations of BL Lac carried out in 1998 also show the γ-rays radiation from this object.

INTRODUCTION

The research of AGNs at the Crimean Astrophysical Observatory is carried out in radio, optics, near ultraviolet and γ-rays regions. The working telescopes and topics are following:

Radio – 22-m radio telescope.

– The milliarcsecond structure of compact extragalactic radio sources; extensive monitoring of compact extragalactic radio sources at 3 mm – 2.5 cm; survey of the northern sky at 3.5 cm.

Optics – 1.25-m and 2.6-m telescopes.

– Extensive spectral monitoring of AGNs with CCD spectrograph; brightness monitoring of AGNs; polarimetry of blazars.

Near ultraviolet – Scanning ultraviolet spectrometer of the telescope "Spica" on the Space Station "Astron".

– Spectral energy distribution of AGNs in the region 1600–3500 Å; stellar content of central regions of AGNs; variability of AGNs.

High energy – Telescope with 48 mirrors, each of 1.2-m, for observation of Cherenkov radiation.

– Search high energy extragalactic γ–rays sources; time variations of γ–rays fluxes.

RADIO OBSERVATION

Radio observations are performed since 1967 by I. G. Moiseev, V. A. Efanov, N. S. Nesterov, S. Volvach, *et al.*

Crimean 22-m telescope is a part of International Very Large Base Interferometer (VLBI) which investigate the milliarcsecond structure of extragalactic compact radio sources [1]. Bright radio source 3C 84 (Seyfert galaxy NGC 1275) was the first object investigated in detail. There were revealed two compact components near the bright central source. The evolution of the structure of the radio nucleus was observed during more than 10 years.

3.8 cm – 1.1 mm variability of several dozens of AGNs was monitoring during 20–30 years at the Crimean Observatory together with the Metsahovi Radio Station (Finland). Since 1978 over 4000 observations of some of 40 sources have been obtained with the 22-m telescope of the Crimean Observatory (1.35 cm – 8 mm) and with the Metsahovi 13.7-m telescope (2.5 cm – 3.3 mm) [2]. Data for several dozens sources of extensive monitoring were combined with the other observations to derive separate quiescent and flare component spectra which are crucial to gain an understanding of structure and evolution of compact radio sources. The simple shape and the overall evolution of the flares agree in far greater detail with the shock–in–jet model by Marscher and Gear than it was possible before [3].

The longest series of observations was obtained for the source 3C 84 (NGC 1275). The flux density variation of this source at 3.75 cm – 1.1 mm obtained at the Crimean Observatory and in Finland were compared with the optical V band flux observed by Lyuty [4]. The radio flux curves are exhibited from 1960 till 1993. Two types of variations have been revealed:

1. Outbursts at radio frequencies which occur 5–6 years after the corresponding optical events. These were identified with shocks forming in the radio jet.

2. Variation which is caused by a slowly changing component having a time delay of ∼8 years between radio and optical domains.

Authors proposed that this variation results from a period of enhanced accretion rate in the nucleus, beginning in the 1950s and leading to the growth and subsequent decay of the radio emitting jet.

Survey of the northern sky was obtained at 3.5 cm. The 30% of the Survey sources are newly revealed.

OPTICS

Multicolour photometry of active regions in normal and peculiar galaxies. Observational link between galaxy activity and AGNs

Foundation of section "active galactic nuclei" belongs to the 50s, when V. Ambartsumian introduced for the first time the term "activity of galactic nuclei" to explain numerous peculiar phenomena in galaxies. First main task of astrophysics was an explanation of very strong radio emission of certain radio galaxies. Baade and Minkovski discussed the hypothesis of a realization of the kinetic energy of "colliding galaxies". Instead of this hypothesis Ambartsumian considered activity in nuclei (see review "Observations of active galactic nuclei at the Crimean Astrophysical Observatory" by V. Pronik [5]).

The study of galaxy activity at the Crimean Observatory begins since the fifties when G. Shajn revealed 82 giant H II regions and about 200 high luminosity regions of recent star formations in the spiral branches of the galaxy M33 using H_α filter [6]. G. Shajn first concluded that interstellar matter is dominant by masses inside the complexes of gaseous nebulae and young stars in spiral branches of galaxies. It was an essential leap in the understanding of processes of star formations. This investigation has been prolonged in the 60s with the 2.6-m Shajn telescope under leadership of A. Severny, V. Nikonov and K. Chuvaev. Hundreds regions of recent star formation and giant H II complexes were revealed in several dozens of galaxies, using 5–9 filters in spectral region 3700–7100 Å and image tube in the prime focus of the 2.6-m telescope [7]. Several thousands images obtained for more than 200 extragalactic objects are contained in the archive of the Crimean Observatory.

Using negatives of the Crimean ultraviolet images obtained at the prime focus of 2.6-m telescope V. Pronik and A. Scherbakov revealed optical variability of a jet in the nucleus of peculiar galaxy Virgo A [8].

Multicolour photometry was used by K. Chuvaev and I. Pronik for investigations of starforming activity of normal and barred spiral galaxies [9], by Pronik and Metik to study the circumnuclear regions of Markarian and Seyfert galaxies and its interactions with the starlike objects [10]. It was shown that current star formations in bar galaxies are higher than in normal ones and there is an interaction of Seyfert nuclei with starlike objects which can cause their powering. BVR photometry of starlike objects interacting with the nuclei of Seyfert galaxies was fulfilled by Prokof'eva *et al.* [11]. They showed that starlike objects are complex by nature including stars both of early and late populations. This fact has confirmed an important role of starlike objects in evolution of Seyfert nuclei. Reviews on centers of starformations in the nuclei of galaxies and various levels of galaxy activity were made by V. Pronik and I. Pronik [12, 13].

Spectral observations

The spectral study of galactic nuclear activity at the Crimean Observatory began in 1963 immediately after identifying an unusually large redshift in the spectrum of quasar 3C 273 by M. Shmidt. The large cosmological distance ($z = 0.35$) and high apparent magnitude of 3C 273 indicated an extremely high luminosity of this object which required an explanation. At the same time, the similarity of its spectrum to the spectra of the nuclei of Seyfert galaxies evidenced a relationship or even an identical nature of these objects. There was a difference only in luminosity which is several orders greater for quasars. But visible brightness of nuclei of the nearest Seyfert galaxies and equivalent widths of emission lines are higher than for quasars. Therefore, it becomes obvious that the key to understanding the nature of quasars should be sought in nuclei of Seyfert galaxies. E. Dibaj and V. Pronik began studies of the physical conditions in nuclei of Seyfert galaxies [14, 15].

The works of Dibaj and V. Pronik were pioneer at that time. The conclusion was made about the presence of two subsystems (two zones) of gas in nuclei of Seyfert galaxies: one emitting narrow lines is more extended region (more than 100 ps) and has a low electron density (10^3–10^4 cm^{-3}) and low velocity dispersion (300–500 km/s); the other emitting broad lines is a small (≤ 10 ps) inner region with high electron density (10^8–10^9 cm^{-3}) and high velocity dispersion of several thousands km/s. They were subsequently called: the narrow–line region (NLR) and broad–line region (BLR). It was suspected that both gas systems are result of successive explosions in the central source of the nucleus responsible for continuum emission.

Obtained spectra of dozens of Markarian galaxies permit to reveal 15 new Seyfert galaxies [16].

V. Pronik (1977) [17] has paid attention that the observed estimates of electron density (n_e) from [OIII] line intensities for almost all galaxies give the same value (2–3)$\times 10^6$ cm^{-3} (critical density for [OIII] lines) despite the large luminosity range about 2–3 orders. It becomes clear that the gas density decreased with radius as r^{-2} and observed large difference of density between BLR and NLR is a result of lack of methods for gas density determination when $n_e \geq 10^7$ cm^{-3}.

Occasional observations of Seyfert galaxies were performing up to the seventies, when principal property of Seyfert nuclei, variability of emission lines and continuum fluxes, became obvious. Since 1971 V. Pronik and K. Chuvaev [18] have begun photographic spectral monitoring of AGNs variability. A line-continuum correlation was established. The method for calibration of spectra by using of [OIII] lines flux was proposed. The Seyfert galaxy Mrk 6 was the first object for which an analysis of systematic spectroscopic observations was made. Variable component in the blue wing of the H_β line of this nucleus was investigated. The changes of Seyfert type was first revealed.

The archive of spectral data created by K. Chuvaev contains photographic spectra for more than 200 Seyfert and Markarian galaxies. More than 20 of them were observed during about 20 years and more than 30 ones during 10 years. The results of long term observations of the H_β and [OIII] line profiles and their intensities in galaxies NGC 7469, NGC 5548, NGC 4151, NGC 1275 have been published in series of papers by K. Chuvaev [19]–[21].

The characteristics of time variability of the hydrogen lines in Seyfert galaxies NGC 1275, NGC 3227 and NGC 7469 have been observed by I. Pronik during 10 years [22]–[24]. Variation of the Balmer $H_\alpha/H_\beta/H_\gamma$ decrement with typical time of 20 days was revealed for the first time.

Seyfert type changes was observed for the nuclei of Mrk 6 [18], NGC 3227 [24], NGC 4151 [25] and NGC 7469 [26] by K. Chuvaev, V. Pronik and I. Pronik with the coauthors.

Special attention was paid to the nucleus of NGC 1275 which contains strong variable radio source. The most wide and complex [OIII] 5007 Å line profile and an extremely strong variations of the nucleus brightness in continuum were observed in 1965–1980. There are numerous gas streams in the vicinity of the nucleus which have a strictly radial motion. The complex structure of the NGC 1275 nucleus was revealed by V. Pronik [27] who investigated burst events by velocities of circumnuclear gas. The attempts to detect the variability of emission line fluxes of H_β and λ 4959, 5007 Å [OIII] have been made by I. Pronik, Merkulova, Metik [28, 29]. There was no common opinion concerning the reality of spectral variations in NGC 1275 (Chuvaev, [30]). The search of such a variability is no void of sense. Suspicion on forbidden line variability was proposed for Seyfert nucleus of the NGC 7469 galaxy too [31]. The theoretical works concerning the possibility of [OIII] lines variability in AGNs were made by V. Pronik and I. Pronik [32, 33].

A fleeting change of the flux in the lines and continuum of the NGC 7469 nucleus over two months was recorded, which led to the temporary disappearance of the broad wings in the H_β and H_α lines (Doroshenko, Sergeev, Chuvaev [34]).

Two reviews on variability of emission lines were published by Lyutyi and V. Pronik [35], and I. Pronik [36].

Since 1988 spectroscopic observations of AGNs have been performing with CCD spectrograph. High accuracy of observations and instantaneous recording of the spectra with their subsequent processing on a PC made possible the permanent monitoring of the behavior of the AGNs spectra on short and long time scales.

The most intensive spectral monitoring over more than 10 years was carried out for NGC 4151, NGC 5548, NGC 7469, Mrk 6, Arp 102-B, 3C 390.3 and other active galaxies by Chuvaev, Malkov, Pronik, Sergeev and Sergeeva. The database containing more than 2000 CCD spectra of AGNs was created. The Crimean Observatory participates in the international programs of spectroscopic and photometric monitoring AGNs (AGN WATCH, see [37]–[39]). The important results concerned the line–continuum correlation and decomposition of broad line profiles for NGC 4151, NGC 5548 and Mrk 6 nuclei were obtained by Malkov, V. Pronik, Sergeev and Sergeeva [40]–[43]. It was shown that the line-continuum diagram for NGC 4151 contradicts to the simplest AGN paradigm where a single central source of continuum caused a steady relation between the visible and ionizing continuum. An explanation of the shape evolution for broad emission line profiles in the NGC 4151 has been given in terms of BLR model with two–component profile [43].

A link between the H_β equivalent width, profile width, the BLR size and optical continuum luminosity have been found from a small sample of well studied AGNs [44]. The radius–luminosity relation of $r \sim L^{0.7}$ and mass–luminosity relation $L \sim M^{1.9}$ have been claimed for AGNs. Different temporal changes of the line–continuum lag in blue and red H_β wings have been found in the spectra of Seyfert galaxy Mrk 6 [45].

The rotational redistribution of matter emitted the broad double-peaked line profiles was revealed in Arp 102B [42]. The model of BLR in Arp 102B represents a great variety of gas clouds rotating predominantly in the same plane. Model explains double-peaked profiles, drift motion of emission details along profile from red to blue wings and observed regular variations of the red-peak-to-blue-peak flux ratio.

Photoelectric brightness monitoring

Since 1982 photoelectric monitoring of flux variation of AGNs with time scale resolution of about 4 min has been performing first at the Crimean Observatory with the 1.25-m telescope by N. Merkulova, L. Metik and I. Pronik. Since 1989 simultaneous $UBVRI$ observations of selected Seyfert galaxies have been carried out.

The character of the flux variability was found to be different for different sources. A light curve of the NGC 1275 continuum near λ 5200 Å in 1982–1987 did not show systematical trends of the brightness during 5 years, but several drops of brightness characterized the flux variations. Intranight variations up to 20% were revealed [46]. Extraordinary brightening of the NGC 4151 nucleus during 7.3 years (1989 – 1996) was observed. The amplitudes of the brightening are $2.^m0$, $1.^m5$, $0.^m9$, $0.^m8$ and $0.^m7$ in $UBVRI$ bands, respectively [47]. Flares with duration of 10–150 days are revealed overlapped on the smooth light curves. An optical energy distribution for flux excesses on smooth light curve and during the flares can be fitted by the power law form: $F_\nu \sim \nu^\alpha$. Obtained data suggested that the nucleus brightness increasing is caused by the emitting synchrotron radiation clouds ejected from the nucleus during its active period.

Types of processes causing the continuum variability in the optical of the nuclei of Seyfert galaxies are determined using Structure Function (SF) analysis [46, 48]. Complex form of SF for variable flux of the NGC 1275 nucleus, obtained for continuum near λ 5200 Å in 1982–1987 and in the $UBVRI$ bands in 1989–1994, allows us to suppose that there are two types of intranight and one type of yearly variations in this nucleus. Obtained data show that there are two sources causing intranight variability and one source of extranight variability in the nucleus of NGC 1275.

SF characteristics of the variable $UBVRI$ fluxes of NGC 4151 nucleus exhibit variations with time. The types of processes caused this variability varied on intranight and extranight time scales in different directions during the increasing of the brightness of its nucleus.

Multisources observational picture of variable optical continuum resembles that of complex structure of central radio sources observed with the VLBI. For instance such structure is well known for radio source 3C 84 (NGC 1275).

The photoelectric monitoring of continuum flux variability of AGNs is performing in the frame of international program AGN WATCH too.

Polarimetrical investigations

The high quality photopolarimetric observations of dozen of BL Lac type objects have been provided by Shakhovskoj and Efimov since the 70s with the 2.6-m Shajn and 1.25-m telescopes to study the structure and geometry of the regions of jets where powerful synchrotron radiation arises [49]–[53]. This job is performing in $UBVRI$ since 1994 in the frame of the great international program OJ-94 [54]–[59].

The large variations of the polarization degree up to 40% and the position angle of polarization on long (months) and short (days) time scales are revealed. These variations confirm the shock wave model of blazar's jets and indicate the long-lived spiral structure of the magnetic field in the inner part of jet. The short-terms variations of the brightness and polarization parameters can be explained by the irregular structure of the flux of relativistic electrons penetrating along the jet.

NEAR ULTRAVIOLET INVESTIGATION

Since 1983 Space Station "Astron" constructed at the Crimean Astrophysical Observatory under leadership of A. Severny and A. Boyarchuk had operated about ten years [60]. It was found that 1600–3500 Å spectral energy distribution of circumnuclear regions of galaxies containing active nuclei shows excess of regions of recent star formation compare to the central regions of normal galaxies.

UBV variability of Seyfert nucleus of galaxy Mrk 573 obtained by Neizvestny, was confirmed by us in near ultraviolet region being about $0.^{m}75$ during about 2.5 years. Mini Seyfert nuclei NGC 598 (M33) and NGC 5236 (M83) were knowns as variable in the UBV system. Observations with the Space Station "Astron" allow to conclude that amplitude of their near ultraviolet variability is about 1^{m}. The first exhibits flare but the second shows drops of brightness compare to the normal state.

VERY HIGH ENERGY INVESTIGATION

The high energy (HE) γ–rays ($E \geq 100\,MeV$) are observed with satellites because γ–rays of these energy are absorbed in Earth atmosphere. One can observe very high energy (VHE) γ–rays ($E \geq 100\,GeV$) using ground-based detectors. The Cherenkov light emitting by high energy electrons generated due to interaction of gamma ray with Earth atmosphere is used. The narrow angle of Cherenkov radiation along the tracks of primary quanta permit us to find the source of γ–rays. There are about 10 detectors of such a type all over the world. Three of them are located at the Southern hemisphere of the Earth and the others are in the Northern one. One of them is at the Crimean Astrophysical Observatory (CrAO). The CrAO Cherenkov detector (gamma-telescope GT–48) consists of two mounting 20 m apart and has mirrors with total area 54 m^2. The energy threshold is equal to 1 TeV. The details may be found in [61]. During 1996–98, the three blazars were observed: Mk 501, 3C 66A and BL Lac. The results of observations are presented in Table 1. Here L is the power of γ–rays radiation: $L = E{\cdot}F(E)$, where E is the photon energy and $F(E)$ is the spectral density of radiation. All values are estimated on the assumption of isotropy of radiation. According to the current models the total radiation is (with high confidence) connected with high energy electrons, partly with synchrotron radiation and partly with inverse Compton radiation of electrons on lower energy electromagnetic radiation.

Table 1: Energy of radiation of several lacertides

Object	Distance (Mpc)	Optics Log$L$ [ref.] (erg/s)	HE Log$L$ [ref.] (erg/s)	VHE Log$L$ [ref.] (erg/s)
BL Lac	280	44.8 [62]	44.9[64]	44.5 [67]
MK–501	160	44.4 [63]	–	44.5 [65]
3C 66A	1800	46.4 [63]	46.2[64]	46.3 [66]

As it is seen from the table, the value of total power in optical range, in the high energy γ-rays and in the very high energy range are nearly the same for these three objects.

Acknowledgements. We acknowledge L. P. Metik for the help with the manuscript preparing.
The research described in this publication was made possible in part by Award N UP1–2116 of the U. S. Civilian Research & Development Foundation for the Independent States of the Former Soviet Union (CRDF).

REFERENCES

[1] *Kellermann K. I., Jauncey D. L., Cohen M. H., et al.* // Astrophys. J.–1971.–**169**, N 1.–P. 1–24.

[2] *Valtaoja E., Haarala S., Lehto H., et al.* // Astron. and Astrophys.–1988.–**203**, N 1.–P. 1–20.

[3] *Nesterov N. S., Kovalev Yu. Yu., Babak S. V., Larionov G. M.* // Astron. J.–1994.–**71**, N 6.–P. 850–857. (in Russian).

[4] *Nesterov N. S., Lyuty V. M., Valtaoja E.* // Astron. and Astrophys.–1995.–**296**, N 3.–P. 628–632.

[5] *Pronik V.* // Bull. Crim. Astrophys. Obs.–1998.–**94**,–P. 1–6.

[6] *Shajn G. A.* // Izv. Krimsk. Astrofiz. Obs.–1954.–**11**.–P. 3–7. (in Russian).

[7] *Butslov M., Kopylov I. M., Nikonov V. B., et al.* // Astron. J.–1962.–**39**, N 2.–P. 315–322. (in Russian).

[8] *Pronik V., Scherbakov A.* // Astrofizika.–1972.–**8**, N 3.–P. 337–342. (in Russian).

[9] *Pronik I., Chuvaev K.* // External galaxies and Quasi–stellar objects: Proc. IAU Symp. **44** / Ed. D. Evans.– Dordrecht: D. Reidel, 1972.–P. 62–65.

[10] *Pronik I., Metik L.* // Extranuclear Activity in Galaxies: Proc. of Workshop ESO **32** / Eds E. Meurs, R. Fosbury.–1989.–P. 25–29.

[11] *Prokof'eva V., Pronik I., Sharipova L.* // Astron. and Astrophys. Transactions.–1995.–**8**, N 4.–P. 285–290.

[12] *Pronik V.* // Highlights of Astronomy.–1980.–**5**.–P. 223–225.

[13] *Pronik I., Pronik V.* // Transactions of GAISH.–1988.–**60**.–P. 295–314.

[14] *Dibaj E., Pronik V.* // Astrofizika.–1965.–**1**, N 1.–P. 78–90. (in Russian).

[15] *Dibaj E., Pronik V.* // Astron. J.–1967.–**44**, N 5.–P. 952–964. (in Russian).

[16] *Kopilov I., Lipovetski V., Pronik V., Chuvaev K.* // Astrofizika.–1976.–**12**, N 2.–P. 189–194. (in Russian).

[17] *Pronik V.* // Astrofizika.–1977.–**13**, N 1.–P. 51–61. (in Russian).

[18] *Pronik V., Chuvaev K.* // Astrofizika.–1972.–**8**, N 2.–P. 187–196. (in Russian).

[19] *Chuvaev K.* // Pisma v Astron. J.–1980.–**6**, N 6.–P. 323–329. (in Russian).

[20] *Chuvaev K.* // Pisma v Astron. J.–1985.–**11**, N 11.–P. 803–810. (in Russian).

[21] *Chuvaev K.* // Izv. Krimsk. Astrofiz. Obs.–1990.–**81**.–P. 138–148. (in Russian).

[22] *Pronik I.* // Astron. J.–1975.–**52**, N 3.–P. 481–490. (in Russian).

[23] *Pronik I.* // Izv. Krimsk. Astrofiz. Obs.–1980.–**61**.–P. 131–144. (in Russian).

[24] *Pronik I.* // Izv. Krimsk. Astrofiz. Obs.–1983.–**68**.–P. 81–93. (in Russian).

[25] *Lyutyj V., Oknyanskiy V., Chuvaev K.* // Pisma v. Astron. J.–1984.–**10**, N 11.–P. 803–807. (in Russian).

[26] *Chuvaev K., Lyutyj V., Doroshenko V.* // Pisma v Astron. J.–1990.–**16**, N 10.–P. 867–876. (in Russian).

[27] *Pronik V.* // Astrofizika.–1979.–**15**, N 1.–P. 51–57. (in Russian).

[28] *Merkulova N., Pronik I.* // Izv. Krimsk. Astrophys. Obs.–1985.–**85**.–P. 160–174. (in Russian).

[29] *Pronik I., Merkulova N., Metik L.* // Astrophys. and Space Sci.–1990.–**171**, N 1/2.–P. 91–95.

[30] *Chuvaev K.* // Pisma v Astron. J.–1985.–**11**, N 11.– P. 803–810. (in Russian).

[31] *Pronik I., Metik L., Merkulova N.* // Astron. and Astrophys.–1997.–**318**, N 3.–P. 721–728.

[32] *Pronik V., Pronik I.* // Astron. J.–1988.–**65**, N 3.–P. 478–487. (in Russian).

[33] *Pronik V., Pronik I.* // Astron. and Astrophys. Transactions.–1992.–**3**, N 1.–P. 57–62.

[34] *Doroshenko V., Sergeev S., Chuvaev K.* // Astron. J.–1994.–**71**, N 2.–P. 200–215. (in Russian).

[35] *Lyuty V., Pronik V.* // Variable Stars and Stellar Evolution: Proc. IAU Symp., **67** / Eds V. Sherwood, L. Plaut.–Dordrecht: D. Reidel, 1975.–P. 591–604.

[36] *Pronik I.* // Observational Evidence of Activity in Galaxies: Proc. IAU Symp., **121** / Eds E. Khachikian, *et al.*–Dordrecht: D. Reidel, 1986.–P. 169–184.

[37] *Peterson B., Burth A., Berlind P., et al.*// Astrophys. J.–1999.–**510**, N 2.–P. 659–668.

[38] *Dietrich M., Peterson B., Albrecht P., et al.* // Astrophys. J. Suppl. Ser.–1998.–**115**, N 1.–P. 185–202.

[39] *Collier S., Horne K., Kaspi S., et al.* // Astrophys. J.–1998.–**500**, N 1.–P. 162–172.

[40] *Sergeev S., Malkov Yu., Chuvaev K., et al.* // Reverberation Mapping of the Broad Line Region in Active Galactic Nuclei: ASP Conf. Ser. / Eds P. Gondhalekar, K. Horne, B. Peterson.–1994.–**69**.–P. 199–209.

[41] *Malkov Yu., Pronik V., Sergeev S.* // Astron. and Astrophys.–1997.–**324**, N 3.–P. 904–914.

[42] *Sergeev S., Pronik V., Sergeeva E.* // Astron. and Astrophys.–2000.–**356**, N 1.–P. 41–49.

[43] *Sergeev S., Pronik V., Sergeeva E.* // Astrophys. J.–2001.–accepted.

[44] *Sergeev S., Pronik V., Malkov Yu., et al.* // Astron. J.–1999.–**118**, N 6.–P. 2659–2667.

[45] *Sergeev S., Pronik V., Sergeeva E., et al.* // Astrophys. J. Suppl. Ser.–1999.–**121**, N 1.–P. 159–169.

[46] *Pronik I., Merkulova N., Metik L.* // Astron. and Astrophys.–1999.–**351**, N 1.–P. 21–30.

[47] *Merkulova N., Metik L., Pronik I.* // Astron. J.–1999.–**117**, N 5.–P. 2177–2184.

[48] *Merkulova N., Metik L., Pronik I.* // Active Galactik Nuclei and Related Phenomena: Proc. IAU Symp., **194** / Eds Ye. Terzian, D. Weedman, E. Khachikian.–Publisher Astron. Soc. Pacif., 1999.–P. 436-438.

[49] *Efimov Yu. S., Shakhovskoy N. M.* // Izv. Krimsk. Astrofiz. Obs.–1972.–**46**.–P. 3–13. (in Russian).

[50] *Shakhovskoy N. M., Efimov Yu. S.* // Izv. Krimsk. Astrofiz. Obs.–1977.–**56**.–P. 39–51. (in Russian).

[51] *Efanov V. A., Moiseev I. G., Nesterov N. S., et al.* // Izv. Krimsk. Astrofiz. Obs.–1972.–**64**.–P. 91–98. (in Russian).

[52] *Doroshenko V. T., Lyuty V. M., Terebizh V. Yu.* // Astron. and Astrophys.–1986.–**163**, N 1/2.– P. 321–325.

[53] *Doroshenko V. T., Efimov Yu. S., Terebizh V. Yu* // Izv. Krimsk. Astrofiz. Obs.–1987.–**73**.–P. 143–153. (in Russian).

[54] *Valtaoja L., Valtaoja E., Shakhovskoy N.M., et al.* // Astron. J.–1991a.–**101**, N 1.–P. 78–87.

[55] *Valtaoja L., Valtaoja E., Shakhovskoy N. M., et al.* // Astron. J.–1991b.–**102**, N 6.–P. 1946–1955.

[56] *Takalo L. O., Sillanpaa A., Pursimo T., et al.* // Astron. and Astrophys. Suppl. Ser.–1996.–**120**, N 2.–P. 313-321.

[57] *Tosti G., Fiorucci M., Luciani M., et al.* // Astron. and Astrophys.–1998.–**339**, N 1.–P. 41–51.

[58] *Massaro E., Maesano M., Montagni F., et al.* // Astron. and Astrophys.–1999.–**342**, N 3.–P. L49–L52.

[59] *Pursimo T., Takalo L. O., Sillanpaa A., et al.* // Astron. and Astrophys. Suppl. Ser.–2000.–**146**.–P. 141–155.

[60] Astrophysical investigations on the Space Station "Astron" / Ed. A. A. Boyarchuk, 1994.

[61] *Vladimirsky B. M., Zyskin Yu. L., Kornienko A. P., et al.* // Izv. Krimsk. Astrofiz. Obs.– 1993.–**91**.–P. 74–105. (in Russian).

[62] *Nikolashvili M. G., Kurtanidze O. M., Richter G. M.* // Proc. of the OJ-94 annual meeting 1999, Torino, Italy, May 19-21, 1999 / Eds C. M. Raiteri, M. Villata, L. O. Takalo.–P. 33–35.

[63] *Perlman E. S., Stocke J. T., Schachter J. F., et al.* // Astrophys. J. Suppl. Ser.–1996.–**104**, N 2.–P. 251–285.

[64] *Hartman R. C., Bertsch D. L., Bloom S. D., et al.* // Astrophys. J. Suppl. Ser.–1999.–**123**, N 1.–P. 79–202.

[65] *Andreeva N. A., Zyskin Yu. L., Kalekin O. R., et al.* // Pisma v Astron. J.–2000.–**26**, N 4.–P. 243–248. (in Russian).

[66] *Neshpor Yu. I., Stepanian A. A., Kalekin O. R., et al.* // Astron. J.–2000.–**77**, N 9.–P. 723–729. (in Russian).

[67] *Neshpor Yu. I., Chalenko N. N., Stepanian A. A., et al.* // Astron. J.–2001.–**78**, N 4. (in Russian).

THE NUCLEI ACTIVITY RECURRENCE AND THE LUMINOSITY PERIODICITY OF QUASARS AND GALAXIES

A. P. Miroshnichenko

Institute of Radio Astronomy, NAS of Ukraine
4 Chervonopraporna St., 61002 Kharkiv-2, Ukraine
e-mail: mir@ira.kharkov.ua

We made the assumption about the cosmological periodicity of quasar and galaxy luminosities from own studies of object samples in the decametric and optical ranges. The corresponding space and time scales of cosmological periodicity were estimated.

INTRODUCTION

We received from our previous studies of the quasar and galaxy luminosity functions in the decametric and optical ranges that the object luminosity changes with cosmological epoch as:

$$L_\nu(z) \sim (1+z)^4. \tag{1}$$

We use this dependence for the estimation of the characteristic luminosity function evolution time $\tau_L = \dfrac{L}{dL/dt}$, taking into account that $dz/dt = H_0(1+z)^2(1+2q_0z)^{1/2}$. Then the τ_L is:

$$\tau_L = \frac{1}{4H_0(1+z)(1+2q_0z)^{1/2}}. \tag{2}$$

The value τ_L is found three times smaller in comparison with the characteristic cosmological evolution time t passed from the beginning of the Universe expanding until given epoch z.

On the basis of own results we assume that nuclei activity may undergo the cyclic changes, that is the quasar and galaxy nuclei activity recurrence may exist. Therefore, the periodicity of the object luminosity distribution should be observed. We assume that the redshift distribution periodicities determined formerly by many authors for quasars and galaxies are caused not only the cell universe structure, but the nuclei activity recurrence too.

SPECTRAL ANALYSIS OF THE QUASAR AND GALAXY LUMINOSITY DISTRIBUTIONS

It is known that the spectral analysis is a good research method of periodicity in the physical value distribution given as the time series. We used this method to two not large, but statistically complete, samples of 114 galaxies and 69 quasars, identificated in the declination zone $\delta = -13^\circ \ldots +20^\circ$ from the UTR-2 catalogue at 25 MHz with optical data. The sample volumes were defined by the object selection criteria: $S_{25} \geq 20$ Jy, $m_v \leq 18.5$, where S_{25} is the flux density at 25 MHz, m_v is the visual magnitude. The UTR-2 sensibility at the regime of the discrete sources 25 MHz measurements is 10 Jy. The sample galaxies occupy the redshift range $z = 0.002 \ldots 0.881$, and the sample quasars occupy the range $z = 0.129 \ldots 2.975$ with mean value $< z >\sim 0.1$ for galaxies and $< z >\sim 1.0$ for quasars.

We derived power spectra (periodograms) P_ν to find periods in the sample quasar and galaxy luminosity distributions upon the redshift:

$$P_\nu = N^{-2}\left|\sum_{n=1}^{N} \Delta B_n \exp(-i2\pi\nu z_n)\right|^2, \tag{3}$$

where $\Delta B_n = B_n - \overline{B}, \overline{B} = N^{-1}\sum_{n=1}^{N} B_n; B_n$ are the observed values ($\log L_{25}$, $\log L_{opt}$ are the object luminosities in decametric and optical ranges), N is the number of observed data intervals, z_n are the object redshifts, ν is the frequency of series counts.

We received the power spectra of the luminosity distributions for total galaxy sample and for separated $FRII$-type (with $\log L_{25} > 25.5$, where values L_{25} are in $\mathrm{W\,Hz^{-1}}$) galaxy subsample, and for the quasar sample in the decametric and optical ranges (for example, see Fig. 1, Fig. 2). Our periodogram analysis revealed the significant peaks (significance level $Q = 97$–99%) for the quasar luminosity distribution at redshifts $z_p = 2.222$; 1.124 in both decametric and optical ranges and at redshift $z_p = 0.448$ in optics. Besides, we found the periodicity peak of optical luminosity at $z_p = 0.224$ ($Q = 93.5\%$).

The galaxy sample luminosity peaks were determined at $z_p = 0.200$ ($Q = 98\%$) in the decametric range and at $z_p = 0.0125$ ($Q = 90.5\%$) in optics.

The subsample of powerful radio galaxies ($FRII$-type) revealed peaks at $z_p = 0.192$ ($Q = 91\%$) in the decametric range, and at $z_p = 0.048$ ($Q = 99\%$) in optics.

The peak significance in the power spectra is estimated with assumption on absence of the periodic component and that the peak ordinate distribution satisfies to exponential law. The probability for given peak amplitude to be random is determined as $q_1(y) = \exp(-y)$, where $y = \frac{P}{\overline{P}}$, P is the peak amplitude, $\overline{P}$ is the mean peak amplitude in the power spectrum. So far as m peaks are observed at periodogram, the probability of the random overcoming of y is:

$$q_m(y) = 1 - (1 - \exp(-y))^m. \tag{4}$$

The number of independent peaks m is estimated as: $m = \frac{\Delta\nu}{\delta\nu} = N/2$, where $\Delta\nu$ is the total interval of the series count frequency ($\Delta\nu = \frac{1}{2\Delta z}$); $\delta\nu$ is the minimum interval of the series count frequency ($\delta\nu = \frac{1}{N\Delta z}$); N is the observed number of data intervals, Δz is the step of the redshift interval in the object luminosity distribution.

The redshift values corresponding to significant peaks in the sample quasar and galaxy luminosity distribution are in agreement with other data on the redshift periodicities. The value $z_p = 0.048$ agrees with result by Broadhurst *et al.* [3] for the galaxy redshifts, the value $z_p = 0.0125$, determined in our galaxy luminosity distribution, is close to the value shown by Duari, Gupta, Narlikar [4] for quasar redshifts ($z_p = 0.0127$). The peak value at $z_p = 0.200$ in the decametric galaxy luminosity distribution corresponds to quasar redshift periodicity shown by Karlsson [7], Barnothy and Barnothy [2], Khodyachyh [8]. The peak position at $z_p = 2.222$ for the quasar luminosity distribution is in agreement with result by Gwyn and Hartwick [5] for the galaxy redshift distribution.

One can see that peak positions in quasar and (or) galaxy luminosity distributions in both decametric and optical ranges may coincide with peak positions in the quasar and (or) galaxy redshift distributions. It is interesting that the peak position at $z_p = 0.200$ for galaxy luminosities is close to the peak position $z_p = 0.224$ for quasar luminosities, and, simultaneously, is close to analogous peak position in quasar redshift distribution. This fact point to the same nature of galaxy and quasar nuclei. In this way, we can suppose about a unique evolution process and the same characteristic evolution scales (in space and in time) for these objects.

The redshift values corresponding to periodicity peaks in the quasar and galaxy luminosity distributions in the decametric and optical ranges are from $z_p = 0.0125$ to $z_p = 2.222$. Let us determine the corresponding space and time scales for luminosity cosmological periodicity on the assumption that values z_p are multiple to smaller value from those ($z_p = 0.0125$). Then, the characteristic size in the object space distribution for $z_p = 0.0125$ is $r_p = 40$ Mpc as the distance r in a comoving volume:

$$r = c\frac{q_0 z + (q_0 - 1)[(1 + 2q_0 z)^{1/2} - 1]}{H_0 q_0^2 (1 + z)}. \tag{5}$$

Note that our value $r_p = 40$ Mpc corresponds to typical size of the galaxy superclusters. Besides, the new fractal analysis [1, 6] of the redshift surveys reveals that the galaxy clustering is described well by the fractal distribution by size $D = 2$ on scale 20–30 Mpc. So, our estimation of the characteristic size r_p in the object space distribution is close to data of other authors.

Also, we determine the characteristic time, connected with peaks of the luminosity periodicity from the expression:

$$t - t_0 = -\frac{1}{H_0}\left[z - (1.5 + 0.5q_0)z^2\right], \tag{6}$$

where t and t_0 are the values of cosmological time for the epoch z and present epoch, respectively [10]. We received that the characteristic time of the luminosity cosmological periodicity of galaxies and quasars (parameters $q_0 = 0.25$, $H_0 = 100$ km s^{-1} Mpc^{-1}) for $z_p = 0.0125$ is $t - t_0 = 1.2\times10^8$ years. This estimation of the periodicity time scale is close to our earlier analogous estimation derived by another method [9].

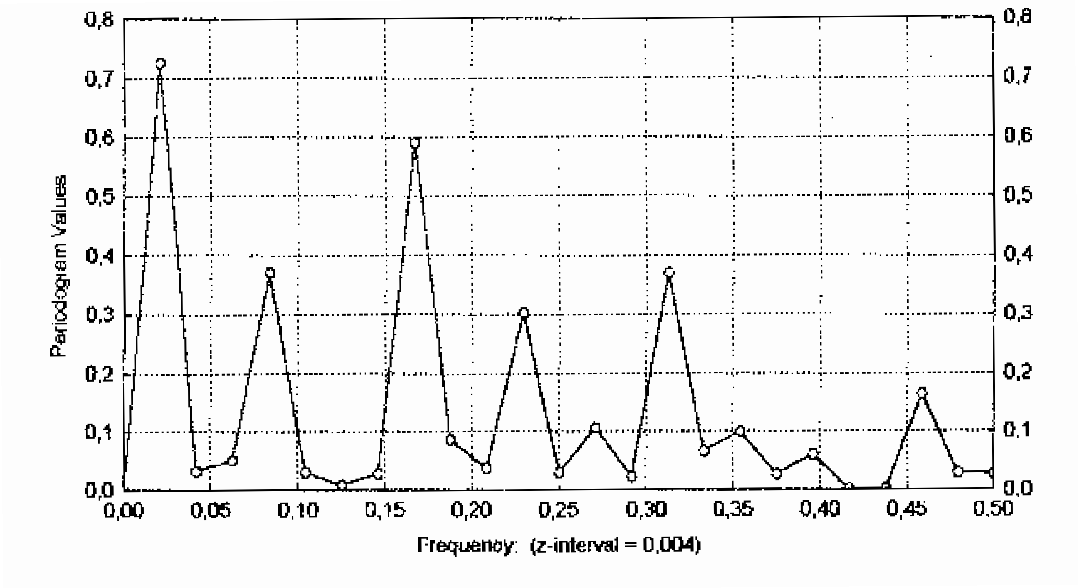

Figure 1: The power spectrum of luminosity distribution for subsample of powerful (FRII type) galaxies at 25 MHz

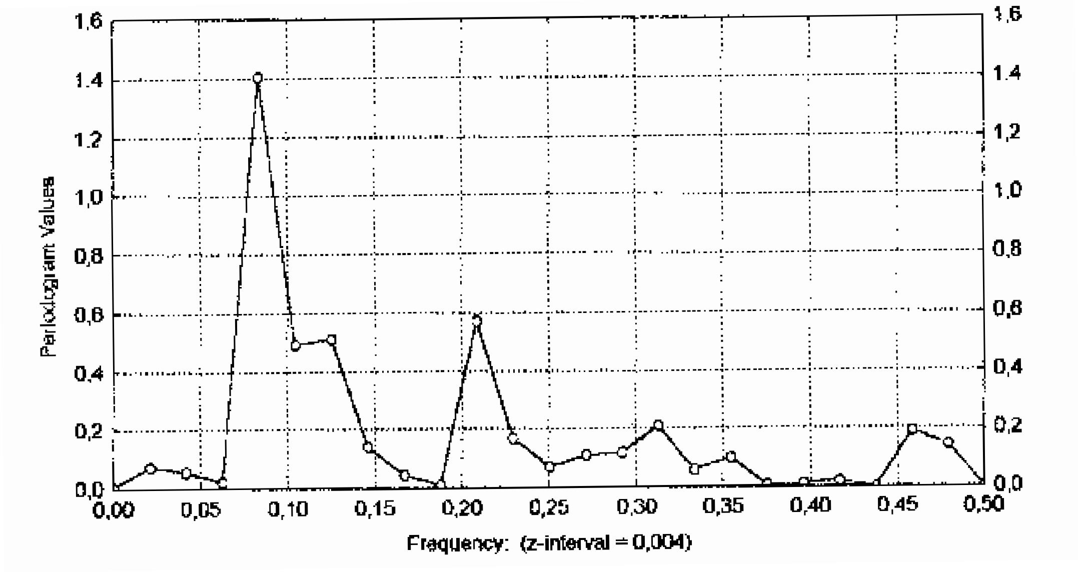

Figure 2: The power spectrum of luminosity distribution for subsample of powerful (FRII type) galaxies in optics

CONCLUSION

Our results are conformed with an assumption about the synchrotron mechanism of active nuclei radiation in wide wavelength range. It is known that time of burning down of the synchrotron radiation sources decreases with increasing of frequency. So, peak periodicity positions z_p in luminosity distributions of the same objects may not coincide in the optical and decametric ranges.

We consider the coincidence of the luminosity periodicity peak positions z_p in different frequency ranges as a manifestation of the cell Universe structure.

Distinctive peak positions z_p in the same object luminosity distributions for mutual distant frequency ranges may testify about the existence of activity recurrence for object nuclei. These nuclei have different characteristic duration of the nonthermal radiation at distant frequencies.

Thus, the cosmological periodicity in the sample luminosity distributions of galaxies and quasars may be an indicator of nuclei activity recurrence, and indicator of cell Universe structure.

REFERENCES

[1] *Amendola L., Palladino E.* The scale of homogeneity in the Las Campanas Redshift Survey // Astrophys. J.–1999.–**514**, N 1.–P. L1–L4.

[2] *Barnothy J., Barnothy M.* Periodicity in the $\ln(1+z)$ distribution of quasars // Publs Astron. Soc. Pacif.–1977.–**88**, N 526.–P. 837–839.

[3] *Broadhurst T., Ellis R., Koo D., Szalay A.* Large-scale distribution of galaxies at the galactic poles // Nature.–1990.–**343**, N 6220.–P. 726–729.

[4] *Duari D., Gupta P., Narlikar J.* Statistical tests of peaks and periodicities in the observed redshift distribution of quasi-stellar objects // Astrophys. J.–1992.–**384**, N 1.–P. 35–42.

[5] *Gwyn S., Hartwick F.* The redshift distribution and luminosity functions of galaxies in the Hubble deep field // Astrophys. J.–1996.–**468**, N 2.–P. L77–L80.

[6] *Joyce M., Montuori M., Sylos Labini F.* Fractal correlations in the CfA2-South redshift survey // Astrophys. J.–1999.–**514**, N 1.–P. L5–L8.

[7] *Karlsson K.* Possible discretization of quasar redshifts // Astron. and Astrophys.–1971.–**13**, N 3.–P. 333–335.

[8] *Khodyachyh M. F.* Cyclic change of the quasar brightness in function of $\ln(1+z)$ // Sov. Astron.–1979.–**56**, N 6.–P. 1174–1178. (in Russian).

[9] *Miroshnichenko A. P.* The effects of the quasar cosmological evolution in the optical and decametric ranges // Kinematics and Physics of Celestial Bodies.–1994.–**10**, N 5.–P. 52–61.

[10] *Zel'dovich Ya. B., Novikov I. D.* The structure and evolution of the Universe.–Moscow: Nauka, 1975.–735 p.

THE LOCAL UNIVERSE

I. D. Karachentsev[1], V. E. Karachentseva[2], W. K. Huchtmeier[3], E. K. Grebel[4], D. Geisler[5], P. Guhathakurta[6], P. W. Hodge[7], A. Sarajedini[8], P. Seitzer[9], A. E. Dolphin[10]

[1] *Special Astrophysical Observatory, Russia*
e-mail: `ikar@luna.sao.ru`

[2] *Astronomical Observatory, Taras Shevchenko National University*
3 Observatorna St., 04053 Kyiv-53, Ukraine

[3] *Max-Planck-Institut für Radioastronomie*
Auf dem Hügel 69, D-53121 Bonn, Germany

[4] *Max-Planck-Institut für Astronomie*
Königstul 17, D-69117, Heidelberg, Germany

[5] *Departmento de Fisica, Grupo de Astronomia, Universidad de Concepcion*
Casilia 160-C, Concepcion, Chile

[6] *UCO/Lick Observatory, University of California at Santa Cruz, Santa Cruz, CA, 95064, USA*

[7] *Department of Astronomy, University of Washington, P.O. Box 351580, Seattle, WA, 98195, USA*

[8] *Astronomy Department, Wesleyan University, Middletown, CT, 06459, USA*

[9] *Department of Astronomy, University of Michigan, 830 Dennison Building, Ann Arbor, MI, 48109, USA*

[10] *Kitt Peak National Observatory, National Optical Astronomy Observatories*
P.O. Box 26732, Tucson, AZ, 85726, USA

We describe first results of international (Germany, Russia, Spain, Ukraine, USA) project to study a population, structure and kinematics of the Local Universe. The prime goal of the project is a creation of representative standard sample of the nearest galaxies with distances $D < 7$ Mpc to get reliable data on their luminosity function, HI-mass function, Dark Matter distribution on scales of [0.1–3] Mpc, star formation function, 3–D map of the Local Volume, and peculiar velocity field. We discuss results of the entire-sky search for new nearby dwarf galaxy candidates and a problem of completeness of the Local Volume sample.

INTRODUCTION

The Local Volume (LV) describes our extragalactic neighborhood out to 7 Mpc and includes galaxies with corrected velocities $V_0 < 500$ km/s. Apart from the Local Group, this volume contains several nearby galaxy groups as well isolated field galaxies. The galaxy census becomes increasingly incomplete for smaller galaxies with low surface brightness (LSB), particularly for dwarf galaxies. Furthermore, while most dwarf galaxies in the Local Group have been studied in great detail, very little is known still about the properties of dwarf galaxies beyond LG boundaries. The original Kraan-Korteweg & Tammann [28] list of 179 galaxies with $V_0 < 500$ km/s was updated by Huchtmeier & Richter [7], Schmidt & Boller [29], and Karachentsev [13] till to $N = 216$. The basic sources of the LV-sample complement are following: Z-surveys of known galaxy catalogues; HI and IR surveys in Zone of Avoidance made by Huchtmeier, Kraan-Korteweg, Henning and others; special searches for dwarf members of the known nearby groups: M81, IC 342 (Borngen & Karachentseva [3]), Centaurus and Sculptor groups (Côté *et al.* [5], Jerjen *et al.* [12]), CVn cloud and M101 group (Binggeli *et al.* [2], Bremnes *et al.* [4]); searches for LSB galaxies in wide sky regions (Shombert *et al.* [30], Impey *et al.* [11]), automated DSS survey around Andromeda (Armandroff *et al.* [1]), *etc.* The increase in the number of the known galaxies with $V_0 < 500$ km/s grows slowly (with a rate of several galaxies per year), and a discovery of very nearby galaxies happens in fact by chance. For example, among 369 LSB galaxies found by Shombert *et al.* [30] there are only 4 galaxies within 500 km/s. For these reasons we began a comprehensive study of dwarf galaxies in the Local Volume. The goal of the project is the creation of representative ($N > 300$ galaxies) standard sample of the nearest ($D < 7$ Mpc) galaxies to get reliable data on their luminosity function, mass function, Dark

Invited paper.

Matter distribution, star formation function, 3–D mapping of the LV, and peculiar velocity field.

THE ENTIRE-SKY SEARCH FOR NEW NEARBY DWARF GALAXY CANDIDATES (KK-SURVEY)

KK- survey has been realized as a comprehensive visual inspection of photographic plates (POSS-II, ESO/SERC, and SERC EJ) to search for new dwarf galaxy candidates in the Local Volume. This project was based on previous experience of searching for LSB galaxies on the POSS-I prints (Karachentseva [21]–[23]), yielded the Catalogue of 1500 low surface brightness galaxies (Karachentseva & Sharina [24]). The project steps and main results were following:

A) Searching for new dwarf galaxies with angular diameters $a > 0'.5$ around 216 LV galaxies within $R = 0.5$ Mpc of each. Totally the 260 objects were found (Karachentseva & Karachentsev [25]), many of them look like Irr galaxies from DDO Catalog (van den Bergh [32]).

B) Searching for dwarf galaxies situated in Hercules-Aquila area $\{$R. A. $= 14.0^h$, 23.5^h, D. $= -3°$, $+60°\}$, so-called the Local Void (Tully [31]). 78 dwarf galaxies were found (Karachentseva *et al.* [26]). It was confirmed that Tully Void remains to be perfectly empty till to the galaxy absolute magnitude of $\mathrm{M} = -14^m$.

C) Inspection of the equatorial SERC EJ zone with D. = [−18°, +2°]. As a result, 50 nearby dwarf galaxies were found (Karachentsev *et al.* [19]).

D) Inspection of a wide region around M31. Two new dwarf spheroidal companions to M31, Cassiopeia and Pegasus, were discovered (Karachentsev & Karachentseva [15]).

E) Survey of the remaining northern (POSS-II) and southern (ESO/SERC) films. At total 182 dwarf galaxy candidates were found (Karachentseva & Karachentsev [27]; Karachentsev *et al.* [20]). Altogether, 1671 fields (6°× 6°) covering 97% of the whole sky were inspected, mostly in B and R bands. At total 570 objects were found, of which 327 objects (57%) were not previously catalogued.

HI STUDIES OF THE LV GALAXIES

The mass HI line observations of KK-objects were carried out by W. Huchtmeier with three different radio telescopes for different declination ranges. The 100-m radio telescope in Effelsberg was used for declinations above −31°, the Nancay radio telescope was used for galaxies in the declination range [−38°, −31°], and the multibeam radio telescope in Australia was used for galaxies south of −38°. The main results are following (Huchtmeier *et al.* [8]; Huchtmeier *et al.* [9]; Huchtmeier *et al.* [10]). About 550 KK-objects have been observed with the detecting rate of 50%. Their median radial velocity is 1200 km/s, the median line width is 60 km/s, and the median linear diameter is 3.5 kpc. About 50 new LV galaxies were revealed. The analysis of HI properties of the LV galaxies (Karachentsev *et al.* [16]) allows to establish the following relations:

- the mean HI mass-to-luminosity ratio increases from giant galaxies towards dwarfs, reaching the maximum value $\sim 5M_\odot/L_\odot$;
- the mean value of HI mass-to-total mass increases from HSB galaxies towards LSB ones;
- for the LV galaxies their HI mass and angular momentum follow a linear relation expected for rotating gaseous disks being near the threshold of gravitational instability, which is favourable for active star formation.

DETAILED OPTICAL STUDIES OF THE LV GALAXIES

The southern and northern telescopes were involved to provide ground-based observations: 6-m BTA, SAO, Russia (Karachentsev, Tikhonov, Kopylov, Sharina, Makarova, Drozdovsky); 1.5-m ESO telescope (Grebel, Geisler), 2.6-m Nordic, La Palma, Spain/Finland (Aparicio, Takalo, Valtonen), 2.4-m MDM and 3.5-m APO, New Mexico (Grebel, Karachentsev); 10-m Keck, Hawaii (Grebel, Guhathakurta). About 130 northern LV galaxies were imaged in 2 or 3 bands. Most of the objects were resolved into stars for the first time, that made it possible to derive photometric distances via brightest blue and red stars with the accuracy of 0.4 mag (much better that can be achieved by the Tully–Fisher relation for dwIrrs). Many new dwarf companions were found in the vicinity of the nearest bright spirals: NGC 628, NGC 672, IC 342, NGC 6949, M 101, *etc.* The nearest BCDG, NGC 6789, was discovered just outside the Local Group at D = 2.1 Mpc. Detailed optical follow-up of the LV dwarf galaxies is being pursued with WFPC2 aboard Hubble Space Telescope (programmes #8192 and 8601 with P. Seitzer as PI) that allows to measure accurate distances to the dwarf galaxies using the tip of the red giant branch, as well as to derive their metallicities via a slope of the red giant branch. The new HST data allow to augment the faint end of galaxy luminosity function, to improve the census of globular clusters in dwarf galaxies, and to check the universality of the relation between mean metallicity, central surface brightness, and luminosity for different types of dwarf galaxies. First results of our HST Snapshot survey are published in several articles, *e.g.*, Karachentsev *et al.* [17], Karachentsev *et al.* [18], Dolphin *et al.* [6].

THE LOCAL VOLUME STRUCTURE

The Local Volume sample contains currently ∼340 members in comparison with 179 in 1979; 189 galaxies of this sample have photometric distances (against 17 in 1979). We estimate a present LV sample completeness to be of about 70%. A new criterion for bound group of galaxies (Karachentsev [13]) was applied to the Local Volume galaxies to study its three-dimentional structure.

The LV structure looks to be fractal. About 80% of the volume is occupied by "minivoids" with typical diameter of 3 Mpc. There are no sings of galaxy segregation according to their masses. No morphological segregation for giant/normal galaxies is seen, but there is a clear segregation among dwarf galaxies: dSphs usually occur within 300 kpc respect to a giant galaxy.

About 24% of the LV galaxies are the "Main Disturbers" (*i.e.*, significant attractors) for the rest galaxies. Each "MD" has its "nest" with a population in a range of (1–34). About 50% of the LV galaxies are isolated objects, *i.e.*, their crossing time with respect to their "MD" exceeds the cosmic time 1/H.

THE LOCAL VELOCITY FIELD

A sample of 145 galaxies with radial velocities relative to the LG centroid $V_0 < 500$ km/s and photometric distances $D < 7$ Mpc was considered. Their peculiar velocity field is described with a tensor of the local Hubble parameter H_{ij}, having the principal axies 81:62:48 (km/s Mpc) with a standard error of ∼4 km/s Mpc each. The minor axis of the Hubble ellipsoid is aligned almost along the polar axis of the Local Supercluster, and the major axis is directed $(29 \pm 5)^\circ$ away from the Virgo cluster center. Such a configuration of the local velocity field disagrees with known models of spherical symmetric Virgocentric flow and may be caused by a possible differential rotation of the Local Supercluster. The observed radial velocity dispersion is 74 km/s within D = 7 Mpc (Karachentsev & Makarov [14]), but for the field galaxies situated between the LG and other nearby groups the radial velocity dispersion does not exceed 25 km/s.

Acknowledgements. This work was supported by DFG grant KS 9112, the Henri Chretien International Research Grant administered by the American Astronomical Society, and NASA grant GO-08192. I. D. Karachentsev thanks the SOC for financial support.

REFERENCES

[1] *Armandroff T. E., Davies J. E., Jakoby G. H.* // Astron. J.–1999.–**118**.–P. 1220.

[2] *Binggeli B., Tarengui M., Sandage A.* // Astron. and Astrophys.–1990.–**228**.–P. 42.

[3] *Borngen F., Karachentseva V. E.* // Astron. Nachr.–1985.–**306**.–P. 301.

[4] *Bremnes T., Binggeli B., Prugniel P.* // Astron. and Astrophys. Suppl. Ser.–1998.–**129**.–P. 313.

[5] *Côté S., Freeman K. C., Carignan C., Quinn P. J.* // Astron. J.–1997.–**114**.–P. 1313.

[6] *Dolphin A. E., Makarova L. N., Karachentsev I. D., et al.* // Mon. Notic. Roy. Astron. Soc.–2001.–submitted.

[7] *Huchtmeier W. K., Richter O.-G.* // Astron. and Astrophys.–1988.–**203**.–P. 237.

[8] *Huchtmeier W. K., Karachentsev I. D., Karachentseva V. E.* // Astron. and Astrophys.–1997.–**322**.–P. 375.

[9] *Huchtmeier W. K., Karachentsev I. D., Karachentseva V. E., Ehle M.* // Astron. and Astrophys. Suppl. Ser.–2000.–**141**.–P. 469.

[10] *Huchtmeier W. K., Karachentsev I. D., Karachentseva V. E.* // Astron. and Astrophys. Suppl. Ser.–2000.–**147**.–P. 187.

[11] *Impey C. D., Sprayberry D., Irwin M. J., Bothun G. D.* // Astrophys. J. Suppl. Ser.–1996.–**105**.–P. 209.

[12] *Jerjen H., Freeman K. C., Binggeli B.* // Astron. J.–1998.–**116**.–P. 2873.

[13] *Karachentsev I. D.* // Astron. and Astrophys. Transactions.–1994.–**6**.–P. 1.

[14] *Karachentsev I., Makarov D.* // Astron. J.–1996.–**111**.–P. 535.

[15] *Karachentsev I. D., Karachentseva V. E.* // Astron. and Astrophys.–1999.–**341**.–P. 355.

[16] *Karachentsev I. D., Makarov D. I., Huchtmeier W. K.* // Astron. and Astrophys. Suppl. Ser.–1999.–**139**.–P. 97.

[17] *Karachentsev I. D., Sharina M. E., Grebel E. K., et al.* // Astron. and Astrophys.–1999.–**352**.–P. 399.

[18] *Karachentsev I. D., Karachentseva V. E., Dolphin A. E., et al.* // Astron. and Astrophys.–2000.–**363**.–P. 117.

[19] *Karachentsev I. D., Karachentseva V. E., Suchkov A. A., Grebel E. K.* // Astron. and Astrophys. Suppl. Ser.–2000.–**145**.–P. 415.

[20] *Karachentsev I. D., Karachentseva V. E., Huchtmeier W. K.* // Astron. and Astrophys.–2001.–**366**.–P. 481.

[21] *Karachentseva V. E.* // Soobsch. Byurakan. Obs.–1968.–**39**.–P. 62. (in Russian).

[22] *Karachentseva V. E.* // Astron. Tsirk.–1972.–**723**.–P. 1. (in Russian).

[23] *Karachentseva V. E.* // Astrophys. Issled. (Izv. SAO).–1973.–**5**.–P. 10. (in Russian).

[24] *Karachentseva V. E., Sharina M. E.* // Comm. Spec. Astrophys. Obs.–1988.–**57**.–P. 3. (in Russian).

[25] *Karachentseva V. E., Karachentsev I. D.* // Astron. and Astrophys. Suppl. Ser.–1998.–**127**.–P. 409.

[26] *Karachentseva V. E., Karachentsev I. D., Richter G. M.* // Astron. and Astrophys. Suppl. Ser.–1999.–**135**.–P. 221.

[27] *Karachentseva V. E., Karachentsev I. D.* // Astron. and Astrophys. Suppl. Ser.–2000.–**146**.–P. 359.

[28] *Kraan-Korteweg R., Tammann G. A.* // Astron. Nachr.–1979.–**300**.–P. 181.

[29] *Scmidt K.-H., Boller T.* // Astron. Nachr.–1992.–**313**.–P. 189.

[30] *Schombert J. M., Bothun G. D., Schneider S. E., McGaugh S. S.* // Astron. J.–1992.–**103**.–P. 1107.

[31] *Tully R. B.* Nearby Galaxy Catalog.–Cambridge Univ. Press, 1988.

[32] *Van den Bergh S.* // Publ. DDO.–1959.–N 5.–P. 147.

FINE STRUCTURE IN THE INTERSTELLAR MEDIUM

J. R. Dickel[1,2]

[1] *ASTRON (Netherlands Foundation for Research in Astronomy)*
P.O. Box 2, 7990AA Dwingeloo, Netherlands

[2] *Astronomy Department, University of Illinois at Urbana-Champaign*
1002 West Green Street, Urbana IL 61801, USA
e-mail: johnd@astro.uiuc.edu

We discuss some peculiar structures in the interstellar medium of the Milky Way and other galaxies which have not been explained. Two are associated with supernova remnants and a third concerns the temperature and density structure of cold interstellar gas.
Several supernova remnants have breakouts or apparent jets emanating from spots in their shells. It remains unclear if the shapes of these features are controlled by ejected material or structures inherent in the surroundings.
The filaments in individual supernova remnants show a great variety of shapes – some appear as if they can be represented by sheets seen from various angles while others appear more like sections of small bubbles centered near the periphery of the shell. In these dense filaments the magnetic field may be compressed enough to control the motion of the material in the plasma and observed structures.
Observations at low radio frequencies of high Rydberg state recombination lines of carbon in both emission and absorption can provide valuable information on the temperature and density of cold gas in the interstellar medium but current data are limited by poor resolution which does not allow separation of several components within the beam along a given line of sight. Newly proposed radio telescopes will improve the resolution and give a better picture of this gas distribution.

INTRODUCTION

The interstellar medium has a great variety of structures on many size scales. These range from large loops many hundreds of pc in size seen in the 21-cm line [13] and radio continuum [3] down to clumps a small fraction of a pc across which cause scintillation of radio sources. In this short presentation, we cannot describe all the types of observed features in the interstellar medium but will discuss some interesting structures, the properties and origins of which have not been fully explained. In all cases new telescopes being planned will have both increased sensitivity and resolution to help us determine the detailed properties of the observed features. Rpid advances in computer power are allowing the calculation of new 3-dimensional hydrodynamic models using the observed properties which will help us to understand the physics behind the formation and evolution of such phenomena.

JETS AND BREAKOUTS ASSOCIATED WITH SUPERNOVA REMNANTS

In general, supernova remnants (SNRs) have reasonably circular outlines although they do show irregularities around the shell. These can be explained by clumps in the interstellar medium which impede the expanding flow in some directions while leaving it unhindered in others. Indeed, the regions which are expanding more slowly are often bounded by molecular clouds or other enhancements in density. Good examples of molecular clouds slowing the expansion occur on the east sides of both W 44 in the Milky Way [4, 30] and N 49 in the Large Magellanic Cloud [5, 2].

In a few other cases, however, there appear to be highly collimated "jets" of emission breaking out of an SNR. The diameter of the opening angle can be less than 10°. A most spectacular example of such a structure is the SNR Kes 32 which has a diameter of about 25 pc, with a 16 pc long jet of width 3 pc extending out of the northeast side at an angle of about 20° to the tangent point in the shell [22]. Beyond the jet, the emission spreads out into a broad plume which rises to over 35 pc above the edge of the shell of the SNR.

A quite different example is N11 L [28] which shows a thick shell of radio emission with an apparent breakout emerging from one spot and then curving around to fill a volume about half that of the SNR along one side. In x-rays, the emergence from the shell is similar but the emission extends further from the remnant and does not spread out as much in angle. In optical emission lines we see the shell and a structure that looks like a hollow tube surrounding the radio and x-ray jet but no emission associated with the more diffuse area seen in the other wavelengths. In both these examples, the emission outside the SNR appears to have a flatter radio spectrum than that from within the shell and polarimetry of the jet from Kes 32 show no detectable polarization (Roger *et al.*, 1985).

All other known jets in astrophysics are double, such as that seen in the binary system SS 433 in the center of the SNR W 50, *e.g.*, [15], or in many star-forming regions (*e.g.*, Shulga, this conference). We see no evidence for counter jets in either Kes 32 or N11 L, however. The remnant CTB 80, on the other hand, appears to have three non-symmetrical jets [26] in addition to an extended plateau of emission associated with a small shell SNR containing an offset pulsar [25].

The lack of symmetry plus the indication that the radio emission from the extended structures may be thermal rather than synchrotron, suggest that, for these SNRs, we may be seeing emission related to some existing structure rather than jets from a central object. Perhaps low density tunnels of neutral gas between denser molecular clouds could be ionized by the progenitor star and remain heated by x-rays from the interior of the SNR. Alternatively, the structures might just represent a break in the shell where the expanding material may be moving outward through a low density hole. A different radio spectral index could be caused by different shock acceleration conditions in the tunnel through which the shock and ejected material is moving. How the initial tube structures formed in the interstellar medium remains a question. Further work to help characterize these features would include: sensitive radio polarimetry to more conclusively establish whether the radio emission is synchrotron or thermal, sensitive optical spectroscopy to provide velocity information and search for any emission within the jets, and theoretical modeling of expansion into a variable interstellar medium to see if such features can be produced with reasonable physical parameters.

Another supernova remnant, MSH 14 − *63*, shows a very different sort of apparent breakout. There is a bright ridge of H_α and [S II] emission from filaments in radiative equilibrium running along the northern side of this remnant and then another broken ridge about 15% of the remnant's radius further out [23]. At first sight this might be thought to show the projection of different parts of the shell of the SNR onto the plane of the sky but closer inspection of only the radiative filaments (there are some Balmer-dominated non-radiative filaments in that ridge as well) reveals that the outer filaments are present only at positions lined up presidely outside definite sharp gaps in the inner ridge. It is difficult to envision a geometry which produces several gaps in the shell all extending to the same distance where a new broken shell is seen. Again, velocity information and modeling would be valuable in explaining this peculiar configuration of filaments.

FILAMENTS IN OLDER SNRS

The filaments seen in the shells of old SNRs are very thin and often break up into substructures with high resolution. There is a one-to-one correspondence between the filaments observed in optical recombination lines and in radio synchrotron emission [20, 24]. The optical emission is proportional to the square of the density while the radio emission depends on the density of relativistic particles and the magnetic field strength. We thus conclude that the relativistic particle density and/or magnetic fields follow the thermal particle density. Measurements of the ratio of the two lines of the [S II] doublet at 671.6 and 673.1 nm give typical densities of 200 cm^{-3}, *e.g.*, [9], in these filaments indicating that they are in radiative equilibrium and compressing as they cool to maintain pressure balance.

The magnetic fields in the filaments are studies by radio polarimetry of the synchrotron radiation which gives us information on both the magnetic field strength and its orientation in the plane of the sky. The procedure is very difficult at high resolution, however, because the emission is faint and the polarized intensity is only a few percent of the total intensity. The limited results to date do not show a consistent pattern. In some places in the adolescent remnant IC 443 the field aligns along the axis of a filament but in others it appears to be directed across the filament [29]. Perhaps theoretical modeling of the compression process in the presence of a magnetic field can tell us how the fields should align.

The morphology of the filaments also needs more investigation. While there are cases of filaments appearing to extend across the full face of a SNR, such as one in the Cygnus Loop when seen at low resolution (Green, 1990) most of them consist of multiple small arcs such as seen in a section of the shell of IC 443 in Figure 1. This is an H_α image taken with the 1-m Prairie Telescope of the University of Illinois with a point spread function of about 2 arcsec. Most of these arcs have a convex shape with a smaller radius of curvature than the overall shell. The emission also appears to become less sharp and more diffuse toward the center if the SNR.

Hester [14] has modeled these filaments in the Cygnus Loop as crinkled sheets seen from different perspectives. A long filament across the face of CTB 1 shows a similar pattern at both optical and radio wavelengths [31, 7] and it might also be represented by such a characterization. This picture seems to work well for filaments on the face of a remnant but it doesn't show the convex pattern of filaments near the rim nor the nearly uniform radius of curvature for individual arcs as seen in Figure 1. The remnant S 147 vividly shows the same pattern of parts of small circular features [31]. Many of these arcs look like parts of bubbles with their centers in the outer parts of the SNR. Figure 2 shows such a model of thin sections of hemispherical shells with the radii, cutoffs,

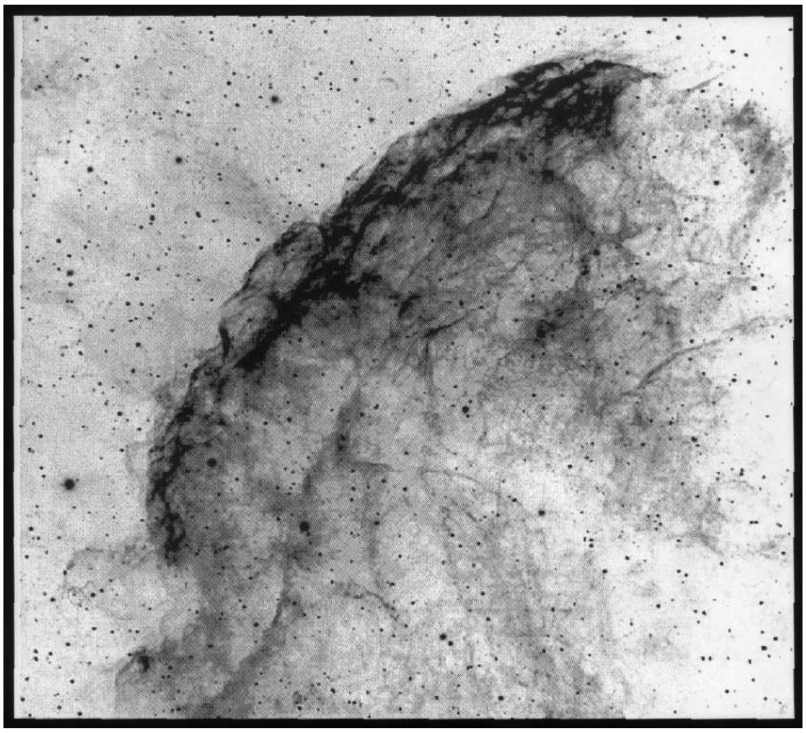

Figure 1: H_α image of filaments in the northeastern section of the supernova remnant IC 443

and locations in the shell set by random numbers. It does quite a good job near the edge but is not as good as the crinkled-sheet model on the face of the remnant. A combination of both effects may be able to reproduce the complex observed patterns.

The main problem with these geometrical models is what physical structures and conditions can cause these collections of mini-expansion centers plus some long kinks in apparent sheets toward other parts of the shell? Again, magnetic fields might give the answer. The magnetic pressure in young SNRs is well below the thermal pressure [19, 6] but it is likely to track the compression and become stronger in the filaments in older remnants [8]. The magnetic fields could then provide the effective surface tension to hold the expanding shock into curved shells as it threads its way past clumps in the surrounding medium and also to tie individual pieces into longer consistent structures.

It is clear that the super sensitivity of the Square Kilometer Array of radio telescopes (SKA) currently being planned is needed to allow accurate magnetic field mapping of these objects. The SKA will have a sensitivity improvement of greater than a factor of 100 over current telescopes which means that we can do high resolution polarimetry of these faint, thin filaments for the first time. Continually improving computer capacity also allows more detailed three-dimensional magnetohydrodynamic modeling of these expansion processes to provide a true physical basis to our understanding. We hope that these developments will take place within the next two decades.

COLD ATOMIC GAS

The distribution and temperature of atomic gas in the interstellar medium remains an important parameter in our understanding of the energetics of the galaxy. A basic question is whether most of the gas is cold material in the vicinity of molecular clouds or warmer material associated with H II regions. While the 21-cm hydrogen line can measure the total gas content along a line of sight, it cannot distinguish different temperatures unless there are absorption components in front of a bright background source. After the discovery of radio recombination lines of carbon near 25 MHz (quantum number about 640) using the UTR-2 telescope of the Institute of Radio Astronomy in Kharkiv [17], it was realized that they offer a valuable tool to probe this gas.

The lines are seen in absorption below about 150 MHz and then in emission at higher frequencies [21]. The absorption lines generally appear wider than the Doppler widths for the temperature of the gas, suggesting pressure broadening. The inclusion of some hydrogen ionization as well at these relatively high pressures and low temperatures also requires consideration of dielectric recombination to assess the properties of the material

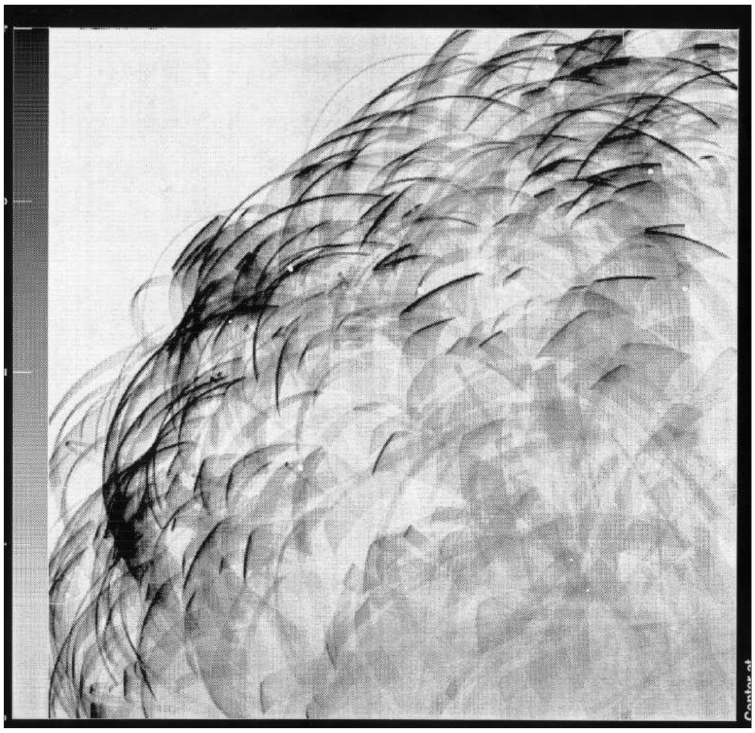

Figure 2: Model image of sections of hemispherical shells centered around the edge of an SNR shell similar to IC 443

[27]. In addition, the presence of emission lines near 322 MHz (quantum numbers of about 275) in the direction of the strong source Cas A indicates that stimulated emission must be present [21].

The observations [18, 10, 21, 16] tend to favor gas in the temperature range of 50–100 K toward most directions in the galactic plane but none of the models incorporating all of the relevant physics fully match the data [1]. In one case toward the dust cloud L1407 it is found that 20 K gas gives a more acceptable fit to the data [11].

A major problem in sorting out the actual temperature and distribution of this gas is that the poor angular resolution available to date at these long wavelengths does not allow determination of the sizes of the clouds producing the lines nor the evaluation of confusion along the line of sight. There may be several components within the observed beam. We need more complete surveys with high angular resolution at a range of wavelengths covering the transition between absorption and emission to sort out the full range of conditions throughout the galaxy. Another new radio telescope currently being discussed, LOFAR, will operate in the meter and decameter wavelength bands and should make vital contributions toward understanding this cold gas.

Acknowledgements. I have benefitted from discussions with many colleagues in thinking about these ideas, in particular Eric van der Swaluw and Richard Strom.

REFERENCES

[1] *Anantharamaiah K., Kantharia N.* High Rydberg state carbon recombination lines from interstellar clouds // New Perspectives on the Interstellar Medium: ASP Conf. Ser. / Eds Taylor *et al.*–1999.–**168**.–P. 197.

[2] *Banas K., Hughes J., Bronfman L., Nyman L.* Supernova remnants associated with molecular clouds in the Large Magellanic Cloud // Astrophys. J.–1997.–**480**, N 2.–P. 607–617.

[3] *Berkhuijsen E., Haslam C., Salter C.* Are the galactic loops supernova remnants? // Astron. and Astrophys.–1971.–**14**, N 2.–P. 252–262.

[4] *Dickel J., Dickel H., Crutcher R.* The supernova remnant W 44 and its surroundings // Publs Astron. Soc. Pacif.–1976.–**88**, N 526.–P. 840–843.

[5] *Dickel J., Chu Y.-H., Geline C., et al.* Negative search for a counterpart to the gamma-ray repeater source 0526-66 // Astrophys. J.–1995.–**448**, N 2.–P. 623–627.

[6] *Dickel J., Milne D.* Five mature supernova remnants in the Large Magellanic Cloud // Astron. J.–1998.–**115**, N 3.–P. 1057–1075.

[7] *Dickel J., Willis A.* The radio emission of the supernova remnants CTB1 and the Cygnus Loop // Astron. and Astrophys.–1980.–**85**, N 1.–P. 55–65.

[8] *Duin R., van der Laan H.* The radio structure of the supernova remnant IC 443 // Astron. and Astrophys.–1975.–**40**, N 1.–P. 111–122.

[9] *Fesen R., Blair W., Kirshner R.* Optical emission-line properties of evolved galactic supernova Remnants // Astrophys. J.–1985.–**292**, N 1.–P. 29–48.

[10] *Golynkin A., Konovalenko A.* Radio recombination lines of highly excited carbon near DR 21 and S 140 // Sov. Astron. Lett.–1991a.–**17**, N 1.–P. 7–10.

[11] *Golynkin A., Konovalenko A.* Decameter-wave carbon recombination lines in the dust cloud L1407 // Sov. Astron. Lett.–1991b.–**17**, N 1.–P. 10–13.

[12] *Green D.* The Cygnus Loop at 408 MHz - Spectral variations and a better overall view // Astron. J.–1990.–**100**, N 6.–P. 1927–1942.

[13] *Heiles C.* H I Shells, supershells, shell-like objects, and "worms" // Astrophys. J. Suppl. Ser.–1984.–**55**, N 4.–P. 585–595.

[14] *Hester J.* A sheet model of the emission from middle-aged supernova remnants // Astrophys. J.–1987.–**314**, N 1.–P. 187–202.

[15] *Hjellming R., Johnston K.* An analysis of the proper motions of SS 433 radio jets // Astrophys. J.–1981.–**246**, N 3.–P. L141–L145.

[16] *Kantharia N., Anantharamaiah K., Payne H.* Carbon recombination lines between 34.5 and 770 MHz toward Cassiopeia A // Astrophys. J.–1998.–**506**, N 2.–P. 758–772.

[17] *Konovalenko A., Sodin L.* Neutral N-14 in the interstellar medium // Nature.–1980.–**283**, N 5745.–P. 360–361.

[18] *Konovalenko A.* Decameter wavelength carbon recombination lines toward Cassiopeia A // Sov. Astron. Lett.–1984.–**10**, N 6.–P. 353–356.

[19] *Matsui Y., Long K., Dickel J., Greisen E.* A detailed x-ray and radio comparison of Kepler's supernova remnant // Astrophys. J.–1984.–**287**, N 1.–P. 295–306.

[20] *Mufson S., McCollough M, Dickel J., et al.* A multiwavelength Iivestigation of the supernova remnant IC 443 // Astron. J.–1986.–**92**, N 6.–P. 1349–1357.

[21] *Payne H., Anantharamaiah K., Erickson W.* High Rydberg state carbon recombination lines toward Cassiopeia A: Physical conditions and a new class of models // Astrophys. J.–1994.–**430**, N 2.–P. 690–705.

[22] *Roger R., Milne D., Kesteven M., et al.* A radio jet associated with the supernova remnant G324.2+0.1 (Kes 32) // Nature.–1985.–**316**, N 6023.–P. 44–46.

[23] *Smith R.* The discovery of Balmer filaments encircling SNR RCW 86 // Astron. J.–1997.–**114**, N 6.–P. 2664–2670.

[24] *Straka W., Dickel J., Blair W., Fesen R.* A comparison of high-resolution radio and optical data for the northeastrRegion of the Cygnus Loop // Astrophys. J.–1986.–**306**, N 1.–P. 266–270.

[25] *Strom R.* Pulsar-like emission from the supernova remnant CTB 80 // Astrophys. J.–1987.–**319**, N 2.–P. L105–L107.

[26] *Strom R., Angerhofer P., Velusamy T.* The unusual supernova remnant CTB 80 // Nature.–1980.–**284**, N 5751.–P. 38–40.

[27] *Walmsley C., Watson W.* The influence if dielectronic-like recombination at low temperatures on the interpretation of interstellar, radio recombination Llnes of carbon // Astrophys. J.–1982.–**260**, N 1.–P. 317–325.

[28] *Williams R., Chu Y.-H., Dickel J., et al.* Supernova remnants in the Magellanic Clouds II. Supernova remnant breakouts from N 11L and N 86 // Astrophys. J.–1999.–**514**, N 2.–P. 798–817.

[29] *Wood C., Mufson S., Dickel J.* The magnetic structure of the filaments in the supernova remnant IC 443 // Astron. J.–1991.–**102**, N 1.–P. 224–233.

[30] *Wooten H.* The molecular cloud associated with the supernova remnant W 44 // Astrophys. J.–1977.–**216**, N 2.–P. 440–445.

[31] *van den Bergh S., Marscher A., Terzian Y.* An atlas of optical galactic supernova remnants // Astrophys. J. Suppl. Ser.–1973.–**26**, N 227.–P. 19–36.

X–RAY EMISSION OF THE SUPERNOVA REMNANTS IN A NON–UNIFORM INTERSTELLAR MEDIUM

B. Hnatyk and O. Petruk

Institute for Applied Problems in Mechanics and Mathematics, NAS of Ukraine
3-b Naukova St., 79053 Lviv, Ukraine
e-mail: hnatyk@lms.lviv.ua, petruk@astro.franko.lviv.ua

Large-scale gradient of the interstellar medium density distribution essentially affects the evolution of supernova remnants. To model this influence, a new approximate analytical method for the full hydrodynamical description of 3D point-like explosions in the non-uniform media with arbitrary density distribution is developed. General features of the evolution of the adiabatic supernova remnants in the medium with a large-scale density gradient are investigated. Real anisotropy of the remnants increases with age, but the visible shape remains close to spherical. X-ray emission characteristics from the entire SNR (luminosity, spectral index) are close to those in the spherical Sedov case with the same initial data. However, the surface distribution of the X-ray emission characteristics is very sensitive to the initial density distribution around the Supernova progenitor.

INTRODUCTION

Investigation of supernova remnants (SNRs) as non-spherical 3-dimensional objects is one of the most actual tasks in studies on these objects [1]. Most important reason for the non-sphericity of adiabatic SNRs is a non-uniformity of ISM. In such cases, self-similar solutions cannot be used, and a real possibility to perform an investigation of the evolution of non-spherical SNRs bases on approximate methods for hydrodynamics. In [2] we have proposed a new approximate analytical method for the complete hydrodynamical description of a point explosion in a medium with an arbitrary large-scale density distribution. On the basis of this method, we investigate here the general features of the thermal X-ray emission of adiabatic SNRs in ISM with a large-scale density gradient. Equilibrium thermal X-ray emission model is taken from [3].

SNR IN A NON-UNIFORM MEDIUM

The exponential density distribution is frequently encountered in ISM. We will use this distribution in the form:

$$\rho^{\mathrm{o}}(z) = \rho^{\mathrm{o}}(0) \cdot \exp\Big(-\frac{z}{H}\Big), \quad z = r\cos\theta, \tag{1}$$

where r is the distance from the center of explosion, θ is the angle between the considered direction and z-direction (opposite to the density gradient) and H is the scale height.

We show in Fig. 1 the evolution of X-ray luminosity and spectral index α. It is easy to see that both X-ray characteristics of non-spherical SNR (NSNR) evolve analogously to the Sedov case ($H \to \infty$).

We have calculated a grid of NSNR models which confirms that this analogy in evolution is an intrinsic property of NSNR X-ray radiation [2]. For a wide range of number density at the point of explosion $n^{\mathrm{o}}_{\mathrm{H}}(0) = 0.1-10\,\mathrm{cm}^{-3}$, the X-ray luminosity of adiabatic NSNR evolving in a medium with strong enough density gradient ($H = 10$ pc) in different energy ranges is not far from the X-ray luminosity of SNR in a uniform density medium with the same initial model parameters. The difference increases with age of the SNR and with decreasing of $n^{\mathrm{o}}_{\mathrm{H}}(0)$. But even for old NSNR (*e.g.*, $t = 3{\times}10^4$ years) in a relatively low density medium ($n^{\mathrm{o}}_{\mathrm{H}}(0) = 0.1$ cm^{-3}), the maximal difference reach only about 60% aat the end of adiabatic phase. The difference in spectral index of adiabatic NSNR does not exceed 10%. Luminosity in range > 4.5 KeV is close to the Sedov case too. These last two facts reveal the similarity of total spectra of non-spherical SNR and its Sedov counterpart.

Therefore, we emphasize here a remarkable fact of proximity of total fluxes and spectrum shapes of SNRs in uniform and non-uniform media even in case of considerable anisotropy of adiabatic NSNRs. The reason of this phenomenon is mutual compensation of emission deficit from low density regions of NSNR and enhanced emission from high density regions, since X-ray emission mainly depends on the emission measure $EM \simeq n_{\mathrm{e}}^2 V \simeq M^2 V^{-1}$, but both masses of swepted up gas M and volume V of NSNR remain close to those of Sedov SNR [2]. This explains the strange circumstance that integral X-ray characteristics of the majority of SNRs with evident

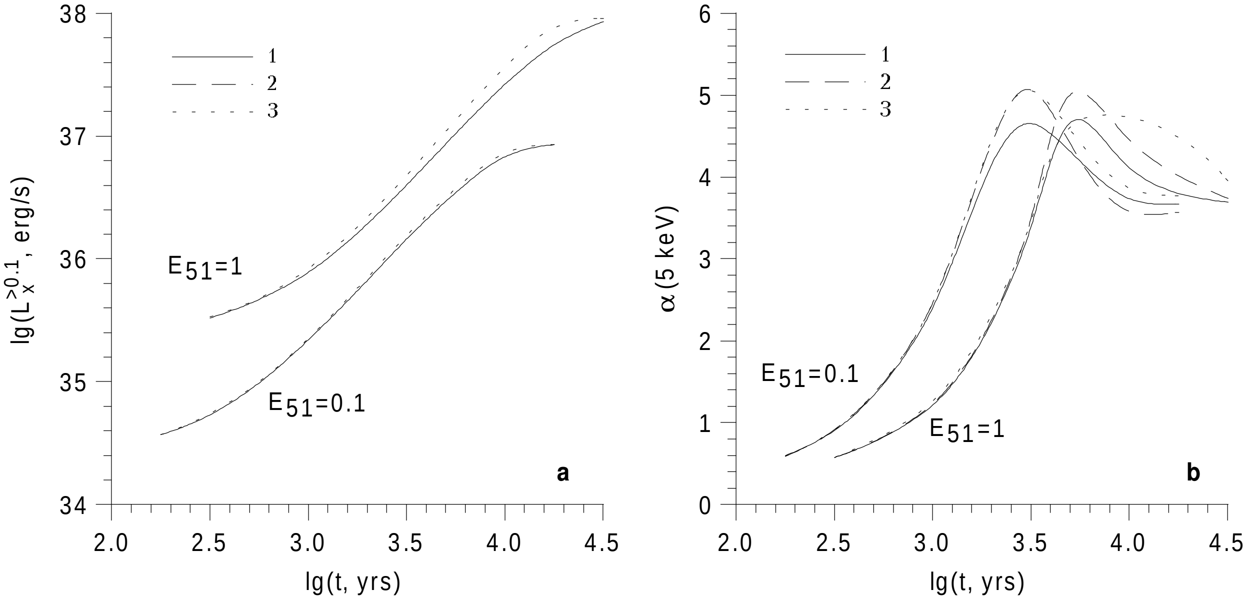

Figure 1: Evolution of luminosity L_x in range > 0.1 KeV and spectral index $\alpha(5$ KeV$)$ of SNR in a uniform medium (line 1), in an exponential medium Eq. (1) with $H = 80$ pc (line 2) and $H = 10$ pc (line 3). In all cases $n_{\rm H}^{\rm o}(0) = 1$ cm^{-3}. E_{51} is the explosion energy in 10^{51} erg. $\gamma = 5/3$

asymmetry in shape and/or surface brightness distribution are described with sufficient accuracy by the Sedov [4] model of SN explosion in a uniform medium. For more correct modelling of physical conditions inside and outside the SNR, it is necessary to analyze the characteristics of X-ray emission distributed over the SNR surface.

Such investigation have been carried out in [2]. The main results are following. 1. The distribution of surface brightness of NSNR differs essentially from a spherical one. 2. The contrast of surface brightness increases with the age of the SNR and may reach a few tens of thousands. 3. Projection effects hide real contrasts of surface characteristics of NSNR's emission. Observational morphology of NSNR depends essentially on its orientation with respect to the line of sight. 4. A harder X-ray range (> 4.5 KeV) is less sensitive to the influence of the non-uniformity of surrounding medium than a range which includes soft emission. This fact may be used for testing ISM non-uniformity. 5. The surface distribution of spectral index α may also be an effective tool for NSNR diagnostics.

CONCLUSIONS

It is shown that the real anisotropy of adiabatic SNR in non-uniform ISM increases with time, but the visible shape remains close to spherical even for strong real asymmetry (ratio of maximal to minimal shock radii) and surface brightness contrast. Projection effects on the sky plane decrease the real shape anisotropy. It is shown also that the integral characteristics of X-ray radiation from the entire SNR (luminosity, spectral index) are close to those in the Sedov case with the same initial data. However, the surface distribution of the X-ray emission parameters is very sensitive to the initial density distribution around the SN progenitor. Therefore, the X-ray maps are needed for recovering of the physical conditions inside and outside of the non-spherical SNR.

REFERENCES

[1] *Jones T., Jun B., Borkowski K., et al.* 10^{51} Ergs: The Evolution of Shell Supernova Remnants // Publs Astron. Soc. Pacif.–1998.–**110**.–P. 125–151.

[2] *Hnatyk B., Petruk O.* Evolution of supernova remnants in the interstellar medium with a large-scale density gradient. I. General properties of shape evolution and X-ray emission. // Astron. and Astrophys.–1999.–**344**.–P. 295–309.

[3] *Raymond J., Smith B.* Soft X-ray spectrum of a hot plasma // Astrophys. J. Suppl. Ser.–1977.–**35**.–P. 419–439.

[4] *Sedov L.* Similarity and Dimensional Methods in Mechanics.–New York: Academic, 1959.

X–RAY EMISSION OF THE REMNANTS OF ASPHERICAL SUPERNOVA EXPLOSIONS

O. Petruk

Institute for Applied Problems in Mechanics and Mathematics, NAS of Ukraine
3-b Naukova St., 79053 Lviv, Ukraine
e-mail: petruk@astro.franko.lviv.ua

Evolution of the adiabatic remnants of an aspherical supernova explosion in uniform medium is considered. Thermal X-ray emission of the remnants is investigated. It is shown that integral thermal X-ray characteristics (X-ray luminosity and spectrum) of the objects do not allow to reveal the asymmetry in the explosion of the progenitor because these characteristics are close to their Sedov counterparts. Surface distribution of the X-ray emission is sensitive to the anisotropy of the explosion and nonuniformity of interstellar medium.

INTRODUCTION

In some models of a supernova explosion the energy is realized anisotropically [1, 5]. Aspherical explosion of supernova (SN) may cause a barrel-like supernova remnant (SNR) [4]. Observations show that SN really may be aspherical, as, *e.g.*, in well-known case of SN1987A [12, 6, 7, 8]. High birth velocities of pulsars also suggest anisotropy in SN explosion [10]. In the past, the morphological evolution and instabilities of asymmetric SN explosion were investigated [3, 2, 16].

In present work we consider the properties of the thermal X-ray emission of adiabatic remnants of aspherical SN explosions. Hydrodynamics is modelled here with the approximate method for description of the adiabatic phase of a remnant of aspherical SN explosion in an arbitrary large-scale nonuniform medium [9]. Equilibrium thermal X-ray emission model is taken from [14] and approximation for the Gaunt factor from [11].

ASPHERICAL SN EXPLOSION IN A UNIFORM MEDIUM

Spherical adiabatic SNR in uniform medium is described by self-similar Sedov solutions [15] where the distributions of thermodynamic parameters are self-similar downstream: $\rho(r,t) = \rho_{\rm s}\cdot\overline{\rho}(\overline{r})$, $P(r,t) = P_{\rm s}\cdot\overline{P}(\overline{r})$, $T(r,t) = T_{\rm s}\cdot\overline{T}(\overline{r})$, where distance from the center $\overline{r}$, density $\overline{\rho}$, pressure $\overline{P}$, temperature $\overline{T}$ are normalized on the values at the shock: $R_{\rm s}$, $\rho_{\rm s}$, $P_{\rm s}$, $T_{\rm s}$.

Let us consider aspherical supernova explosion

$$E(\vartheta,\phi) = E_o\ \psi(\vartheta,\phi), \quad \text{where} \quad \int\limits_0^{2\pi} d\phi \int\limits_0^{\pi} \psi(\vartheta,\phi)\sin\vartheta d\vartheta = 4\pi. \tag{1}$$

As an example of aspherical energy distribution we will consider the function:

$$\psi(\vartheta,\phi) = \left(1-\frac{b}{2}\right) + b|\cos\vartheta|, \qquad 0\le b<2, \tag{2}$$

SNR 3C 58, which is probably on the free expansion phase of his evolution, has maximal axis ratio among known young SNRs: 1.67. So, possible anisotropy of explosion energy distribution is $E_{\max}/E_{\min} = (R_{\max}/R_{\min})^2 = 2.8$. Such anisotropy takes place for (2) if $b\approx 1$.

Let us consider uniform medium. Our hydrodynamic method works within the framework of sector approximation approach where the flows in sectors are independent. This causes essential simplification in modelling of the object. Namely, in such a case, we have only to re-normalize energy in each sector and distributions of parameters in each sectors remain to be self-similar since each sector may be described by the Sedov solution with a relevant value of explosion energy. Thus, the flow characteristics may be written as

$$\begin{aligned} &R_{\rm s}(\vartheta,\phi) = \tilde{R}_{\rm s}\ \psi(\vartheta,\phi)^{1/5}, \qquad D(\vartheta,\phi) = \tilde{D}\ \psi(\vartheta,\phi)^{1/5},\\ &\rho_{\rm s}(\vartheta,\phi) = \rho_{\rm s}, \qquad P_{\rm s}(\vartheta,\phi) = \tilde{P}_{\rm s}\ \psi(\vartheta,\phi)^{2/5}, \qquad T_{\rm s}(\vartheta,\phi) = \tilde{T}_{\rm s}\ \psi(\vartheta,\phi)^{2/5}, \end{aligned} \tag{3}$$

where $\tilde{R}_{\rm s}$, $\tilde{D}$, $\tilde{P}_{\rm s}$, $\tilde{T}_{\rm s}$ coinside with the relevant values in case of Sedov SNR.

Luminosity of an SNR

$$L_{\rm x} = \int\limits_0^{2\pi} d\phi \int\limits_0^{\pi} \sin\vartheta d\vartheta \int\limits_0^{R_{\rm s}(\vartheta,\phi)} \Lambda(T) n_{\rm e} n_{\rm H} r^2 dr, \tag{4}$$

where emissivity $\Lambda(T) = \int \big(\Lambda_{\rm c}(T,\varepsilon) + \Lambda_{\rm l}(T,\varepsilon)\big) d\varepsilon$, subscript "c" refer to continuum and "l" to line emission, in the case of the Sedov SNR is

$$L_{\rm x} = C(\gamma,\mu) \cdot E_{51}\ n_{\rm H}\ T_{\rm s}^{-1} \cdot I_o(T_{\rm s}) \quad {\rm erg/s}, \tag{5}$$

where

$$I_o(T_{\rm s}) = 4\pi \int\limits_0^1 \Lambda\big(T_{\rm s} \cdot \overline{T}(r)\big)\ \overline{n}^2(r)\ r^2\ dr, \tag{6}$$

and $C = 3.65{\times}10^{66}$ for $\gamma = 5/3$, $\mu = 0.609$. Thermal X-ray spectral index

$$\alpha = -\frac{\partial \ln}{\partial \ln\varepsilon} \int\limits_V \Lambda_{\rm c}(T,\epsilon) n_{\rm e} n_{\rm H} dV \tag{7}$$

is, in the case of the Sedov SNR,

$$\alpha_o = -\frac{\partial}{\partial \ln\varepsilon}\ \ln I_{o,\rm c}(T_{\rm s}), \tag{8}$$

where

$$I_{o,\rm c}(T_{\rm s}) = \int\limits_0^1 \Lambda_{\rm c}\big(T_{\rm s} \cdot \overline{T}(r)\big)\ \overline{n}^2(r)\ r^2\ dr. \tag{9}$$

Luminosity of the remnant of aspherical supernova explosion $E(\vartheta,\phi) = E_o\ \psi(\vartheta,\phi)$ in uniform medium is

$$L_{\rm x} = C(\gamma,\mu) \cdot E_{51}\ n_{\rm H}\ \tilde{T}_{\rm s}^{-1} \cdot I(\tilde{T}_{\rm s}) \quad {\rm erg/s}, \tag{10}$$

where the integral

$$I(\tilde{T}_{\rm s}) = \int\limits_0^{2\pi} d\phi \int\limits_0^{\pi} \psi(\vartheta,\phi)^{3/5}\ \sin\vartheta d\vartheta \int\limits_0^1 \Lambda(\tilde{T}_{\rm s}\ \psi(\vartheta,\phi)^{2/5}\ \overline{T}(r))\ \overline{n}^2(r)\ r^2\ dr. \tag{11}$$

Thermal X-ray spectral index of such SNR is

$$\alpha = -\frac{\partial}{\partial \ln\varepsilon}\ \ln I_c(\tilde{T}_{\rm s}), \tag{12}$$

where $I_c(\tilde{T}_{\rm s})$ is the same integral as (11) with Λ_c instead of Λ. In general case, the temperature $\tilde{T}_{\rm s}$ in (10)–(12) is a characteristic parameter, the value of $\tilde{T}_{\rm s}$ coincides with real temperature $T_{\rm s}$ on the shock front in the case of Sedov SNR.

Since volume, mass and effective temperature of a remnant of aspherical SN explosion differ from spherical SNR within 1% only [13], we may expect that luminosity L_x and spectral index α of such SNR will be close to their Sedov counterparts because these characteristics essentially depend on emission measure $EM \simeq n_{\rm e}^2 V \simeq M^2 V^{-1}$. Really, Fig. 1a shows integrals $I_o(T_{\rm s})$ and $I(\tilde{T}_{\rm s})$ and Fig. 1b demonstrates variation of thermal X-ray spectral indexes $\alpha_o(T_{\rm s})$ and $\alpha(\tilde{T}_{\rm s})$. We see that luminosity in the band $\varepsilon > 0.1$ KeV has maximal differences of order 2% for $b = 0.5$ and 5% for $b = 1.5$; they are 2% and 17% in the band $\varepsilon > 4.5$ KeV. Relative differences in spectral index are less then 1% for $b = 0.5$ and 5% for $b = 1.5$.

So, summarizing, we cannot distinguish the cases of spherical and aspherical supernova explosions in uniform ISM having characteristics of SNR as a whole object, because such characteristics are very close to their Sedov counterparts.

It is easy to show that surface brightness along the radius of the projection of Sedov SNR distributes as

$$S_o(x) = {\rm const} \cdot E_{51}^{1/3} n_{\rm H}^{5/3} T_{\rm s}^{-1/3} \int\limits_x^1 \Lambda(T_{\rm s}\overline{T}(r))\ \frac{\overline{n}^2(r)\ dr}{\sqrt{r^2 - x^2}}, \tag{13}$$

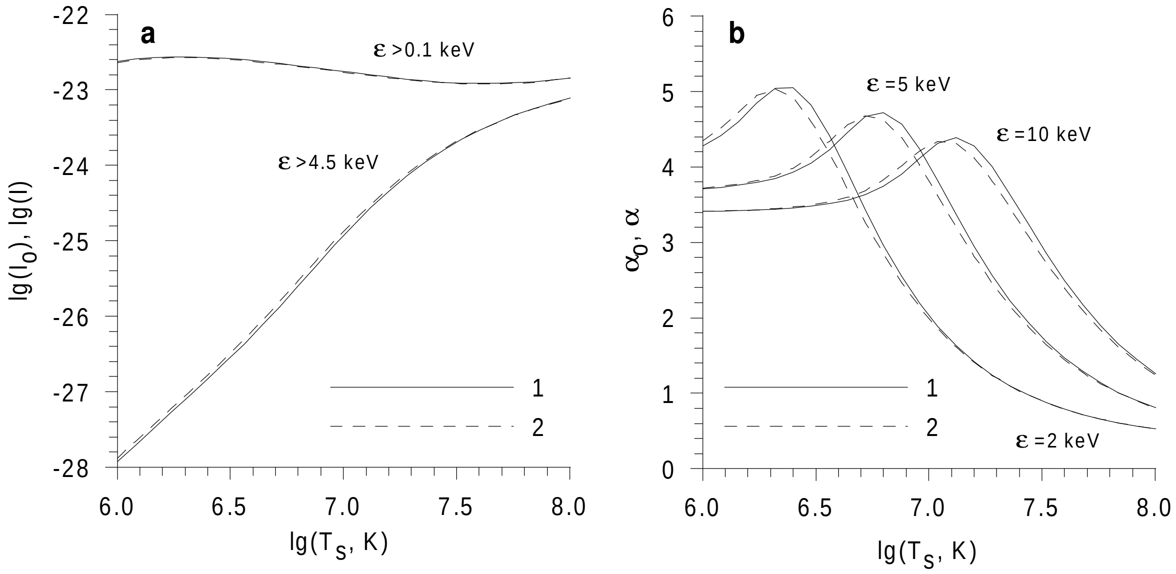

Figure 1: **a** Integrals $I_o(T_s)$ and $I(T_{ch})$ for various emission band and different distribution of supernova explosion energy. 1 – $I_o(T_s)$, 2 – $I(T_{ch})$ for $b = 1.5$. **b** Spectral indexes $\alpha_o(T_s)$ and $\alpha(T_{ch})$ at different photon energy. 1 – $\alpha_o(T_s)$, 2 – $\alpha(T_{ch})$ for $b = 1.5$

where x is the position along the SNR radius of the projection in the units of the radius ($0 \le x \le 1$), const $= 1.1\times10^{21}$ for $\gamma = 5/3$ and $\mu = 0.609$.

If explosion is axially-symmetrical $E(\vartheta, \phi) = E_o\psi(\vartheta)$ $(\partial E/\partial\phi = 0)$ then the shape of the shock front is a circulation figure with profile $R(\vartheta) = \tilde{R}_s\psi(\vartheta)^{1/5}$. If, additionally, the symmetry axis of the distribution $\psi(\vartheta)$ lies in the plan of projection (inclination angle $\delta = 0°$), the surface brightness distribution of such an SNR is given by

$$S(x,\ z) = S_o\psi(\vartheta)^{1/5}\sin\vartheta, \tag{14}$$

where $z = R(\vartheta)\cos\vartheta$ is the coordinate along the symmetry axis of the distribution $\psi(\vartheta)$, x is the coordinate perpendicular to z in the plane of projection. This indicates that the surface brightness distribution profiles parallel to axis x are re-normalized profiles of the surface brightness distribution in Sedov SNR. This fact may be used to test the orientation of the axis-symmetrical SNRs in uniform medium. Distribution of the spectral index has a similar behaviour in case of $\delta = 0°$: profiles parallel to axis x are like to profile of the Sedov SNR when $\delta = 0°$. Cases $\delta \neq 0°$ are considered in [13].

Evolution of an adiabatic remnant of aspherical SN explosion in nonuniform medium is investigated in a further paper [13] where integral characteristics as well as spatial distributions of thermal X-ray and synchrotron emission are considered.

CONCLUSIONS

The aspherical supernova explosion causes only small differences in thermal X-ray luminosity and spectral index of adiabatic SNR comparing to a spherical explosion case. Such a behaviour takes place in different X-ray bands and for a spectral index at different frequencies in X-rays. Thus, the thermal X-ray spectrum of a remnant of aspherical explosion is close to the spectrum of Sedov SNR.

These facts do not allow us to distinguish between the cases of spherical and aspherical SN explosion, if we consider only the integral characteristics of X-ray emission of an adiabatic SNR.

X-ray properties of an SNR essentially depend on features of a disturbed plasma flow behind the shock because the emission depend on density squared and temperature on velocity squared. Therefore, surface distributions of the X-ray emission characteristics are a sensitive test on the conditions in which the object evolves. Asphericity of explosion reveals in the surface distributions of thermal X-ray characteristics. In the case of an axially-symmetrical explosion in uniform medium and when the axis of symmetry lies in the plan of projection, the profiles of X-ray surface brightness and spectral index along the lines perpendicular to the axis are re-normalized profiles of relevant distributions of the Sedov SNR.

REFERENCES

[1] *Bisnovatyi-Kogan G.* About the mechanism of explosion of rotating star as supernova // Astron. Zh.–1970.–**47**.–P. 813–816. (in Russian).

[2] *Bisnovatyi-Kogan G.* Spherization of the remnants of asymmetrical SN explosion in a uniform medium // Supernova Remnants and Their X-Ray Emission / Eds J. Danzinger, P. Gorenstein.–Dortrecht: Reidel, 1983.–P. 125–130.

[3] *Bisnovatyi-Kogan G., Blinnikov S.* Spherization of the remnants of asymmetrical SN explosion in a uniform medium // Astron. Zh.–1982.–**59**.–P. 876–888. (in Russian).

[4] *Bisnovatyi-Kogan G., Lozinskaja T., Silich S.* Axially-symmetrical supernova remnant // Astrophys. and Space Sci.–1990.–**166**.–P. 277–287.

[5] *Bodenheimer P., Woosly S.* A two-dimensional supernova model with rotation and nuclear burning // Astrophys. J.–1983.–**269**.–P. 281–291.

[6] *Chevalier R., Soker N.* Asymmetric envelope expansion of supernova 1987A // Astrophys. J.–1989.–**341**.–P. 867.

[7] *Chugaj N.* Asymmetry of an SN 1987A envelope // Astron. Zh.–1991.–**68**.–P. 349–361. (in Russian).

[8] *Gaensler B. M., et al.* The Asymmetric Radio Remnant of SN 1987A // Astrophys. J.–1997.–**479**.–P. 845.

[9] *Hnatyk B., Petruk O.* Evolution of supernova remnants in the interstellar medium with a large-scale density gradient. I. General properties of shape evolution and X-ray emission // Astron. and Astrophys.–1999.–**344**.–P. 295–309.

[10] *Lyne A., Lorimer D.* High birth velocities of radio pulsars // Nature.–1994.–**369**.–P. 127.

[11] *Mewe R., Lemen J. R., van den Oord G. H. J.* Calculated X-radiation from optically thin plasmas. VI. Improved calculations for continuum emission and approximation formulae for nonrelativistic average Gaunt factors // Astron. and Astrophys. Suppl. Ser.–1986.–**65**.–P. 511–536.

[12] *Papaliolios C., et al.* Asymmetry of the envelope of supernova 1987A // Nature.–1989.–**338**.–P. 565.

[13] *Petruk O.* Evolution of supernova remnants in the interstellar medium with a large-scale density gradient. III. Remnants of aspherical supernova explosions // Astron. and Astrophys.–2000.–submitted.

[14] *Raymond J., Smith B.* Soft X-ray spectrum of a hot plasma // Astrophys. J. Suppl. Ser.–1977.–**35**.–P. 419–439.

[15] *Sedov L.* Similarity and Dimensional Methods in Mechanics.–New York: Academic, 1959.

[16] *Yamada S., Sato K.* Rayleigh-Taylor instability in the asymmetric supernova explosion // Astrophys. J.–1991.–**382**.–P. 594.

A ROBOTIC WIDE–ANGLE H_α SURVEY OF THE SOUTHERN SKY

J. E. Gaustad[1], W. Rosing[2], P. McCullough[3], and D. Van Buren[4]

[1] *Dept. of Physics & Astronomy, Swarthmore College, Swarthmore PA 19081, USA*
e-mail: jgausta1@swarthmore.edu

[2] *Las Cumbres Observatory, 1500 Miramar Beach, Montecito CA 93108, USA*
e-mail: wrosing@lco.org

[3] *Dept of Astronomy, University of Illinois at Urbana-Champaign, Urbana IL 51801, USA*
e-mail: pmcc@astro.uiuc.edu

[4] *Extrasolar Research Corporation, Niskayuna NY 12309, USA*
e-mail: vanburen@crd.ge.com

We are conducting a wide-angle imaging survey of the southern sky at 656.3 nm wavelength, the H_α emission line of hydrogen. Each image of the survey covers an area of the sky 13° square at an angular resolution of approximately one arcminute, and reaches a sensitivity level of 0.5 Rayleigh (3×10^{-18} erg cm^{-2} s^{-1} arcsec^{-2}), corresponding to an emission measure of 1 cm^{-6} pc, and to a brightness temperature for microwave free-free emission of 3 μK at 30 GHz. The survey is being done with a CCD detector, a commercial camera lens, and narrow-band interference filters, mounted on a robotic telescope platform located at Cerro Tololo Inter-American Observatory in Chile. As of June 2000 the data-gathering phase of the survey was 96% complete, and publication is expected by early 2001.

SCIENTIFIC PURPOSE

This survey will produce detailed information on the structure of the diffuse, warm, ionized component of the interstellar medium, information necessary for understanding the dynamics and evolutionary history of the interstellar gas. Since the survey will cover the entire southern sky south of +10° declination, and reach a fainter intensity level than does any previous survey, we expect to discover several new structures, such as stellar wind bubbles, supernova remnants, bow shock nebulae, planetary nebula shells, and other interesting objects.

Even where H_α emission is not seen, the images will be scientifically useful. The intensity of the microwave free-free emission from Galactic hydrogen is directly proportional to the brightness at H_α. The production of both kinds of emission results from the interaction of a proton with an electron, in the one case leading to a transition to another unbound energy state with emission of a microwave photon, and in the other case leading to recombination at a high energy level, followed by a cascade down through the third and second energy levels with emission of an H_α photon. The ratio of intensities of the free-free and H_α emission thus depends primarily on quantum-mechanical factors, with only a slight dependence on temperature and no dependence on density (Bennett *et al.*, 1992). Thus, these images will allow accurate measurement of anisotropies in the Galactic free-free emission at microwave wavelengths (or proof that these are negligible), emission which must be subtracted from satellite or ground-based measurements to obtain the true cosmic background fluctuations. For example, in an early pilot study for this project (Gaustad *et al.*, 1996) we showed that no more than 7% of the 44 μK anisotropy in the CMBR measured in the Saskatoon experiment (Netterfield *et al.*, 1995) could be due to contamination by Galactic free-free emission.

INSTRUMENTATION AND OPERATIONS

The survey is being conducted from Cerro Tololo Inter-American Observatory (CTIO) near La Serena, Chile, located at longitude W 70°49′, latitude S 30°10′, and elevation 2200 m. The system is housed in a 10-foot dome (from Technical Innovations, Inc.) on a concrete pad located near the 1-meter telescope building at CTIO.

Our CCD camera, from SpectraSource, Inc., contains a 1024 × 1024 TI chip with 12-μm pixels. The sky is imaged onto the chip with a 52-mm f.l. Canon lens operated at f/1.6, yielding a field of view of 13°×13° and a scale of 48″/pixel.

The advantage of the small lens over a large telescope, of course, is the field of view. The CTIO 4-meter telescope has the focal length of 11.2 m compared to the 52-mm focal length of our camera lens, and thus has

Invited paper.

an angular scale 215 times smaller. It would take 46000 times longer to survey the sky to the same sensitivity with this large telescope (if operated at the same focal ratio and with the same CCD), although of course one would get much higher angular resolution. (The small size of the instrument and dome has caused the CTIO staff to give our instrument the nickname of El Enano–The Dwarf.)

A filter wheel mounted in front of the lens contains an H_α filter of 3-nm bandwidth and a dual-band notch filter, which excludes H_α but transmits two 6-nm bands of continuum radiation on either side of H_α. The filter wheel is encased in Styrofoam and maintained at a constant 25 C temperature to provide wavelength stability of the filters and to prevent condensation on the filters or the lens.

The camera is attached to a Byers Series 2 German mount with microstepping motors and Dynamics Research encoders on each axis. The pointing resolution is better than 0.25 arcseconds, and the accuracy is better than 5 arcseconds up to $Z = 75$ degrees. The unguided tracking accuracy is better than 2 arcseconds per hour. Thus, no external guider is needed.

Since the twilight sky is not uniform over our wide field of view, we have built a lightbox, for obtaining calibration flats, containing a translucent screen illuminated by incandescent light bulbs and by hydrogen emission lamps.

A Texas Weather Instruments weather station completes the system. Two PCs running scheduling and control programs written in Visual Basic under Windows 95 control the camera, mount, dome, weather station, and light box. Data is recorded on disk during operations, and later transferred to DAT tape.

One of the robot's computers positions of the telescope and dome while the other operates the camera, schedules the observations, and runs the ftp and e-mail communication links. A log of the night's operations and sample images are sent to the PI at Swarthmore each morning via e-mail and ftp, but the full data set is recorded on disk and then transferred to magnetic tape during the day. We can inquire of the status of the robot via e-mail, and make changes in the program or observing schedule via ftp. But we do not operate the camera in real time – it is a true robot. The robot has its own weather station and will not attempt observations if humidity or wind conditions exceed safe limits, but as an extra precaution it also asks permission (via e-mail) of the 4-meter telescope operator before opening the dome. The operator can also close the dome via e-mail command. The only other human intervention, during normal operations, is for weekly tape-changing and preventive maintenance.

OBSERVATIONS AND DATA REDUCTION

All observations are taken after twilight and with the moon below the horizon. A normal set of scientific observations consists of five 20-minute exposures through the H_α filter interspersed among six 5-minute exposures through the dual-band continuum filter. Between observations of each science field, we take a few exposures pointed at the pole to obtain data on changes in extinction during the night. We also take occasional short exposures of bright standard objects for intensity calibration. Biases, darks, and flats are taken during twilight at the beginning and end of each night.

Reduction of the calibration exposures is done on site automatically, but all science images are shipped to Swarthmore on tape for later processing. The H_α and continuum images are aligned and coadded separately. Then, after scaling to make the star images the same brightness, the continuum image is subtracted from the H_α image, divided by the transmission function for the H_α filter, and smoothed to remove residual stars. In Figure 1, images of the Orion region are shown as an example of the process.

SURVEY STATUS

The survey consists of 283 fields covering the sky from $-90°$ to $+15°$ declination, with the same centers as those in the IRAS Sky Survey Atlas. In order to reduce the noise and to confirm objects discovered at the faintest brightness levels, we repeat all fields with 5° offsets. As of June 2000, we had completed 96% of the survey. A mosaic consisting of all images obtained so far is shown in Figure 2. When the data are fully processed, the survey will be made available to the scientific community on the web and on CD-ROM. We expect the data-gathering phase of the project to be finished towards the end of 2000, and the survey to be published in early 2001.

PRELIMINARY RESULTS

Images of the Large Magellanic Cloud have already been published (Gaustad *et al.*, 1999). Several other preliminary results have also been obtained. For example, some cirrus dust clouds show a rim of ionized hydrogen on the side towards the Galactic plane (McCullough *et al.*, 1999). A filamentary bubble just north of the Gum Nebula may be a new supernova remnant (McCullough *et al.*, 2000). Planetary nebulae often have the extended ionized regions surrounding their bright cores (Hall, 1999). Abell 36, for example, has an ionized halo 5° in diameter, formed by ultraviolet photons escaping through its optically thin shell (McCullough *et al.*, 2000).

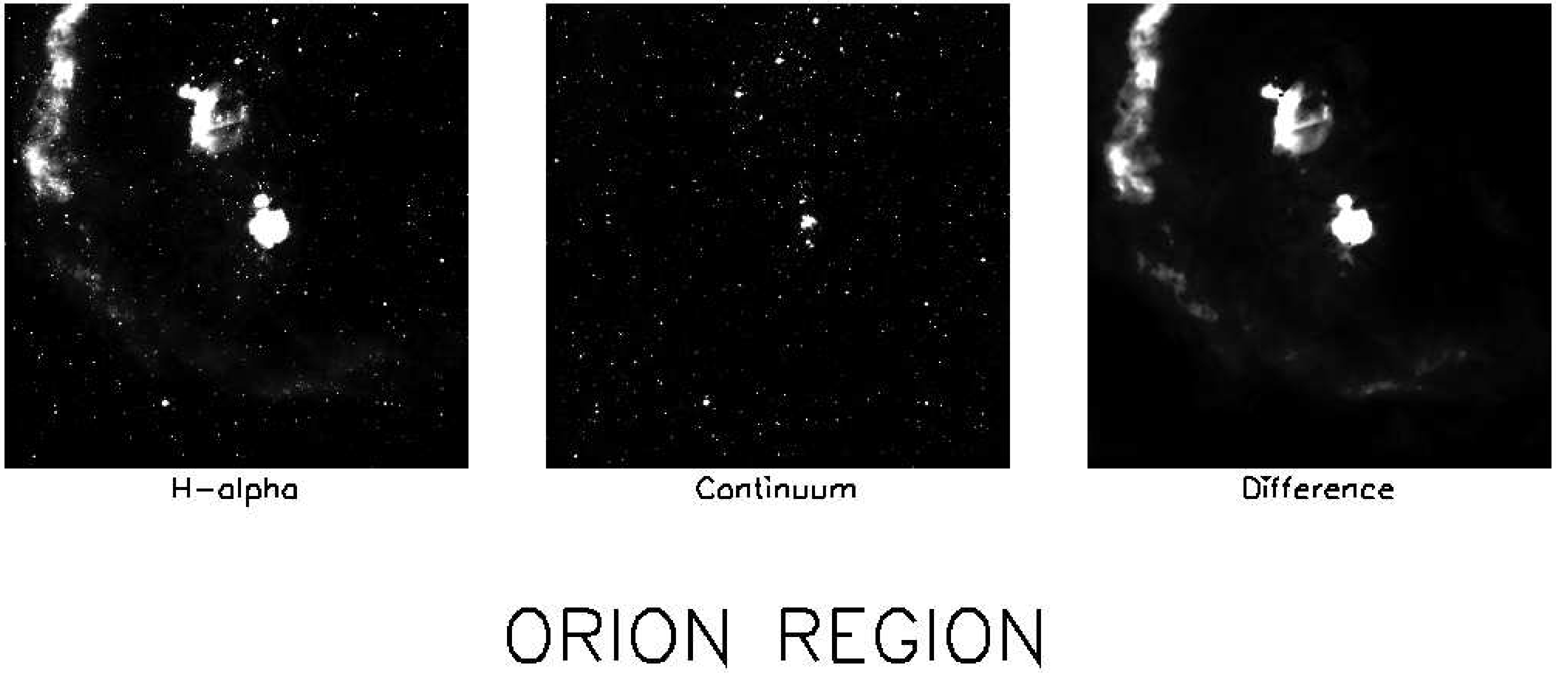

Figure 1: Three images of the southern region of Orion, showing Barnard's Loop and the Orion Nebula:
left – taken through the H_α filter, showing both stars and nebulosity;
center – taken through the continuum filter, showing only the stars;
right – the difference of the two images, showing only the nebulosity

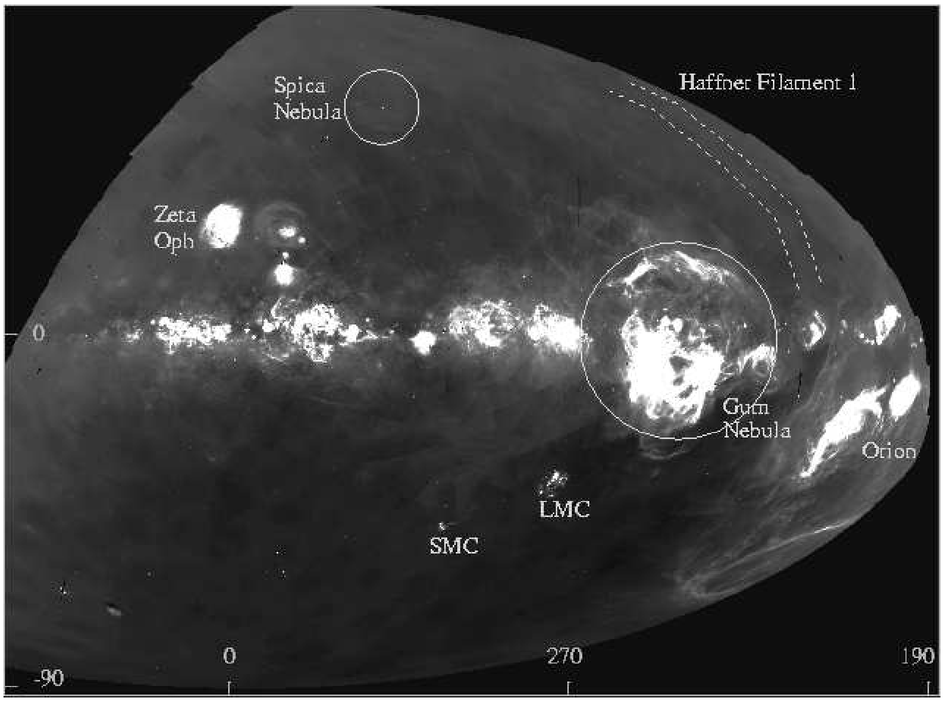

Figure 2: A mosaic of the southern sky in H_α

ASTRONOMY IN UKRAINE

What does this project have to do with the theme of this conference? Nothing, really, other than that the fact that the data have been gathered in Chile, analyzed in the United States, and reported in Ukraine shows that astronomy does not recognize national boundaries. Astronomy in Ukraine is Astronomy in the World. We invite Ukranian astronomers, and in fact all astronomers, to make use of our survey once it is complete, and the data are fully reduced, calibrated, and published.

Acknowledgements. The project has been supported by grants from Las Cumbres Observatory, the National Science Foundation, NASA, Dudley Observatory, the Fund for Astrophysical Research, Research Corporation, the University of Illinois at Urbana-Champaign, and Swarthmore College. This work was performed in part at the Jet Propulsion Laboratory of the California Institute of Technology, which is operated under contract with the National Aeronautics and Space Administration.

The observations were obtained at Cerro Tololo Inter-American Observatory, which is operated by the Association of Universities for Research in Astronomy, Inc., under cooperative agreement with the National Science Foundation. We are extremely grateful to the staff of CTIO for their support of this project. Without their hard work on our behalf, the survey would have proceeded much more slowly, and might never have been completed.

REFERENCES

[1] *Bennett C. L., et al.* // Astrophys. J.–1992.–**396**.–P. L7.

[2] *Gaustad J. E., McCullough P. R., Van Buren D.* // Publs Astron. Soc. Pacif.–1996.–**108**.–P. 351.

[3] *Gaustad J. E., Rosing W., McCullough P. R., Van Buren D.* // New Views of the Magellanic Clouds: IAU Symp. N 190 / Eds Y.-H. Chu, N. Suntzeff, J. Hesser, D. Bohlender.–San Francisco: ASP.–1999.–P. 99.

[4] *Hall K. J.* Senior Thesis.–Swarthmore College: Swarthmore, Pennsylvania, USA, 1999.

[5] *McCullough P. R., Gaustad J. E., Rosing W., Van Buren D.* // Microwave Foregrounds: ASP Conf. Ser. / Eds A. de Oliveira-Costa, M. Tegmark.–San Francisco: ASP, 1999.–**181**.–P. 253.

[6] *McCullough P. R., Gaustad J. E., Rosing W., Van Buren D.* // Fourth Tetons NASA Conf.–Wyoming, USA, 2000.–in press.

[7] *Netterfield C. B., Jarosik N., Page L., et al.* // Astrophys. J.–1996.–**108**.–P. 351.

DUST INFLUENCE ON ^{12}CO MOLECULAR SPECTRUM IN MOLECULAR–DUST CLOUDS

V. Shulga, A. Antuyfeyev, I. Lavrik

Institute of Radio Astronomy, NAS of Ukraine
4 Chervonopraporna St., 61002 Kharkiv-2, Ukraine
e-mail: shulga@rian.kharkov.ua

The study of space molecular clouds is of particular interest due to star-birth occurrence. The analysis of their molecular radiative spectra is one of the principal methods to get information about their spatial structure, temperature and density. The existence of dust in clouds can lead to an appreciable variation of radiation line parameters. Therefore, for correct understanding the observational data it is necessary to build up the model describing the radiation transport processes in a gas-like dust substance. In the present paper we determine the rate of dust influence on molecular CO radiative spectra, using a spherical cloud model.

An effective method of solving the radiative transfer problem is the Monte-Carlo method. This method was developed by Bernes [1] for a cloud model containing only the gas component. Including the dust component in this method does not lead to noticeable complications and comes to the following. The model photons should present now not only the radiation of molecules, but also the dust radiation. The model photon weight on $j-i$ transition will be written in the form:

$$W_{ij} = \left\{ n_{j,m} A_{ji} + \frac{16\pi}{h\nu_{ij}} B_{\nu_{ij}}(T_d) k_d(\nu_{ij}) \right\} \frac{V_m}{N},$$

where $n_{j,m}$ is the population of j level in the m cell, ν_{ij} is the frequency of the $j-i$ transition, A_{ji} is the Einstein coefficient for spontaneous radiation, $B_{\nu_{ij}}(T_d)$ is the Plank function at the frequency ν_{ij} for the dust temperature T_d, $k_d(\nu_{ij})$ is the coefficient of dust absorption, V_m is the cell volume, h is the Plank constant, N is the total number of the model photons.

The expression in brackets is the number of the true photons born in 1 cm^3 in 1 sec at the frequency ν_{ij} in a cell by number m due to molecules as well as to dust grains. The second addendum (which gives the contribution from the dust) is written on the assumption that the dust grains are absolute black bodies.

During the propagation, the radiation is attenuated due to absorption by molecules and dust grains (the scattering by dust in the (sub) millimeter-wavelength range can be neglected), but when calculating the mean intensity on every transition the account is made only for that part of radiation which was absorbed by molecules, therefore, the number of absorption events per 1 molecule in every cell through which the model photon is passing can be written as following:

$$D_{ij,m+k} = \frac{h\nu_{ij}}{c} \varphi_{ij}(\nu) B_{ij} \frac{l_k W_{ij,m}}{\tau^{(\mathrm{g})}_{ij,m} V_{m+k}} e^{-\sum\limits_{s=1}^{k-1} \tau_{ij,s}} \left(1 - e^{-\tau^{(\mathrm{g})}_{ij,m+k}} \right),$$

$$\tau_{ij,k} = \tau^{(\mathrm{g})}_{ij,k} + \tau^{(d)}_{ij,k} = \frac{h\nu_{ij}}{c} \varphi_{ij}(\nu)(n_{i,m+k} B_{ij} - n_{j,m+k} B_{ji}) l_k + k_d(\nu_{ij}) l_k.$$

Here $\tau^{(\mathrm{g})}_{ij,k}$ and $\tau^{(d)}_{ij,k}$ are the optical thicknesses of the gas and the dust substance taken apart, l_k is the path passed by the photon at the k step, B_{ij} and B_{ji} are the Einstein coefficients. It is assumed that the line profile is determined by the Doppler broadening which takes place for majority of molecular dust clouds.

The values $D_{ij,m+k}$ obtained after taking account of all the model photons are no other than the mean intensities in every cell at every transition, and they can be used when calculating new populations in the next iteration.

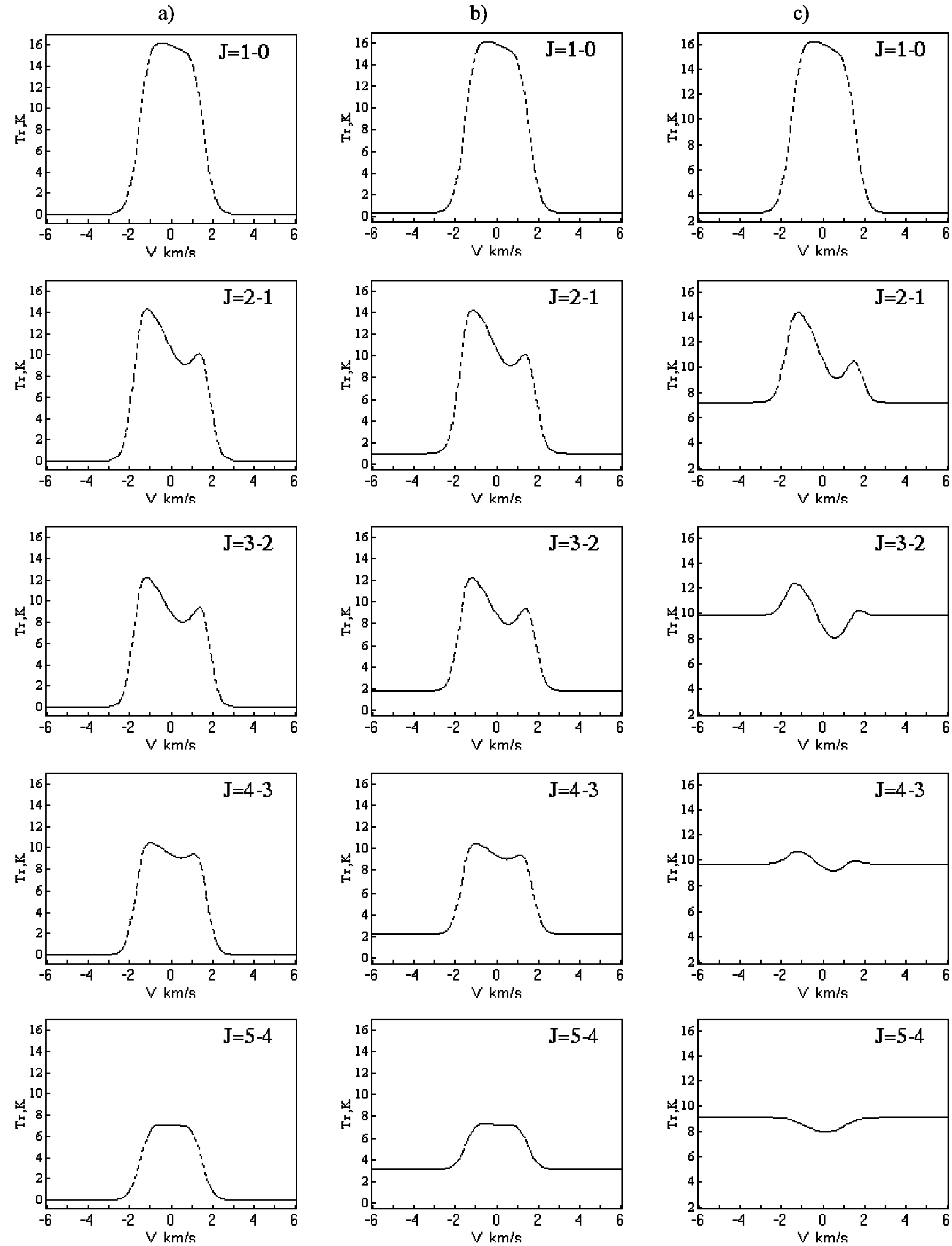

Figure 1: CO lines at the different transitions in the collapsing cloud with various dust-to-molecule density ratio. The cloud radius is $R_{cloud} = 1$ pc, the kinetic temperature of gas is equal to the dust temperature $T_{kin} = T_{dust} = 20$ K, concentrations of compounds of gaseous component in the cloud center are $n(CO) = 0.1$ cm^{-3}, $n(H_2) = 10^4$ cm^{-3}, $n(He) = 2{\times}10^3$ cm^{-3}: a) $\rho_d/\rho_g = 0$; b) $\rho_d/\rho_g = 10$; c) $\rho_d/\rho_g = 100$

After calculation of populations with the required precision, one can calculate the intensities of emerging radiation:

$$I_{ij}(\nu) = I_0 e^{-\tau(X)} + \int\limits_0^X \left(k_d(\nu_{ij}) B_{\nu_{ij}}(T_d) + \frac{h\nu_{ij}}{4\pi} \varphi_{ij}(\nu) n_{j,m(x)} A_{ij} \right) e^{-\tau_{ij}(X-x)} dx,$$

where I_0 is the intensity of external radiation incident on the cloud, $m(x)$ is the cell number, and $\tau_{ij}(x)$ is the optical thickness of the gas-dust medium.

We consider the model of a cloud with spherical geometry only. This model can be used for analysis of the observation data because it is assumed that the molecular dust clouds have a spherical form at early stages of star formation.

The gas component in a cloud is represented by H_2 and ^{12}CO molecules, and also by He atoms, and the dust one is represented by spherical particles covered by dirty ice. By the calculation six lower rotational levels of the ground vibratory state of ^{12}CO molecules are considered. It is assumed that ^{12}CO molecules are excited by collisions with Helium and molecular Hydrogen (the excitation by collisions with the dust grains as well as adsorption of molecules by dust grains is not accounted).

The absorbing and scattering properties of dust particles are defined using the Mie theory taking account of the effective value of the dielectric permeability calculated for the dust grain of the "core-mantle" type. The dielectric permeabilites for silicate and dirty ice are taken from [3, 4]. It is assumed that the dust particles are distributed with radius as $n(a) \sim a^{-3.5}$ ($a_{min} = 40$ nm, $a_{max} = 1$ μm) [2].

The calculation was carried out for a collapsing cloud in which the systematical velocity increases proportionally with the distance r from the cloud center taking value 1 km/sec at its boundary, and the gas and dust densities vary as r^3. The characteristic velocity of micro-turbulent motion was taken 1 km/sec and the microwave background radiation temperature $T_{bg} = 2.7$ K.

The results are presented in Fig. 1. In the collapsing cloud the noticeable dust influence on spectra is observed at significant dust quantities. When the density ratio of the dust component to the gaseous one is equal to $\rho_d/\rho_g = 10$, the spectrum of molecules is observed on the background of continual radiation of a dust. When the dust density exceeds 100 times the gaseous one, a "conversion" of the emission molecular spectrum to the absorption spectrum occurs. For CO this effect is observed only at transitions between the upper excited levels. The radiation at lower transition $J = 1-0$ which is observed the most frequently is weakly sensitive to the dust presence. The effects may allow to proceed the examination of the dust component by spectra of CO molecule radiation.

REFERENCES

[1] *Bernes C.* A Monte Carlo approach to non-LTE radiative transfer problems // Astron. and Astrophys.–1979.–**73**.–P. 67–73.

[2] *Mathis J. S., Rumple W., Nordsieck K. H.* The size distribution of interstellar grains // Astrophys. J.–1977.–**217**.–P. 319–326.

[3] *Ossenkopf V., Henning Th., Mathis J. S.* Constraints on cosmic silicates // Astron. and Astrophys.–1992.–**279**.–P. 567–578.

[4] *Preibisch Th., Ossenkopf V., Yorke H. W., Henning Th.* The influence of ice-coated grains on protostellar spectra // Astron. and Astrophys.–1993.–**279**.–P. 577–588.

MODEL OF THE CO MOLECULE EMISSION FROM THE CLOUD WITH BIPOLAR OUTFLOWS

V. Shulga, A. Antuyfeyev

Institute of Radio Astronomy, NAS of Ukraine
4 Chervonopraporna St., 61002 Kharkiv-2, Ukraine
e-mail: shulga@rian.kharkov.ua

INTRODUCTION

A lot of interstellar clouds are the sources of star formation. Observations of bipolar outflows testify the process of star birth and their evolution in a cloud. Millimeter and infrared emissions from molecular clouds are under investigation in many observational programs. Interpretation of the observational data requires to develop molecular cloud models in order to compare the observed and simulated emission characteristics.

We propose a numerical model for calculation of radiation of molecular lines from a cloud having the bipolar structure. It is assumed that the cloud has two kinds of symmetry: axial symmetry around the Z axis, and symmetry relative to the plane XY (Fig. 1). In this paper we calculate the CO molecule radiation, but the method can be easily applied to the calculation of arbitrary molecules having known excitation coefficients. The first 6 rotation transitions of CO molecule are considered under its excitation by Hydrogen molecules with account of cosmic microwave background.

The model allows to specify any distribution laws for concentration of CO, H_2, the kinetic temperature, and velocities in the plane XZ. Using the linear approximation allows to obtain higher than in Monte-Carlo [1, 2] method accuracy of the determination of the mean intensity of the radiation field, and the excitation temperature in a cloud.

SOLVING RADIATIVE TRANSFER EQUATION

The cloud is considered as consisting of elementary volumes (cells) which have a toroidal form and locate equidistantly on axes X and Z. All the cloud parameters (CO, H_2 molecule densities, the kinetic temperature, micro turbulent and systematic velocities) are assumed to be constant within any cell. It should be noted that the method accuracy becomes higher with decreasing the space gradient of any parameter.

The radiation transport equation together with a system of equations of the population balance has been solved by an iterative method. Initially, it was assumed that the populations in any cell are defined by the Boltzman law. Then, for all the cells, the average intensity $\langle J(\vec{r})\rangle$ has been calculated by the formula:

$$\langle J(\vec{r})\rangle = \frac{1}{4\pi}\int\limits_{4\pi} d\Omega \int\limits_{-\infty}^{+\infty} d\nu\varphi(\nu)I(\nu,\vec{n},\vec{r}). \tag{1}$$

The integral over frequencies was approximated by a sum over fixed set of frequencies. The integral over solid angle was also calculated over limited number of random directions. The intensity $I(\nu,\vec{n},\vec{r})$ in the line of $\vec{n}$ was calculated by formulas for plane-parallel geometry:

$$I(\nu,n,r) = \sum_{p=1}^{k}\left[S_{ij}^{p}\left(1-e^{-\tau_{ij}^{p}}\right)\exp\left(-\sum_{m=p+1}^{k}\tau_{ij}^{n}\right)\right] + I_B\exp\left(-\sum_{p=1}^{k}\tau_{ij}^{n}\right), \tag{2}$$

$$\tau_{ij}^{p} = \frac{h\nu_{ij}}{c}\varphi\left(\nu-\nu_{ij}\left(1-\frac{\vartheta_{\vec{n}}^{p}}{c}\right)\right)\Delta l(B_{ji}n_j - B_{ij}n_i), \tag{3}$$

where I_B is the background radiation field, S_{ij}^{p} is the source function, τ_{ij}^{p} is the optical depth at the point P in the line of $\vec{n}$, i and j are the upper and lower energy level populations at the point P.

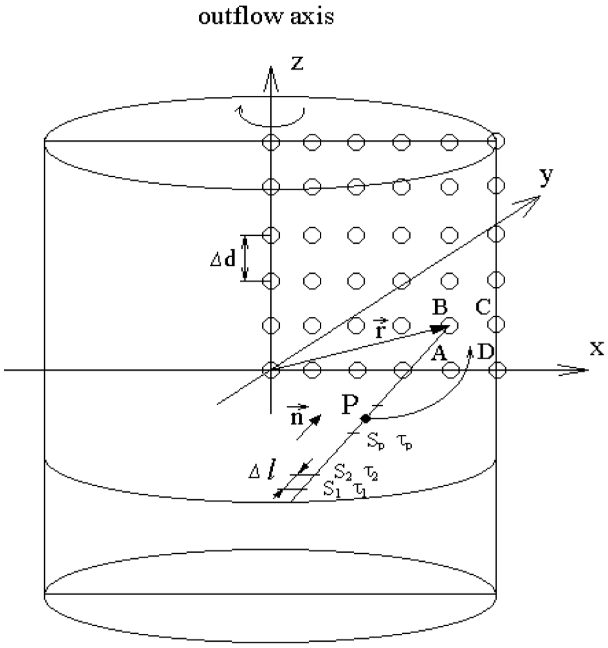

Figure 1: The structure of the cloud calculated:
$\vec{r}$ is the radius-vector of a cell for which $\langle J(\vec{r})\rangle$ is calculated;
$\vec{n}$ is the direction along which the intensity I is calculated;
Δl is the step on which the intermediate values I are calculated

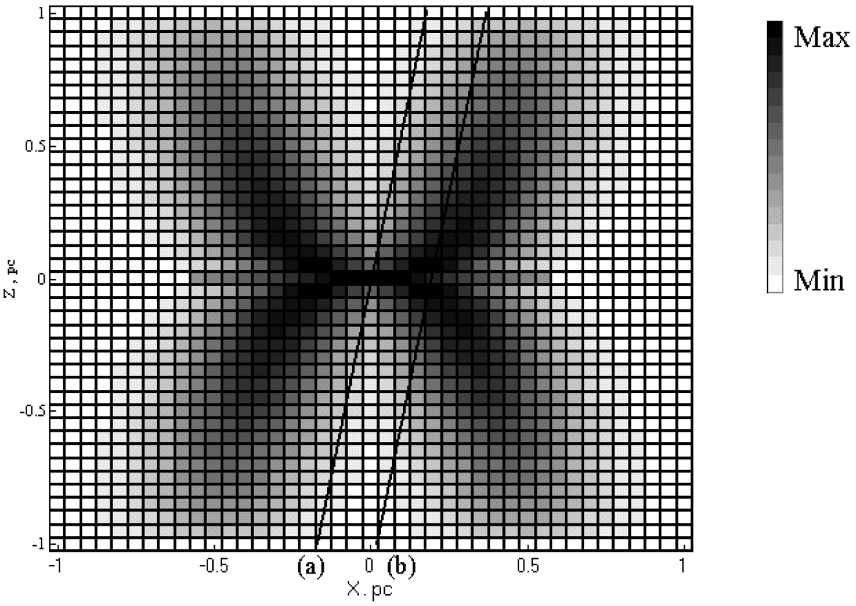

Figure 2: The CO molecule density distribution:
Min $n_{CO} = 0.001$ cm^{-3};
Max $n_{CO} = 0.01$ cm^{-3}

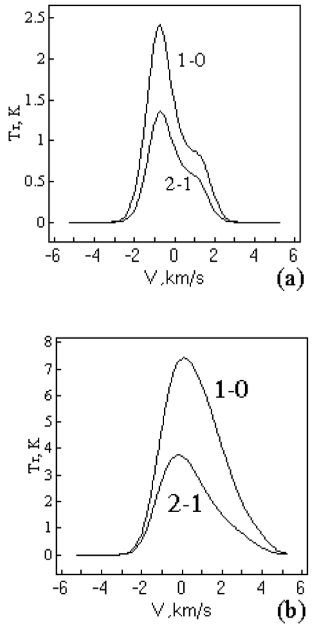

Figure 3: The profiles of lines corresponding to location of the telescope ray (a) and (b) in Fig. 2

The populations, velocities and other parameters at the point P were calculated using the linear approximation over the nearest four cells (A, B, C, D in Fig. 1). The step Δl must satisfy the conditions:

$$\frac{\Delta\vartheta_t}{\Delta l} \gg Q, \quad \Delta l > \Delta d, \tag{4}$$

where $\Delta\vartheta_t$ is the micro-turbulent velocity, Q is the systematical velocity gradient which are taken in the cloud point where the ratio $\dfrac{\Delta\vartheta_t}{Q}$ is maximal.

There after, for all cells the system of population balance equations was solved and the refined population values were calculated. The process was iterated till the given population error became obtained.

As an example, the molecular cloud was taken with disk and bipolar outflows. The CO concentration distribution is shown in Fig. 2. The outflow velocity is assumed to be proportional to the distance from the cloud center. The kinetic temperature distribution is the same as CO concentration (min $T_{kin} = 5$ K, max $T_{kin} = 20$ K). In Fig. 3 the line profiles of the transitions $J = 1-0$ and $2-1$ are shown which correspond to the telescope rays (a) and (b) in Fig. 2. In Fig. 4 (a, b, c) the calculated excitation temperatures are shown for transitions $J = 1-0$, $J = 2-1$ and $J = 3-2$ of the CO molecule. The population mean relative error obtained in calculation is near 1%; the program run time on PC IBM with a processor Pentium III 550 is nearly 3 hours.

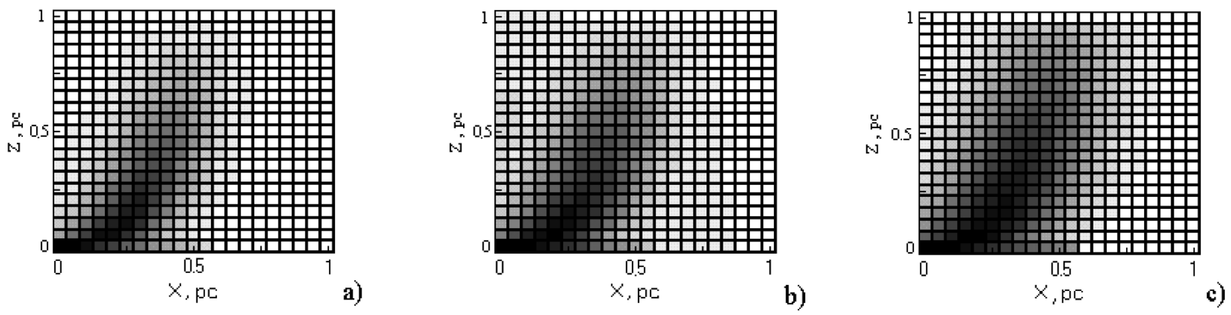

Figure 4: The calculated excitation temperatures for transitions $J = 1-0$ (a), $J = 2-1$ (b), $J = 3-2$ (c)

Min $Tex_{1-0} = 3$ K	Min $Tex_{2-1} = 3$ K	Min $Tex_{3-2} = 3$ K
Max $Tex_{1-0} = 25$ K	Max $Tex_{2-1} = 9.7$ K	Max $Tex_{3-2} = 8.5$ K

REFERENCES

[1] *Bernes C.* A Monte Carlo approach to non-LTE radiative transfer problems // Astron. and Astrophys.–1979.–**73**.–P. 67–73.

[2] *Choi M., Evans N. J., Gregerzen E. M., Wang Y.* Modeling line profiles of protostellar collapse in B 335 with Monte Carlo method // Astrophys. J.–1995.–**448**.–P. 742–754.

COSMOLOGICAL PARAMETERS FROM OBSERVATIONAL DATA ON THE LARGE SCALE STRUCTURE OF THE UNIVERSE

B. Novosyadlyj[1], **R. Durrer**[2], **and S. Apunevych**[1]

[1]*Astronomical Observatory, Ivan Franko National University*
8 Kyryla i Mephodia St., 79005 Lviv, Ukraine
e-mail: novos@astro.franko.lviv.ua, apus@astro.franko.lviv.ua

[2]*Department de Physique Théorique, Université de Genève*
Quai Ernest Ansermet 24, CH-1211 Genève 4, Switzerland
e-mail: ruth.durrer@physics.unige.ch

The observational data on the large scale structure (LSS) of the Universe are used to determine cosmological parameters within the class of adiabatic inflationary models. We show that a mixed dark matter model with cosmological constant (ΛMDM model) and parameters $\Omega_m = 0.37^{+0.25}_{-0.15}$, $\Omega_\Lambda = 0.69^{+0.15}_{-0.20}$, $\Omega_\nu = 0.03^{+0.07}_{-0.03}$, $N_\nu = 1$, $\Omega_b = 0.037^{+0.033}_{-0.018}$, $n_s = 1.02^{+0.09}_{-0.10}$, $h = 0.71^{+0.22}_{-0.19}$, $b_{cl} = 2.4^{+0.7}_{-0.7}$ (1σ confidence limits) matches observational data on LSS, the nucleosynthesis constraint, direct measurements of the Hubble constant, the high redshift supernova type Ia results and the recent measurements of the location and amplitude of the first acoustic peak in the CMB anisotropy power spectrum. The best model is Λ dominated (65% of the total energy density) and has slightly positive curvature, $\Omega = 1.06$. The clustered matter consists in 8% massive neutrinos, 10% baryons and 82% cold dark matter (CDM). It is shown that the LSS observations together with the Boomerang (+MAXIMA–1) data on the first acoustic peak rule out zero-Λ models at more than 2σ confidence level.

INTRODUCTION

The comparison of recent experimental data on the large scale structure of the Universe with theoretical predictions of inflationary cosmology have shown since quite some time that the simplest cold dark matter (CDM) model is ruled out and we have to allow for a wider set of parameters to fit all observational data on the state and history of our Universe. These include spatial curvature (Ω_k), a cosmological constant (Ω_Λ), the Hubble parameter ($h \equiv H_0/(100\,\mathrm{km\ s}^{-1}\ \mathrm{Mpc}^{-1})$), the energy density of baryonic matter (Ω_b), cold dark matter (Ω_{cdm}), the number of species of massive neutrinos (N_ν) and their density (Ω_ν), the amplitude of the power spectra of primordial perturbations in scalar (A_s) and tensor (A_t) modes and the corresponding power-law indices (n_s and n_t), and the optical depth to early reionization (τ). Constraining this multidimensional parameter space, determining the true values of fundamental cosmological parameters, the nature and content of the matter which fills our Universe is an important and exciting problem of cosmology which has now become feasible due to the enormous progress in cosmological observations (short reviews and references see in [18, 7]).

The goal of this paper is to determine cosmological parameters of the sub-class of models without tensor mode and no early reionization on the basis of LSS data related to different scales and different redshifts. We test ΛMDM models with non-zero curvature. Since the sum $\Omega_k + \Omega_\Lambda + \Omega_m = 1$ according to Friedmann's equation, we treat Ω_Λ and Ω_m as free parameters. Furthermore, we use the data on the location and amplitude of the first acoustic peak determined from the most accurate recent measurements of the CMB power spectrum. We also use the SNIa constraint for comparison.

The outline of the paper is as follows: in Sect. 1 we describe the experimental data set which is used here and the method employed to determine cosmological parameters. In Sect. 2 we present and discuss our results. Our conclusions are presented in Sect. 3.

1. THE EXPERIMENTAL DATA SET AND METHOD OF CALCULATION

Our approach is based on the comparison of the observational data on the structure of the Universe over a wide range of scales with theoretical predictions from the power spectrum of small (linear) density fluctuations. The form of the spectrum strongly depends on the cosmological parameters Ω_m, Ω_b, Ω_ν, N_ν, h and n_s. If its amplitude at one given scale is fixed by some observational data then predictions for observations on other scales can be calculated and compared with corresponding observational data. Minimization of the quadratic differences between the theoretical and observational values divided by the observational errors, χ^2, determines the best-fit values of the above mentioned cosmological parameters. For this we use the following observational data set:

1. The location $\tilde{\ell}_p = 197 \pm 6$ and amplitude $\tilde{A}_p = 69 \pm 8\mu$K of the first acoustic peak in the angular power spectrum of the CMB temperature fluctuations deduced from CMB map obtained in Boomerang experiment [3] (these data are sensitive to the amplitude and form of the initial power spectrum in the range $\approx 200\,h^{-1}$Mpc);

2. The power spectrum of density fluctuations of Abell–ACO clusters ($\tilde{P}_{A+ACO}(k_j)$) obtained from their space distribution by [21] (scale range $10 - 100\,h^{-1}$Mpc);

3. The constraint for the amplitude of the fluctuation power spectrum on $\approx 10\,h^{-1}$Mpc scale derived from a recent optical determination of the mass function of nearby galaxy clusters [10] gives $\tilde{\sigma}_8\Omega_m^{\alpha_1} = 0.60 \pm 0.04$ where $\alpha_1 = 0.46 - 0.09\Omega_m$ for flat low-density models and $\alpha_1 = 0.48 - 0.17\Omega_m$ for open models (at the 90% C. L.);

4. The constraint for the amplitude of the fluctuation power spectrum on $\approx 10\,h^{-1}$Mpc scale derived from the observed evolution of the galaxy cluster X-ray temperature distribution function between $z = 0.05$ and $z = 0.32$ derived by [25] $\tilde{\sigma}_8\Omega_m^{\alpha_2} = 0.56 \pm 0.19\Omega_m^{0.1\log\Omega_m+\alpha_2}$, $\alpha_2 = 0.34$ for open models and $\tilde{\sigma}_8\Omega_m^{\alpha_2} = 0.56 \pm 0.19\Omega_m^{0.2\log\Omega_m+\alpha_2}$, $\alpha_2 = 0.47$ for flat models (both with 95% confidence limits);

5. The constraint for the amplitude of the fluctuation power spectrum on $\approx 10\,h^{-1}$Mpc scale derived from the existence of three very massive clusters of galaxies observed so far at $z > 0.5$ [1] $\tilde{\sigma}_8\Omega_m^{\alpha_3} = 0.8 \pm 0.1$, where $\alpha_3 = 0.24$ for open models and $\alpha_3 = 0.29$ for flat models;

6. The constraint on the amplitude of the linear power spectrum of density fluctuations in our vicinity obtained from the study of bulk flows of galaxies in sphere of radius $50\,h^{-1}$Mpc $\tilde{V}_{50} = (375 \pm 85)$ km/s [14];

7. The constraint for the amplitude of the fluctuation power spectrum on $0.1 - 1\,h^{-1}$Mpc scale and $z = 3$ derived from the Ly-α absorption lines seen in quasar spectra $1.6 < \tilde{\sigma}_F(z = 3) < 2.6$ (95% C. L.) at $k_F \approx 38\Omega_m^{1/2}\,h$/Mpc [11, 22, 12];

8. The constraints for the amplitude and inclination of the initial power spectrum on $\approx 1\,h^{-1}$Mpc scale and $z = 2.5$ scale derived by Croft *et al.* (1998) from the Ly-α forest of quasar absorption lines $\tilde{\Delta}_\rho^2(k_p) \equiv k_p^3 P(k_p)/2\pi^2 = 0.57 \pm 0.26$, $\tilde{n}_p \equiv \dfrac{\Delta \log\, P(k)}{\Delta \log\, k}\,|_{k_p} = -2.25 \pm 0.18$, $k_p = 1.5\Omega_m^{1/2}h$/Mpc (95% C. L.);

9. The data on the direct measurements of the Hubble constant $\tilde{h} = 0.65 \pm 0.10$ which is a compromise between results obtained by two groups [24] and [16];

10. The nucleosynthesis constraint on the baryon density derived from a observational content of inter galactic deuterium $\widetilde{\Omega_b h^2} = 0.019 \pm 0.0024$ (95% C. L.) given by [5];

11. The constraint on the matter and vacuum (cosmological constant) energy density derived from the distance measurements of super novae of type Ia (SNIa) [23, 19, 20] in the form $[\widetilde{\Omega_m - 0.75\Omega_\Lambda}] = -0.25 \pm 0.125$.

One of the main ingredients for the solution for our search problem is a reasonably fast and accurate determination of the linear transfer function for dark matter clustering which depends on the cosmological parameters. We use accurate analytical approximations of the MDM transfer function $T(k;z)$ depending on the parameters Ω_m, Ω_b, Ω_ν, N_ν and h given by [9]. The linear power spectrum of matter density fluctuations $P(k;z) = A_s k^{n_s} T^2(k;z) D_1^2(z)/D_1^2(0)$, where A_s is the normalization constant for scalar perturbations and $D_1(z)$ is the linear growth factor. We normalize the spectra to the 4-year COBE data [2] which determine the amplitude of density perturbation at horizon scale, δ_h [15, 4]. Therefore, each model will match the COBE data by construction. The normalization constant A_s is then given by $A_s = 2\pi^2\delta_h^2(3000\,\mathrm{Mpc}/h)^{3+n_s}$.

The Abell–ACO power spectrum is related to the matter power spectrum at $z = 0$, $P(k;0)$, by the cluster biasing parameter b_{cl}: $P_{A+ACO}(k) = b_{cl}^2 P(k;0)$. We assume scale-independent linear bias as free parameter of which best-fit values will be determine join with other cosmological parameters.

The dependence of the position and amplitude of the first acoustic peak in the CMB power spectrum on cosmological parameters n_s, h, Ω_b, Ω_{cdm} and Ω_Λ can be calculated using the analytical approximation given in [8] which has been extended to models with non-zero curvature ($\Omega_k \equiv 1 - \Omega_m - \Omega_\Lambda \neq 0$) in [7]. Its accuracy in the parameter ranges which we consider is better then 5%.

The theoretical values of the other experimental constraints are calculated as described in [18]. There one can also find tests of the method.

2. RESULTS AND DISCUSSION

The determination of the parameters Ω_m, Ω_Λ, Ω_ν, N_ν, Ω_b, h, n_s and b_{cl} by the Levenberg-Marquardt χ^2 minimization method can be realized in the following way: we vary the set of parameters Ω_m, Ω_Λ, Ω_ν, Ω_b, h, n_s and b_{cl} with fixed N_ν and find the minimum of χ^2. Since N_ν is discrete we repeat this procedure three times for

N_ν=1, 2, and 3. The lowest of the three minima is the minimum of χ^2 for the complete set of free parameters. Hence, we have seven free parameters. The formal number of observational points is 25 but, as it was shown in [18], the 13 points of the cluster power spectrum can be described by just 3 degrees of freedom, so that the maximal number of truly independent measurements is 15. Therefore, the number of degrees of freedom for our search procedure is $N_F = N_{\rm exp} - N_{\rm par} = 8$ if all observational points are used. In order to investigate to what extent the LSS constraints on fundamental parameters match the constraints implied by SNIa [20] we have determined all 8 parameters without (i) and with (ii) the SNIa constraint. In the case without LSS constraints (iii) the number of residual experimental points equals with number of free parameters[1] ($N_F = 0$). The results are presented in Table 1. Note that for all models χ^2_{min} is in the range $N_F - \sqrt{2N_F} \le \chi^2_{\rm min} \le N_F + \sqrt{2N_F}$

Table 1: Cosmological parameters determined from the different set of observational data: (i) – LSS, $\tilde{\ell}_p$, $\tilde{A}_p$, $\tilde{h}$, $\widetilde{\Omega_b h^2}$, (ii) – LSS, $\tilde{\ell}_p$, $\tilde{A}_p$, $\tilde{h}$, $\widetilde{\Omega_b h^2}$, SNIa constraint, (iii) – $\tilde{\ell}_p$, $\tilde{A}_p$, $\tilde{h}$, $\widetilde{\Omega_b h^2}$, SNIa constraint

Data set	χ^2_{min}/N_F	Ω_m	Ω_Λ	Ω_ν	Ω_b	n_s	h	b_{cl}
(i)	5.90/7	$0.37^{+0.25}_{-0.15}$	$0.69^{+0.15}_{-0.20}$	$0.03^{+0.07}_{-0.03}$	$0.037^{+0.033}_{-0.018}$	$1.02^{+0.09}_{-0.10}$	$0.71^{+0.22}_{-0.19}$	$2.4^{+0.7}_{-0.6}$
(ii)	6.02/8	$0.32^{+0.20}_{-0.11}$	$0.75^{+0.10}_{-0.19}$	$0.0^{+0.09}_{-0.0}$	$0.038^{+0.033}_{-0.019}$	$1.00^{+0.13}_{-0.10}$	$0.70^{+0.28}_{-0.18}$	$2.2^{+0.8}_{-0.5}$
(iii)	0/0	0.33±0.07	0.77±0.08	–	0.045±0.014	0.96±0.06	0.65±0.1	–

which is expected for a Gaussian distribution of N_F degrees of freedom. This means that the cosmological paradigm which has been assumed is in agreement with the data. Including the MAXIMA–1 [13] data into the determination of the first acoustic peak does not change the results essentially (see [7]). The errors in the best-fit parameters presented in Table 1 for cases (i) and (ii) are obtained by maximizing the (Gaussian) 68% confidence contours over all other parameters, the errors for the case (iii) are the square roots of the diagonal elements of the covariance matrix.

The model with one sort of massive neutrinos provides the best fit to the data, $\chi^2_{min} = 5.9$. However, there is only a marginal difference in χ^2_{min} for $N_\nu = 1, 2, 3$. With the given accuracy of the data we cannot conclude whether massive neutrinos are present at all, and if yes what number of degrees of freedom is favored. We summarize that the considered observational data on LSS of the Universe can be explained by a ΛMDM inflationary model with a scale invariant spectrum of scalar perturbations and small positive curvature.

Including of the SNIa constraint into the experimental data set decreases Ω_m, increases Ω_Λ slightly and prefers $\Omega_\nu \approx 0$, a ΛCDM model. Excluding the LSS constraints (items 2–8 in Sect. 2) does not significantly change the best-fit values (of those parameters which are determined), which demonstrates nicely the concordance of different experimental data sets and their theoretical interpretation.

In the cases (i) and (ii), the calculated characteristics of the LSS are within the 1σ error bars of the observed values. The predicted age of the Universe agrees well with recent determinations of the age of globular clusters.

Comparing the results obtained without and with the SNIa constraint, we conclude that the values of the fundamental cosmological parameters Ω_m, Ω_Λ and Ω_k determined by the observations of large scale structure match the SNIa test very well. This can be interpreted as independent support of the SNIa result in the framework of the standard cosmological paradigm. However, in order to elucidate how LSS data constraint cosmological parameters, we analyze further only the model obtained without the SNIa constraint.

The best fit values of cosmological parameters determined by LSS characteristics are presented in the 1-st row of Table 1. The best-fit CDM density parameter is $\Omega_{cdm} = 0.30$ and $\Omega_k = -0.06$, slightly positive curvature.

The value of the Hubble constant is close to the result by [16] and [17]. The spectral index coincides with the prediction of the simplest inflationary scenario, it is close to unity. The neutrino matter density $\Omega_\nu = 0.03$ corresponds to a neutrino mass of $m_\nu = 94\Omega_\nu h^2 \approx 1.4$ eV but is compatible with 0 within 1σ. So, ΛCDM model ($\Omega_\nu = 0$) is within the 1σ contour of the best-fit ΛMDM model. The estimated cluster bias parameter $b_{cl} = 2.4$ fixes the amplitude of the Abell–ACO power spectrum.

The errors shown in Table 1 (i) define the range of each parameter within which by adjusting the remaining parameters a value of $\chi^2_{min} \le 11.8$ can be achieved. Of course, the values of the remaining parameters always

[1] Ω_ν and b_{cl} are not determined in this case.

lay within their corresponding 68% likelihoods given in Table 1. Models with vanishing Λ are outside of this marginalized 1σ range of the best-fit model determined by the LSS observational characteristics used here even without the SNIa constraint. Indeed, if we set $\Omega_\Lambda = 0$ as fixed parameter and determine the remaining parameters in the usual way, the minimal value of χ^2 is $\chi^2 \approx 24$ with the following values for the other parameters: $\Omega_m = 1.15$, $\Omega_\nu = 0.22$, $N_\nu = 3$, $\Omega_b = 0.087$, $n_s = 0.95$, $h = 0.47$, $b_{cl} = 3.7$ ($\sigma_8 = 0.60$). This model is outside the 2σ confidence contour of the best-fit model (i). The experimental data which disagree most with $\Lambda = 0$ are the data on the first acoustic peak. If we exclude it from the experimental data set, $\chi^2_{min} \approx 5.8$ for an open model with the following best-fit parameters: $\Omega_m = 0.48$, $\Omega_\nu = 0.12$, $N_\nu = 1$, $\Omega_b = 0.047$, $n_s = 1.3$, $h = 0.64$, $b_{cl} = 2.5$ ($\sigma_8 = 0.82$). This model is within the 1σ confidence contour of the best-fit ΛMDM model obtained without data on the first acoustic peak. The reason for this behavior is clear: the position of the "kink" in the matter power spectrum at large scales demands a "shape parameter" $\Gamma = \Omega_m h^2 \sim 0.25$ which can be achieved either by choosing an open model or allowing for a cosmological constant. The position of the acoustic peak which demands an approximately flat model then closes the first possibility.

Results change only slightly if instead of the Boomerang data we use Boomerang+MAXIMA–1. Hence, we can conclude that the LSS observational characteristics together with the Boomerang (+MAXIMA–1) data on the first acoustic peak already rule out zero-Λ models at more than 95% C. L. and actually demand a cosmological constant in the same bulk part as direct measurements. We consider this a non-trivial consistency check!

Flat Λ models in contrary, are inside the 1σ contour of our best-fit model. Actually, the best fit flat model has $\chi^2_{min} \approx 8.3$ and the best fit parameters $\Omega_m = 0.35 \pm 0.05$, $\Omega_\Lambda = 0.65 \mp 0.05$, $\Omega_\nu = 0.04 \pm 0.02$, $N_\nu = 1$, $\Omega_b = 0.029 \pm 0.005$, $n_s = 1.04 \pm 0.06$, $h = 0.81 \pm 0.06$, $b_{cl} = 2.2 \pm 0.2$ ($\sigma_8 = 0.96$) are close to our previous [18] results with a somewhat different observational data set. It is obvious that flat zero-Λ CDM and MDM models are ruled out by the present experimental data set at even higher confidence limit than by data without the Boomerang and MAXIMA–1 measurements in [18].[2]

3. CONCLUSIONS

The main observational characteristics on LSS together with recent data on the amplitude and location of the first acoustic peak in the CMB power spectrum, and the amplitude of the primordial power spectrum inferred by the COBE DMR four year data prefer a ΛMDM model with the following parameters: $\Omega_m = 0.37^{+0.25}_{-0.15}$, $\Omega_\Lambda = 0.69^{+0.15}_{-0.20}$, $\Omega_\nu = 0.03^{+0.07}_{-0.03}$, $N_\nu = 1$, $\Omega_b = 0.037^{+0.033}_{-0.018}$, $n_s = 1.02^{+0.09}_{-0.10}$, $h = 0.71^{+0.22}_{-0.19}$, $b_{cl} = 2.4^{+0.7}_{-0.7}$ (1σ marginalized ranges).

The central values correspond to a slightly closed ($\Omega_k = -0.06$) ΛMDM model with one sort of 1.4 eV neutrinos. These neutrinos make up about 8% of the clustered matter, baryons are 10% and the rest (82%) is in a cold dark matter component. The energy density of clustered matter corresponds to only 35% of the total energy density of matter plus vacuum which amounts to $\Omega = 1.06$.

The values for the matter density Ω_m and the cosmological constant Ω_Λ for the best-fit model are close to those deduced from the SNIa test. Including this test in the observational data set, results to a somewhat larger value of Ω_Λ (7%) and slightly lowers Ω_m.

The observational characteristics of large scale structure together with the Boomerang (+MAXIMA–1) data on the first acoustic peak rule out zero-Λ models at more than 2σ confidence limit.

REFERENCES

[1] *Bahcall N. A., Fan X.* The most massive distant clusters: determining Ω and σ_8 // Astrophys. J.–1998.–**504**.–P. 1–6.

[2] *Bennett C. L., et al.* Four-Year COBE DMR Cosmic Microwave Background Observations: Maps and Basic Results // Astrophys. J.–1996.–**464**.–P. L1.

[3] *de Bernardis P., et al.* A flat Universe from high-resolution maps of the cosmic microwave background radiation // Nature.–2000.–**404**.–P. 955.

[4] *Bunn E. F., White M.* Four-year COBE normalization and large-scale structure // Astrophys. J.–1997.–**480**.–P. 6–11.

[5] *Burles S., Nollett K. M., Truran J. N., Turner M. S.* Sharpening the predictions of big-bang nucleosynthesis // Phys. Rev. Lett.–1999.–**82**.–P. 4176–4179.

[6] *Croft R. A. C., Weinberg D. H., Katz N., Hernquist L.* Recovery of the Power Spectrum of Mass Fluctuations from Observations of the Ly-alpha Forest // Astrophys. J.–1998.–**495**.–P. 44–62.

[2] The more detailed comparison of results presented here with other parameter estimations one can find in the accompanying journal paper [7].

[7] *Durrer R., Novosyadlyj B.* Cosmological parameters from complementary observations of the Universe // 2000.–astro-ph/0009057.

[8] *Efstathiou G., Bond J. R.* Cosmic confusion: degeneracies among cosmological parameters derived from measurement of microwave background anisotropies // Mon. Notic. Roy. Astron. Soc.–1999.–**304**.–P. 75–97.

[9] *Eisenstein D. J., Hu W.* Power Spectra for Cold Dark matter and its Variants // Astrophys. J.–1999.–**511**.–P. 5–15.

[10] *Girardi M., Borgani S., Giuricin G., Mardirossian F. and Mezzetti M.* The Observational Mass Function of Nearby Galaxy Clusters // Astrophys. J.–1998.–**506**.–P. 45–52.

[11] *Gnedin N. Y.* Probing the Universe with the Ly-alpha forest – II. The column density distribution // Mon. Notic. Roy. Astron. Soc.–1998.–**299**.–P. 392–402.

[12] *Gnedin N. Y.* // 2000.–private communication.

[13] *Hanany, S. et al.* MAXIMA–1: A measurement of the cosmic microwave background anisotropy on angular scales of $10'$ to 5° // 2000.–astro-ph/0005123.

[14] *Kolatt T., Dekel A.* Large-Scale Power Spectrum from Peculiar Velocities // Astrophys. J.–1997.–**479**.–P. 592–605.

[15] *Liddle A. R., Lyth D. H., Viana P. T. P., White M.* Cold dark matter models with a cosmological constant // Mon. Notic. Roy. Astron. Soc.–1996.–**282**.–P. 281–290.

[16] *Madore B.F., et al.* The Hubble Space Telescope Key Project on the Extragalactic Distance Scale. XV. A Cepheid Distance to the Fornax Cluster and Its Implications // Astrophys. J.–1999.–**515**.–P. 29–41.

[17] *Mould J.R., et al.* The Hubble Space Telescope Key Project on the Extragalactic Distance Scale. XXVIII. Combining the Constraints on the Hubble Constant // Astrophys. J.–2000.–**529**.–P. 786–794.

[18] *Novosyadlyj B., Durrer R., Gottloeber S., et al.* Cosmological parameters from large scale structure observations // Astron. and Astrophys.–2000.–**356**.–P. 418–434 (astro-ph/9912511).

[19] *Perlmutter S., et al.* Discovery of a supernova explosion at half the age of the universe // Nature.–1998.–**391**.–P. 51.

[20] *Perlmutter S., et al.* Measurements of Omega and Lambda from 42 High-Redshift Supernovae // Astrophys. J.–1999.–**517**.–P. 565–586.

[21] *Retzlaff J., Borgani S., Gottlober S., et al.* Constraining cosmological models with cluster power spectra // New Astronomy.–1998.–**3**.–P. 631–646.

[22] *Ricotti M., Gnedin N. Y., Shull J. M.* The Evolution of the Effective Equation of State of the Intergalactic Medium // Astrophys. J.–2000.–**534**.–P. 41–56 (astro-ph/9906413).

[23] *Riess A., et al.* Observational Evidence from Supernovae for an Accelerating Universe and a Cosmological Constant // Astron. J.–1998.–**116**.–P. 1009–1038.

[24] *Tammann G. A., Federspiel M.* Focussing in on H_0 // The Extragalactic Distance Scale / Eds M. Livio, M. Donahue, N. Panagia.–Cambridge: Cambridge Univ. Press, 1997.

[25] *Viana P. T. P., Liddle A. W.* Galaxy clusters at $0.3 < z < 0.4$ and the value of Omega // Mon. Notic. Roy. Astron. Soc.–1999.–**303**.–P. 535–545.

THE SUBCLUSTERING IN RICH AND POOR cD CLUSTERS OF GALAXIES

P. Flin and J. Krywult

Pedagogical University, Institute of Physics
ul. Konopnickiej 15, 25-406 Kielce, Poland
e-mail: sfflin@cyf-kr.edu.pl, krywult@pu.kielce.pl

The wavelet analysis of 40 rich and poor galaxy clusters having supergiant cD galaxy shows that the frequency of occurrence of substructure in both type of structure is the same.

INTRODUCTION

The investigation of substructures in galaxy clusters can be useful for study the origin and evolution of large – scale structure. Galaxy clusters are systems in which dynamic play an important role. It is interesting to check the difference between structures containing cD galaxy, which are embedded into rich and poor environments in order to see if the richness of environment, this is the number of galaxies in the vicinity of cD galaxy influences the subclustering properties of galaxy clusters.

Despite of the great progress in the determinations of galaxy redshifts, the 2-D data, this is when galaxy coordinates are available, can still be instrumental in achieving properties of subclustering and testing various theoretical considerations. In this paper we test the frequency of subclustering in poor and rich cD galaxy clusters.

OBSERVATIONAL DATA

There are different sources of our 2-D observational data, but all they came from automatic scans, when the personal bias is not existing.

Automatic scans of plates, taken with the 48-inch Palomar Schmidt Telescope, performed at The Royal Observatory, Edinburgh using COSMOS machine give data for 18 rich clusters [12]. From this paper we selected 12 galaxy clusters classified as cD cluster. The other 8 catalogues of nearby cD clusters were constructed from scans of plates, taken with the same telescope, performed in the Rome Observatory [16, 17, 8, 10].

We analysed galaxies within the magnitude range $m_3, m_3{+}3$, where m_3 is the magnitude of the third brightest galaxy. All galaxies situated within the circle outline from the centre with the radius 1.5 Mpc ($h = 0.75$) were regarded as cluster members.

The 23 poor galaxy clusters MKW/AWM were find by Morgan *et al.* [13] and Albert *et al.* [1]. The photometric data for 16 objects came from Yamagata [19]. This data were obtained scanning plates taken with 105 cm Schmidt telescope of the Kiso Observatory. When there are no data of poor clusters in Yamagata data, there were extracted from Digitised Sky Survey, which is also the result of plates from Palomar Sky Survey. The squares $1^\circ \times 1^\circ$ centred on the coordinates of the brightest galaxy, *i.e.*, D/cD galaxy, were selected. To the images in the region the FOCAS package was applied for object detection and star/galaxy separation.

The poor cluster data were analysed with magnitude limit $17\overset{m}{.}75$ and galaxy size cutoff ($A > 5$ arcmin). From the sample of 23 poor clusters, we analysed 20 objects, containing D/cD galaxy.

THE METHOD OF ANALYSIS

The existence of substructure in galaxy clusters has bee checked using the wavelet method [4]. The wavelet method is a convolution on a grid of 256×256 pixels between the signal $s(r, a)$ and an analyzing wavelet function $g(r, a)$. We use two-dimensional radial function called the Mexican Hat given by the formula:

$$g(r, a) = (2 - r^2/a^2)\exp(-r^2/2a^2), \tag{1}$$

where r is the distance between the position of a galaxy and a point (x, y) where the wavelet coefficient is calculated and a is a scalelength for the wavelet. The set of the wavelet coefficients resulting from the convolution is given by:

$$w(r, a) = g(r, a) \otimes s(r). \tag{2}$$

Each point in the grid has the corresponding wavelet coefficient connected with it. The usage of different scales a allows one to detect structure having the size comparable to particular value of a. In order to ensure the correct sampling for Mexican Hat we use the scalelength a differentiating one from another with the factor $\sqrt{2}$ [3].

The scales increased from $a = 8$ pixels, through 11, 16, 22, 32, 45 till 64 pixels, which corresponds to the linear scale at the cluster distance in kpc: 125, 172, 250, 344, 500, 703 and 1000 assuming $H_0 = 75$ km/(s Mpc).

The statistical significance of detected substructures, having at least 4 objects, were calibrated using Monte Carlo simulations. The number of points in the simulation is equal to the number of galaxies in real sample. The radial coordinate of points were the same as in the investigated sample, while the angular coordinates were random ones. The reality of substructure was accepted when the probability that it is due the random fluctuation is smaller than 0.001.

For each cluster and each scalelength of the wavelet 1000 simulations were made.

The procedure allows us to detect structures in the field of galaxy cluster studied here, as well as to perform [5] the classification of structures into three types, namely: unimodal, bimodal and complex.

Table 1: Data

Cluster	z	N	a	morph. type
A85	0.0518	643	64	U
A133	0.0604	470	45	B
A151	0.0526	226	32	S
A261	0.0467	519	64	U
A279	0.0797	515	64	U
A496	0.0320	604	45	S
A505	0.0543	244	16	S
A644	0.0704	1376	64	U
A655	0.1245	49	64	U
A754	0.0528	329	16	S
A1413	0.1427	318	16	B
A1650	0.0845	738	16	S
A1651	0.0825	1140	32	S
A1837	0.0376	734	22	S
A2052	0.0348	346	16	S
A2124	0.0654	66	16	S
A2175	0.0978	76	64	U
A2199	0.0303	368	11	S
A2597	0.0852	74	64	U
A2670	0.0745	836	64	U
MKW1	0.0202	51	64	U
MKW2	0.0299	77	11	S
MKW4	0.0196	40	16	S
MKW5	0.0290	62	22	S
MKW6	0.0545	172	64	U
MKW7	0.0289	124	16	S
MKW8	0.0265	68	64	U
MKW9	0.0382	328	11	S
MKW11	0.0224	77	64	U
MKW1s	0.0165	73	11	S
MKW2s	0.0381	69	64	U
MKW3s	0.0453	194	64	U
MKW4s	0.0271	62	64	U
AWM1	0.0272	33	64	U
AWM2	0.0219	50	22	S
AWM3	0.0290	136	64	U
AWM4	0.0338	145	32	B
AWM5	0.0384	142	64	U
AWM6	0.0356	105	8	S
AWM7	0.0290	291	64	U

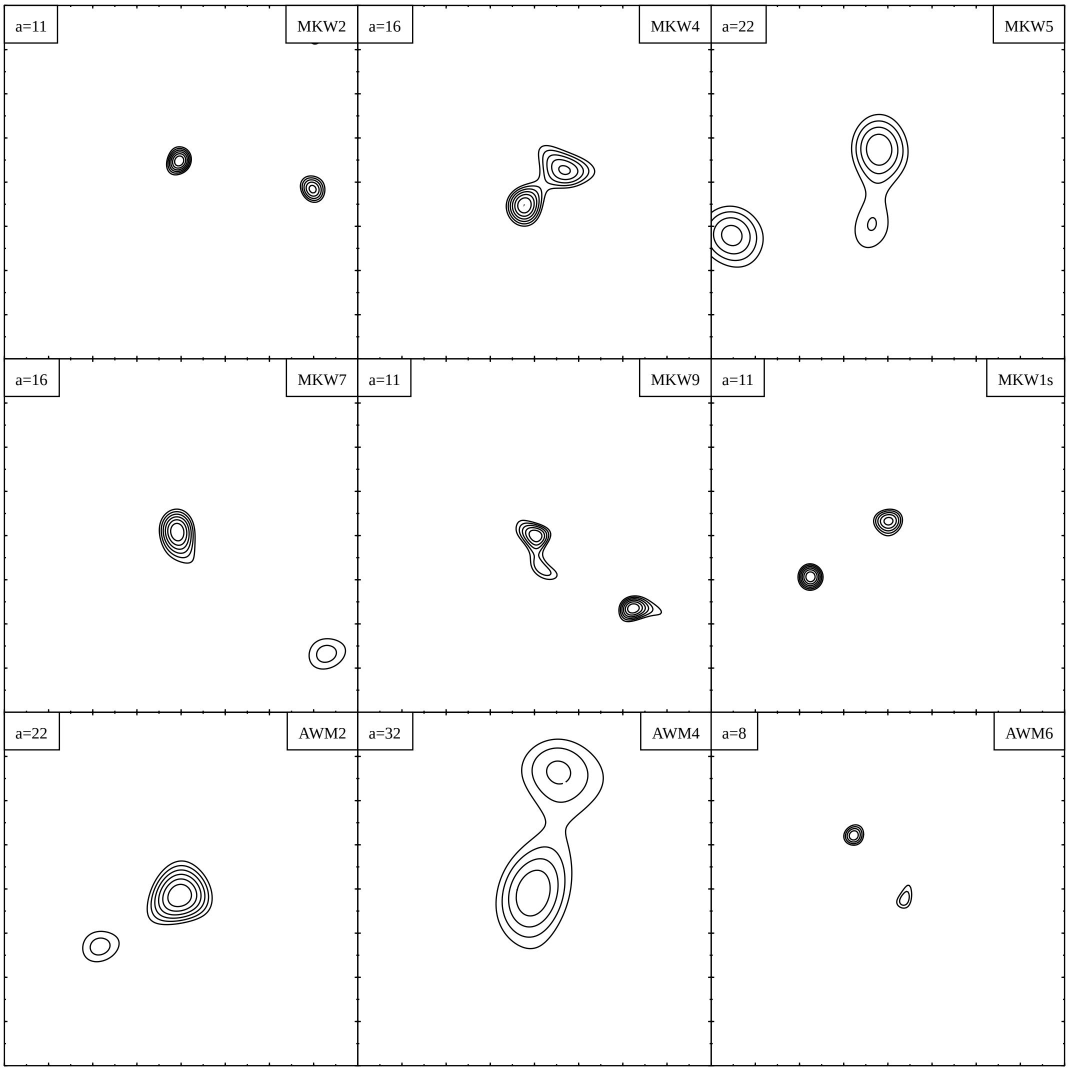

Figure 1: Structures of the investigated poor clusters. The right corner contains the cluster designation, the left one the scalelenght at which significant substructure is observed

RESULT

The result of our analysis is given in Table 1. The first column of Table 1 presents the cluster name, the second the redshift of the cluster z taken from literature, the next one gives the the total number of galaxies N in the field, while the fourth column shows the scalelength a corresponding to the size of detected structure. The last column displays the morphology of the cluster, when letters: U, B and S denote unimodal, bimodal and complex structure of a cluster, respectively. The number of galaxies within structure is smaller than the total number N.

Fig. 1 presents some structures of the investigated poor clusters.

The wavelet analysis allows us to find substructures (in various scalelength a) in 12 objects. This means that the frequency of subclustering in the sample is $12/20 = 0.60$.

The subclustering in 20 MKW/AWM poor clusters containing D/cD galaxy, when checked applying the wavelet analysis too, occurred in the case of 9 structures, which gave the frequency of subclustering $9/20 = 0.45$. The χ^2-test shows that the frequency of subclustering in rich and poor clusters is the same at the significance level $\alpha = 0.001$.

The comparison of Abell clusters with other data for the sample of 12 objects has been performed [12], showing that the change of the morphology type of cluster structure do not influence the estimated frequency of subclustering. The same conclusion is also valid when remaining Abell clusters are compared with other data.

Subclustering in MKW/AWM clusters, based on Yamagata data too, has been checked using adaptive kernel method supplemented by galaxy redshifts for selected galaxies [2]. Beside the discrepancy in the existence of non-existence or substructures in individual cases, the estimations of frequency of occurence of subclustering, as determined from Beers *et al.* [2] is quite comparable with ours, this is 46%.

CONCLUSION

Our statistical analysis is based on 20 Abell clusters of galaxies and 20 poor clusters. The data were derived from automatic scans, which procedure ensured their objectivity.

The wavelet analysis, regarded as very sensitive tool for study the structure properties, applied to poor and rich cluster, yields the lack of difference in substructure occurrence in this two set of data.

If the light traces matter in the same manner in both types of structures, the result shows the same dynamical interaction of objects in poor and rich clusters. This is consistent with the same type of alignment of the dominant brightest cluster galaxies in both rich and poor clusters [7, 9, 15, 11]. This mean that process leading to the formation of D/cD galaxy are independent of the cluster richness.

Acknowledgements. This work was partially supported by grant KBN/IBMSP/WSP/Kielce/073.

REFERENCES

[1] *Albert C. E., White R. A., Morgan W. W.* // Astrophys. J.–1978.–**211**.–P. 309.

[2] *Beers T. C., Kriessler J. R., Bird C. M., Huchra J. P.* // Astron. J.–1995.–**109**.–P. 874.

[3] *Daubechies I.* // IEEE Trans. Inform. Theory.–1990.–**36**.–P. 961.

[4] *Escalera E., Mazure A.* // Astrophys. J.–1992.–**388**.–P. 23.

[5] *Escalera E., Biviano A., Girardi M., et al.* // Astron. J.–1994.–**423**.–P. 539.

[6] *Flin P., Krywult J.* // Clustering at High Redshift: ASP Conf. Ser. 200 / Eds A. Mazure, O. Le Fevre, V. Le Brun.–2000.–P. 406.

[7] *Flin P., Olowin R. P.* // Physical Cosmology Editions Frontieres Gif-sur-Yvette / Eds A. Blanchard, L. Celniker, M. Lachieze-Rey, J. Tran Thanh Van.–1991.–P. 512.

[8] *Flin P., Trevese D., Cirimele G., Hickson P.* // Astron. and Astrophys. Suppl. Ser.–1995.–**110**.–P. 313.

[9] *Flin P., Trevese D., Krywult J., Cirimele G.* // Astrophys. Lett. Comm.–1997.–**36**.–P. 119.

[10] *Flin P., Krywult J., Trevese D., et aL.* // Astron. and Astrophys. Suppl. Ser.–2000.–in press.

[11] *Fuller T. M., West M. J., Bridges T. J.* // Astrophys. J.–1999.–**519**.–P. 22.

[12] *Krywult J., MacGillivray H. T., Flin P.* // Astron. and Astrophys.–1999.–**351**.–P. 883.

[13] *Morgan W. W., Kayser S., White R. A.* // Astrophys. J.–1975.–**199**.–P. 545.

[14] *Struble M. F., Rood H. J.* // Astrophys. J. Suppl. Ser.–1987.–**63**.–P. 555.

[15] *Trevese D., Cirimele G., Flin P.* // Astron. J.–1992.–**104**.–P. 935.

[16] *Trevese D., Flin P., Migliori L., et al.* // Astron. and Astrophys. Suppl. Ser.–1992.–**94**.–P. 327.

[17] *Trevese D., Cirimele G., Cenci A., et al.* // Astron. and Astrophys. Suppl. Ser.–1997.–**125**.–P. 459.

[18] *West M. J., Oemler A., Dekel A.* // Astrophys. J.–1988.–**327**.–P. 1.

[19] *Yamagata T.* // Tokyo Obs. Ann. 2nd Ser. 21.–1986.–P. 31.

WAVELET ANALYSIS AS APPROACH TO RECOGNIZE ABUNDANCE ZONE IN GALAXY DISTRIBUTION

I. B. Vavilova

[1] *Astronomical Observatory, Taras Shevchenko National University*
3 Observatorna St., Kyiv, 04053 Ukraine
e-mail: `vavilova@rcrm.freenet.kiev.ua`

The algorithm to recognize an abundance zone in galaxy distribution is proposed. The method used is the 3–D wavelet analysis which allows to construct a "tree" of wavelet coefficients keeping information about the distribution of galaxies in zones surrounding an abundance zone. These coefficients are to be used for prediction of galaxy distribution in an abundance zone.

Use of the wavelet analysis for detachment of the large-scale galaxy distribution and galaxy cluster structure has such advantages, which allows to apply it for recognition and prediction of galaxy distribution in "non-visible" zones for observations, *i.e.*, abundance zone. To check this idea, it is proposed to apply the reversed wavelet analysis to the complete samples of galaxies surrounding an abundance zone.

The algorithm is as follows.

1) Data: using various catalogues (in first turn, catalogues of galaxies visible in IR) to compile 3–D samples of galaxies surrounding an abundance zone;

2) Samples: using these samples to compile samples of galaxies with limit stellar magnitude (up to 14^m, 15^m, ..., 24^m);

3) Completeness: to apply tests for completeness for each of these samples;

4) Wavelet coefficients: to search a set of wavelet coefficients for each of these samples;

5) Test: to test for a web of wavelet coefficients to be corrected for each of subsequent (by stellar magnitude) sample;

6) "Tree" of wavelet coefficients: to form a real "tree" of wavelet coefficients;

7) "Visible" galaxy distribution: applying a set of wavelet coefficients to testify actual galaxy distribution (a real "tree" of wavelet coefficients should reproduce 3–D distribution of galaxies involved in processing);

8) Abundance zone: applying a final set of wavelet coefficients to predict galaxy distribution in "non-visible" zone.

The work is in progress.

MAGNETIC FIELDS OF NEUTRON STARS: OBSERVATIONS AND MODELS

G. S. Bisnovatyi-Kogan

Space Research Institute of Russian Academy of Sciences
84/32 Profsoyuznaya St., 117810 Moscow, Russia
e-mail: gkogan@mx.iki.rssi.ru

Estimations of magnetic fields of neutron stars, observed as radio and X-ray pulsars, are discussed. It is shown that theoretical and observational values for different types of radiopulsars are in good correspondence. Magnetic fields of X-ray pulsars are estimated from the cyclotron line energy. In the case of Her X-1 this estimation exceeds considerably the value of its magnetic field obtained from long term observational data related to the beam structure evolution. Another interpretation of the cyclotron feature, based on the relativistic dipole radiation mechanism, could remove this discrepancy. Observational data about soft gamma repeaters and their interpretation as magnetars are critically analyzed.

INTRODUCTION

First theoretical estimations of neutron star magnetic fields have been done from the condition of the magnetic flux conservation during contraction of a normal star to a neutron one [9]: $B_{ns} = B_s \left(\frac{R_s}{R_{ns}}\right)^2$. For the main sequence stellar magnetic field $B_s = 10 \div 100$ Gs, and the stellar radius $R_s = (3 \div 10)R_\odot \approx (2 \div 7)\times 10^{11}$ cm, we get $B_{ns} \approx 4\times 10^{11} \div 5\times 10^{13}$ Gs, for a neutron star radius $R_{ns} = 10^6$ cm. As shown below, this simple estimation occurs to be in a good correspondence with most observational data.

RADIO PULSARS

It is now commonly accepted that radio pulsars are rotating neutron stars with inclined magnetic axes. For rotating with angular velocity Ω dipole, the rotational energy losses [17, 29] are determined as $\dot{E} = AB^2\Omega^4$. The rotational energy is $E = \frac{1}{2}I\Omega^2$, I is the inertia momentum of a neutron star. By measuring of $P = 2\pi/\Omega$ and $\dot{P}$, we obtain the observational estimation of the neutron star magnetic field as

$$B^2 = \frac{IP\dot{P}}{4\pi^2 A}. \tag{1}$$

It was shown in [11] that energy losses by a pulsar relativistic wind are important also when the magnetic and rotational axes coincide, and one may use (1) with $A = \frac{R_{ns}^6}{6c^3}$, and B_{ns} corresponding to the magnetic pole, at any inclination angle. Magnetic fields of radio pulsars estimated using (1) with observational values of P and $\dot{P}$ lay in the wide range between 10^8 and 10^{13} Gs [21]. There are two distinctly different groups: single radiopulsars with periods exceeding 0.033 sec and magnetic fields between 10^{11} and 10^{13} Gs, and recycled pulsars (RP), present or former members of close binary systems with millisecond periods and low magnetic fields between 10^8 and 10^{10} Gs. Low magnetic field of recycled pulsars is probably a result of its damping during preceding accretion stage [6].

X-RAY BINARIES

There are several ways to estimate observationally the magnetic field of an X-ray pulsar. During accretion, matter is stopped by the magnetic field at the alfvenic surface, where gaseous and magnetic pressures are in balance. At stationary state, the Keplerian angular velocity of an accretion disk at the alfvenic surface is equal to the stellar angular velocity [30] $\Omega_K = \Omega_s = \Omega_A$. Otherwise a neutron star would be accelerated due to absorption of matter with large angular momentum, or decelerated due to throwing away matter with additional angular momentum [15] . X-ray pulsars may have spin-up and spin-down stages [2], but most of them show average spin-up, indicating that their angular velocity is less than the equilibrium one. This is observed in the best studied X-ray pulsar Hex X-1 [34, 7, 33]. Analysis of spin-up/down phenomena in the X-ray pulsars indicate important role of the mass loss [19], and to stochastic origin of spin-up/down transitions [20].

For a given luminosity $L_{36} = L/(10^{36}\,\mathrm{erg/s})$ and dipole magnetic field at the stellar equator $B_{12} = B/(10^{12}\,\mathrm{Gs})$, we get the following value of the equilibrium period [18] for the neutron star mass $M_s = 1.4\,M_\odot$

$$P_{eq} \approx 2.6\,B_{12}^{6/7}\,L_{36}^{3/7}\ \mathrm{s}. \tag{2}$$

For Her X-1 parameters $L_{36} = 10$, $P = 1.24$ s, we get a magnetic field corresponding to the equilibrium rotation $B_{12}^{eq} = 0.9$. Taking into account the average spin-up of the pulsar in Her X-1, we may consider this value as an upper limit of its magnetic field. Even more rough estimations of the magnetic field in X-ray pulsars follow from the average spin-up rate under condition $\dot{J}_{rot} = \dot{M}\,\Omega_A$, or restrictions on the polar magnetic field value following from the observed beam structure and a condition of local luminosity not exceeding the critical Eddington one. These conditions lead to smaller values of the magnetic field of Her X-1 on the level $10^9 - 10^{10}$ Gs [4].

Observations of low mass X-ray binaries (LMXB) point to very low values of their magnetic fields due to absence of X-ray pulsar phenomena. Modulation of the X-ray flux allowed to reveal the rotational period of the neutron star in the LMXB SAX J1808.4-3658 corresponding to the frequency 401 Hz, due to RXTE observations (see review [37]). This observations fill a gap and form a long-awaited link between LBXB and recycled millisecond pulsars [31], as neutron stars with very low magnetic field (up to 10^8 Gs).

The most reliable estimation of the magnetic field of the X-pulsar Her X-1 comes from detailed observations of the beam variation in this pulsar on different stages, made on the satellites ASTRON [34], GINGA and RXTE [7, 33]. This pulsar, in addition to 1.24 s period of the neutron star rotation, is in a binary system with an orbital period 1.7 days, and shows a 35 day cycle, where during only 12 days its luminosity is high. During other 23 days its X-ray luminosity strongly decreases, but small changes in the optical luminosity and remaining strong reflection effect indicate that the X-ray luminosity remains almost the same during all 35 day cycle. A visible decrease of the X-ray flux is due to an occultation phenomena. The model which explains satisfactory the phenomenon of the 35 day cycle is based on the precession of the accretion disc with the 35 day period, and occultation of the X-ray beam during 23 days. Analysis of the beam structure during high and low X-ray states leads to the conclusion that during the low state we observe not the direct X-ray flux from the neutron star, but the flux, reflected from the inner edge of the accretion disc. This conclusion is based on the 180 deg phase shift between the X-ray beams in high and low states. In order to observe the X-ray flux reflected from the inner edge, situated near the Alfven radius of the accretion disc, it cannot be very far away from the neutron star. The estimations give an upper limit to the ratio of the Alfven and stellar radii $\dfrac{r_A}{r_s} \leq 20$. The schematic picture of the accretion disc and its inner edge orientation around the neutron star at different stages of the 35 day cycle is shown in Fig. 1, taken from [34]. As was indicated above, the value of the Alfven radius is determined by the neutron star mass ($M_s = 1.4\,M_s$), mass flux $\dot{M} = 3\times10^{16}$ g/s, corresponding to the luminosity $L = 10^{37}$ erg/s, and the value of the magnetic field. Taking dipole radial dependence of the magnetic field $B = B_s(r_s/r)^3$, and the neutron star radius $r_s = 10^6$ cm, we obtain the ratio in the form $r_A/r_s \approx 300 B_{12}^{4/7}$. To have this ratio not exceeding 20 we get an inequality $B \leq 3\times10^{10}$ Gs.

The feature in the spectrum of Her X-1 at energies between 50 and 60 KeV was found in [36]. Its interpreting as a cyclotron line feature according to $E_X = \frac{\hbar e B}{m_e c}$ leads to the value of the magnetic field $B_{cycl} = (5-6)\times10^{12}$ Gs that is much higher than any other above mentioned estimations. Spectral features were observed also in other X-ray sources. Recent observations on RXTE [13], and Beppo-SAX [32] of the pulsating transient 4U 0115+63 have shown a presence of 3 and 4 cyclotron harmonics features, corresponding to the magnetic field strength of 1.3×10^{12} Gs. A comparison of the shapes of the beam in cyclotron harmonics may be used for testing the nature of these features. Cyclotron features have been observed in several X-ray sources [27], and they always have corresponded to large values of magnetic fields $B_{cycl} > 10^{12}$ Gs. Such a situation is not in good accordance with a well established observational fact, that all recycled pulsars, going through a stage of an X-ray source, have much smaller magnetic fields, usually not exceeding 10^{10} Gs. Particularly, for the Her X-1 the value of its magnetic field, following from the cyclotron interpretation of the spectral feature, is in contradiction with all other observations, including the most reliable, based on the beam shape variability during 35 day cycle.

RELATIVISTIC DIPOLE INTERPRETATION OF THE SPECTRAL FEATURE IN HER X-1

It seems likely that this conflict is created by using the non-relativistic formula connecting cyclotron frequency with a value of the magnetic field. According to [5] , ultrarelativistic electrons with a temperature $\sim 10^{11} K$, may be formed in the non-collisional shock during accretion, emitting a relativistic dipole line. The mean energy of

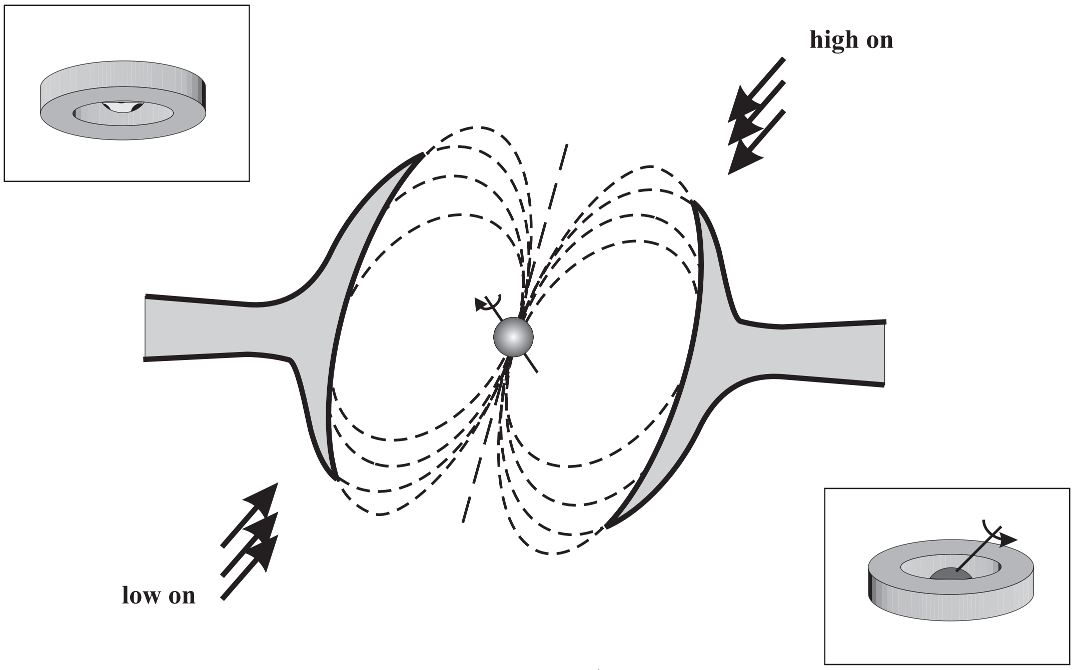

Figure 1: Configuration of the inner edge of the disk and the neutron star; neutron star and the disk in the "high-on" state (left top box), and in the "low-on" state (right bottom box)

this line is broadened and shifted relativistically, in comparison with the cyclotron line, by a factor of $\gamma \simeq \dfrac{kT}{mc^2}$. The spectrum profile of the relativistic dipole line is calculated in [1] for various electron distributions, where the model of the hot spot for Her X-1 is considered, and it is shown that the overall observed X-ray spectrum (from 0.2 to 120 KeV) can arise under the fields near 5×10^{10} Gs which are well below B_{cycl}, and are not in the conflict with other observations.

According to [10, 3], in the magnetic field near the pulsar the cross component of a momentum of electrons is emitting rapidly, while the parallel velocity remains constant. Hence, the momentum distribution of the electrons is anisotropic $p_\perp^2 \ll p_\parallel^2$, with $p_\perp \ll mc$, $p_\parallel \gg mc$. Assume for simplicity that the transverse electron distribution is two-dimensional Maxwellian $dn = \dfrac{N}{T_1}\exp\left(-\dfrac{mu^2}{2T_1}\right) d\dfrac{mu^2}{2}$, $T_1 \ll mc^2$.

In the relativistic dipole regime of radiation, the electron is non-relativistic in the coordinate system, connected with the Larmor circle. In the laboratory system, where the electron is moving with a velocity V, the angle between the magnetic field and electron momentum vectors is smaller than the angle of the emitting beam. At these conditions we may consider that the radiation is all emitted along the magnetic field with an intensity $J(0)$, at frequency ω_{md} [1]

$$J(0) = \frac{2Ne^4B^2T_1}{\pi c^5 m^3(1-\frac{V}{c})}, \qquad \omega_{md} = \omega_{cycl}\sqrt{\frac{1+\frac{V}{c}}{1-\frac{V}{c}}} \approx 2\omega_{cycl}\frac{E_\parallel}{m_e c^2}, \tag{3}$$

where $\omega_{cycl} = \dfrac{eB}{mc}$. That gives $1 - \dfrac{V}{c} = \dfrac{2\omega_{cycl}^2}{\omega^2}$. Let us consider the parallel momentum distribution of the electrons as: $dn = f(p_\parallel)\,dp_\parallel$. Substituting dn for N and using $p_\parallel = \dfrac{mc}{2}\dfrac{\omega}{\omega_{cycl}}$, we obtain for the spectral density

$$J_\omega = \frac{e^2T_1}{2\pi c^2\omega_{cycl}}\omega^2 f\left(\frac{mc}{2}\frac{\omega}{\omega_{cycl}}\right) d\omega. \tag{4}$$

Let us consider two cases. The first is the relativistic Maxwell distribution $f = \dfrac{n_0 c}{T_2}\exp\left(-\dfrac{p_\parallel c}{T_2}\right)$, where n_0 is

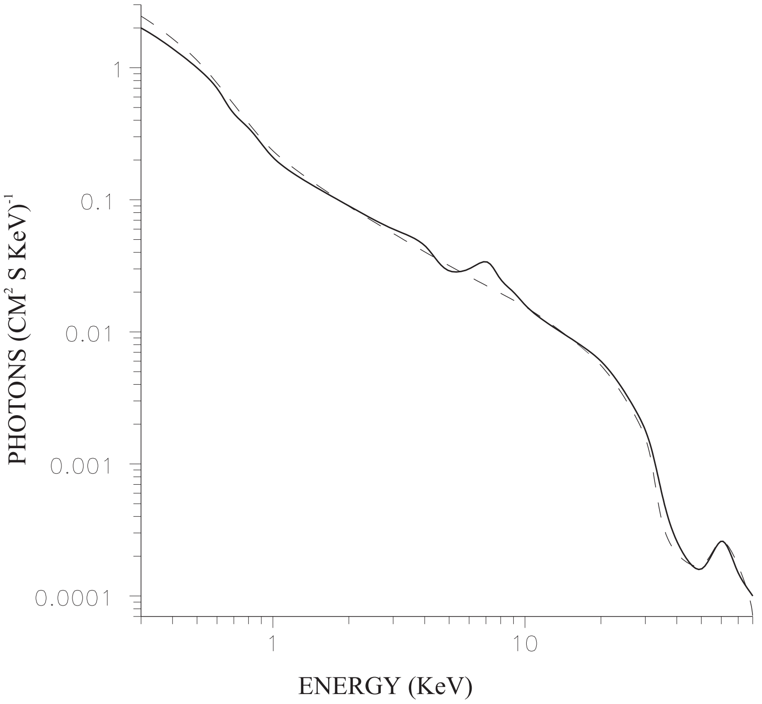

Figure 2: Comparison of the observational and computational X-ray spectra of Her X-1. The solid curve is the observational results taken from McCray *et al.* (1982), the dot curve is the approximation with $T_s = 0.9$ KeV, $T_e = 8$ KeV, $\tau_e = 14$, $a = 7\times10^{-4}\ \frac{\text{eV}\cdot\text{s}}{\text{cm}}$, $\sigma = 10^{-4}\ \frac{\text{eV}\cdot\text{s}}{\text{cm}}$, $B = 4\times10^{10}$ Gs

the number of emitting electrons. The spectrum is

$$J_\omega = \frac{n_0 e^2}{2\pi c\omega_{cycl}} \frac{T_1}{T_2} \omega^2 \exp\left(-\frac{mc^2\omega}{2\omega_{cycl}T_2}\right)\, d\omega. \tag{5}$$

It has a single maximum at $\dfrac{\omega}{\omega_{cycl}} = \dfrac{4T_2}{mc^2}$. In the second case $f = \dfrac{n_0}{\sqrt{\pi}\sigma}\exp\left[-\dfrac{(p_\| - a)^2}{\sigma^2}\right]$. The spectrum of radiation is

$$J_\omega = \frac{n_0 e^2 T_1}{2\pi^{3/2}c^2\omega_{cycl}\sqrt{\sigma}}\omega^2 \exp\left(-\frac{\left(\dfrac{mc}{2}\dfrac{\omega}{\omega_{cycl}} - a\right)^2}{\sigma^2}\right)\, d\omega. \tag{6}$$

When $\sigma \ll a$ this spectrum has a single maximum at $\omega \simeq \dfrac{2a}{mc}\omega_{cycl}$. The experimental spectra taken from [26, 25] have been approximated in [1]. The last spectrum (solid line) and its fitting (dashed line) are shown in Fig. 2. In accordance with [5] it was taken $a = 7\times10^{-4}\ \frac{\text{eV}\cdot\text{s}}{\text{cm}}$, corresponding to average electron energy $E_\| = ac \approx 20$ MeV. The best fit for the line shape was then obtained at the magnetic field strength $B = 4\times10^{10}$ Gs. In this model the beam of the "cyclotron" feature is determined by the number distribution of the emitting relativistic electrons, moving predominantly along the magnetic field, over the polar cap.

In order to obtain the whole experimental spectrum of the Her X-1 the following model of the hot spot (Fig. 3) was considered in [1]. A collisionless shock wave is generated in the accretion flow near the surface on the magnetic pole of a neutron star. In its front the ultrarelativistic electrons are generated. Under the shock there is a hot turbulent zone with the temperature T_e and the optical depth τ_e, situated over a heated spot with smaller temperature on the surface of the neutron star.

The whole X-ray spectrum of pulsar Her X-1 from [25] is represented in Fig. 3 by the solid line. There are three main regions in it: a quasi-Planckian spectrum between 0.3 and 0.6 KeV that is generated (re-radiated) near the magnetosphere of the X-ray pulsar; power-law spectrum $(0.6 \div 20)$ KeV with a rapid decrease at

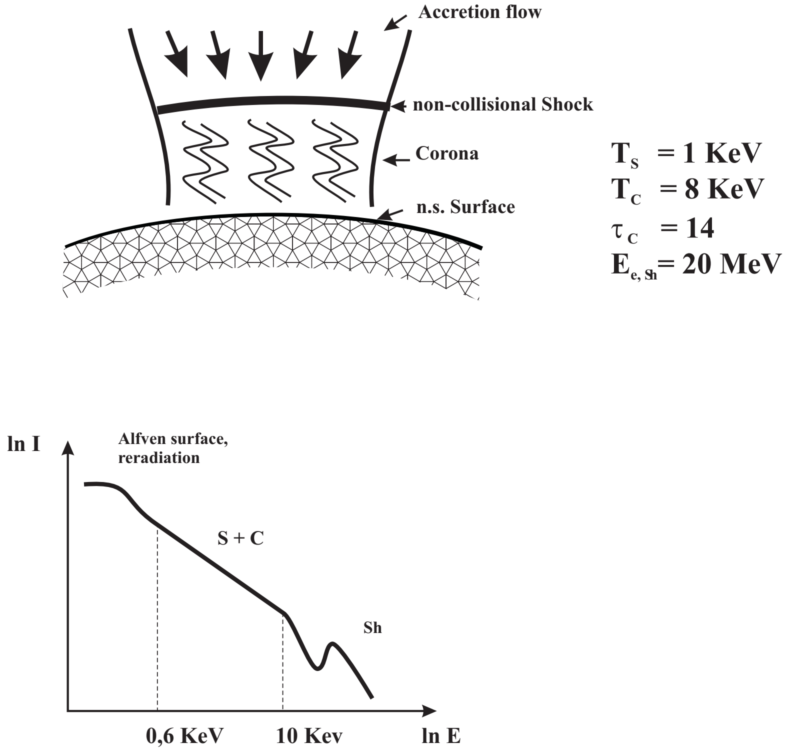

Figure 3: Schematic structure of the accretion column near the magnetic pole of the neutron star (top), and its radiation spectrum (bottom)

20 KeV, and the "cyclotron" feature. The power-law spectrum is a result of comptonization in the corona of a black-body spectrum emitted by the stellar surface. The comptonized spectrum has been calculated according to Sunyaev and Titarchuk (1980). Setting the neutron star radius equal to 10 km, distance to the X-ray pulsar 6 Kps, hot spot area $S = 2{\times}10^{12}$ cm^2, the best fit is found at $T_s = 1$ KeV, $T_e = 8$ KeV, $\tau_e = 14$, which is represented in Fig. 3 by the dashed line.

The observations of the variability of the "cyclotron" lines are reported in [27]. Ginga detected changes of the cyclotron energies in 4 pulsars. The change is as much as 40% in the case of 4U 0115+63. Larger luminosity of the source corresponds to smaller average energy of the cyclotron feature. These changes might be easily explained in our model. The velocity of the accretion flow decreases with increasing of the pulsar luminosity because locally the luminosity is close to the Eddington limit. As a result, the shock wave intensity drops as well as the energy of the ultrarelativistic electrons in its front, leading a decrease of the relativistic dipole line energy.

MAGNETARS

Among more than 2000 cosmic gamma ray bursts (GRB) 4 recurrent sources had been discovered, and were related to a separate class of GRB, called soft gamma repeaters (SGR). Besides observations of short, soft, faint recurrent bursts, three of them had given giant bursts, most powerful among all GRB. All four SGR are situated close or inside SNR, three of them show long periodic pulsations. These properties had separated SGR, situated in our or nearby galaxies, in a quite special class, very different from other GRB, which are believed to have a cosmological origin at red shifts $z \sim 1$. One SGR 1627-41 was discovered by BATSE [38] and three other were discovered in KONUS experiment in 1979 [23, 12]. Three of SGR show regular pulsations, and for two of them $\dot{P}$ were estimated, indicating to very high values of the magnetic fields, up to 10^{15} Gs, and small age of these objects [14, 16, 23, 24].

The physical connection between SGR and related SNR is not perfectly established: SNR ages are much larger than ages of SNR estimated by P and $\dot{P}$ measurements, and all four SGR are situated at the very edge of the corresponding SNR, or well outside them. Using the pulsar age estimation we come to conclusion of a very high speed of the neutron star at several thousands km/s, exceeding strongly all measured speeds of radiopulsars. Physical properties of the pulsars observed in SGR are very unusual. If the connection with SNR is real, and the distances to SGR are the same, then the pulsar luminosity during giant bursts is much larger than the critical Eddington luminosity. As follows from simple physical reasons, when the radiation force is much larger than the force of gravity, the matter would be expelled at large speed, forming strong outflow and dense envelope around the neutron star which could screen pulsations. No outflowing envelope around SGR have been found. The large difference between $\dot{E}_{rot}$ and average $L_x + L_\gamma$ luminosity needs to suggest a source of energy, much larger than the one coming from the rotational losses. It is suggested that in magnetars the energy comes from the magnetic field annihilation [8]. It is rather surprising to observe the field annihilation without formation of relativistic particles, where considerable part of the released energy should go. Radio emitting nebula should be formed around the SGR, but have not been found. So, it is not possible to exclude that there is no physical connection between SNR and SGR, that SGR are much closer objects, their pulsar luminosity is less than the Eddington one, and their magnetic fields are not so extremely high.

There is a striking similarity between SGR and special class of X-ray pulsars called anomalous X-ray pulsars (AXP). Both have periods in the interval 6–12 seconds, binarity was not found, spin-down of the pulsar corresponding to small age ~ 1000 years, observed irregularities in $\dot{P}$. The main difference is an absence of any visible bursts in AXP, characteristic for SGR. Suggestions have been made about their common origin as magnetars [16]. We may expect that the establishing of the nature of AXP would help strongly for the determination of the nature of SGR.

CONCLUSIONS. SOME QUESTIONS AND ANSWERS ABOUT MAGNETARS

1. Magnetic fields of radiopulsars are in good correspondence with theoretical estimations. **2**. RP and LMXB have small magnetic fields, which very probably were decreased by damping or screening during accretion stage. **3**. Contradiction between high B_{cycl} and other observational estimations of B in the LMXB Her X-1 may be removed in the model of relativistic dipole mechanism of the formation of a hard spectral feature by strongly anisotropic relativistic electrons, leading to conventional value of $B \approx 5\times10^{10}$ Gs. **4**. Very high magnetic fields in magnetar model of SGR needs further confirmation and investigation.

1. **Q**. Is it possible to observe an influence of a giant burst on the related SNR ? **A**. Maybe. Radio observations of SNR are needed with search for changes, wisps like in the Crab nebula.

2. **Q**. What could we see if SGR would be 10 times farther ? **A**. Ordinary short GRB.

3. **Q**. How many "SGR" we should have seen in neighboring galaxies (Andromeda) by their giant busts? **A**. ~ 10 in Andromeda. Better statistical estimation and search in BATSE/KONUS data are needed.

4. **Q**. Are short GRB identical with distant SGR? **A**. Maybe yes.

5. **Q**. How many SGR remnants should be in the Galaxy if SGR-SNR connection is real? **A**. About 10^8 neutron stars.

6. **Q**. Is it possible to provide γ-radiation by magnetic field annihilation without appearance of the large number of ultra-relativistic particles and strong nonthermal emission in other spectral bands? **A**. Solar flashes produced by field annihilation are characterized by very broad spectrum, from radio to gamma.

7. **Q**. Is it possible to use pulsar-like formula for age estimation of SGR and its magnetic field from P and $\dot{P}$ measurements, when $L_{tot} \gg \dot{E}_{rot}$? **A**. Probably not [22].

REFERENCES

[1] *Baushev A. N., Bisnovatyi-Kogan G. S.* // Astron. Reports.–1999.–**43**.–P. 241.

[2] *Bildsten L., et al.* // Astrophys. J. Suppl. Ser.–1997.–**113**.–P. 367.

[3] *Bisnovatyi-Kogan G. S.* // Astron. Zh.–1973.–**50**.–P. 902. (in Russian).

[4] *Bisnovatyi-Kogan G. S.* // Astron. Zh.–1974.–**51**.–P. 443. (in Russian).

[5] *Bisnovatyi-Kogan G. S., Fridman A. M.* // Astron. Zh.–1969.–**46**.–P. 721. (in Russian).

[6] *Bisnovatyi-Kogan G. S., Komberg B. V.* // Astron. Zh.–1974.–**51**.–P. 373. (in Russian).

[7] *Deeter J., Scott D. M., Boynton P., et al.* // Astrophys. J.–1998.–**502**.–P. 802.

[8] *Duncan R. C., Thompson C.* // Astrophys. J.–1992.–**392**.–P. L9.

[9] *Ginzburg V. L.* // Dokl. Akad. Sci. USSR.–1964.–**156**.–P. 43. (in Russian).

[10] *Gnedin Yu. N., Sunyaev R. A.* // Astron. and Astrophys.–1973.–**25**.–P. 233.

[11] *Goldreich P., Julian W.* // Astrophys. J.–1969.–**157**.–P. 869.

[12] *Golenetskii S. V., Il'inskii V. N., Mazets E. P.* // Nature.–1984.–**307**.–P. 41.

[13] *Heindl W. A., et al.* // Astrophys. J.–1999.–**521**.–P. L49.

[14] *Hurley K., Cline T., Mazets E., et al.* // Nature.–1999.–**397**.–P. 41.

[15] *Illarionov A. F., Sunyaev R. A.* // Astron. and Astrophys.–1975.–**39**.–P. 185.

[16] *Kouveliotou C., Strohmayer T., Hurley K., et al.* // Astrophys. J.–1999–**510**.–P. L115.

[17] *Landau L. D., Lifshitz E. M.* Teoriya Polya. (Field Theory).–Moscow: Nauka, 1962.

[18] *Lipunov V. M.* Astrophysics of Neutron Stars.–Germany: Springer, 1992.

[19] *Lovelace R. V. L, Romanova M. M., Bisnovatyi-Kogan G. S.* // Mon. Notic. Roy. Astron. Soc.–1995.–**275**.–P. 244.

[20] *Lovelace R. V. L, Romanova M. M., Bisnovatyi-Kogan G. S.* // Astrophys. J.–1999.–**514**.–P. 368.

[21] *Lyne A. G., Graham-Smith F.* Pulsar Astronomy.–Cambridge: Cambridge Univ. Press, 1998.

[22] *Marsden D., Rothschild R. E., Lingenfelter R. E.* // 1999.–astro-ph/990424.

[23] *Mazets E. P., Golenetskii S. V., Il'inskii V. N., et al.* // Nature.–1979.–**282**.–P. 587.

[24] *Mazets E. P., Aptekar R. L., Butterworth P., et al.* // Astrophys. J.–1999.–**519**.–P. L151.

[25] *McCray R. A., Shull J. M., Boynton P. E., et al.* // Astrophys. J.–1982.–**262**.–P. 301

[26] *Mihara T., Makishima K., Ohashi T., et al.* // Nature.–1990.–**346**.–P. 250.

[27] *Mihara T., Makishima K., Nagase F.* // All-sky X-ray Observations in the next decade: Proc. Workshop.–1997.–P. 135.

[28] *Murakami T., et al.* // Astrophys. J.–1999.–**510**.–P. L119.

[29] *Pacini F.* // Nature.–1967.–**216**.–P. 567.

[30] *Pringle J., Rees M.* // Astron. and Astrophys.–**21**.–P. 1.

[31] *Ruderman M., Shaham J.* // Comments Astrophys.–1983.–**10**.–P. 15.

[32] *Santangelo A., et al.* // 1999.–astro-ph/9907158.

[33] *Scott D. M., Leahy D. A., Wilson R. B.* // 2000.–astro-ph/0002327.

[34] *Sheffer E. K., Kopaeva I. F., Averintsev M. B., et al.* // Sov. Astron.–1992.–**36**.–P. 41. (in Russian).

[35] *Sunyaev R. A., Titarchuk L. G.* // Astron. and Astrophys.–1980.–**86**.–P. 121.

[36] *Trümper J., Pietsch W., Reppin C., et al.* // Astrophys. J.–1978.–**219**.–P. L105.

[37] *Van der Klis M.* // 1998.– astro-ph/9812395.

[38] *Woods P. M., et al.* // Astrophys. J.–1999.–**519**.–P. L139.

SHORTENING OF CORE COLLAPSE TIME IN STAR CLUSTERS WITH TWO MASS COMPONENTS

E. Khalisi

Astronomisches Rechen–Institut
Mönchhofstr. 12–14, 69121 Heidelberg, Germany
e-mail: khalisi@ari.uni-heidelberg.de

We present high–accuracy Nbody simulations of isolated star clusters consisting of two distinct mass components, m_1 and m_2, and vary their relative ratio $\mu = m_2/m_1$. The mass fraction of the more massive component to the total mass, $q = M_2/M_{\mathrm{tot}}$, is set equal to 0.1 in all cases. We determine the average star mass within a fixed "Lagrangian shell". It is found that the time of first core collapse is reduced by the ratio μ with respect to a cluster with uniform masses.

INTRODUCTION

Stars are usually formed in the community of clusters, which may range from small associations of some tens of stars (Hillenbrand & Hartmann, 1998) to very dense and rich ones containing some thousand stars such as the Trapezium in the Orion Nebula Cloud (McCaughrean & Stauffer, 1994). The most massive stars are often found near the cluster centres, indicating an undergone process of mass segregation. There are two different physical explanations for the mechanism: On one side, the fragmentation of a star forming cloud occurs with tendency of the high mass stars forming near the bottom of the potential well due to the accelerated accretion of more and more gas; they remain near their place of birth at the cluster centre from the early stages of the star forming scenario (Bonnell & Davies, 1998). On the other side, massive stars may form elsewhere and sink to the centre through two–body relaxation after the formation process has already finished (Spitzer, 1969). Both mechanisms are reasonable, but they should differ in the time scales until the cluster achieves its observed radial mass stratification. Dynamical models are challenged to answer this question by comparison with models of star formation.

SIMULATION TOOLS AND CONDITIONS

The simple case of a two–component cluster is regarded as a first step of tackling a mass spectrum to the single–component models hitherto. A pioneering work by Spitzer & Hart (1971) used Monte Carlo methods to study the evolution of a system with two types of stars. The heavy stars of individual masses m_2 were chosen five times heavier than the light ones, m_1, and they made up a fraction $q = M_2/M_{\mathrm{tot}}$ of 10% of the total cluster mass. Inagaki & Wiyanto (1984) varied this fraction q and found that the evolution is delayed for different values: For higher fractions, the massive stars play a more dominant role in the dynamics, and for smaller fractions their total number becomes too small to make significant contributions.

In this paper, we fix q throughout all models to Inagaki & Wiyanto's value, and examine the evolutionary differences for various ratios of individual masses $\mu = m_2/m_1$ ranging from 2 to 15. We use the most accurate method in order to follow the evolution of a two–mass component cluster, the direct force integration with Nbody6 (Aarseth, 1999a,b) in its special version Nbody6++ for massively parallel computers (Spurzem, 1999). Moreover, we deal with point masses without softening or merging of close particles. Close encounters are regularized, *i.e.*, the time between two integration steps is reduced for the sake of exactness. The scaling is done to standard Nbody–units (Heggie & Mathieu, 1986). In these units the crossing time of a particle is $t_{\mathrm{cr}} = t_{\mathrm{NBU}}/(2\sqrt{2})$, and the virial radius is 1.

The simulations have been performed with various particle numbers (N = 500, 1000, 2500, and 5000). Initially, all particles are distributed randomly according to a Plummer sphere, and the system is in a global virial equilibrium. Moreover, we neglect any kind of stellar evolution, external galactic field, and primordial binaries. The renunciation of stellar evolution is permissible, since this study aims to isolate the essential physical process of mass segregation; with μ being a *relative* quantity, these simulations can be applied to dynamics of any kind of self–gravitating system which does not require stellar evolution (*e.g.*, cometary fragments, asteroids or brown dwarfs).

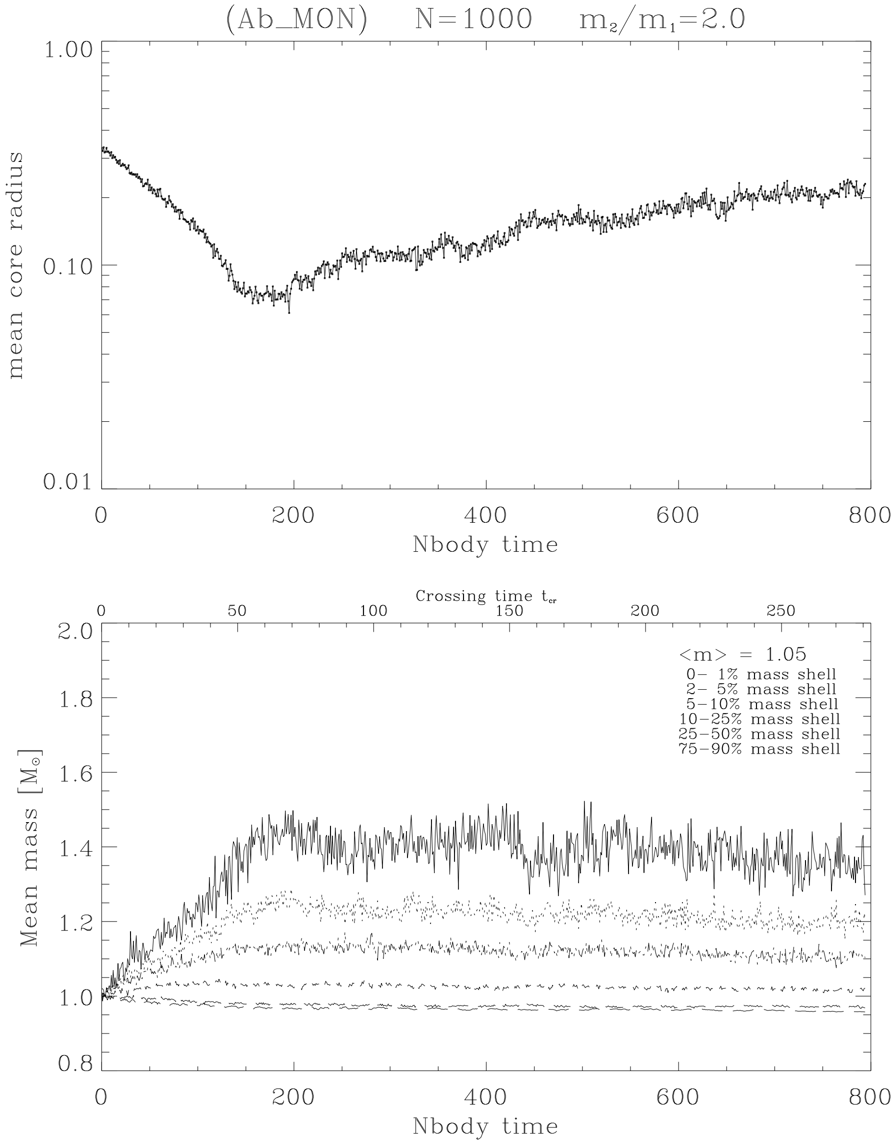

Figure 1: The time evolution of the core radius (upper panel), and the stratification of masses (lower panel) for a model with $N = 1000$ and $\mu = 2$. A conversion from Nbody time units to crossing times $t_{\rm cr}$ is given at the upper axis

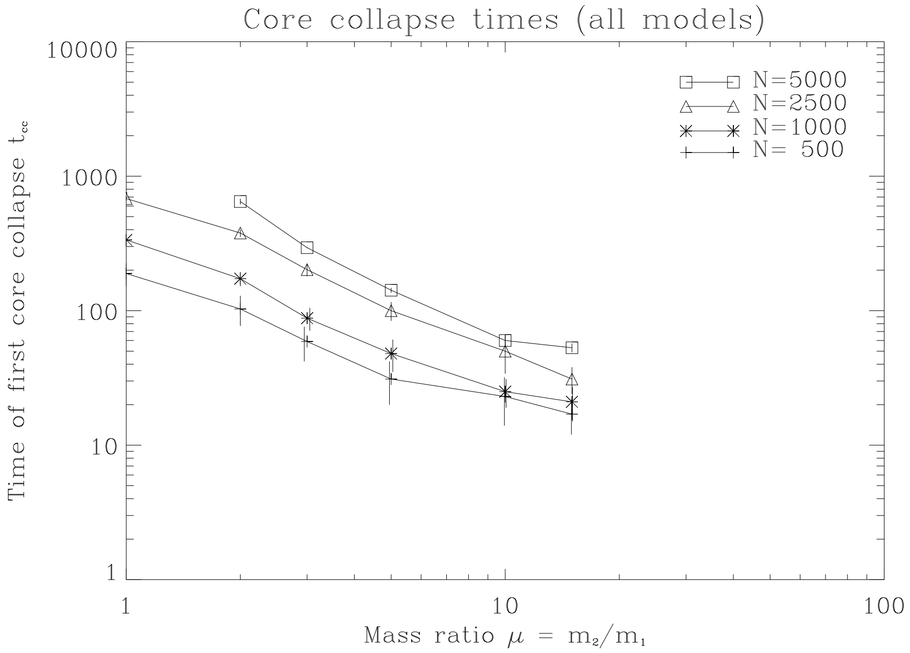

Figure 2: Shortening of the core collapse time in two–component star clusters

RESULTS

Our simulations are summarized in Table 1. Each model, depending on N and μ, is averaged over the number of particular runs given in brackets of the first column. The particular runs differ in the initial seed only, which leads to a randomized setup. Giersz & Heggie (1994) pointed out that the statistical value of such ensemble averages are well balanced. For example, a set of 40 runs containing 500 particles is statistically comparable with one single run containing 20,000 particles. Because of the large calculation efforts only some few simulations for $N = 5000$ are available.

Table 1: Times of first core collapse [in Nbody–time units]

$\mu = \frac{m_2}{m_1} =$	1	2	3	5	10	15
$N = 500$	189	103	59	31	23	17
(40×)	±36	±26	±18	±11	±9	±5
$N = 1000$	336	173	88	48	25	21
(20×)	±36	±21	±17	±13	±6	±6
$N = 2500$	683	378	202	100	50	31
(8×)	±27	±24	±22	±16	±16	±7
$N = 5000$	–	648[a]	294[a]	142[a]	60[b]	53[b]
		± 32	± 2	± 6	± 6	± 4

[a]based on 2 simulations
[b]based on 3 simulations

In the field of intersection, the mean time of the core collapse and its standard deviation is given. The core collapse has been determined from the minimum core radius and the maximum of the central density. An example for the averaged evolution of the core radius is given in the upper panel of Figure 1 (model $N = 1000$ and $\mu = 2.0$).

For investigating mass segregation, the cluster has been split up into shells, in which the average mass of the particles within is computed. The lower panel of Figure 1 demonstrates the time evolution of the mean mass in the inner shells for a the same model. At the beginning the heavier masses are distributed throughout the cluster in the same way as the light masses, and all shells show a similar value of the mean mass. In the course of the dynamical evolution the innermost shell (solid line) gathers a large number of the heavier particles, and its average mass increases at the expense of the outer shells (dashed lines). The core collapse occurs at 170 Nbody-time units when the mass segregation has been largely completed. After that, a binary–driven post–collapse follows.

The results of all simulations are shown in Figure 2. It illustrates the gradual shrinking of the core collapse time with increasing μ. For all particles numbers investigated, the slope is -0.98 ± 0.06.

SUMMARY

Our results can be summarized as follows: (i) The process of mass segregation is governed by the ratio of the individual particles $\mu = m_2/m_1$. (ii) The time of core collapse is reduced by μ in comparison to the core collapse time of a cluster with uniform masses ($\mu = 1$):

$$t_{cc,\mu} \propto \frac{1}{\mu} t_{cc,1}.$$

This result is not a big surprise for experts in the field, but it has never been directly and quantitatively proven in ensemble averaged N-body models with two mass components, as in the present work. Further studies are in preparation (Spurzem, Lin & Khalisi, 2001).

REFERENCES

[1] *Aarseth S. J.* // Celest. Mech. Dyn. Astron.–1999a.–**73**.–P. 127.

[2] *Aarseth S. J.* // Publs Astron. Soc. Pacif.–1999b.–**111**.–P. 1333.

[3] *Bonnell I. A., Davies M. B.* // Mon. Notic. Roy. Astron. Soc.–1998.–**295**.–P. 691.

[4] *Giersz M., Heggie D. C.* // Mon. Notic. Roy. Astron. Soc.–1994.–**268**.–P. 257.

[5] *Heggie D. C., Mathieu R. D.* // Use of Supercomputers in Stellar Dynamics / Eds P. Hut, S. McMillan.–1986.–P. 233.

[6] *Hillenbrand L. A., Hartmann L. W.* // Astrophys. J.–1998.–**492**.–P. 540.

[7] *Inagaki S., Wiyanto P.* // Publs Astron. Soc. Jap.–1984.–**36**.–P. 391.

[8] *McCaughrean M. J., Stauffer J. R.* // Astron. J.–1994.–**108**.–P. 1382.

[9] *Spitzer L. Jr.* // Astrophys. J.–1969.–**158**.–P. L139.

[10] *Spitzer L. Jr., Hart M. H.* // Astrophys. J.–1971.–**164**.–P. 399.

[11] *Spurzem R.* // J. Comput. and Appl. Math.–1999.–**109**.–P. 407.

[12] *Spurzem R., Lin D. N. C., Khalisi E.* // 2001.–in preparation.

FACTOR ANALYSIS OF GALACTIC GLOBULAR CLUSTERS ON STRUCTURAL PARAMETERS

O. Eigenson, O. Yatsyk

Astronomical Observatory, Ivan Franko National University, Lviv, Ukraine
e-mail: `yatsyk@astro.franko.lviv.ua`

Principal component method is used to study galactic globular clusters in 7- and 8-axis space of structural parameters. It is shown that the manifold properties of clusters with this set of parameters is determined mainly by two independent factors. This result may be useful for the theory of formation and evolution of clusters.

In our paper [2], the factor analysis (principal component method) of globular clusters on some main physical parameters was performed. It was shown that the manifold properties of clusters is determined mainly by two independent factors. The first of them is metallicity which is connected with the distance to Galaxy center, and the second one reflects the richness of the cluster. Analogous studies were performed by Broche and Lendes [1], and later by Djorgovski and Meylan [3] and Djorgovski [4].

In this paper we return to this problem with some other set of parameters, different not only from our former set but also from the set used by Djorgovski and Meylan. The database was the catalogue of 125 clusters [6] with the following parameters of clusters: concentration c, core-radius r_c, a half-light radius r_h, and other fraction-of-light radii r_{10}, r_{20}, r_{30}, r_{40}. In the second case the quantity $\mu_V(0)$, central surface brightness, was also included. The details of calculation one may find either in our cited paper or in [5].

The correlation matrix is given in Table 1.

Table 1: Matrix of the correlation coefficients

	r_c	r_{10}	r_{20}	r_{30}	r_{40}	r_h	c
r_c	1.000	.848	.773	.712	.661	.619	−.687
r_{10}	.848	1.000	.989	.971	.951	.930	−.420
r_{20}	.773	.989	1.000	.994	.983	.969	−.331
r_{30}	.712	.971	.994	1.000	.997	.989	−.262
r_{40}	.661	.951	.983	.997	1.000	.997	−.207
r_h	.619	.930	.969	.989	.997	1.000	−.163
c	−.687	−.420	−.331	−.262	−.207	−.163	1.000

Eigenvalues (characteristic roots) are the following: $\lambda_1 = 5.635$, $\lambda_2 = 1.180$, $\lambda_3 = 0.170$, $\lambda_4 = 0.012$, $\lambda_5 = 0.002$, $\lambda_6 = 0.001$, $\lambda_7 = 0.000$. We see that these roots decrease rapidly enough, and we shall confine ourselves to the first two roots. The matrix of factor projections is the following (Table 2):

Table 2: Matrix of the factor projections

	r_c	r_{10}	r_{20}	r_{30}	r_{40}	r_h	c
F_1	0.825	0.996	0.994	0.982	0.967	0.950	–0.415
F_2	–0.472	–0.023	0.094	0.178	0.241	0.289	0.880

This may be illustrated by Fig. 1.

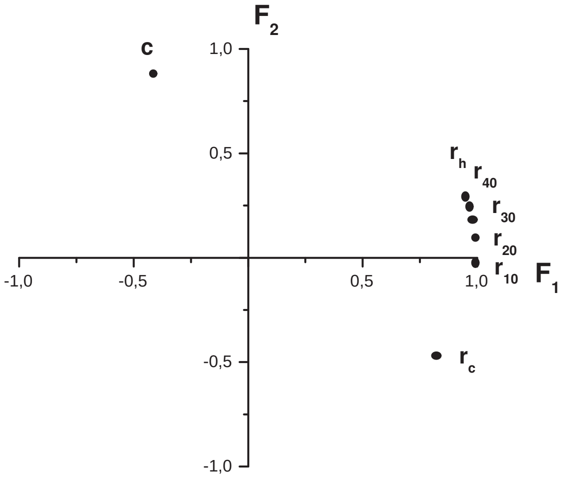

Figure 1: Diagram $F_1 - F_2$ for 7 parameters

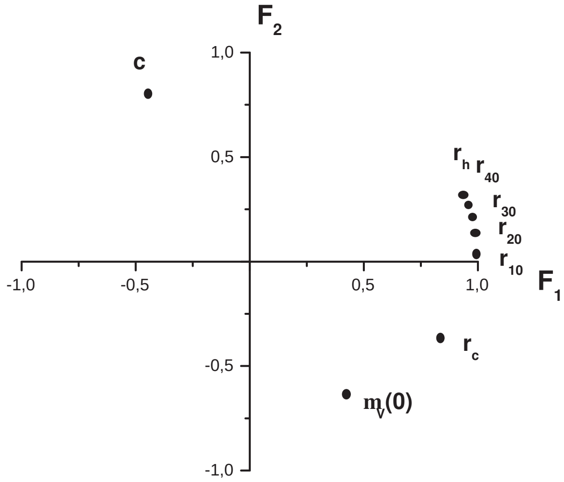

Figure 2: Diagram $F_1 - F_2$ for 8 parameters

If we include the central surface brightness $\mu_V(0)$, the picture becomes more complicated (Fig. 2). So, this brightness is determined simultaneously by both two factors.

We see that the manifold properties of clusters is determined mainly by two independent factors. This result may be useful for the theory of formation and evolution of globular clusters.

REFERENCES

[1] *Broche P., Lendes F.* The manifold of globular clusters // Astron. and Astrophys.–1984.–**139**, N 2.–P. 474–476.

[2] *Eigenson A. M., Yatsyk O. S.* Factor analysis of globular clusters - the principal components method // Sov. Astron.–1986.–**30**, N 4.–P. 390–394. (in Russian).

[3] *Djorgovski S., Meylan G.* The galactic globular cluster system // Astron. J.–1994.–**108**.–P. 1292–1311.

[4] *Djorgovski S.* The fundamental plane correlations for globular clusters // Astrophys. J.–1995.–**438**, N 1.–P. L29–L32.

[5] *Murtagh F., Heck A.* An annotated bibliographical catalogue of multivariate statistical methods and of their astronomical applications // Bull. Inform. Centre Donnees Stellaires.–1986.–**31**.–P. 183.

[6] *Trager S. C., King I. R., Djorgovski S.* Catalogue of galactic globular-cluster surface-brightness profiles // Astron. J.–1995.–**109**.–P. 218–241.

ON THE COUNTERFLOWS OF MATTER IN SELF–GRAVITATING SYSTEMS

O. A. Zheleznyak

Laboratory of Theoretical Astrophysics and Gravitation, Uman' University
2 Sadova St., 20300 Uman', Ukraine
e-mail: uman_astro@yahoo.com

Characteristics of the opposite rotation of matter in self-gravitating systems are discussed. It was shown that counterflows could arise from accretion of matter in asymmetric gravitational fields in the presence of considerable turbulence. It was formed a hypothesis of existence of a massive Sun's nucleus which revolves in the opposite direction than solar atmosphere does. On the base of this hypothesis it was attempted to explain the problem of angular momentum of the solar system and a possible source of solar oscillations.

The opposite rotation of different components of self-gravitating systems begets counterflows of matter. Such phenomenon has been discovered at first in the solar system. Some external planetary satellites have orbital motion that is opposite to the direction of revolution of their planets [8]. Later, the existence of counterflows of matter has been found in some gaseous dust clouds of interstellar medium where a nucleus and an envelope revolve in opposite directions [10, 11]. Detailed modern investigations have allowed to discover the opposite rotation of nuclei in some elliptical galaxies [2, 4, 5]. Now, the counterflows have been found in spiral galaxies where some portion of the stellar component rotates in opposite direction [6]. The opposite rotation of gaseous dust components (*i.e.*, disks and rings) with respect to the stellar component has been discovered in many elliptical galaxies [3, 9]. In our Galaxy the portion of globular stellar clusters has the orbital motion which is opposite to the orbital motion of other galactic components [7].

Foregoing facts acknowledge that the phenomenon of counterflows in self-gravitating systems exists in the wide range of masses and sizes of space bodies. Therefore, it may have common origin.

According to our investigations, an accretion of matter can cause such a process in asymmetric gravitational fields in the presence of considerable turbulence in the medium. The approximate solution of the dynamical equations of accretion in elliptical galaxies indicates the possibility of appearing the counterflows of stellar and gaseous dust components, if asymmetry of gravitational field exists [1]. It is possible to suppose that opposite rotation of a nucleus and an envelope exists in binary systems where synchronization between the self-rotation and the orbital motion is not reached. Using the existence of counterflows in the solar depths, it is possible to explain the problem of angular momentum of the solar system. If full angular momentum of the solar system is supposed to be approximately compensated, then a massive nucleus, which rotates inversely with respect to the Sun's envelope, should exist. If the radius of the Sun nucleus is approximately 0.2 the Sun radius, then it should rotate in opposite direction with the period about 40^m.

Approximate hydrodynamical evaluations indicates that the opposite rotation of the Sun nucleus leads to appearance of a turbulent stratum between the nucleus and the atmosphere. The global circulation of matter arises in this turbulent zone. It can serve as a stimulus of global solar oscillations with period about 160^m. Merger of Sun's rotation peculiarities and the large-scale turbulence can serve as a mechanism of amplification of internal magnetic field and its modification during some period.

REFERENCES

[1] *Antonov V. A., Zheleznyak O. A.* // Astron. J.–1994.–**71**, N 3.– P. 377–382. (in Russian).

[2] *Bender R.* // Astron. and Astrophys.–1988.–**202**, N 1.–P. L5–L8.

[3] *Francesco B., Paniela B.* // Astrophys. J.–1988.–**229**, N 1.–P. 102–106.

[4] *Franx M.* // Astrophys. J.–1989.–**334**, N 2.–P. 612–636.

[5] *Jedrzejewski R., Schechter P. L.* // Astron. J.–1989.–**98**, N 1.–P. 147–165.

[6] *Merrifield M. R., Kuijke K.* // Astrophys. J.–1994.–**432**, N 2.–P. 575–589.

[7] *Rodgers A. W., Paltozlou G.* // Astrophys. J.–1984.–**71**, N 3.–P. 377–382.

[8] *Ruskol E. L.* Satellites of planets.–Moscow: VINITI, 1986.–**28**.–115 p.

[9] *Varnas S. R. et al.* // Astrophys. J.–1987.–**313**, N 1.–P. 69–88.

[10] *Young J. S. et al.* // Astrophys. J.–1981.–**251**, N 2.–P. 81–84.

[11] *Young J. S. et al.* // Astrophys. J.–1982.–**261**, N 2.–P. 513–531.

A PROGRAM OF INTERNATIONAL COOPERATIVE INVESTIGATION OF GRAVITATIONAL LENS SYSTEMS

V. Dudinov[1], P. Bliokh[2], B. Paczynski[3], H. N. Omma[4], R. Schild[5], W. Colley[5], V. Vakulik[1], A. Zheleznyak[1], A. Sergeyev[1], B. Artamonov[6], S. Nuritdinov[7], and Sh. Ehgamberdiev[7]

[1]*Astronomical Observatory, Kharkiv National University, 61022 Kharkiv, Ukraine*
e-mail: `dudinov@astron.kharkov.ua`

[2]*Institute of Radio Astronomy, NAS of Ukraine, 61002 Kharkiv, Ukraine*

[3]*Princeton University Observatory, NJ 08544-1001, USA*

[4]*Maidanak Foundation, N-5006 Bergen, Norway*

[5]*Center for Astrophysics, MA 02138 Cambridge, USA*

[6]*Sternberg Astronomical Institute, 119899 Moscow, Russia*

[7]*Ulugh Beg Astronomical Institute, 70052 Tashkent, Republic of Uzbekistan*

Since 1997, a program of observations of gravitational lens systems (GLS) with the 1.5-m telescope of the high-altitude Maidanak Observatory has been carried out by joint efforts of seven institutions from five countries. The Q2237+0305, Q0957+561, SBS 1520+530, and other GLS were observed in VRI spectral bands using the TI 800×800, Pictor 416 and ST-7 CCD cameras with the aim to obtain the high-precise estimates of magnitudes and colours of the lensed quasar components at different epochs. The results of photometric image processing are presented. This work was made possible in part by Award No.UP2-302 of the U. S. Civilian Research and Development Foundation for the Independent States of the former Soviet Union (CRDF), and with the kind support of the Maidanak Foundation established in 1998 in Norway. Funding from the Uzbek-Ukrainian program of developing the Maidanak Observatory was also very important, as well as the 98–02–17490 and 1.2.5.5 grants from the Russian Basic Research Foundation. The Maidanak Observatory also participated in the successful Qouc-around-the-Clock program monitoring the Q0957+561 quasar continuously with 8 telescopes around the globe for 10 nights in January 2000.

INTRODUCTION

Because of bending the light rays from remote quasars in gravitational fields of lensing galaxies situated close to the line of sight, the observer can see various more or less complicated patterns, depending on a particular arrangement of a source, a lens, and an observer with respect to the line of sight.

Very useful astrophysical information about a quasar, a galaxy and a medium between the quasar and the observer can be obtained from observations of GLS. The observable quantities are the brightness of quasar components in different wavelengths and at different epochs, the geometry of the object, and the brightness profile of the lensing galaxy. Since the intrinsic quasar brightness variation can be seen in different lensed images somewhat shifted in time, there exists a possibility to measure the time delays between the lightcurves of individual quasar images and thus, with a good knowledge of the mass distribution of a lensing galaxy, to determine the Hubble parameter. In addition to the brightness variations inherent in quasars, the individual lensed images sometimes change their brightness independently from each other. It happens in microlensing events when an object from the lensing galaxy passes close to the line of sight of the specific lensed image. The analysis of microlensing lightcurves allows to estimate the masses of microlenses and to examine the quasar spatial structure at extremely small angular scales.

OBSERVATIONS

Most of GLS are faint and compact objects with a rather complicated spatial structure, therefore, their photometry is a difficult task demanding very good seeing conditions. That is why the excellent 1.5-m AZT-22 telescope on Maidanak Mountain known by its superb seeing conditions, high atmosphere transparency and large number of clear nights, was used for observations. The telescope was specially designed for high-resolution imaging and has a perfect optics of almost diffraction quality. The tower and the dome are equipped with a system of forced ventilation.

A professional TI 800×800 Pitt CCD and an amateur Pictor-416 cameras were used for observations in 1995–1998, at the scales of 0.13 arcsec/pixel and 0.16 arcsec/pixel, respectively. The images were usually taken in series, consisting of 5–10 frames, with an exposure of 3–5 minutes for a frame. Since 1999, a new ST-7 CCD camera provided by the Maidanak Foundation has been used. It is sufficiently linear and has rather good parameters, which made possible to increase the accuracy of photometry. About 10 gravitational lens systems were observed in V, R and I spectral bands during 1997-99 with these cameras. A new large professional CCD camera is expected to be installed at the 1.5-m telescope this year. The camera was ordered by the Maidanak Foundation in the laboratory of Copenhagen University, under supervision of Prof. Andersen who had kindly agreed to build it free of charge.

SBS 1520+530

The SBS 1520+530 system was identified as a gravitationally lensed BAL quasar in 1996 in spectroscopic observations with the 6-m BTA telescope [2]. The spectra of the A and B components separated by approximately $1''.5$ are almost identical [2], and give the same redshifts of about 1.855 for both images. The third, much fainter, NW component located at about $2''.5$ to the north-west from A, is almost the same in its colour. The fourth star-like object (SE hereafter) which is even fainter and redder than NW has been also discovered at about $4''.5$ to the south-east. These two objects are supposedly the foreground stars.

Table 1: VRI magnitudes of SBS 1520+0305 (July 1998)

Component	V	R	I
A	17.98 ± 0.02	18.02 ± 0.02	17.77 ± 0.02
B	18.72 ± 0.05	18.72 ± 0.06	18.52 ± 0.04
NW	19.30 ± 0.08	19.24 ± 0.08	19.08 ± 0.12
SE	20.49 ± 0.10	19.95 ± 0.10	19.02 ± 0.09

Crapmton *et al.* [3] reported a discovery of a faint ($19^m.2$ in H band) object located $0''.4$ from the B component. Supposing it is a lensing galaxy, the authors of [3] predicted its R magnitude of about $21^m.6$.

Our observations in VRI bands made with the TI 800×800 CCD camera on July 18–20, 23, and 28, 1998, on Maidanak are presented in Table 1. Since there were no significant changes in the components brightness from night to night during this time period, the averaged magnitudes are shown in this table. The image of a 17-magnitude star situated $25''$ to the north-east from the object was used for the PSF estimation.

Table 2: Relative magnitudes of SBS 1520+0305 components in R band at different epochs

Component	1996, [2]	1997, [3]	Maidanak, July 1998	Maidanak, July 1999	Maidanak, Sept.1999
A	0.00	0.00	0.00	0.00	0.00
B	0.65	0.66	0.70	0.78	0.79
NW	1.17	1.25	1.22	1.16	1.17
SE	3.05	–	1.95	1.95	1.93

The photometry of R images taken with the new ST-7 CCD camera in July 1999 (four dates), and in September 1999 (five dates) was also made. Comparing these data with those of previous measurements, [2, 3], the photometric changes in the system can be seen from Table 2 where the relative magnitudes (with respect to the A component) are presented.

PHOTOMETRY OF Q0957+561 ("FIRST LENS")

This double quasar, which is the first object identified as a gravitational lens system, demonstrates variability in optical and in radio wavelengths and thus is a good candidate for the Hubble constant estimation. The time delay of 417 days in optical wavelengths is now considered to be accurate to better than 1%, giving the value of a Hubble parameter of $63 \pm 12\,\mathrm{km/(s\ Mpc)}$.

In January 2000, the observations of Q0957+561 with the 1.5-m Maidanak telescope were fulfilled in the framework of the International round-the-clock monitoring campaign launched by Prof. Schild. The data containing over 500 Mb were taken on Maidanak during 10 days in January. These have been reduced and can be seen plotted on the project home page:
http : //cfa-www.harvard.edu/~wcolley/Q0957/newsletter000831.html.
On these plots, the Maidanak (grey) data importantly contribute to the observed continuous brightness curve and show no systematic problems. The second run is expected to start in March 2001.

VRI PHOTOMETRY OF Q2237+0305

The Q2237+0305 gravitationally lensed quasar (the Einstein Cross) constitutes one of the most impressive effects of gravitational lensing phenomenon. Four images of a distant quasar are arranged almost symmetrically around the nucleus of a lensing galaxy within a circle of less than $2''$ in diameter.

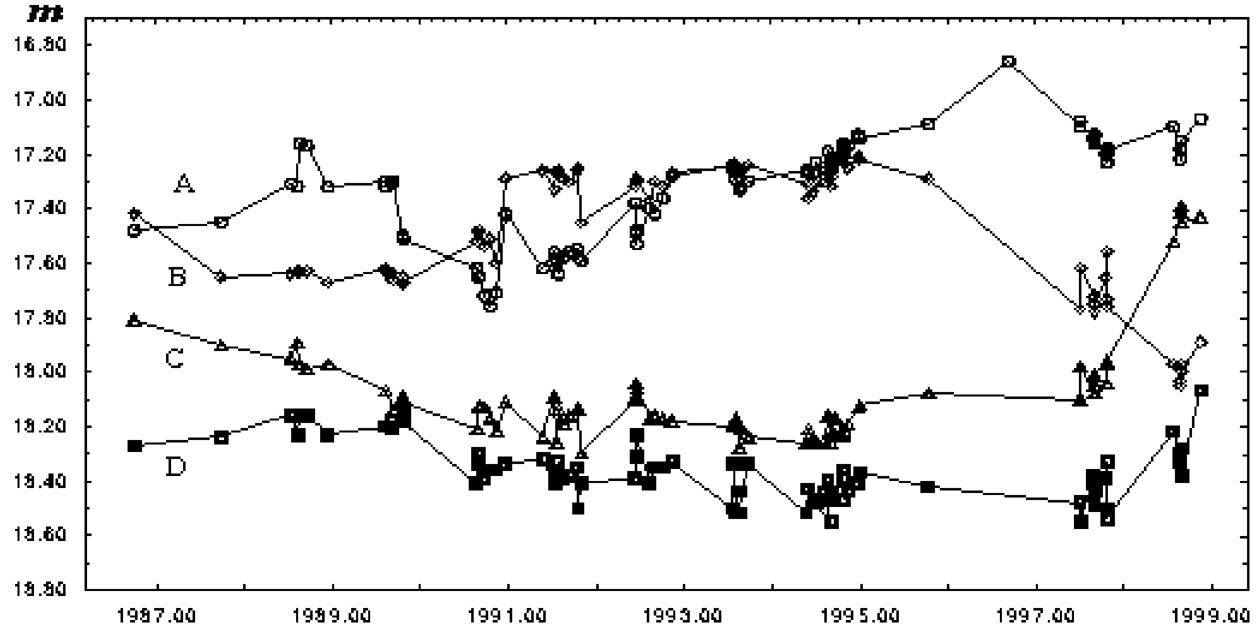

Figure 1: Historic lightcurves of Q2237+0305 components

In this work, the results of Q2237 photometry in the R band for 12 dates during 133 days in 1997, and for 15 dates during 115 days in 1998 are presented, as well as the results of VRI photometry in 1997–1999. In Fig. 1 historic lighcurves of the Einstein Cross components in the R band are presented. The lightcurves, composed of all available data, demonstrate high microlensing activity which is typical for this system. In this picture, the data from 1995 to 1998 were obtained on Maidanak. A noticeable increase of the component C brightness is the most important event of the 1997–98 time period. In 1998 it exceeded B in brightness for the first time since the system discovery, while the latter became 0.8 magnitudes fainter as compared to 1995. Our photometry is in a good agreement with the results of the Einstein Cross monitoring in the V band, presented in [9].

Even the first multicolour photometry of the Q2237+0305 system have shown that the components noticeably differ in their colour [10]. The further observations, in particular [6] and the observations of 1995 from Maidanak [7] demonstrated that the colour of the components might have changed in time. That is why the multicolor observations of Q2237+0305 were continued in 1997, 1998 and 1999 on Maidanak [4].

Below we analyse the relative colours which are less sensitive to the difference in photometric systems and the errors of zero-pointing as compared to the absolute colours, and thus can be used for comparing and a qualitative analysis even for different bases in various observational datasets. The result of such a comparison can be seen from Table 3, where the relative colours of the components calculated from the results of our observations and with the use of the available multicolour photometry of other observers are presented. The table shows that colour variations in the Q2237 system are real and significant, at least for the B and C components. First of all, an obvious reddening of the B component with a decrease of its brightness in 1998 should be noted. At the same time, the C component became more blue in 1998 when a prominent increase of its brightness took place.

Table 3: Variations of relative colours in the Q2237+0305

Epoch, colour base	A	B	C	D
1987, (g-i), [10]	0.00	0.08	0.33	0.19
1990, (U-R), [6]	0.00	0.03	0.24	0.42
1995, (V-I), [1]	0.00	−0.08	0.12	0.15
1995, (V-I), [7]	0.00	−0.12	0.23	0.08
1997, (V-I), [4]	0.00	−0.12	0.09	0.14
1998, (V-I), [4]	0.00	0.04	−0.12	0.25
1999, (V-I), Maidanak	0.00	0.08	−0.15	0.26

Unfortunately, the available data don't permit to fulfill a quantitative analysis and to trace, for example, a relationship between the colour and brightness variations. Sometimes a qualitative dependence can be noticed, *e.g.*, when a component increases its brightness often becomes more blue at the same time. There are two explanations of the observed colour variations in GLS: either (1) the value of light extinction by the lensing galaxy matter changes in time or (2) microlensing reveals the fact that the effective size of the quasar is different in various wavelengths. The last explanation were proposed in 1991 by [8]. More precise and detailed lightcurves of the longer duration, taken in several spectral bands are needed to choose between the two explanations.

CONCLUSIONS

The data presented here shows great potentials of the Maidanak site and the 1.5-m AZT-22 telescope for high spatial resolution photometry of gravitational lens systems. The excellent properties of the Maidanak Mountain have been also confirmed by the recent cooperative seeing investigation, [5], resulting in as small as 0.69 arcsec median FWHM estimation. The new data on the recently discovered SBS 1520+530 system should be especially noted, as well as VRI photometry of the Q2237+0305 which had definitely demonstrated that variations of the components colour are real and significant.

REFERENCES

[1] *Burud I., Stabell R., Magain P., et al.* Three photometric methods tested on ground-based data of Q2237+0305 // Astron. and Astrophys.–1998.–**339**.–P. 701–708.

[2] *Chavushyan V., Vlasyuk V., Stepanyan J., Erastova L.* Results of Observations // Astron. and Astrophys.–1997.–**318**.–P. L67–L60.

[3] *Crampton D., Schechter P. L., Beuzit J.-L.* Detection of the galaxy lensing the doubly-imaged quasar SBS 1520+530 // Astron. J.–1998.–**115**.–P. 1384–1387.

[4] *Dudinov V. N., Vakulik V. G., Zheleznyak A. P., et al.* Brightness and colour variations in the Q2237+0305 // Kinematics and Physics of Celestial Bodies.–2000.–in press. (in Russian).

[5] *Ehgamberdiev S. A., Baijumanov A. K., Ilyasov S. P., et al.* The astroclimate of Maidanak Observatory in Uzbekistan // Astron. and Astrophys. Suppl. Ser.–2000.–**145**, N 2.–P. 293–304.

[6] *Rix H.-W., Schneider D. P., Bachcall J. N.* Hubble Space Telescope camera imaging of the gravitational lens 2237+0305 // Astron. J.–1992.–**104**.–P. 959–960.

[7] *Vakulik V., Dudinov V., Zheleznyak A., et al.* VRI photometry of the Einstein Cross // Astron. Nachr.–1997.–**318**, N 2.–P. 73–80.

[8] *Wambsganss J., Paczynski B., Schneider P.* Interpretation of the microlensing event in QSO 2237+0305 // Astrophys. J.–1990.–**358**.–P. L33–L41.

[9] *Wozniak P. R., Alard C., Udalski L., et al.* The optical gravitational lensing experiment monitoring of QSO 2237+0305 // Astroph. J.–2000.–**529**.–P. 88–96.

[10] *Yee H. K. C.* High-resolution imaging of the gravitational lens system candidate 2237+0305 // Astron. J.–1988.–**95**,–N 5.–P. 1331–1339.

GLOBULAR CLUSTERS AS GRAVITATIONAL LENSES. RESULTS OF SUPERAMPLIFICATION

A. V. Yushchenko

Astronomical Observatory, Odesa National University
T. G. Shevchenko Park, 65014 Odesa–14, Ukraine
e-mail: yua@lens.tenet.odessa.ua

In previous works we showed that amplification of small sources by cores of globular clusters or dwarf galaxies can reach 5–10 magnitudes, if the cores are transparent. This amplification can explain the significant part of Arp's objects. The lenses for Arp's objects are globular clusters in the halos of foreground galaxies. The nuclei of Seyfert or other active galaxies can be sources for this superamplification. VLBI or other high-precision observations will confirm or reject this hypothesis.
Here we propose new simple observational test. Let this hypothesis is valid. It is known that there can be near 10^2 globular clusters near ordinary galaxy. These globular clusters can produce amplification not only of active nuclei, but of ordinary nuclei and any other sources. Now ordinary galaxies are discovered at high redshifts, up to $Z = 5$. If globular clusters in the halos of distant foreground galaxies can act as gravitational lenses, we can expect the overdensity of star-like images near foreground galaxies. We analyzed USNO A2.0 catalog in the vicinity of 35862 galaxies with redshifts 0.01–0.33, and found that mean overdensity of objects brighter than 21^m is near 100 objects per galaxy. We show that this overdensity can not be explained by usual clustering of galaxies.

Quasi-stellar objects were discovered near 40 years ago. The first who proposed gravitational lensing for explanation of quasars was Barnotti [3]. But it was shown that neither galaxies nor stars in the halos of galaxies cannot explain all observed properties of quasars. Arp pointed that quasi-stellar objects can concentrate near bright galaxies [1]. There are a lot of papers where authors confirm or reject the clustering of quasars near foreground galaxies or clustering of galaxies near quasars (see [2] or [8] for example). Burbidge *et al.* [6] found about 500 associations of quasars with foreground galaxies. It is near one tenth of the total number of bright quasi-stellar objects. But small statistics do not permit them to find or reject the clustering and explain its nature.

Baryshev, Raikov and Yushchenko [4] proposed that these associations can be explained as gravitational lensing of distant active nuclei by cores of globular clusters, dwarf galaxies, and other middle mass objects (MMO) located in the halos of foreground galaxies. It should be noted that Yakovlev *et al.* [11] developed an analytical theory for calculations of amplification of objects like globular clusters. They showed that amplification by core of transparent object of this type can reach infinity for point sources.

In 1994 Yushchenko, Baryshev and Raikov [12] developed the software for direct calculations of amplification by cores of objects like globular clusters for extended sources. They found that amplification can reach 5–10 magnitudes for typical cases and quasar-galaxy associations (Arp's objects) can be explained by this effect. The superamplification by the cores of MMO can be easily explained. Under some reliable conditions all light rays from the source to the solid angle of the core of MMO will be focused near observer. That is why the amplification can be estimated as the ratio of angular squares of the MMO's core and of the source. The typical diameter of the core of MMO is 10–50 pc, while the size of emitting region of quasi-stellar objects can be significantly less than 1 pc. The square ratio of these quantities give us the amplification coefficient from 10^2 to 10^4: from 5 to 10 magnitudes. The angular sizes of amplified images are equal to the angular sizes of the cores of globular clusters in the halos of foreground galaxies - these are star-like images for our optical telescopes.

Later the detailed investigation of this effect was published by Baryshev & Ezova [5]. They listed a set of observational tests for validation of this hypothesis. We can only say that these tests require new precision observations and are quit hard for observers.

Yushchenko & Raikov [13] proposed that not only Arp's objects, but significant part or all quasi-stellar objects can be explained as gravitational lensing by cores of globular clusters and dwarf galaxies.

This hypothesis can work if the cores of globular clusters are transparent. The necessary condition is also the existence of distant Seyfert nuclei or other active nuclei with spectral properties similar to that of quasars. Typically, only one globular cluster per foreground galaxy can act as gravitational lens because the number of background Seyfert or other active nuclei is too small.

Yushchenko [14] proposed a new observational test for verifying this hypothesis. This is a very simple test. Not only one globular cluster per foreground galaxy can produce the amplification of the images of distant sources. All globular clusters and dwarf galaxies in the halo can do it. But the number of active nuclei as sources is insufficient. That is why the sources must be ordinary galaxies or any other objects located on the higher redshift behind these MMOs.

Let us assume that there are not only Seyfert nuclei at high redshifts, but galaxies of all types. Now ordinary galaxies up to redshifts near 5 can be discovered (see [7] for example). That is why the sufficient number of sources exist, and they can be significantly amplified due to gravitational lensing.

It is known that the number of Seyfert galaxies is of order only 1% of all galaxies. If all types of galaxies are gravitationally amplified by cores of globular clusters and dwarf galaxies by 5–10 magnitudes we can expect the excess of number density of star-like images near foreground galaxies. We know that the usual number of globular clusters per galaxy vary from 10 to 10^4. The mean value is near 10^2.

That is why the expected number density of high redshift ordinary galaxies, gravitationally amplified by globular clusters, must be two orders higher than the number density of quasi-stellar objects. The last catalogues of bright quasars contain near 10^4 objects. Thus, we can expect near 10^6 high redshifts star-like objects located near foreground galaxies. The expected spectral properties of these objects will be similar to spectral properties of usual galaxies with a correction for redshift and evolution. In any case, their colors will be more redder than quasars.

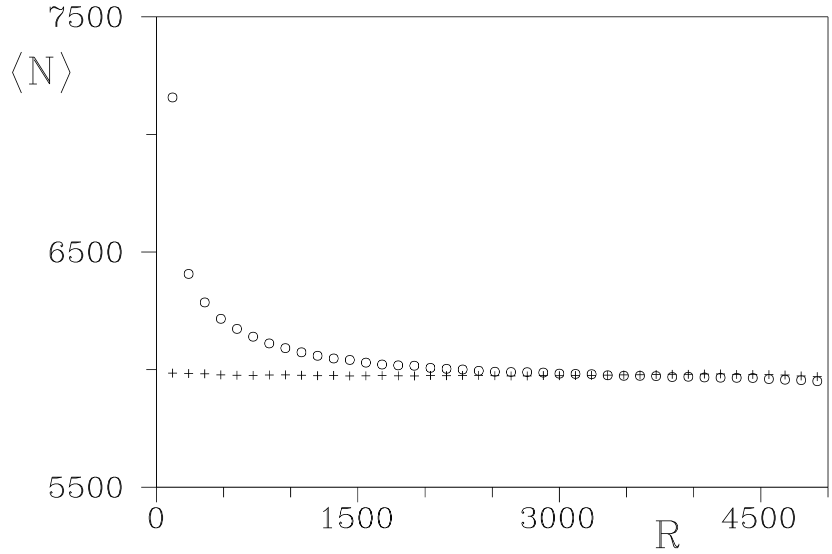

Figure 1: The mean density of objects in concentric rings around 35862 galaxies (circles), and around random centers (crosses). The axes are the radii of concentric rings in arcseconds and mean density of objects per square degree

For checking the validity of our assumption we used digitized Palomar survey with extension to southern sky – USNOA2.0 catalog [10] – as a catalog of star-like images. This catalog contains more than 500 millions of objects brighter than 21^m. We used CfA catalog [9] as a catalog of foreground galaxies. We selected 35862 galaxies with redshifts more than 3000 km/s from CfA catalog. We calculated the number densities of all objects in the concentric rings around each galaxy up to 1.5 degree in diameter. We made calculations for two values of the distances between concentric rings – 20 arcseconds and 2 arcminutes. The similar calculations were made for four random centers around each galaxy at the distance 1.5 degree.

The mean results are shown in Fig. 1 (see also [14]). We can see a well detected over-density of objects around galaxies. Random centers show zero overdensity. The overdensity around galaxies is near 100 objects per galaxy. It should be noted that the mean density of objects in the investigated regions is near 6000 objects per square degree. 100 objects is near 1.5% over-density. Only mean results for 35862 galaxies permit us to claim that the overdensity exist. This means that about 35862×10^2, *i.e.*, several millions objects in USNOA2.0 are star-like images of distant galaxies amplified by cores of globular clusters or dwarf galaxies by 5–10 magnitudes.

We should mention that USNOA2.0 catalog does not contain star/galaxy classification of the objects. Therefore, we can expect that part of the overdensity can be explained by usual clustering of galaxies. But in this case we must detect the stronger effect for foreground galaxies with small redshifts and weaker effect for foreground galaxies with higher redshifts. Is it true?

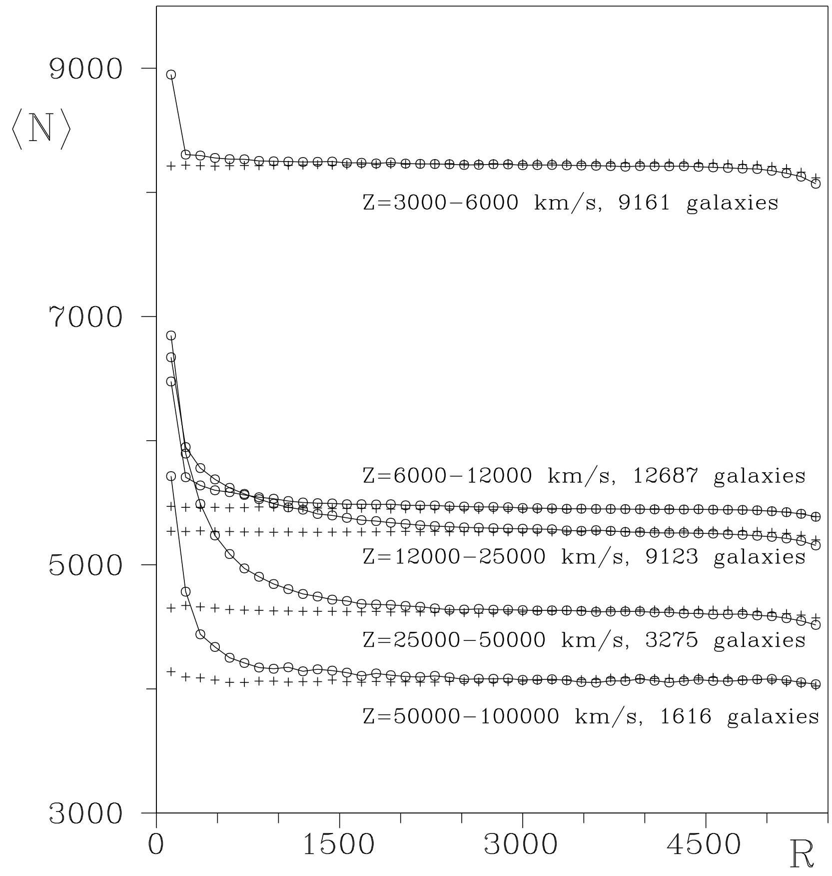

Figure 2: The same as Fig. 1 but for groups of foreground galaxies with different redshifts, namely 3,000–6,000 km/s, 6,000–12,000 km/s, 12,000–25,000 km/s, 25,000–50,000 km/s, 50,000-100,000 km/s

The statistics is sufficient and we were able to plot the overdensity as a function of galaxy redshifts. Fig. 2 shows the same as Fig. 1 but for groups of foreground galaxies with different redshifts. We can see that the strongest overdensity is observed for the groups of galaxies with redshifts from 12,000 km/s to 50,000 km/s and that the overdensity for nearest group of galaxies is the smallest.

This result permit us to claim that usual galaxy clustering can not strongly influence on the overdensity of objects around galaxies.

Different mean density of objects per square degree in different groups (see Fig. 2) can be easily explained by different mean galactic latitude of galaxies with different redshifts.

We predicted and found the overdensity of star-like images around galaxies. These star-like images are the images of high redshift galaxies, amplified by cores of globular clusters (or dwarf galaxies). Only small part of this overdensity can be explained by usual images of galaxies.

The overdensity of objects near galaxies is an observational fact and in any case it is necessary to investigate this problem in detail. Even if our explanation is false, it will be necessary to find other reason for this overdensity.

REFERENCES

[1] *Arp H.* Relation Between Quasi-Stellar Radio Sources and Radio-Compact and Radio N Galaxies // Astrophys. J.–1968.–**153**, N 1.–P. L33–L37.

[2] *Arp H.* The distribution of high-redshift (z>=2) quasars near active galaxies // Astrophys. J.–1999.–**525**, N 2.–P. 594–602.

[3] *Barnotti J. M.* Quasars and the gravitational image intensifier // Astron. J.–1965.–**70**, N 9.–P. 666.

[4] *Baryshev Yu. V., Raikov A. A., Yushchenko A. V.* Quasar-galaxy associations as a result of gravitational lensing by objects of medium masses // Gravitational lenses in the Universe: Proc. 31 Liege Astrophys. Coll., Liege, Belgium.–1993.–P. 307–310.

[5] *Baryshev Yu. V., Ezova Yu. L.* Gravitational mesolensing by King objects and quasar-galaxy associations // Astron. Rep.–1997.–**41**, N 4.–P. 436–446.

[6] *Burbidge G., Hewitt A., Narlikar J. V., Das Gupta P.* Associations between quasi-stellar objects and galaxies // Astrophys. J. Suppl. Ser.–1990.–**74**, N 3.–P. 675–730.

[7] *Eisenhardt P., Stern D., Spinrad H., et al.* Drop-Outs at High Redshift: Quasars and Galaxies at z>5 // Amer. Astron. Soc. Meeting.–2000.–**196**.–51.09.

[8] *Fried J. W.* Faint galaxies around quasars at z=1 and gravitational lensing of distant objects // Astron. and Astrophys.–1997.–**319**, N 2.–P. 365–370.

[9] *Huchra J. P., Geller M. J., Clemens C. M., et al.* // ADC CD ROM, 1995.–Vol. **3**.

[10] *Monet D. et al.* USNO A2.0. A catalog of astrometric standards (CD edition), 1998.

[11] *Yakovlev D. G., Mitrofanov I. G., Levshakov S. A., Varshalovich D. A.* Effects of spherically-symmetric gravitational lenses produced by galaxies and clusters // Astrophys. and Space Sci.–1983.–**910**, N 1.–P. 133–155.

[12] *Yushchenko A. V., Baryshev Yu. V., Raikov A. A.* Quasar-galaxy associations as a lensing by middle mass objects // Astron. and Astrophys. Transactions.–1998.–**17**.–P. 9–14.

[13] *Yushchenko A. V., Raikov A. A.* Associations of quasars with galaxies - consequence of gravitational lensing by globular clusters in the halos of galaxies // Selected problems of astronomy and astrophysics: Proc. of the II conf., Lviv, Ukraine.–1998.–P. 185.

[14] *Yushchenko A. V.* Globular clusters as gravitational lenses. Observational test // Odessa Astron. Publ.–1999.–**12**.–P. 85–86.

OPTIMAL EXTRACTION OF MULTIPLE OVERLAPPING SPECTRA: A NEW ALGORITHM BASED ON THE MAXIMUM ENTROPY METHOD

S. V. Khmil[1] **and J. Surdej**[2,3]

[1]*Astronomical Observatory, Taras Shevchenko National University*
3 Observatorna St., 04053 Kyiv-53, Ukraine
e-mail: khmil@aoku.freenet.kiev.ua
[2]*Institut d'Astrophysique et de Géophysique, Université de Liège*
Avenue de Cointe 5, B-4000 Liège, Belgium
e-mail: surdej@astro.ulg.ac.be
[3]*Directeur de Recherches au FNRS (Belgium)*

A general algorithm of slit spectra extraction for a system of point-like sources (*e.g.*, multiple lensed images of the same quasar) has been developed, assuming that the point-spread function (PSF) of the measuring instrument and the positions of the spectra relative to the CCD frame are unknown. The main idea of the algorithm is to successively apply the maximum entropy method to each set of parameters, such as the spectra, the PSF, and the spectra positions, in order to iteratively improve their values. The algorithm uses all the a priori knowledge about the spectra (*e.g.*, flux positivity, relative magnitudes between the components, astrometry, *etc.*) to compute the initial parameter sets. After careful testing, the algorithm was applied to extract the spectra of the gravitationally lensed system Q1009-0252 A & B ($I_B/I_A = 0.1$, $\theta_{AB} = 1''.55$, $1\,\mathrm{pxl} = 0''.44$, typical seeing FWHM = $0''.8$).

INTRODUCTION

Spectra of quasars multiply imaged by gravitational lensing contain unique information about the structure and the physical properties of the lensed sources, the intergalactic medium, and the lensing objects (galaxies and their clusters). Since the angular separation between such images is typically less than one or several arcseconds, their spectra very often overlap, are curved and noisy because of the atmospheric turbulence, instrument aberrations, detector noise, *etc.* Moreover, sometimes we are forced to process data which, for some reason, are incomplete. Thus, whenever we deal with observational data, some restoration technique is necessary to extract as much information as possible from them. In order to improve the reliability of such an extraction, it is very important to supplement the observational data with prior knowledge about the image. Powerful examples of such a priori information are the flux positivity, relative magnitudes of the image components, astrometric data, and so on.

We present here a new, sufficiently general, algorithm of slit spectra extraction for a system of point-like sources, which is based on the maximum entropy method (MEM). The algorithm uses all the a priori knowledge on the restored spectra and iteratively improves the spectra themselves, the numerical profile of the PSF, and the positions of the spectra within the CCD frame.

As an application of the algorithm, we present the extracted spectra for the gravitationally lensed quasar Q1009-0252 A & B.

DESCRIPTION OF THE ALGORITHM

Let us assume that we deal with standard, sky-subtracted, CCD observational data of slit spectra of an astronomical object which consists of N_{sp} point-like components. Typically, it may be a gravitationally lensed quasar or another system of multiple point sources. Hereafter, for convenience, spectra are labelled with the discrete index A ($A = 1, \ldots, N_{\mathrm{sp}}$) whereas the indices λ and i refer to pixel coordinates along the spectral and spatial directions of the CCD frame. In order to describe the spectra, let us introduce the following three sets of parameters: the set of spectral fluxes $C_{A\lambda}$; the profile of the PSF $\phi(x)$ which is supposed to be normalized to unity, generally nonsymmetric, and discretely given by its numerical values ϕ_n at N_{PSF} evenly separated points; the set of spectra positions relative to the CCD frame $x_{A\lambda}$.

Generally speaking, these three sets of parameters are unknown. *The main idea of the proposed method is to successively apply the MEM to each set of parameters in order to iteratively improve their values.* To implement this idea, we follow, with *some generalizations*, the simple maximum entropy deconvolution algorithm proposed by Cornwell & Evans [2]. The essence of the algorithm is directly bound to the concept of relative entropy.

Suppose that we are to reconstruct some object which is not obligatory an image and which is represented by *several* discrete sets of uniform *positive* parameters, like the three sets previously discussed. Following our main idea, consider separately one of the sets, say b_i $(i = 1, \ldots, M)$, assuming that all the others are known. For convenience, we shall treat this set as a vector $\boldsymbol{b}$ in the M-dimensional space. Suppose also that a priori knowledge about the object can be expressed in the form of the vector $\boldsymbol{m}$ of the same dimension. The relative entropy

$$H(\boldsymbol{b}|\boldsymbol{m}) = -\sum_i b_i[\ln(b_i/m_i) - b_i + m_i] \tag{1}$$

is then a useful measure of the differences between these two objects. It is easy to see that the relative entropy has the maximum $H = 0$ at $\boldsymbol{b} = \boldsymbol{m}$, *i.e.*, in the case of no data, optimization of H just gives the a priori object.

If there are some observational data, they will pull the reconstructed object away from the a priori one. It can be shown that the MEM selects a single object from a variety of objects consistent with the data. The other advantages of the MEM are as follows: (i) the least assumption about unknown information, (ii) introducing no structure in the image without evidence in the data, (iii) the possibility to express a priori information in terms of a default image rather than the properties of an algorithm itself [2, 4].

The chi-square statistic is usually used to describe the deviations between the observed and the reconstructed data sets. To write the χ^2 function in our case, note that the contribution of every spectrum to the flux in the pixel (λ, i) is given by $C_{A\lambda}\phi(i - x_{A\lambda})$. Denoting the observed flux by $F_{\lambda i}$ and the corresponding standard deviation by $\sigma_{\lambda i}$, we can write the following expression for χ^2:

$$\chi^2 = \sum_{\lambda,i} \frac{1}{\sigma^2_{\lambda i}} \left(\sum_A C_{A\lambda}\phi(i - x_{A\lambda}) - F_{\lambda i} \right)^2 . \tag{2}$$

Thus, in order to reconstruct our object, we should optimize the relative entropy (1), subject to the constraint that the chi-square function (2) has a value which is statistically compatible with the data (see below). Sometimes, however, it is worth using another constraint $G = \text{const}$ with some function $G(\boldsymbol{b})$ whose explicit form depends on the nature of the parameters under consideration. According to the general method of Lagrange multipliers, we construct the objective function

$$Q = H - \alpha\chi^2 - \beta G, \tag{3}$$

where α and β are the Lagrange multipliers.

The optimization problem then consists in finding a vector $\boldsymbol{b}$ such that the gradient of Q, *i.e.*, the vector $\boldsymbol{\nabla} Q$ whose components are equal to $\partial Q/\partial b_i$, is zero. Following Cornwell and Evans [2], we use the Newton-Raphson iterative optimization of the objective function (3) with automatic adjustment of the Lagrange multipliers α and β at every step of iteration. The algorithm starts with $\boldsymbol{b} = \boldsymbol{m}$ and $\alpha = \beta = 0$. The step to the next trial vector $\boldsymbol{\Delta b}$ is then given by

$$\boldsymbol{\Delta b} = (-\nabla\nabla Q)^{-1} \cdot \boldsymbol{\nabla} Q. \tag{4}$$

According to Eq. (4), in order to obtain $\boldsymbol{\Delta b}$ it is necessary to calculate a matrix inverse to the Hessian $\nabla\nabla Q$. Fortunately, in our case it is possible to do this directly because $\nabla\nabla Q$ is block diagonal with block dimension of at most $N_{\rm sp}$ or $N_{\rm PSF}$. For this purpose, we use the singular value decomposition algorithm. Note that the inverse matrix $g = (-\nabla\nabla Q)^{-1}$ provides a useful metric for the M-dimensional parameter space, which can be used to judge the closeness of the actual vector $\boldsymbol{b}$ to the true MEM one, for adjusting the Lagrange multipliers α and β, and for a diagnostic of successful iteration (for more details, see [2]).

As the criterion to stop the iterations, we request at least one of the following two conditions to be satisfied:

$$\chi^2 \approx N \quad \text{or} \quad |\Delta\chi^2| < \varepsilon\chi^2, \tag{5}$$

where N is the number of observations, and ε is usually chosen of order 0.01 or less. The former condition in (5) is the usual chi-square test whereas the latter one means stopping due to the slow convergence of iteration, which especially takes place, if the other sets of parameters are not yet fitted.

Let S, F, and X denote symbolically the implementations of the MEM to process the spectra, the PSF, and the spectra positions, respectively. Then the general scheme of our algorithm may be displayed as a sequence of MEM steps:

$$Start: \ S \to [F \to X \to S] \to \cdots \to [F \to X \to S] \to Stop. \tag{6}$$

Thus, we start with some initial values of the spectra, the PSF, and the spectra positions whose choice is dictated by the wide use of a priori information, *e.g.*, flux positivity, magnitudes of the components, astrometric data, an observational estimate of FWHM for atmospheric seeing, *etc.* Each step of the algorithm contains the MEM iteration, as previously described. We optimize the relative entropy subject to the following constraints (*cf.* the objective function (3)): χ^2 and flux conservation during the processing of spectra, χ^2 and the PSF normalizing condition during the PSF processing, only χ^2 while the positions are being processed. The transitions from one step to another, which are indicated with the arrows in the scheme (6), are carried out after successfully checking the stopping conditions (5). Every step ends with putting $\boldsymbol{m} = \boldsymbol{b}$, *i.e.*, with improvement of our prior knowledge about the corresponding set of parameters. The brackets symbolize undivided parts of the algorithm. In other words, computations have to be finished only after processing the spectra. We proceed in this way because we are mainly interested in obtaining the spectra.

The corresponding computer program was written in the C language. At first, all the different segments as well as the whole program have been carefully tested and continuously improved, using simulated observational data without noise and with noise. The latter one essentially consists of the photon (Poisson) noise due to the sources and to the sky, and of the readout (Gaussian) noise of the CCD detector. Testing and debugging of the program clearly showed that the algorithm is very reliable, robust and works very fine for a large range of the input parameters.

APPLICATION TO Q1009-0252 A & B

The gravitational lens system Q1009-0252 A & B (magnitudes $m_V = 17.9$ and 20.5, angular separation $1\overset{''}{.}55$) was identified during a systematic search for multiply imaged quasars within a sample of Highly Luminous Quasars carried out at the European Southern Observatory (La Silla, Chile). Various spectra were obtained with EMMI at the NTT (seeing between $0\overset{''}{.}7$ and $1\overset{''}{.}2$, slit width of $1''$, pixel size of $0\overset{''}{.}44$, exposure times between 15 and 30 min, spectral resolution of about 10Å). Photometry and spectroscopy of Q1009-0252 have first been reported by Surdej *et al.* [5] who have found that the redshifts of both the A and B components are identical ($z = 2.74$) and the line profiles of Lyα+NV, CIV, and CIII] look very similar but there is an excess in the continuous spectrum of A near $\lambda = 5000$Å. They have proposed that Q1009-0252 A & B are multiple lensed images of the same quasar, and that the blue excess is possibly due to microlensing of image A. An independent observational study by Hewett *et al.* [3] has confirmed the gravitational lens nature of this system.

The spectra presented by Surdej *et al.* [5] were extracted, using a complete artisanal technique. In order to check those results, we decided to re-extract the spectra using the algorithm described here. Fig. 1 displays the extracted spectra for images A and B obtained by co-adding the results after processing the observational data from three CCD frames (exposure time of 30 min, seeing between $0\overset{''}{.}7$ and $0\overset{''}{.}85$) which have been recognized as being the best. The obtained spectra are in very good agreement with those reported in [5].

Interpretation of the spectral differences observed between the two lensed images Q1009-025 A & B in terms of differential macro-lensing, micro-lensing, extinction arising in the lensing galaxy as well as intrinsic source variations combined with the time delay has been proposed by Claeskens *et al.* [1].

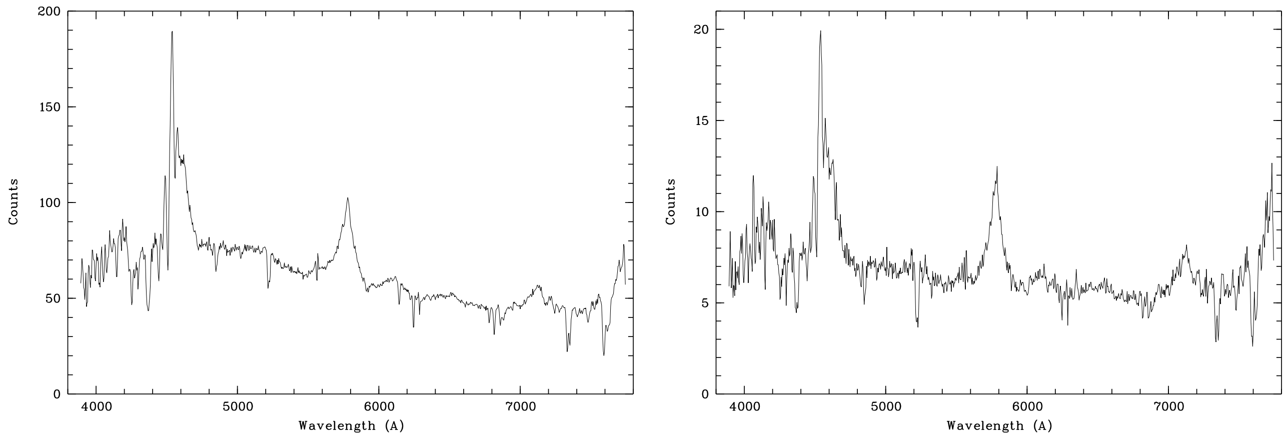

Figure 1: Spectra of Q1009-0252 A (left graph) and B (right graph) extracted using the proposed algorithm

CONCLUSIONS

The algorithm of optimal spectra extraction described in this report will be used in order to process some additional observations of gravitational lens systems observed in the framework of the ESO key program *Gravitational Lensing*. Finally, we intend to adapt this new algorithm to observations which will be obtained with the International 4-m Liquid Mirror Telescope (ILMT). This telescope ought to be constructed by the AMOS industrial company in Liège (Belgium) and be operated in Chile. A full description of this international project in which astronomers from Liège and from the Belgian Royal Observatory (Uccle) are involved is available at the URL: *http : //vela.astro.ulg.ac.be/lmt*.

As to the gravitationally lensed quasar Q1009-0252 A & B, it should be emphasized that only a systematic spectro-photometric monitoring of this doubly imaged quasar will enable us to disentangle the various effects (macro-lensing, micro-lensing, differential extinction, time delayed variability, ...) which are probably at work for this gravitational lens system.

Acknowledgments. We are grateful to M. Remy for some fruitful discussions about the algorithm. One of us (S. Kh.) would like to thank the Belgian OSTC for the research fellowship granted to him within the programme of scientific and technical cooperation with Central & Eastern Europe. Our research was supported in part by PRODEX (Gravitational lens studies with HST), by contract P4/05 'Pôle d'attraction interuniversitaire' (OSTC, Belgium) and by the 'Fonds National de la Recherche Scientifique' (Belgium).

REFERENCES

[1] *Claeskens J.-F., Khmil S. V., Lee D.-W., Sluse D., Surdej J.* HST and ground-based observations of the gravitational lens Q1009-0252 A & B // Astron. and Astrophys.–2000.–accepted.

[2] *Cornwell T. J., Evans K. F.* A simple maximum entropy deconvolution algorithm // Astron. and Astrophys.–1985.–**143**, N 1.–P. 77–83.

[3] *Hewett P. C., Irwin M. J., Foltz C. G., et al.* The close-separation gravitational lens candidate Q1009-0252 // Astron. J.–1994.–**108**, N 5.–P. 1534–1541.

[4] *Skilling J., Bryan R. K.* Maximum entropy image restoration: general algorithm // Mon. Notic. Roy. Astron. Soc.–1984.–**211**, N 1.–P. 111–124.

[5] *Surdej J., Remy M., Smette A., et al.* Two new very close pairs of quasars with discordant redshift and a gravitational lens candidate // Gravitational Lenses in the Universe / Eds J. Surdej, D. Fraipont-Caro, E. Gosset, *et al.*–Université de Liège, 1994.–P. 153–159.